SELECTIVE LASER MELTING OF HIGH STRENGTH-TO-MODULUS RATIO TNTZ AND TNTZ-O ALLOYS TAILORED FOR LOAD-BEARING BIOMEDICAL APPLICATIONS

by

Weihuan Kong

A thesis submitted to the University of Birmingham for the degree of DOCTOR OF PHILOSOPHY

School of Metallurgy and Materials
College of Engineering and Physical Sciences
The University of Birmingham
May 2022

ACKNOWLEDGEMENTS

My sincere thanks go to a great many people who guided and helped me on this piece of work. I wish to express my sincere gratitude to my supervisors, Prof. Moataz Attallah and Dr. Sophie Cox for their extensive support, patience, encouragement, and broad scientific expertise throughout the course of this research.

I feel grateful to enjoy an amount of precious Q&A and discussions with professionals whose work overlapping with a building named Netshape Interdisciplinary Research Centre, the University of Birmingham. Acknowledge to Prof. Mike Loretto, Prof. Yu-Lung Chiu, and Dr. Feng Wang for their knowledge and expertise in Ti alloys and electron microscopy characterisation; Prof. Alison Davenport thanks to her references recommendation in the scope of biomaterial corrosion and suggestions about electrochemical testing and corrosion fatigue; acknowledge to Prof. Hanshan Dong and Dr. Xiaoying Li for providing suggestions for thermal oxidation treatment and surface engineering facilities access; Dr. Victor Villapun thanks to his experimental suggestions and extensive cell culture work; acknowledge to Prof. Paul Bowen, Dr. Timothy Doel, Mr. David Price for rendering tensile/fatigue characterisation threads and machine access; acknowledge to Dr. Nick Adkins for his help in finding an affordable Nb powder supplier.

My thanks also go to people who offered their technical assistance. Acknowledge to Dr. Luke N. Carter and Dr. Sam Cruchley for their training of SLM machine, etc; Thanks to SEMs training from Mr. Paul Stanley, the help from Mr. Frank Biddlestone for his DSC runs, Mr. Christopher Stark for his ICP-MS runs, and Mr. Grant Holt for his vacuum HT runs. Acknowledge to Mr. Jaswinder Singh for etchant preparation and Miss Amy Newell for XRD set up during COVID-19 period. Thanks to all my colleagues in group.

Finally, I wish to express my sincere gratitude to my family members and friends who financially support my self-funded PhD project, and thank you so much for the love from my wife Xiang Wei.

LIST OF ABBREVIATIONS

3D	three-dimensional
ALP	alkaline phosphatase
AM	additive manufacturing
APT	atom probe tomography
ASTM	American Society for Testing and Materials
bcc	body centred cubic
BF	bright-field
BSE	backscattered electron
CCD	charge-coupled device
CE	chemical etching
CFD	computational fluid dynamic
CoCrMo	cobalt chromium molybdenum alloy
COF	Coefficient of friction
CP Ti	commercially pure titanium
DF	dark-field
DFT	theory functional theory
DLD	direct laser melting
DM	DigitalMicrograph
DSC	differential scanning calorimetry
E. coli	*Escherichia coli*
EBM	electron beam melting
EBSD	electron-backscatter diffraction
EDM	electrical discharge machining
EDS	energy dispersive X-ray spectroscopy
EPMA	electron probe microanalyser
ESEM	environmental scanning electron microscope
FCS	foetal calf serum

FEG	field-emission gun
FFT	fast Fourier transform
FIB	focused-ion beam
HAADF	high-angle annular dark-field
H_2O_2	hydrogen peroxide
HCF	high cycle faigue
HCl	hydrochloric acid
hcp	close packed hexagonal
hDPC	human periosteum-derived cell
HE	hydrostatic extrusion
HF	hydrofluoric acid
HGF	human gingival fibroblasts
HIP	hot isostatic pressing
HNO_3	nitric acid
HPT	high pressure torsion
HRTEM	high-resolution transmission electron microscope/microscopy
HT	heat treatment
ICP-MS	inductively coupled plasma mass spectrometry
ICP-OES	inductively coupled plasma optical emission spectrometry
IFFT	inverse fast Fourier transform
MEM	Minimum Essential Medium Eagle
MIC	minimum inhibitory concentrations
Nb_2O_3	niobium trioxide
Nb_2O_5	niobium pentoxide
OCP	open circuit potential
OIM	orientation-imaging microscopy
PBF	powder bed fusion
PBS	phosphate buffered saline

PJI	peri-prosthetic infection
ppb/m	parts per billion/million
PSD	particle size distribution
S. aureus	*Staphylococcus aureus*
S. epidermidis	*Staphylococcus epidermidis*
SAD(P)	selected-area diffraction (pattern)
SE	secondary electron
SEM	scanning electron microscope/microscopy
SIM	stress induced martensite
SLM	selective laser melting
ST	solution treatment/treated
STA	solution treatment then aging
STEM	scanning transmission electron microscope/microscopy
Ta_2O_5	tantalum pentoxide
TE	tissue engineering
TEM	transmission electron microscope/microscopy
THR	total hip replacement
TiO_2	titanium dioxide
TJR	total joint replacement
TKR	total knee replacement
TNT(Z)	Ti-Nb-Ta-(Zr)
TNTZ-O	Ti-Nb-Ta-Zr-O
TO	thermal oxidation
TPMS	triply periodic minimal surface
UTS	ultimate tensile strength
XRD	X-ray diffraction
XSAM	X-ray scanning analytical microscope
YAG	Yttrium-aluminium garnet
ZrO_2	

TABLE OF CONTENTS

ABSTRACT

In the study of TNT and TNTZ alloy design and manufacturing, the authors investigated Ti-Nb-Ta based β alloys with different zirconium additions (0, 5, 9 wt. %) manufactured by SLM. A low level of as-fabricated defects is obtained: the relative density of TNT(Z) alloys is >99.97% with the keyhole size in a range of 3—20 μm. BF-TEM images combining SAD patterns of TNT(Z) alloys show single β phase obtained inside the beta matrix; BF-STEM images reveal potential nano-scale grain boundary alpha phase precipitation. Zirconium functions as a neutral element in these high β-stabilized Ti-Nb-Ta based alloys. An increase in Vickers hardness and UTS caused by zirconium additions is observed, which is explained by beta grain refinement because higher degree of undercooling occurs. Corrosion ions of TNT(Z) alloys released from immersion testing at each time intervals show extremely small concentrations (<10 μg/L). It indicated that good biocompatibility during culture with the negligible corrosion ions. High strength-to-modulus ratio β Ti alloys together with excellent biological response show their prospect for biomedical applications.

In the study of TNTZ post-processing treatment, a Ti-34Nb-13Ta-5Zr (TNT5Zr) β Ti alloy with high strength-to-modulus ratio has been developed, showing its potential to become another candidate material in load-bearing implant applications. This work mainly investigates the microstructural evolution, mechanical properties, and biocompatibility of post-processing treated TNT5Zr alloy manufactured by selective laser melting (SLM). TEM observation shows

the existence of single beta grain matrix and alpha precipitates along grain boundary in SLM+HIP manufactured TNT5Zr alloy (TNT5Zr-AF+HIP), and ellipsoidal nano-sized intragranular α'' precipitates (approx. 5~10 nm) were introduced after subsequent low temperature aging treatment. The precipitation strengthening makes SLM+HIP+aging manufactured TNT5Zr (TNT5Zr-AF+HIPA) alloy obtained a comparable ultimate tensile strength (853 ± 9 MPa) to the reference material (Ti64-AF+HIP, 926 ± 23 MPa). Including the inferior notch-like surface of the test-pieces, slip-band cracking occurs in this ductile TNT5Zr-AF+HIPA alloy are regarded as the main factors to determinate its fatigue strength (170 MPa). *In vitro* short-term biocompatibility evaluation reveals that almost no significant difference of preosteoblast viability, differentiation, and mineralization between TNT5Zr-AF+HIPA and the reference biomaterial (Ti64-AF+HIP).

In the study of Ti-34Nb-13Ta-5Zr-0.2O post-processing treatment, advanced hot isostatic pressing (HIP) subjected to high and intermediate cooling rate (HCR & ICR) were exploited to close keyholes and tune the microstructure of SLMed Ti-34Nb-13Ta-5Zr-0.2O alloys (TNT5Zr-0.2O, wt. %). XRD analysis along with SEM and TEM micrographs reveal single beta phase in grain matrix of as-fabricated TNT5Zr-0.2O (TNT5Zr-0.2O-AF), TNT5Zr-0.2O-HCR, TNT5Zr-0.2O-ICR alloys. Additionally, high-angle annular dark-field (HAADF) micrographs show discrete large Ti-rich α grain boundary precipitates in TNT5Zr-0.2O-ICR alloy. Tensile properties show that TNT5Zr-0.2O-AF alloy possessed high UTS of 975 ± 12 MPa, and elongation of 4.9% ± 0.3%; the TNT5Zr-0.2O-ICR alloy obtained slightly higher

UTS (1036 ± 26 MPa) and lower elongation (3.0% ± 0.3%). S-N curves demonstrate fatigue limit of TNT5Zr-0.2O-ICR alloy (150 MPa) is slightly higher than the counterpart of TNT5Zr-0.2O-AF alloy (130 MPa), and slip-band cracking phenomenon was observed in both alloys. Advanced HIP subjected to intermediate cooling rate functions well to close SLM-processed keyholes but the resistance to fatigue is not markedly enhanced; the addition of proper amount oxygen interstitial solutes in TNTZ-O alloy is regarded as an inexpensive, effective strengthening technique for load-bearing biomedical applications.

In the study of TNT5Zr-0.2O surface treatment, the authors innovatively investigated the feasibility of thermal oxidation (TO) for improving the wear and fatigue properties of TNT5Zr-0.2O alloys manufactured by selective laser melting (SLM). Static chemical etching (CE) as a pre-treatment for TO successfully removed the SLM-induced surface adhered powders. A mixture of rutile, Nb_2O_5, Ta_2O_5, and ZrO phases were formed as an oxide layer after TO. It can be found a better wear resistance was retained in this β-titanium alloy after TO, as demonstrated by the wear scar features with ploughing grooves changing into brittle peeling of oxides. Plain fatigue strength of CE treated alloy (150 MPa) was 1.5 times higher than the value of CE+TO treated alloy (60 MPa), as a result of multiple premature fatigue cracks possibly developing in the compounds region after TO. *In vitro* biocompatibility results showed no significant differences in metabolic activity of pre-osteoblasts seeded on the treated surfaces. In addition, early and late mineralisation assays revealed similar levels of 14-day ALP activity, and 28-day mineral deposits formed on the two biocompatible TNT5Zr-0.2O alloy surfaces. Overall,

though the oxide layer is corrosion-resistant in the aggressive environment (3M HCl solution), showing potential application of TO in additively manufactured titanium medical devices. TO should be cautiously exploited due to the mechanical properties deterioration.

Three-dimensional (3D) porous structures have been receiving more attention for orthopedic implant development mainly due to their lower elastic moduli to prevent aseptic loosening, however, their low yield strengths may increase failure risk in load-bearing implants. In the study of TNT5Zr-0.2O lattice design and manufacturing, scaffolds infilled with sheet-based triply periodic minimal surface (TPMS) unit cells, namely diamond, gyroid, splitP, were manufactured with different design porosity (50%, 35%, 18%) via selective laser melting (SLM). Quasi-static compression tests showed that low elastic moduli (10~22 GPa) and high yield strengths (358~1045 MPa) were obtained in the varying TPMS cylindrical specimens, with both elastic modulus and yield strength increasing with density in each type of scaffolds. Metabolic activity and epifluorescence microscopy revealed lower osteoblastic cell adhesion and proliferation in denser scaffolds, possibly resulting from lower available area and limited transport into the inner pores. A good balance of high strength and low modulus is obtained in low-porosity TNT5Zr-0.2O TPMS scaffold implants, which potentially work well in human body and provides long service time.

1 THESIS INTRODUCTION

Musculoskeletal disorders, including bone and joint pathologies affect millions of people across the world, especially those aged 50 years or older [1]. Medical treatments associated with these conditions also bring substantial economic burden, for example total joint replacement (TJR) surgery, revision surgery of total joint prosthesis, or long-term hospitalization for infection healing [2,3]. Furthermore, intangible costs associated with chronic pain and a reduced quality of daily living have produced a deep effect on work absenteeism and lower performance [1]. Hence, biomaterials, which possess mechanical properties similar or superior to the counterparts of bone, combined with excellent biocompatibility should be carefully developed then employed in human joint replacement implant market aiming to overcome variety of bone diseases and prolong an implant's lifespan after employment.

Some as-below descriptions make researchers concern about the reliability of currently used load-bearing implant materials, of which the most popular are cobalt-chromium alloy, 316L stainless steel and Ti-6Al-4V. Of particular relevance to this thesis is the much higher elastic modulus of these alloys compared with bone, which may lead to localised resorption of native tissue referred to as the "stress shielding" effect and eventual loosening of prosthetic devices [4–6]. Moreover, surface oxide film is disrupted in the presence of wear and fretting [7,8]. Thus, the formation of fine particulate debris significantly contributes to the overall rate of corrosion and released cations. According to the former work, cytotoxicity caused by high concentration

of released metallic ions has been observed when performing cell culture assays [9,10]. Beta titanium alloys with the addition of enough human-friendly β stabilizers such as niobium, molybdenum, and tantalum have been investigated for high strength-to-modulus ratio biomechanical material development, demonstrating the potential for load-bearing implant application [11–14]. The ratio is generally considered as the higher ratio may eventually lead to a lower risk of prosthesis failure through loosening of fracture. Hanada et al. [15] illustrated the feasibility to obtain a Young's modulus of approximately 40 GPa by optimizing the composition of β Ti-Nb-Sn alloys, which is extremely close to cortical bone (approx. 10~30 GPa [16]). Another advantage of Ti-Nb based beta titanium is its excellent corrosion resistance, Atapour et al. [17] conducted cathodic polarization and 10-day immersion experiment of different types of Ti-alloys in 5 M HCl electrolyte at 37°C, reporting that Ti-35Nb-7Zr-5Ta alloy (wt. %) is more corrosion resistant than Ti-6Al-4V ELI due to the presence of less chemical dissoluble Nb_2O_5, ZrO_2 and Ta_2O_5 in the titanium oxide thin film. In addition, Gordin et al. [18] and Neacsu et al. [19] presented similar short-term *in vitro* MC3T3-E1 results (e.g., cell viability, proliferation and differentiation) between conventionally manufactured Ti-Nb-X alloys and commercially pure (CP) titanium. These advantages potentially make TNTZ alloys more competent for long-term clinical use than other metallic biomaterials.

Considering some factors like supply chain simplification, component design flexibility, life-cycle energy consumption of tailored parts, environmental impact reduction [20], selective laser melting (SLM) technique can be a good option for manufacturing high-end beta titanium

alloy biomedical implants when comparing with conventional manufacturing techniques. Even so, it is necessary to consider what are the main disadvantages of SLM Ti-Nb based β Ti alloys. The first concern arises from the relatively low UTS caused by main beta phase matrix with body-centred cubic (bcc) lattice arrangement, commonly observed in high β-stabilized Ti alloys after undergoing fast cooling rate. Therefore, it increases the risk of implant early-stage failure in service. Another concern is that the existence of as-fabricated defects (e.g., keyhole, adhered powder, etc.) may also deteriorate material's mechanical properties [21–23].

The **aim** of this thesis is to manufacture high strength-to-modulus ratio biomechanical Ti-Nb-Ta-Zr and Ti-Nb-Ta-Zr-O implant by SLM and reveal the corresponding phase transformations using XRD & EM characterisations. At the same time, the thesis is also designed to showcase the comprehensive properties of these alloys combining mechanical behaviour and biocompatibility. In **chapter 2**, the literature review started from those characteristics of bone on the scope of tissue engineering (TE), and the major concerns about metallic candidates in load-bearing implant applications. Furthermore, the author also covered SLM processing features, and performed a systematic review including physical metallurgy, material design, microstructural evolution, mechanical properties, wear and corrosion, *in vitro* and *in vivo* response of beta Ti-alloys fabricated by the commonly used conventional manufacturing and becoming-popular additive manufacturing (AM) techniques.

Although some studies have been carried out to characterise the microstructure and mechanical properties of TNTZ alloys with scattered compositions [24–26], there is a lack of previous

investigation into the impact of additions of zirconium in AMed TNTZ alloys on the mechanical properties and biocompatibility. Accordingly, **objective 1** in **chapter 3** is to investigate systematically, the microstructural evolution and mechanical properties in different zirconium addition TNT(Z) alloys manufactured by SLM. **Objective 2** in **chapter 3** is to characterise the long-term ion release behaviour in TNT(Z) immersion test and conduct an initial evaluation of cytocompatibility using MC3T3-E1 pre-osteoblast cells.

It can be found microstructural evolution and mechanical properties evaluation have been performed on conventionally manufactured TNTZ alloys after underwent heat treatments [27,28], but no publications referring to the influence of hot isostatic pressing (HIP) and low-temperature aging on microstructure, mechanical properties of AMed TNTZ alloys have been found. Hence, **objective 1** in **chapter 4** is to investigate the microstructural evolution, defect distribution, strengthening effect of mechanical properties from SLMed Ti-34Nb-13Ta-5Zr alloy after post-processing treatment, such as traditional HIP, low temperature aging treatment. **Objective 2** in **chapter 4** is to compare tensile properties and *in vitro* MC3T3-E1 preosteoblast response of this alloy with benchmark Ti-6Al-4V, which is commonly found in load-bearing biomedical implants.

The effect of oxygen concentration on phase transformations in TNTZ-O alloy (also known as Gum Metal [29]) manufactured using conventional manufacturing techniques is not commonly accepted. There exist different standpoints like: (i) Oxygen addition retards the formation of athermal ω and α'' phases in Gum Metal [30,31]. (ii) Oxygen function as interstitial atoms, then

tends to form extremely short-range atom clusters around zirconium atoms in Gum Metal [32]. (iii) High concentration of oxygen within Gum Metal is regarded as the potential reason for β → isothermal ω phase transformation during aging [33]. Additionally, the prior investigations have shown that the microstructure observed in TNT(Z) alloys is sensitive to cooling rate after high temperature homogenization treatment. **Objective 1** in **chapter 5** is to investigate the oxygen effect on microstructure and mechanical properties of SLMed Ti-34Nb-13Ta-5Zr-0.2O alloy. **Objective 2** in **chapter 5** is to tune the material's microstructure and mechanical properties using advanced HIP subjected to high/intermediate cooling rate.

Available literature shows a lack of surface hardening treatment attempts for additive manufactured components aiming to develop long-term durable artificial joints. In **chapter 6**, the author investigated the feasibility of thermal oxidation (TO) for improving the comprehensive properties of SLMed Ti-34Nb-13Ta-5Zr-0.2O alloy. **Objective 1** in **chapter 6** is to demonstrate its surface and matrix microstructure after chemical etching (CE) and TO treatment via XRD, SEM-EDS characterisation, and discuss the oxidation behaviour and its mechanism of the β titanium alloy at high temperature (1000℃). **Objective 2** in **chapter 6** is to evaluate the tribological behaviour and find out the corresponding wear mechanisms for the alloy before & after TO. **Objective 3** in **chapter 6** is to compare the plain fatigue strength, and investigate fatigue crack initiation, propagation behaviour difference in TNT5Zr-0.2O-CE and TNT5Zr-0.2O-CE+TO alloy. Additionally, the aggressive 3M HCl solution was used to form chemically induced notches, then evaluate the anti-corrosive protection of TO formed oxide

layer in chemical-interfering fatigue test. **Objective 4** in **chapter 6** is to showcase the *in vitro* performance, including cell metabolic activity, differentiation, mineralisation when culture onto the two biocompatible TNT5Zr-0.2O alloy surfaces.

Not much research has been performed to evaluate the comprehensive properties including compression properties and biocompatibility of sheet-based triply periodic minimal surface (TPMS) β titanium alloys to date. In **chapter 7**, the author SLM processed & heat treated Ti-34Nb-13Ta-5Zr-0.2O scaffolds with different design porosity level (18, 35, 50%) via the selection of three sheet-based minimal surfaces including diamond, gyroid, splitP, which have been regarded as the ones received the special interest by investigators. **Objective 1** in **chapter 7** is to measure Young's moduli, compressive offset stress of these as-built lattices by performing quasi-static compression tests. **Objective 2** in **chapter 7** is to conduct the *in vitro* investigation aiming to show how the spreading, viability of preosteoblasts onto the β titanium alloy gyroid meshes. The conclusions relevant to the development of high strength-to-modulus ratio biomechanical TNTZ(O) implant, and the further work in the scope of a better understanding its comprehensive properties were detailed in **Chapter 8.**

2 LITERATURE REVIEW

2.1 Bone and its replacement

2.1.1 Bone mechanics

Some snapshots in the scope of bone mechanics provide significant guidance in bone replacement research and development. Bone, important to human body both biomechanically and metabolically, possesses a lightweight composite matrix that combines collagen fibres, mineral and non-collagenous proteins [34]. As one extraordinary multifunctional hard tissue, it is responsible for mechanical support, soft tissue protection from inner cavity and supply the framework for mineral homeostasis, and haematopoiesis [35]. Long bones like humerus, femur, and tibia have been regarded as classical models for investigation at the macroscopic scale. The above-mentioned bones have a common structural feature: the cross-section area of ends is wider than the central part due to the ends have joints covered by articular cartilage. Bone can be divided into cortical and cancellous bone with different microscopic structure, as shown in Fig. 2-1. At a tissue level, human cortical bone consists of secondary osteons surrounding Haversian canals and embedded in interstitial tissue, which is the remnant of old osteons [36]. Moreover, cortical bone constitutes the primary component (approx. 80% skeletal mass) in adult human skeleton, which forms the outer wall of all bones and is largely responsible for the supportive and protective function of the skeleton [34]. The remaining 20% of the bone mass is cancellous bone with a lattice of large plates and rods known as trabecula, found in the inner parts of bone [34]. It is noteworthy that the distribution of cortical and cancellous bone varies

between individual long bones. For example, the percentage of cortical bone mass in ulna (92%) is much higher than the counterpart in vertebra (62%). Furthermore, the mass ratio of cortical to cancellous bone also changes along with skeleton development, demonstrating magnitude of the sexuality and age-dependent changes [34].

Young's modulus is an important constant to reveal mechanical properties of human bone. It has been shown that the average elastic modulus of diaphyseal cortical bone ranges for adults aged 53 to 93-year, measured by nano-indentation, was 20.1 ± 5.4 GPa and that of cancellous bone was 11.4 ± 5.4 GPa [37]. In addition, it should be stressed that there distributes delicate routing of vascular and nervous supply in skeleton. Most of the blood supply to the cortex of long bone come from medullary vessels with variety of arteries (e.g., nutrient, metaphyseal, epiphyseal ones), which have been regarded as proteins and other substances exchange pathway for relevant tissues. Nerve fibres have also been found in localised sites like Haversian canals and bone marrow [38].

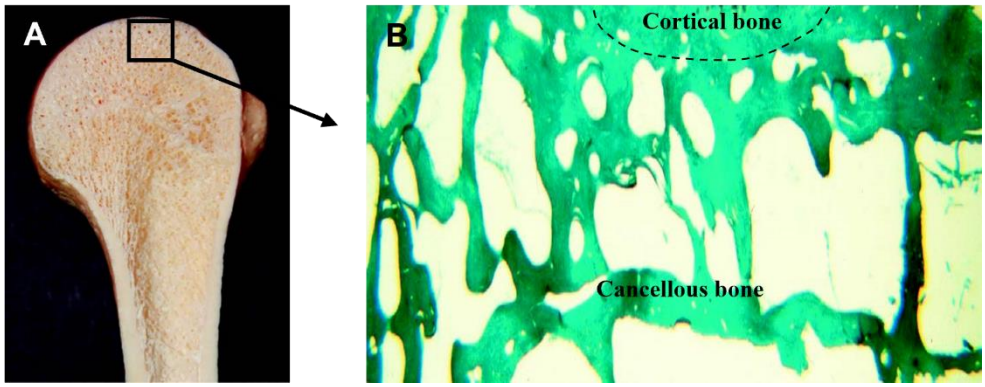

Fig. 2-1. Schematic of the formation of skeleton with cortical and cancellous bone (A) macroscopic bone (B) microscopic bone [35].

Three major cellular elements of bone, namely osteoclasts, osteoblasts and osteocytes are involved in bone growth and maintenance. It can help to analyse some *in vitro* or *in vivo* results after acknowledging the function, differentiation and apoptosis of them. Osteoclasts are the primary cells involved in bone resorption. The typical feature of mature osteoclasts is multinucleation from 1 to more than 50 nuclei and range in diameter from 20 to over 100 μm. Osteoclasts are derived from the hematopoietic monocyte-macrophage lineage. At the initiation stage of bone remodelling, hematopoietic precursors are controlled by different factors to accumulate nuclei and proliferation, as shown in Fig. 2-2. Osteoclasts undergo programmed cell apoptosis after bone resorption completion. By comparison, osteoblasts are responsible for bone formation and indicate as a layer of contiguous cuboidal cells. They are recognized by the site of bone surface with exhibiting high levels of Alkaline Phosphatase (ALP) and speciallized bone proteins. Osteoblasts originate from mesenchymal progenitors in the mesenchyme or in the marrow stroma. The lifespan of osteoblasts can be devided into five steps, namely proliferation, extracellular matrix development and maturation, mineralisation and apoptosis, which are dominated by the specific factors and genes, as shown in Fig. 2-3.

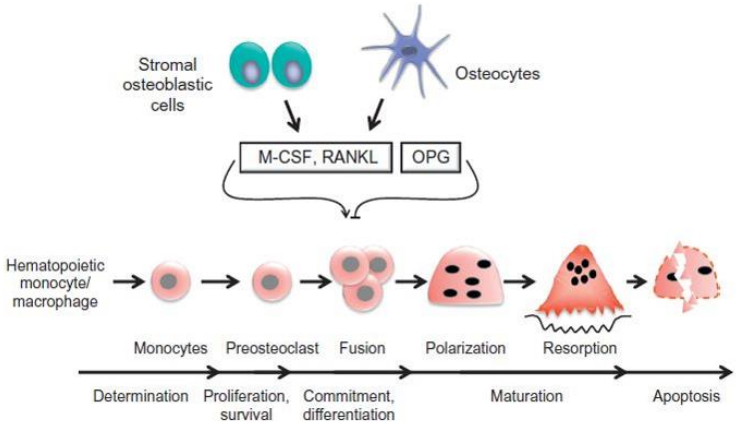

Fig. 2-2. The scheme of osteoclast differentiation and apoptosis governed by main transcription factors [35].

Osteocytes, as the most abundant cells in bone, which comprise more than 90% of cells within the matrix or on the bone surfaces. Increasing evidence has been demonstrated that osteocytes secrete factors to regulate the function of osteoblasts and osteoclasts in respond to mechanical and hormonal cues. For example, osteocytes detect bone micro-damage and signal to

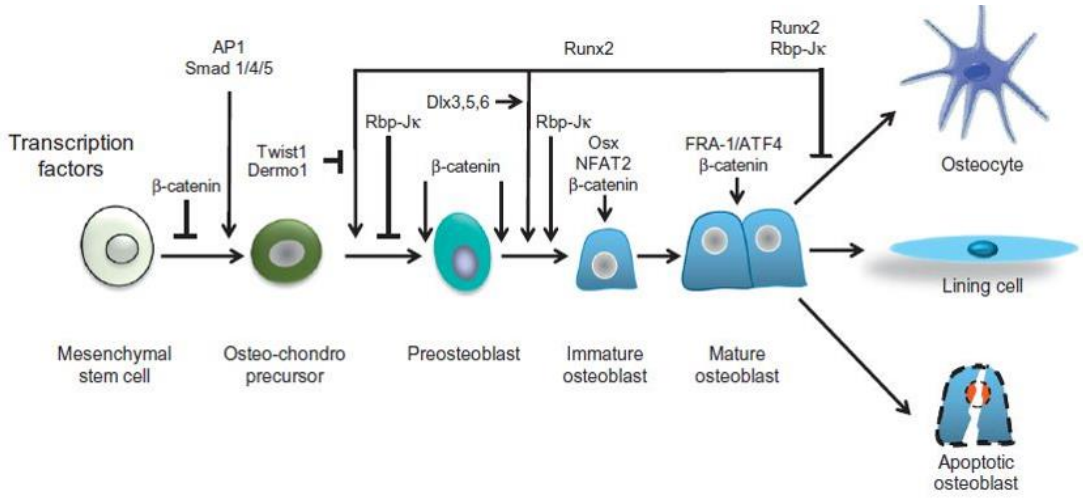

Fig. 2-3. The scheme of osteoblast generation which relevant to main transcription factors [35].

osteoblasts to induce the replacement of damaged bone. They also signal to osteoclasts to create local skeleton mass and geometry changes when mechanical load increases. Additionally, an important phenomenon reported by researchers is that the number of osteocytes declines at old age [35].

Unfortunately, replacement of bone is very common, in particular synovial joint arthroplasty. Osteoarthritis is the most common degenerative human joint disease worldwide, which has been characterised by loss of joint cartilage that leads to pain and even loss of load-bearing function. It mainly occurs in older individuals affecting 9.6% of men and 18% of women

aged >60 years [39]. The clinical necessity to effectively treat osteoarthritis is expected to increase as population ageing continues to grow [40]. Traditionally, the end-stage pain cannot be removed by conservative modalities like intra-articular injections, weight loss unless operating joint replacement operations [41], which are mainly well recognised as total hip replacement (THR) and total knee replacement (TKR) aiming to mitigate pain and restore mobility and strength for daily activities. In the surgical procedure, the damaged bone and cartilage is removed and replaced with prosthetic components, see Fig. 2-4. As metallic implants are the primary biomaterials used for joint replacement and becoming increasingly important [42], the following sections will review the comprehensive properties, challenges and development of metallic biomaterials rather.

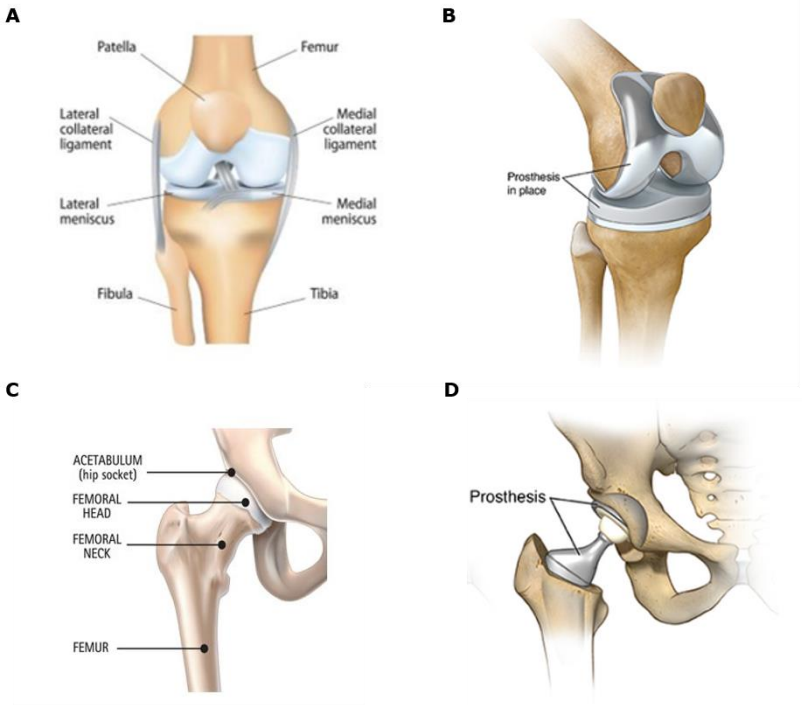

Fig. 2-4. (A) Schematic of a normal knee joint and (B) total knee replacement; (C) A normal hip joint and (D) total hip replacement. Sourced from https://www.medicalnewstoday.com/.

2.1.2 Essential considerations for load-bearing metallic implants

(1) Implant biocompatibility. Biocompatibility has been defined as the ability of a material to perform with an appropriate host response in a specific biological environment [43]. It could involve the terms such as cytotoxicity, irritation, chronic systemic toxicity, genotoxicity, hemocompatibility, carcinogenicity [44]. As shown in **section 2.1.1**, delicate vessels and nerves distribute inside bone, and variety of cells in bone and these vessels, therefore load-bearing metallic implants inevitably interplay with cells or tissues after joint replacement. For long-term efficacy, a metallic material should receive a favourable host response during service without sacrificing local or systemic responses of the living system or tissue [45]. Referring to cobalt-chromium alloy implant, it has been presented potential carcinogenic hazards for human body [46,47], *in vitro* and *in vivo* genotoxic effects [48], also adverse effects on the immune system caused by wear particles and released ions [49,50]. The cytotoxicity caused by high concentration nickel and chromium released from 316L stainless steel has been proposed when performing osteoblast-like cell culture test [9]. In addition, some descriptions make investigators concerned about the reliability of prosthesis manufactured from Ti-6Al-4V (wt. %). Higher vanadium concentration exceeding the reference has been detected from patients after 4.9-year (mean value) prosthesis exposure even though the minor vanadium element addition in Ti-6Al-4V [51]. According to the cell culture results, sharp inhibition of murine MC3T3-E1 preosteoblasts, L929, V79 fibroblast cell growth has been observed with the presence of high concentration released aluminium and vanadium ions [52].

(2) Implant mechanical properties. The elastic moduli of ever served load-bearing implant materials are much higher than the one of natural bone (approx. 10~30 GPa). Cobalt-chromium alloy obtained bimodal ($\alpha + \varepsilon$) phases has been measured with a very high Young's modulus (210~250 GPa) in tensile testing [53], and the counterpart of 316L austenitic stainless steel is also very high (approx. 200 GPa) [54]. Ti-6Al-4V, one bimodal ($\alpha + \beta$) Ti-alloy has been reported possessing a relatively high elastic modulus ranging from 100~120 GPa. According to Wolff's law, bone is formed and strengthens along lines of mechanical stress [55]. Therefore, the "stress shielding" effect occurs after metallic artificial prosthesis long-term instalment. Originally, the load is carried by bone, but it is carried by both the implant and bone after total joint replacement (TJR) surgery [56]. Stress shielding effect is considered as a stiffer implant sustains the majority of the patient's weight and causes a reduction in the stress level within bone, which leads to the detrimental remodelling of peri-prosthetic bone, thus resorption of tissue surrounding the implant occurs due to the change in the load transfer after TJR surgery [4–6,57]. Some cases after the replacement of S-ROM modular HIP implant (DePuy Synthes) have shown extensive loss of bone mineral content proximally (up to 50%) [57], see an example in Fig. 2-5. Due to a loss of bone around the old prosthesis, it has been reported that the further revision surgery can be more difficult and less successful than primary THR [58]. The former research results [59] suggested that lower elastic modulus stem causes lower level of stress shielding and change in medullary bone density adjacent to the implant were fundamentally different as a function of stem stiffness. Moreover, strength levels (e.g., ultimate tensile strength)

of implant materials, as defined in a standard tensile testing at room temperature are regarded as crucial values to evaluate the mechanical reliability. In order to stress the importance of the two values (Young's modulus and strength) in implant material development, strength-to-modulus ratio is introduced, which is generally considered as the higher ratio may eventually lead to a lower risk of prosthesis failure through loosening of fracture. Cyclic loading applied to orthopaedic implants during body motion may result in alternating plastic deformation. Fatigue fracture has been regarded as the major cause of premature failure in implants when exposed to millions of cyclic deformations over their lifetime [16]. Besides, stress concentration possibly occur in the sites of the unsmooth surface, corrosion induced notches or inhomogeneous microstructure of implants [54]. Historically, orthopaedic device fatigue failures of those aforementioned ever served materials have been reported after TJA caused by the inferior surface roughness or embrittled microstructure [16,60,61]. Even though the fatigue testing standards [62,63] of metallic biomaterials can be found, there is no standard or paper showcase the requirements of fatigue strength for ever-served material's long-term survival (e.g., 5-year without failure).

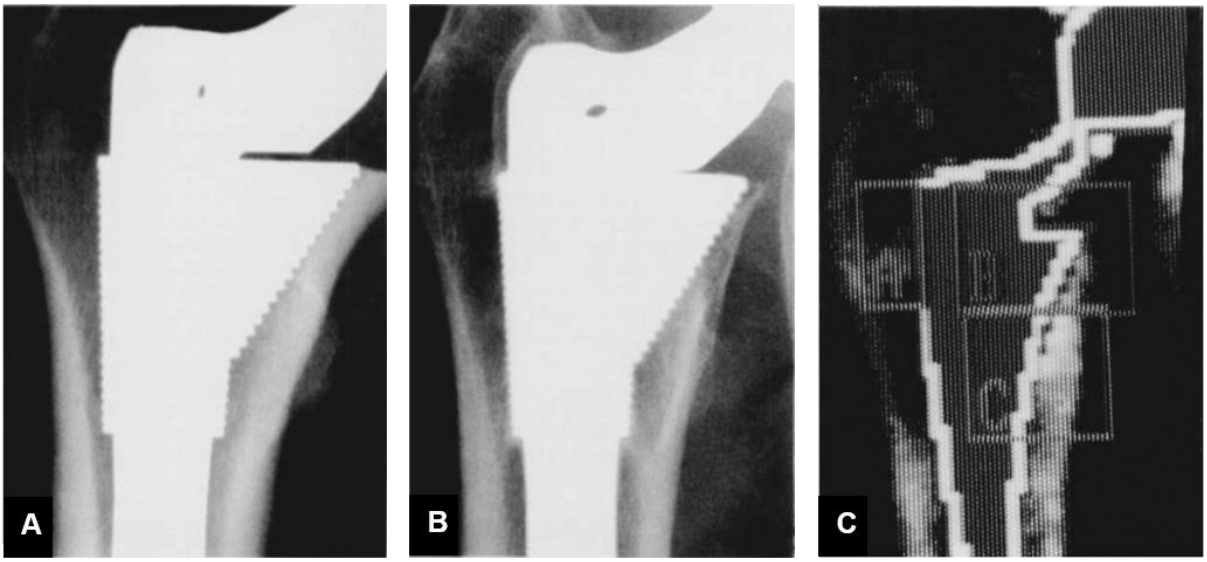

Fig. 2-5. (A) immediate postoperative and (B) two-year AP roentgenograms of an S-ROM stem (Joint Medical Products, Stamford, Connecticut) used in a 62-year-old woman with osteoarthritis. (C) computer-generated image of the two-year in use stem after scanning by dual energy X-ray absorptiometry [57].

(3) Corrosion and wear resistance. When metallic implants are exposed to the *in vivo* environment, the major concern is a possible long-term cytotoxicity in human body due to the presence of accumulated corrosion products during implant degradation [64]. Moreover, electrochemical corrosion increases crack propagation rate when experiencing cyclic mechanical loading, thus affecting implant structural stability, and shortening its lifespan. It has been mentioned the working environment of warm serum solution would stretch any alloy to its limits; implants supposed to last twenty years maybe need replacement after only two or three [65]. Therefore, manufacturers must face serious underperformance of current designs. Besides, it is well known that wear happens at the two surface interaction regions that caused by displacement and detachment of the material [66]. Therefore, the surface oxide film of implant is disrupted in the presence of wear and fretting [7,8]. The formation of fine particulate debris contributes significantly to the overall rate of corrosion and cations. It is noteworthy that

excessive wear of the components may increase the risk of implant loosening [54,67].

(4) Implant infection. Peri-prosthetic joint infection (PJI) is considered as one significant complication following total joint replacement (TJR), which increases the necessity of implant two-stage revision operation [68]. Despite continuous efforts and progresses in the development of preventive strategies over the years, the rate of PJI remains at 1% to 2% [69,70]. The PJI process is described as below: the implant-infection relevant bacteria (e.g., *S. aureus*) approach the surface of prosthesis through an interaction of physical or chemical force, then host proteins subsequently strengthen peri-prosthetic bacteria aggregation and forms slimy biofilm [71], which is developed to resist cellular and humoral immune responses. Particularly in the treatment of PJI, patients have to suffer from severe pain during long interval treatment (more than 6 weeks) in hospital for revision surgery. Additionally, direct therapy expenses for eradication of infection, and restoration of function normally are extremely high [71,72].

2.2 Metallic implants manufactured via selective laser melting (SLM)

2.2.1 Brief overview of SLM processing features

Powder bed fusion (PBF) techniques typically involve selective sintering or melting of powder feedstock using either a laser or an electron beam based on a powder-bed [73]. Selective laser melting (SLM) is developed according to the principle of incremental layer-by-layer material consolidation, facilitating the fabrication of complex and delicate components through the controlled melting of metallic feedstock powder with the aid of high-energy laser supply [74]. Main-stream SLM system has been introduced Nd: YAG fibre laser (wavelength 1064 nm) as

energy supply that is capable to selectively melt powder in purified argon or nitrogen atmosphere. In addition, build platform could be optionally heated to the temperature range at approx. 100~200℃. The main components of SLM system are shown in Fig. 2-6 [75]. Notably, build parameters like laser power, scan speed, scan spacing, layer thickness, and scan strategies should have been systematically optimised before on-demand component manufacturing. Considering these factors like supply chain simplification, component design flexibility, life-cycle energy consumption of tailored parts, environmental impact reduction, SLM technique could be a good option for manufacturing high-end components when comparing with conventional manufacturing techniques [20]. As mentioned in **section 2.1.1**, the skeleton related issues (e.g., sexuality or age-dependant mechanical properties difference of long bones, dimensional diversity of individual long bone), and varying prosthesis failure rates caused by inappropriate femoral head size or implant geometry manufactured by substrative manufacturing [58], which has led to an increasing prevalence of SLM since it may enable the production of customised medical devices.

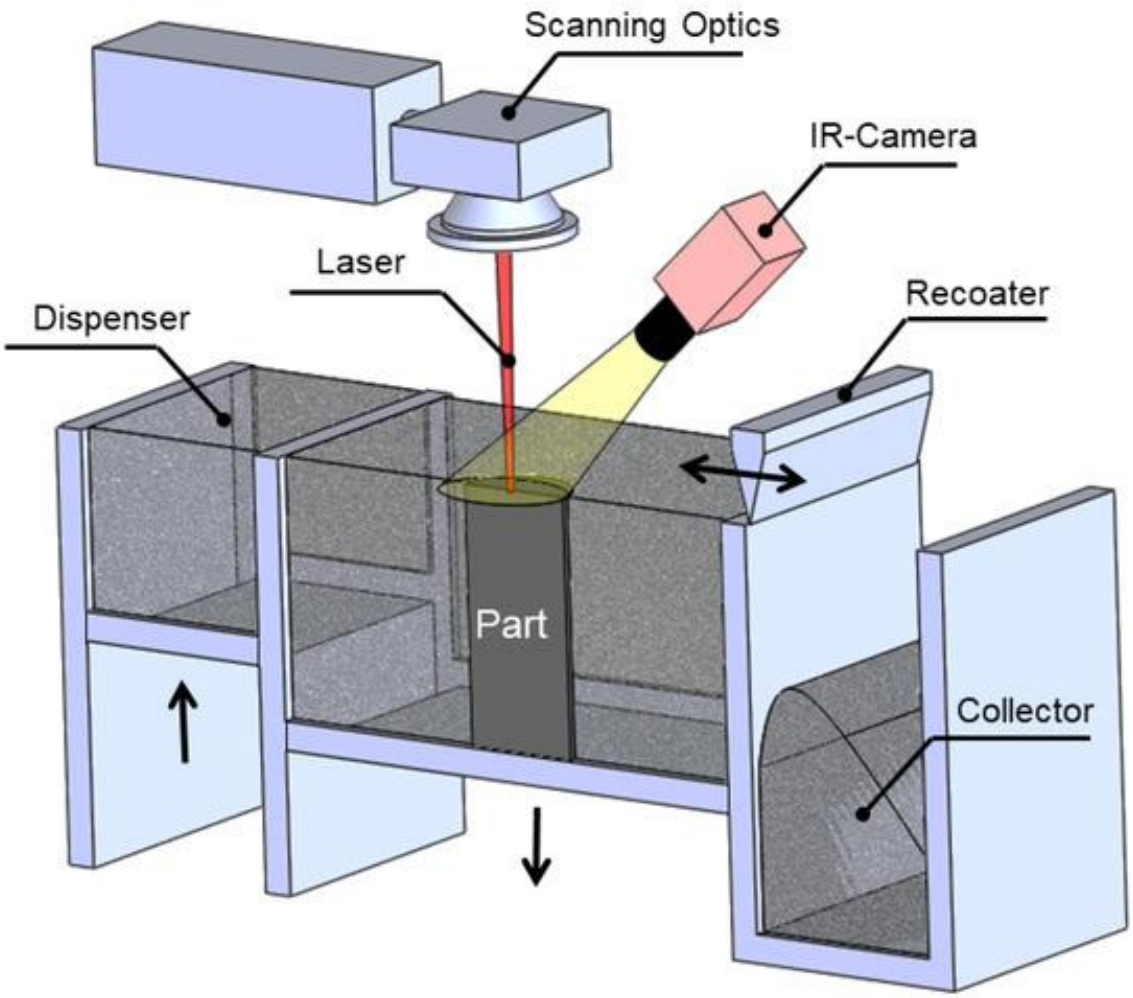

Fig. 2-6. Schematic of the selective laser melting system [76].

Here show some characteristics of SLM processing including heat source, interaction between laser and powder feedstock, cooling rate. The power density distributions of laser often follow the axisymmetric Gaussian profile. It indicates that higher power density is obtained at the heat source axis and the power density decreases at all radial locations caused by laser spot radius coarsening. Powder energy becomes more focused resulting in a high peak temperature underneath the heat source, with the increase of the laser distribution factor [77]. During laser scanning, the photon energy is transformed into thermal energy by absorption by the feedstock. Notably, the absorption is highly relevant to the thermal properties of powder material, the

distriution of particle sizes, and the spatial distribution of the particles [78]. The energy absorption affects the temperature profiles, solidification, microstructure and properties of the AMed part [77]. When SLM forming an incident on the powder bed, part of the energy is absorbed by the particle and the rest is reflected, which continues till the beam emerges outside of the powder bed or its intensity becomes negligible. Notably, the interaction can appear multiple reflections within the powder layers, which is used to decrible the energy penetration [79]. The processes such as thermal radiation, thermal convection, evaporation of alloying elements cause a heat loss during SLM. Heat convection between the material and the shielding gas occurs; the absorbed thermal energy is distributed into the powder and solidified parts due to heat condution (see Fig. 2.7) [80]. Markl et al. [80] mentioned the high surface tension in combination with the wetting ability of metals results in a smooth surface for stable melt pools. Generally, rapid cooling occurs in SLM process owing to its relatively high scan speed. That said, cooling rates may vary significantly depending on the alloy system and the location of the build where measurements are taken [81], which may result in inhomogenous microsturtcure across the part.

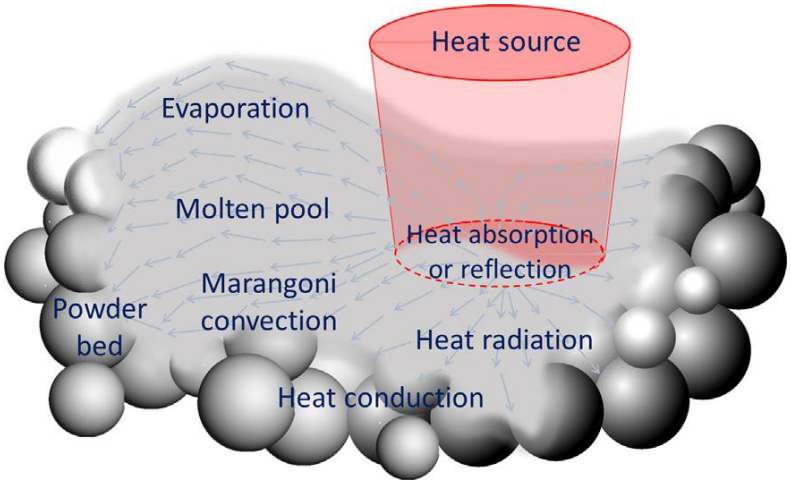

Fig 2.7. Heat transfer and molten pool dynamics during powder based additive manufacturing [77].

Except for the aformentioned advantages and characteristics of SLM processing, the typical SLM process-induced defects should also be stressed. The mechanism of keyhole formation has been mentioned like that rear part of molten pool bears with intensive local evaporation due to incident beam reaction, then dynamic recoil pressure of vapor jet and surface tension pressure dent the adjacent wall, thus it forms keyhole [22,82] as illustrated in Fig. 2-8A. It has been reported that the keyhole was not stable but fluctuated considerably and this periodical instability (generation and degeneration) was closely related to the porosity formation [82]. The keyhole porosity should be regarded as one of the serious problems in very high energy input SLM manufacturing. Besides that, the machanism of lack of fusion voids (Fig. 2-8B) has been concluded that inadequate penetration of molten pool from upper layers into the previous layer [83,84]. Zhang et al. [85] demonstrated the lack of fusion defect may contain numerous un-melted powders inside the poor bonding zone. To avoid the lack of fusion voids, key SLM variables should be appropriately adjusted to attain an adequate depth of penetration in molten pool. At the same time, the defects such as internal un-melted particle and external

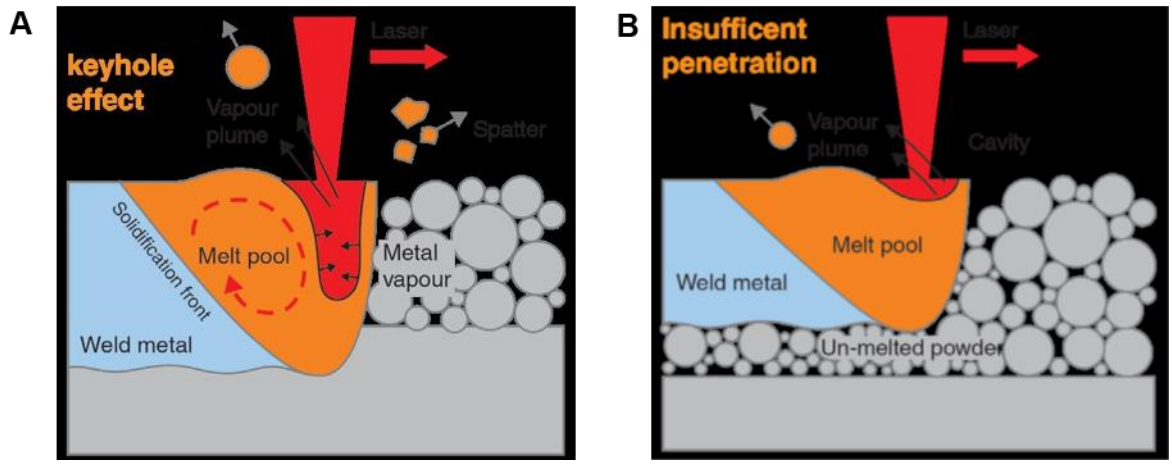

Fig. 2-8. (A) Keyhole effect- a deep cavity is formed by an intense laser spot. (B) Insufficient penetration of the laser energy leaves un-melted material in the component. Sourced from *www.renishaw.com*.

adhered powder are commonly found in SLM manufacturing. The former feature is typical for melting alloys without enough laser energy input. As a consequence, un-melted particles may cause localized alloy composition deviation when performing *in-situ* alloying with different pure element powders [86]. The latter mechanism is supposed to be that limited amount of liquid blocks the sufficient growth of sintering necks between metal agglomerates on high-speed AM [87]. The presence of voids and inferior surface roughness (caused by external adhered powder) have been considered as the preferred crack initiation sites, which lowers the fatigue limit of engineering materials [88].

2.2.2 Biomedical lattice structures build

Some porous scaffolds allow bone cell migration during the colonisation process and provide pathways for transport nutrients and waste from cells [89]. Besides that, smaller mismatch between the elastic modulus of bone and the implant can reduce risks associated with "stress shielding" effect [90]. The most well-known model generated by Gibson and Ashby [91], is based on the definition of a simple cubic unit cell and the use of beam theory to predict the response to load. Example relations for predicting elastic modulus of the three dimensional open-cell or closed-cell foam (E^*) and constituent solid material (E_s) is given below.

$$\frac{E^*}{E_s} = C_1 \rho_r^2 \quad (open\ cells) \tag{2.1}$$

$$\frac{E^*}{E_s} = C_2 \rho_r^3 \quad (closed\ cells) \tag{2.2}$$

where the terms C_1 and C_2 are constants and ρ_r is the reletive density of foams. The relative density essentially defines how much solid material is present in the overall volume occupied

by the cellular material. The complement to unity of the relative density is porosity, calculated as $1 - \rho_r$. Note that the same relative density lattices (with different unit cell strctures) may bahave differently in mechanical tests, relative density alone is not sufficient to characterise the properties of a cellular material [92]. A brief review of the key findings in additive manufactured common use Ti-6Al-4V lattice structures is shown as-below.

Nava et al. [93] inverstigaed the relationship between structural porosity and mechanical propeties of Ti-6Al-4V stochastic foam manufactured by electron beam melting (EBM). They concluded that Gibson and Ashby equation was incapable to predict elastic moduli of their porous specimens due to a wrong exponent in that model. Notably, mechanical performance of these AMed lattices were poor in compression testing; maximum 0.1% offset yield strength was 119.4 ± 5.8 MPa obtained from the foams with 0.44 releative density. In addition, complex implantable AMed scaffolds with different unit cell or porosity and their properties have been widely investigated [94–98]. They considered that geometry difference caused by relative density settings is the dominant constraint for the variation of as-measured mechanical properties. Weißmann et al. [99] designed and manufactured diverse Ti-6Al-4V lattice structures by using twisted unit cell with several orientations. They considered that unit cell orientation should be under consideration when predicting the relationship between relative density and mechanical properties. Moreover, the maximum compressive strength of these scaffold arrays is approx. 400 MPa, which shows the potential of bearing the impact loads. A similar study [100] investigated the influence of unit cell pose of Ti-6Al-4V lattice structure on

its mechanical properties. The authors found that the elastic modulus and ultimate compressive strength in the Z-direction significantly improved when the sample pose is ≥30° but without any explaination. At the same time, the extremely low ultimate compressive strength (14.8 MPa) was measured in a sample with the best mechacnial performance even though it possessed a low Young's modulus (0.6 GPa).

Li et al. [101] investigated compression fatigue behaviour of additive manufactured Ti-6Al-4V scaffolds with different porosity. All the as-fabricated specimens were measured with low fatigue limit (less than 50 MPa) run out at 10^7 cycles in high cycle faigue (HCF) testing. They concluded that fatigue crack initiation and growth through the mesh struts when they underwent cyclic ratcheting. Hooreweder et al. [90] and Dallago et al. [97] both introduced HIP to modify mechanical properties of the SLMed Ti-6Al-4V. The process was effective to close internal porosity and improve fatigue performance to some extent. At the same time, they regarded inferior surface roughness as a fatigue deterioration factor for these manufactured porous scaffolds. Recently, Liu et al. [102] and Wu et al. [103] produced SLMed cellular structures with typical unit cell and porosity using CP-Ti and Ti-6Al-4V. In both studies, normalized S-N (fatigue stress/yield stress, cycles) curves of these scoffolds were collected, showing the fatigue endurace ratio of the high values at 0.65 and 0.5 at 10^6 cycles. However, it can be clearly found the rapid fatige failure at low fatigue strength (≤110 MPa) occurs in both porous structures, which raises the concern for load-bearing lattice implant during long-term clinical use.

Bael et al. [104] investigaed the *in vitro* viability, proliferation and differentiation of human periosteum-derived cell (hDPC) casued by different pore shapes/sizes of SLM-produced Ti-6Al-4V scaffolds. They concluded that cell growth difference on the periphery of 500 μm and 1000 μm pore size using live-dead staining assay, the scaffolds with a 1000 μm designed pore size had a significantly higher cell density compared with the scaffolds with a 500 μm. In addition, they also provided a design thread for manufacturing functionally graded scaffolds with good cell-attachment, which combines large pores on the outside to aviod pore occlusion and internal small pores to decrease permeability. Nune et al. [105] also considered that porous architecture provided a convenient route for cell-material interaction and also facilitated flow of nutrient for cell proliferation. *In vivo* results revealed that higher porosity DLD-produced Ti-6Al-4V implant showed a fast tissue generation and integration in male Sprague-Dawley rats in a 16-week study [106]. In the study by Zhang et al. [107], it can be found that bone tissue experienced growth in compact bone but fewer bone tissues at the cancellous bone sites caused by “stress shielding” effect after 4-month implantaion within porous Ti-6Al-4V scaffolds (1-5 GPa elastic modulus) in compact & cancellous bone sites of Beagle dogs.

2.2.3 Drug-eluting implants

Surface modification with functionalised drugs has been performed to improve implant biocompatibility and reduce post-implant complications [108]. Besides that, AM provides an attractive approach for manufacturing tailored 3D shape drug delivery systems. In some cases, antibiotic eluting implant can maintain high concentration released drugs at peri-prosthetic joint sites to get the maximum therapeutic effect then avoid implant infection. Cox et al. [109]

utilised SLM technique to manufacture Ti-6Al-4V drug-delivery implants with internal reservoir and pore channel features (see Fig. 2-9). The reservoir is designed for the carrier vehicle with gentamicin loaded calcium phosphate cement; pore channels with different orientations are designed and used for antibiotic eluting pathways.

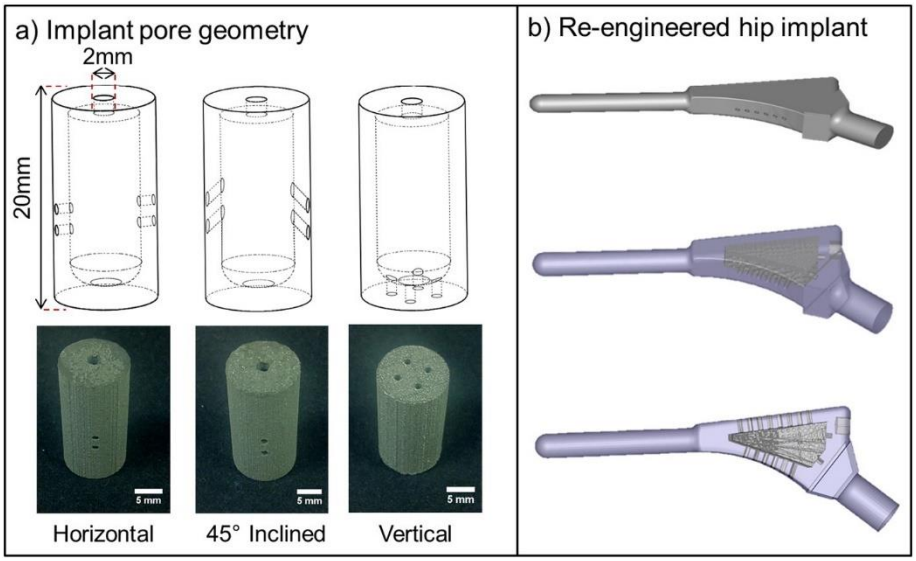

Fig. 2-9. Drug delivery implant models (a) CAD schematics and photomicrographs of Ti-6Al-4V implants manufactured via selective laser melting. (b) re-engineered demonstration hip prostheses of varying transparency designed using Solidworks [109].

They found that after 6-hour antibiotic release from these implants, gentamicin concentrations all exceed the minimum inhibitory concentrations (MIC) of the two representative bacterial species (*S. aureus and S. epidermidis*) associated with peri-prosthetic infection. Bezuidenhout et al. [110] presented their preliminary work of building permeable thin walls by utilising SLM technique, then vancomycin released through the delicate thin wall to show its activity against *S. aureus*. From the drug release profile, it revealed the linear relationship between antibiotics and relative porosity (up to 21.17%) of thin wall. These cases demonstrated that researchers

are now trying to manufacture the functionalised implants by exploiting the design freedom of AM. In addition, Vaithilingam et al. [111] immobilised an antibacterial drug (Ciprofloxacin) to phosphonic acid based self-assembled monolayers on SLMed Ti-6Al-4V structure, then performed some assays e.g., drug elution and antibacterial susceptibility. The drug elution study revealed that nearly 13% drugs eluted to the Rris-HCl buffer solution after 1 week. After 4-week and 6-week of immersion, nearly 50% and 40% of the drug was still observed to be eluted from the surface, respectively. The antibacterial susceptibility study showed that an increased diameter of inhibition zone for both *S. aureus* and *E. coli* were formed when immersion time interval was increased. Thus, this approach to deliver therapeutics directly from customised implant surfaces shows its potential to against implant infection. Hengel et al. [112] bio-functionalized SLMed implants with silver nanoparticles in an oxide surface layer grown using plasma electrolytic oxidation (PEO) in AgNPs -dispersed Ca/P-based electrolytes. In their findings, antimicrobial assays consistently showed strong antimicrobial activity of the developed implants against *S. aureus* by means of a released activity, surface antimicrobial activity and prevention of biofilm formation. Notably, they concluded that larger surface area of porous structure manufactured by SLM induced larger amount of released Ag ions and wider inhibition zones after subsequent typical PEO treatment compared to solid PEO specimen.

A controlled and continuous local drug delivery from implants has a substantial potential to replace the use of systematic drugs due to the adequate physiological stability and availability at the local implant site, thus reducing the toxicity risks and higher cost [113]. It is important

to highlight the challenges for drug carrier scaffolds manufacturing. One challenge for drug-eluting implant manufacturing is to finalise the structure which satisfies the internal shape or microarchitecture for tissue regeneration and integration [114]. Another challenge is to control the release kinetics of antimicrobial agents. The entire drug might invalidate before the infection is stopped if drug release too quickly or lack of thermal stability. If the release of drugs is delayed, bacteria aggregation and forms biofilm will highly happen during that period [40]. Therefore, the local antibiotic release profiles should exhibit a high initial release rate in order to respond to the elevated risk of infection from bacteria's initial shock, followed by a sustained release at an effective level for inhibiting the occurrence of potential infection [115]. Besides, regulatory challenges should not be neglected due to no guidance cover 3D printed drug products or biomedical implants to date [116]. The authors further mentioned that there is an increased interest in PBF manufacturing drug-loaded products. This particularly due to its ability to produce solid amorphous dispersions, which aids in improving the solubility of poorly soluble drugs. Moreover, PBF offers flexibility in altering the dose, shape, and release characteristics of drug delivery systems, making them become useful tools in early preclinical and clinical studies.

2.3 Post-processing treatment for SLMed components

2.3.1 Hot isostatic pressing for SLMed components

HIP is a technique that involves the simultaneous application of elevated temperature and high pressure applied with inert gas to workpieces in a specific vessel [117]. HIP equipment is

basically an electric furnace which is contained in a pressure vessel. Fig. 2-10 shows the basic concept of the HIP furnace. HIP furnace produces the power to heat up the workload to the temperature at the desired heating rate with the required accuracy. The pressure medium used is an inert gas such as argon or nitrogen, which is pumped into a vessel and pressurised to 200 MPa [117]. The nature of the high-pressure transmitting gas in the pressure vessel is: the viscosity of the gas is very low, and its density is very high, so that the heating transferred mainly by the natural convection of the gas [118]. The fundamentals of pores removal and some relevant work based on AMed components are demonstrated as below. Pores may generate from lack of fusion or localized evaporation during AM, as mentioned in **section 2.21**. Unlike the process flow for powder metallurgy involves powder filling and encapsulation, no capsule is required to densify AMed components, as their outer surfaces work as capsules. The driving force to achieve densification is regarded as surface energy reduction of the pores [119]. Argon atoms are pressed every surface of a component in a normal direction like “hot forge”, thus the pores are eliminated from the component after a dwell with proper reaction. Loh et al. [117] mentioned that there are several possibilities if pores are filled with gases: if soluble, the gas may dissolve in the metal; if insoluble, it may react with the metal to form a non-metallic inclusion or without reaction. Qiu et al. [120] demonstrated the successful porosity removal of SLMed Ti-6Al-4V specimens by HIP technique. The considerable improvement in ductility and reduction in strength was caused by not only re-densification but also microstructural evolution (main acicular martensite α' was transformed to lamellar $\alpha+\beta$) during slow furnace cooling process [120,121]. Both Jamshidi et al. [122] and Su et al. [123] observed HIP

treatment enhanced fatigue resistance of SLMed Ti-6Al-4V. The microstructure transformation and porosity enclosure resulted in the improvement of fatigue performance, but without clarification which one is the dominant factor.

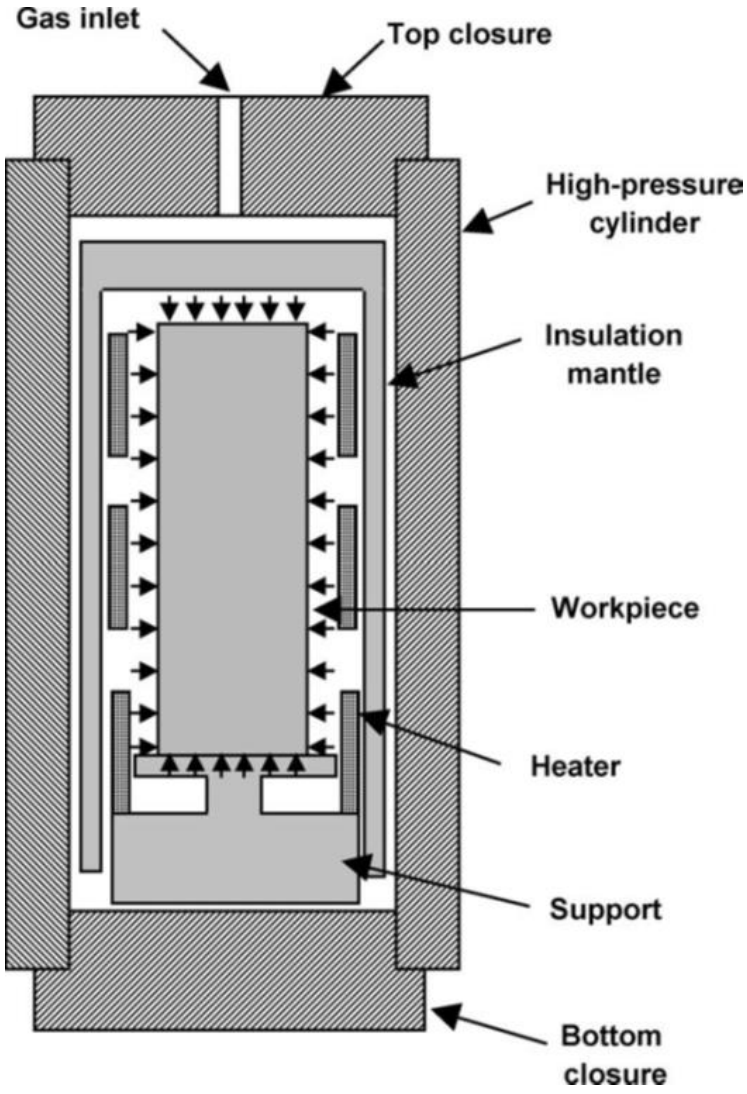

Fig. 2-10. Schematic drawing of HIP unit, sourced from https://www.kobelco.co.jp/.

2.3.2 SLM adhered powder removal fromTi-6Al-4V alloy

Continuous wave fibre laser polishing has been investigated for selective polishing SLMed Ti-6Al-4V [124]. The researchers presented some conclusions after conducting experimental and

three-dimensional computational fluid dynamic (CFD) model simulation. They believed that this method could polish specimen without noticeable changes on mechanical properties and microstructure. They also mentioned the excessive thermal energy input can result in surface oxidation and carbonisation. Additionally, poor surface profile was obtained if the polished region with high molten pool velocity and appeared without proper parameter optimisation of laser power and scan speed. Besides that, chemical polishing has been adopted for some researchers to modify surface roughness of SLMed Ti-alloy components. The titanium dissolution process in nitric-hydrofluoric acid solution has been widely recorded [125,126]. Due to different chemical reactions existence, Ti^{3+} adsorbed cations can be oxidized either as soluble titanium fluorides or insoluble titanium oxide [125]. Hooreweder et al. [90] introduced chemical etching (CE) as a post-SLM treatment for Ti-6Al-4V lattice structure. It observed that the adhered powder from these scaffolds was removed by CE, and meanwhile CE involved treatment significantly improved the fatigue life due to the reduction of strut surface roughness. Wysocki et al. [127] investigated the influence of chemical polishing on mechanical properties and *in vitro* cell response from SLMed Ti-6Al-4V scaffolds. From their investigation, compressive strength of lattice structure was decreased after powder removal, but chemical treatment did not affect negatively on cell proliferation and differentiation. Additionally, it has been reported that sandblasting treatment improved the fatigue resistance of SLMed 316L gyroid cellular structure lattices [128]. To explain this, nano-crystalline zone together with the work hardening surface obtained from sandblasting retards the plastic strain, micro-crack nucleation or growth resulted in the higher cyclic stability. Moreover, sandblasting also

decreased the crack initiation sites of struts by removing the bonded powder particles. In order to improve the surface quality of struts in lattice structure, Ahmadi et al. [129] also exploited sandblasting and CE treatments and investigated their effect on fatigue properties. They concluded that sandblasting removed the adhered particles and markedly increased the fatigue life of Ti-6Al-4V lattice structures; CE treatment in this work did not improve the quasi-static mechanical properties or the fatigue behaviour of SLMed lattice structures. By comparison, Jamshidi et al. [122] investigated different post-processing strategies like polishing, CE for modifying surface condition of SLM + HIPed Ti-6Al-4V. They observed a comparative four-point bending fatigue performance between CE and polishing treated condition. Additionally, an enhanced cellular affinity and degree of confluence was found in CE surface compared with the counterpart of the particle-adhered one, which is probably caused by the difference of initial cell attachment onto these substrates.

2.4 Beta titanium alloys development for load bearing implants

2.4.1 Physical metallurgy of beta titanium alloys

Beta titanium alloys have received intense interest for biomedical applications over last two decades, due to their relative lower Young's moduli and comparable biocompatibility to the commonly selected Ti-6Al-4V [130]. The development of beta titanium alloys is fulfilled by adding alloying elements to stabilize the high temperature bcc β phase to room temperature. Generally, the β stabilizing elements are divided into β isomorphous elements and β eutectoid forming elements. Both types of phase diagrams are shown schematically in Fig. 2-11A. The

frequently used β isomorphous elements (eg., Mo, Nb, Ta) and β eutectoid forming elements (eg., Fe, Si) have been found in biocompatible beta titanium alloys R&D. The stable β alloys are formed after adding enough β stabilizers (Fig. 2-11B), and the following martensitic transformation during quenching is suppressed upon fast cooling from the β phase field [131]. To indicate the overall beta phase stability of a titanium alloy with various alloying elements, the empirical "moly equivalent" defined by the following equation by selecting molybdenum as a baseline:

$$Mo\ Eq=1.0[Mo]+0.67[V]+0.44[W]+0.28[Nb]+0.22[Ta]+1.6[Cr]+...-1.0[Al] \quad (2\text{-}3)$$

has been used historically [132]. In general, high Mo Eq indicates it is a heavily beta stabilized alloy.

Various phases including α', α'', grain boundary α, ω may be presented in stable or metastable beta titanium alloys during manufacturing or post-processing heat treatments. Martensite has a structure of supersaturated α solid solution and is denoted as α' phase [133]. Hcp α' phase has been observed with fine acicular martensitic morphology, which was dominated in metastable β titanium alloys (eg., Ti-13Nb-13Zr) in solution treating then quenching condition [134,135]. Different crystallographic lattice martensitic phase can be formed during martensitic transformation (see Fig. 2-12). Orthorhombic α'' phase is regarded as a distorted hcp structure, with the analogous atomic positions as hcp structure. The formation of α'' phase has been explained based on atomic movement, as orthorhombic structure is an intermediate phase between the bcc and hexagonal structures [136]. Low cooling rate cooling upon the beta transus

temperature leads to the formation of non-homogenous distribution of grain boundary α phase. Duerig et al. [137] believed that the nucleation of grain boundary α is independent of alloy composition due to high lattice distortion on grain boundaries, and interstitial elements segregation on grain boundaries probably makes precipitation occur at these sites. Two types of ω phases, namely athermal and isothermal ω in beta titanium alloys have been extensively investigated [138]. The former type is displacement-type transformations controlled by local atomic shuffles can occur rapidly. The latter type is diffusion-controlled, occur slowly expect at high temperatures [138]. The isothermal ω is regarded to follow the conventional nucleation and growth process at the aging temperature. Brammer Jr. et al. [139] revealed well-developed omega with an elliptical morphology in Ti-35Nb (wt. %) after duplex aging treatment via BF-TEM.

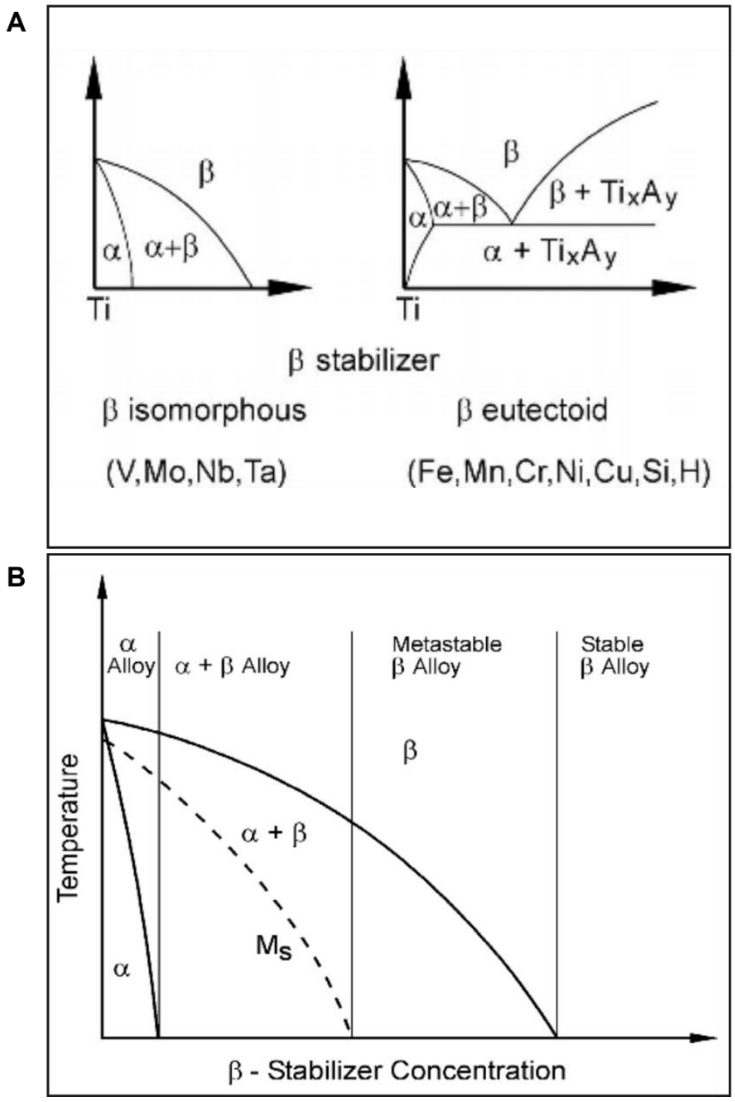

Fig. 2-11. (A) Effect of β stabilizing elements on phase diagrams of titanium alloys (schematically). (B) Pseudo-binary section through a β isomorphous phase diagram (schematically). Reproduced from the *Titanium* textbook [131].

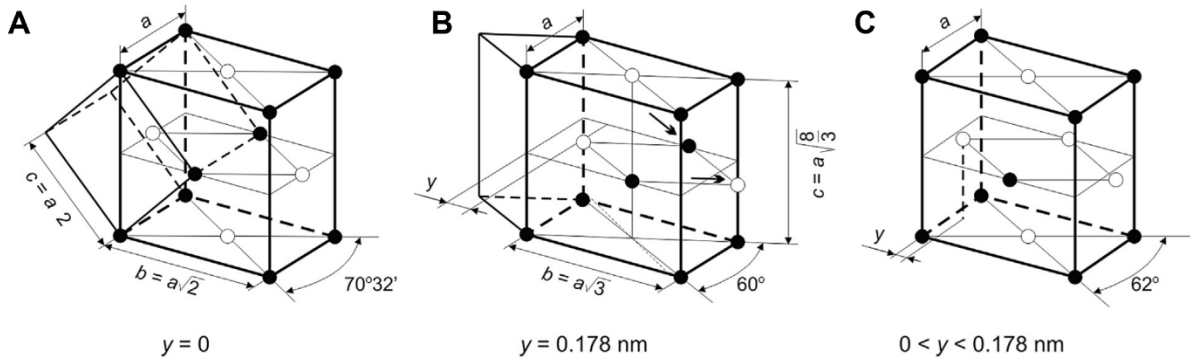

Fig. 2-12. Location of atoms in unit cells of (A) β phase, and α and (B) α' phases, and α'' phases [133].

2.4.2 Low modulus beta titanium alloys design criteria

For beta titanium alloy design, the molecular orbital approach is a theory based on the electronic structure calculations of transition-metal based alloys using the DV-Xα cluster method. It is a first-principle calculation method that is more appropriate to the simulation of the local electronic structure around alloying element as compared with the conventional band calculation method [140]. This calculation bears some inverse relationship to electron affinities: the more positive the energy the lower the electron affinity. Two crucial parameters for determining phase stability are: the bond order (hereafter referred to *Bo*) and the *d* orbital energy level (hereafter referred to *Md*). Here *Bo* is overlapping of the electron clouds between alloying element (M) and mother metal (X) showing the strength of the covalent bond between M and X atoms; *Md* reflects the energy level between alloying element (M) and mother metal (X). Different energy level of an alloy is obtained by hybridizing the *d* orbitals of the involved atoms. This approach is introduced to explain beta Ti-alloys design principle. $\overline{Bo}$ (average covalent bond strength between Ti, and other elements) and $\overline{Md}$ (average *d* orbital energy level of these involved alloying elements) have been used to form $\overline{Bo}$-$\overline{Md}$ diagram (see Fig. 2-13) for roughly predicting phase formation and Young's moduli range of the specified beta Ti-Nb-X, Ti-Mo-X, Ti-Ta alloy [141–143]. In Table 2-1, the *Bo* and *Md* parameters are listed for different alloying elements in bcc Ti, which are calculated by Morinaga and co-workers [144]. It is noteworthy that the parameters obtained from bcc Ti are employed for evaluation the stability of beta phase and analysis of mechanical properties [142].

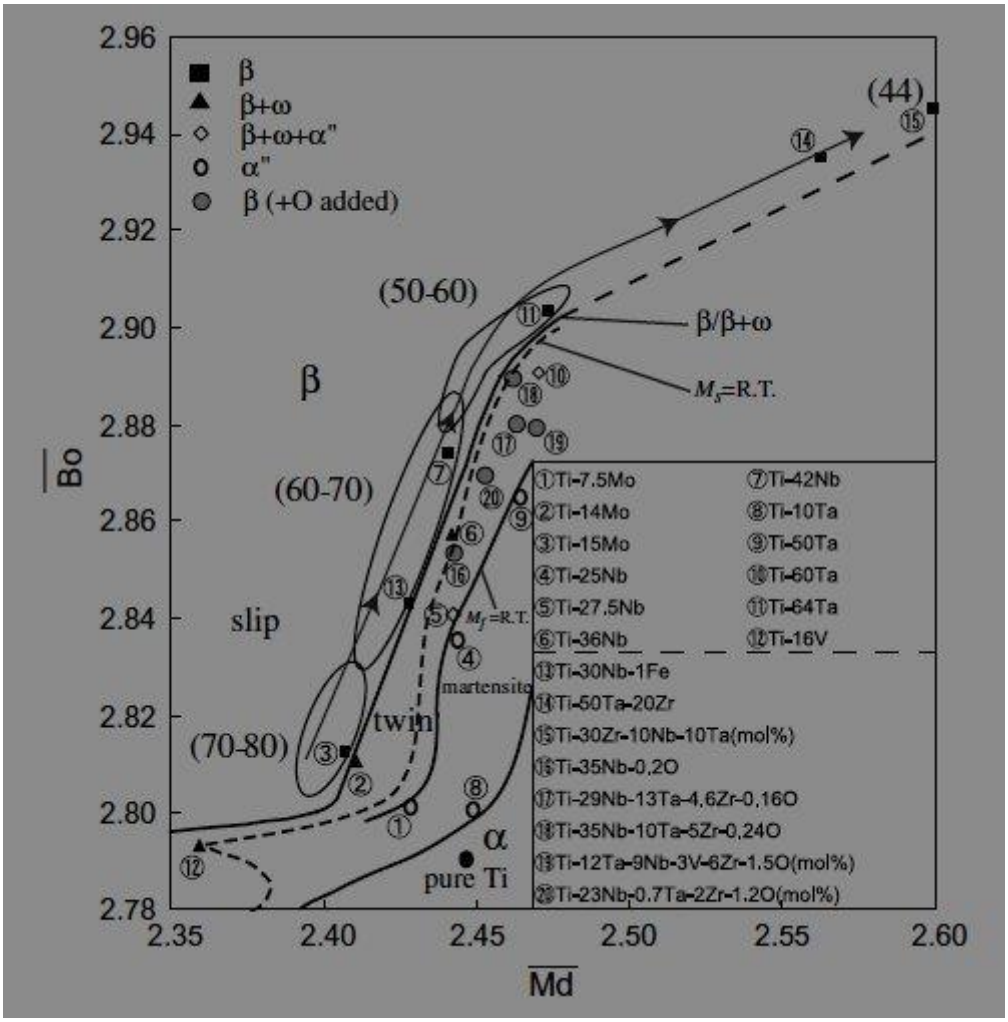

Fig. 2-13. Extended $\overline{Bo}$-$\overline{Md}$ diagram in which the *β*/*β* + *ω* phase boundary and the value of the Young's modulus (GPa) is given in parentheses for typical alloys [145].

Table 2-1

List of *Md* and *Bo* for different alloying elements in bcc Ti [142].

3d	*Bo*	*Md* (eV)	4d	*Bo*	*Md* (eV)	5d	*Bo*	*Md* (eV)	other	*Bo*	*Md* (eV)
Ti	2.790	2.447	Zr	3.086	2.934	Hf	3.110	2.975	Al	2.426	2.200
V	2.805	1.872	Nb	3.099	2.424	Ta	3.144	2.531	Si	2.561	2.200
Cr	2.779	1.478	Mo	3.063	1.961	W	3.125	2.072	Sn	2.283	2.100
Mn	2.723	1.194	Tc	3.026	1.294	Re	3.061	1.490			
Fe	2.651	0.969	Ru	2.704	0.859	Os	2.980	1.018			
Co	2.529	0.807	Rh	2.736	0.561	Ir	3.168	0.677			
Ni	2.412	0.724	Pd	2.208	0.347	Pt	2.252	0.146			
Cu	2.114	0.567	Ag	2.094	0.196	Au	1.953	0.258			

Besides that, Raabe et al. [146] presented the simulation results of binary Ti-Nb and Ti-Mo *β* titanium alloys using an *ab initio* quantum mechanical approach. The compositional dependent

alpha and beta phase formation energy were quantified by a Gibbs construction, showing the alpha phase destabilisation with increasing temperature. They demonstrated that the calculated Young's modulus of beta phase along the soft [001] crystal direction almost increases linearly with the β stabilizing element addition in those binary alloys, which is contradictory with the experimental elastic moduli measured by ultrasonic resonance frequency method. They concluded both the thermodynamic stability and the elastic properties of β Ti-alloys could be well predicted by using parameter-free density functional theory (DFT) calculations in conjunction with experiments.

There has considerable evidence demonstrated that shear modulus $C' = (C_{11} - C_{12})/2$ in bcc structure is a key parameter to estimate the relative stability of beta Ti-alloys [147]. The softening in C' of bcc based alloys increases the instability with {1 1 0} <110> shear, forming a more stable closed-packed structure when underwent martensitic transformation, which is regarded as the origin of low Young's modulus [148]. Nagasako et al. [149] mentioned the key factors for low modulus Gum Metal development is to control compositions with vanishing of C', and obtain a valence-electron concentration per atom (e/a) close to 4.24. Talling et al. [29] demonstrated a $C_{11} - C_{12}$ value increase of Ti-10V-2Fe-3Al (wt. %) after employing aging thermomechanical treatment. Considering the $C_{11} - C_{12}$ change of bcc structure happened after precipitates formation or oxygen induced microstructural evolution, they suspected that *Bo* and *Md* parameters cannot be regarded as complete indicators of beta phase stability when designing low-modulus beta Ti-alloys.

2.4.3 Microstructural evolution via different processing techniques

Over several decades, a multitude of studies have been contributed to the microstructure characterisation of beta titanium alloys. Hao et al. [25] investigated the microstructural evolution of Ti-24Nb-4Zr-7.9Sn alloy (wt. %), which experienced hot forging at 850℃ and rolling at 800℃ duplex treatment before the final aging at 500℃. Bright/dark-field TEM micrographs of specimens after aging at 500℃ (10 & 30 min) presented alpha precipitates width broadening in beta matrix after increasing aging dwell time. Plus, XRD profile of the specimen after aging (500℃ for 30 min) disclosed the existence of α and β phases. Niinomi et al. [150] recorded the phase identification of Ti-29Nb-13Ta-4.6Zr (wt. %) by conventional TEM analysis. It showed ω and α precipitates co-existence in β phase matrix of the aged specimen (400℃ for 72 hours) after solution treatment (790℃ for 1 hour), which sectioned from cold rolling plate after hot forging. Ti-33Nb-4Sn [151] and its similar compositions (Ti-32Nb-2Sn & Ti-32Nb-4Sn) (wt. %) [152] were investigated by researchers sequentially for microstructure and properties evaluation. Lath-shaped α'' martensite within the β matrix was found in solution treated Ti-33Nb-4Sn after hot forging. Bright/dark-field TEM micrographs of aged specimens at 400℃ for 2 hours in Ti-32Nb-2Sn & Ti-32Nb-4Sn alloys after hot rolling presented the microstructure of fine α precipitates in equiaxed beta grain. Acharya et al. [153] demonstrated TEM phase identification of Ti-34Nb-2Ta-0.5O alloy (wt. %) sectioned from hot rolling plates after aging treatment. They concluded that no ω precipitates but with alpha precipitates was found in beta matrix combining DF image and SAD pattern. They suspected that the existence of oxygen in the interstitial sites, which impedes the atomic displacements

needed for the collapse of {111}β planes then suppresses β to ω transformation [154]. Brammer. et al. [139] observed the omega phase occurrence in beta-stabilized Ti-35Nb (wt. %) fabricated by aging treatment at 450℃ after solution treatment at 800℃. It revealed the precipitates growth from unresolvable to well-developed elliptical omega particles of an average size of 130 nm after increasing the aging time from 1 to 24 hours. Banerjee et al. [27] revealed the microstructural evolution of Ti-34Nb-9Zr-8Ta and Ti-13Mo-7Zr-3Fe (wt. %) when experienced furnace cooling after solution treatment. SEM & TEM characterisation shows the grain boundary α and fine scale α'' were found in both alloys due to a slow cooling. Except for those second-phases, diffraction pattern of nano-size ω precipitates were also observed in Ti-13Mo-7Zr-3Fe after aging treatment at 600℃ for 4 hours.

Wang et al. [155] revealed the microstructure of cast metastable β Ti-xMo alloys (x=10, 15, 20 wt. %) after solution treatment and water quenching. The DF TEM micrographs and corresponding SAD patterns obtained from Ti-10Mo showed the morphology of the β grain and lath-shaped α'' martensite. Meanwhile, the same conventional TEM characterisation was also introduced to demonstrate the microstructure of Ti-15Mo and Ti-20Mo, suggesting that the nanoscale athermal ω phase dispersed in the β matrix. Xu et al. [156] investigated the microstructure of Ti-5Mo-Fe-3Sn (at. %) after water quenching from annealing temperature at 900℃. SAD pattern did not reveal athermal ω phase occurrence at the 1/3 and 2/3 location between (000) and {112} reflection of the β planes. They concluded that omega phase has been fully suppressed, and the low Young's modulus (52 GPa) is retained. A dissimilar results were

demonstrated from Ti-12Mo (wt. %) manufactured by Zhang et al. [157] and Mantri et al. [158], showing nano-size athermal ω precipitate phase inside β phase matrix was retained in ST condition.

Microstructural evolution of scattered-composition Ti-Nb-X, Ti-Ta-X alloys manufactured by AM have been revealed using TEM in recent ten years. Zhao et al. [86] *in-situ* fabricated Ti-25Nb (wt. %) alloy with blended powders by SLM. TEM results demonstrated SLM-processed alloy obtained a width of ~100 nm acicular α' phases inside beta grain. Nag et al. [159] manufactured Ti-34Nb-7Zr-7Ta (wt. %) using direct laser melting (DLD) technique. It showed ω and α'' phase reflections within β matrix in as-deposited condition, while the athermal ω precipitate phase almost completely dissolved after solution treatment. Yan et al. [160] exhibited the XRD profiles of biocompatible Ti-15Ta-xZr (1.5, 5.5, 10.5, 15.5 wt. %) alloys fabricated by SLM. Alpha and beta phase coexistence was found in as-mentioned composition beta Ti-alloys. Brodie et al. [161] demonstrated the lath martensite α' microstructure of nominal composition regions from single melt and remelt scan Ti-25Ta (wt. %); orthorhombic α'' martensite was found in Ta-rich region fabricated by remelt scan strategy probably because of further homogenisation of the structure in the vicinity of partially melted Ta particles.

2.4.4 Wear resistance

Wear is a serious problem after joint replacement as wear resistance of implants and the biologic reactivity of wear particles play a key role in long-term implant survival [162]. The

fine particulate wear debris initiated from implant surface area contribute significantly to its overall rate of corrosion and metal ion release to neighbouring tissues [67]. The hard oxide debris induced by friction in relative motion generically work as third body abrasive components during metal-on-metal contact, may be divided into three steps, (i) particle detachment caused by adhesion, corrosion, fatigue, etc. (ii) trapped particles appear in the interface region, (iii) particle ejection. Subsequently, the exposed base metal surface may reform a passive layer after the continuous breakdown during the function of high normal or shear stresses [54].

Available literature shows that Li et al. [163] performed sliding wear tests of before and after oxidation treated Ti-29Nb-13Ta-4.6Zr, Ti-39Nb-13Ta-4.6Zr and Ti-6Al-4V (wt. %) in a 0.9% NaCl solution. The wear loss data of two beta phase Ti alloys were smaller than the counterpart of Ti-6Al-4V. The authors mentioned that oxidation treatment markedly improved wear resistance of Ti-29Nb-13Ta-4.6Zr alloy, due to the formation of a hard, thick lubricating Nb_2O_5 oxide layer. Alagic´et al. [164] observed that Ti-13Nb-13Zr alloy (wt. %) underwent severe delamination with ridges and cracks perpendicularly to the sliding direction. They concluded that the wear occurs predominantly by adhesion mechanism. Haghighi et al. [165] designed a group of Ti-*x*Nb-7Fe (*x*=0, 1, 4, 6, 9, 11 wt. %) alloys and investigated the relationship of niobium addition and wear resistance. They introduced abrasive mechanism to describe surface delamination and material removal. Moreover, they believed that surface delamination was the severest in highest niobium addition alloy due to

the existence of smallest proportion of strengthening phase (α''). Okazaki et al. [10] carried out wear test using Ti-15Zr-4Nb-4Ta-0.2Pd (wt. %) and Ti-6Al-4V against apatite ceramic pins and continued a cytotoxicity evaluation. The relative growth of L929 and MC3T3-E1 after incubation with wear debris medium of the former alloy remained almost 1. On the contrary, the relative growth steeply decreased from almost 1 to 0. In order to improve corrosion resistance and biocompatibility of Ti-13Nb-13Zr, Hee et al. [166] deposited 1µm tantalum coating to the base material. Wear test results showed that the coating was abraded through rapidly but no significant wear performance improvement over the uncoated surface.

2.4.5 Corrosion and ion release characterisation

It is noteworthy that one critical life-limiting factor for load-bearing implant is its corrosion performance. Atapour et al. [17] conducted cathodic polarisation and 10-day immersion experiment of different types of Ti-alloys in 5 M HCl electrolyte at 37°C. They concluded that Ti-35Nb-7Zr-5Ta (wt. %) exhibited superior corrosion resistance compared to Ti-6Al-4V ELI because of the presence of less chemical dissoluble Nb_2O_5, ZrO_2 and Ta_2O_5 in the titanium oxide. Karthega et al. [167] investigated electrochemical behaviour of Ti-29Nb-13Ta-4.6Zr (TNTZ) and Ti-15Mo (TiMo) in Hank's solution. By using electrochemical impedance spectroscopy, it indicated a presence of compact single passive layer on TiMo surface and two layers on TNTZ surface, namely an inner layer for corrosion resistance and an outer porous layer to favourable for osteointegration. They also reported that TNTZ alloy indicated a noble OCP compared to TiMo alloy. Monteiro et al. [168] recently carried out three-electrode electrochemical cell test in 0.9 wt. % sodium chloride solution for comparison of corrosion

behaviour of different heat-treated Ti-47Nb, Ti-30Nb-7Zr (wt. %) with benchmark Ti-6Al-4V. The anodic polarization curves of the involved alloys indicated that the solution treated β matrix Ti alloys possessed better corrosion resistance than Ti-6Al-4V. They believed that the addition of Nb and Zr improved the thermodynamic stability and decreased the dissolution rate of titanium provoked by corrosive processes. However, it lacks explanation about why there exists enormous corrosion properties difference between the same composition alloys with different microstructures (e.g., ST and STA Ti-30Nb-7Zr alloys).

Khan et al. [169] preformed electrochemical tests for Ti-13Nb-13Zr alloy in protein solution biological environments (phosphate buffered saline with bovine albumin solutions or foetal calf serum) and reported material corrosion resistance reduction in the presence of protein in comparison with the counterpart in PBS solution. They have noted that proteins could potentially interplay with the corrosion reactions in several ways. Proteins bind to metal ions and transport away from the solid-liquid interface thus accelerating further ion dissolution. Plus, proteins may adhere alloy surface and restrict the diffusion of oxygen to the surface, then may block the metal surface re-passivation. Alagic´ et al. [164] mentioned the corrosion stability of Ti-13Nb-13Zr in Ringer's solution is due to the existence of Nb_2O_3 and ZrO_2 in passive TiO_2 layer, which reduces Cl^- ingress into the oxide layer and increases its structural integrity. Hanawa [50] mentioned the importance of quantification of the released ion and discussed the mechanism of metal ion release from titanium alloys; large amount of metal ions released from fresh metal surface and they were inhibited by the surface oxide as a passive film.

Okazaki et al. [170] performed static immersion tests using various simulated body fluids in order to investigate metal release behaviour of Ti-15Zr-4Nb-4Ta (wt. %) and other common use Ti-based alloys. From their findings, the amount of the evolved metallic ions of Ti-15Zr-4Nb-4Ta was considerably lower than the counterpart of other alloys measured by ICP-MS, mainly because the corrosion resistance of TiO_2 oxide film was strengthened by ZrO_2, Nb_2O_5, Ta_2O_5. Oliveira et al. [171] investigated pure Ti and Ti-Mo alloys with molybdenum contents ranging from 4 to 20 wt. % in Na_2SO_4 (0.15 mol/L) and Ringer solutions. The results strongly indicated a valve-metal behaviour with anodic formation of barrier-type oxide films in Ti-Mo alloy, and Mo improved the stability of the anodic oxide film.

2.4.6 Tensile and fatigue performance

The mechanical properties are believed to decide the type of material that will be selected for a specific application [172]. Some attractive tensile testing results relevant to Ti-Nb-X, Ti-Mo-X, Ti-Ta-X beta titanium alloys manufactured by conventional manufacturing have been reported. Hanada et al. [15] illustrated the feasibility to obtain about 40 GPa Young's modulus by optimizing alloy composition based on β Ti-Nb-Sn alloys. The underlying mechanism was relevant to Sn addition retarding ω transformation, thereby reducing Young's modulus. Laheurte et al. [143] based on bio-friendly elements such as Ti, Nb, Ta, Zr for designing beta Ti alloys using the electronic approach. They concluded that incipient modulus of β Ti-alloy can be reduced to a low value (30 GPa), which is extremely close to the counterpart of cortical bone. Panigrahi et al. [173] demonstrated the mechanical properties of Ti-45Nb alloy (wt. %) fabricating by severe plastic deformation (SPD). They found that elastic moduli of samples

after hydrostatic extrusion (HE) and high pressure torsion (HPT) kept the same as initial ingot at the level of 65 GPa, hypothesizing that the volume fraction of ω phase induced by deformation is too small to influence its elastic modulus. Kuroda et al. [174] exhibited the low ultimate tensile strength (approx. 500 MPa) and high elongation (approx. 40%) of solution treated Ti-29Nb-13Ta-4.6Zr; the UTS underwent a big improvement to approx. 950 MPa after conducting aging treatment at 400℃ for 3 hours.

Min et al. [175] investigated the microstructure evolution of solution treated Ti-15Mo after experiencing a series of hot & cold working procedures via EBSD characterisation. They concluded that the reason of high UTS (765 MPa) and large uniform elongation (40%) is due to twinning activity of this β-type Ti-alloy. Zhang et al. [157] demonstrated the similar aforementioned microstructural evolution of the as-quenched Ti-12Mo under tension. The two deformation mechanisms, combining mechanical twinning and stress induced martensite (SIM) phase transformation, lead to its high ductility and strength.

Recently, AM has been used to develop Ti-Nb-X, Ti-Mo-X, Ti-Ta-X beta titanium alloys. Zhang et al. [21] recorded typical stress-strain curves of Ti-24Nb-4Zr-8Sn alloy (wt. %) manufactured by SLM at different scan speeds. Those samples obtained a low Young's modulus of ~53 GPa, an UTS of ~660 MPa and elongation exceeding 10%. They concluded that the ductility difference at each scan speed is due to the density of the specimens. It can be observed that intergranular and transgranular cleavage fracture dominated the fracture of the lowest density sample produced at the highest scan speed. Ishimoto et al. [176] provided a

thread to control low-modulus of Ti-15Mo-5Zr-3Al via scan strategy settings in SLM. The low elastic modulus (68.7 ± 0.9 GPa) was fulfilled by controlling the growth behaviour of columnar grains in the molten pool, which shows the potential for development of implants that can suppress "stress shielding" effect. Sing et al. [177] studied microstructure and mechanical properties of Ti-50Ta (wt. %) using SLM, as compared to SLMed commercially pure (CP) titanium and Ti-6Al-4V. Equiaxed grains with laminar β phase substructures were observed in SLMed Ti-50Ta; primary α, and lath-shaped α' phase was found in CP titanium, and Ti-6Al-4V after SLM process, respectively. From the measured tensile properties, Ti-50Ta obtained the lowest elastic modulus (75.77 ± 4.04 GPa) and higher ductility than CP titanium and Ti-6Al-4V. Brodie et al. [161] investigated the feasibility of Ti-25Ta *in-situ* alloying via SLM. Even though low scan speed provided possibility to well melt the refractory tantalum, but un-melted powders were still observed from the tensile specimen fracture. They also found that the tensile properties of the alloy manufactured by SLM are similar with conventionally wrought one.

Niinomi et al. [178] carried out fatigue testing using different heat treated Ti-29Nb-13Ta-4.6Zr (TNTZ) alloys at a frequency of 10 Hz with a stress ratio, R=0.1, under a tension-tension stress mode in air at room temperature. Fatigue S-N curves exhibited the lowest fatigue limit (320 MPa) of solution treated TNTZ alloy, and a greatest fatigue limit (700 MPa) was obtained from solution treatment +aging (STA) processed TNTZ alloy aged at 400°C for 72 hours, which was close to the upper limit of the counterpart of Ti-6Al-4V ELI. They concluded that high fatigue

strength of STA TNTZ alloy may be relevant to the increase of resistance against small fatigue crack initiation and propagation caused by the precipitation of nano-size alpha and omega phases. SEM fractographs of ST TNTZ alloy showed relatively wide striations from crack propagation area and equiaxed dimples from fast fracture area; SEM fractographs of STA TNTZ alloy showed smaller striation width and dimple size were in the corresponding areas. Li et al. [179] demonstrated high-cycle fatigue testing results of different treated Ti-24Nb-4Zr-7.6Sn (TNZS, wt. %) at a stress ratio R of 0.1, a frequency of 30 Hz in 0.9% NaCl solution at room temperature. They found there exists fatigue limit gap between the highest performance as-aged TNZS (~375 MPa) and Ti-6Al-4V ELI (~550 MPa). They introduced the same explanation (precipitation strengthening) as-above to show the high fatigue limit of the as-aged TNZS alloy.

2.4.6 In vitro cell response and in vivo response

Xie et al. [180] obtained nanocrystalline Ti-36Nb-2.2Ta-3.7Zr-0.3O (at. %) using HPT for dental implant application. The *in vitro* biocompatibility results showed that the adhesion of human gingival fibroblasts (HGF) on nanocrystalline β titanium surface is significantly higher than coarse-grained β titanium and control group after 5-day cell culture. To explain this, two potential reasons have been mentioned to understand the better cell-substrate interaction on nanocrystalline titanium. The first potential reason was that oxide layers difference between nanocrystalline and coarse-grained β Ti substrates, which enhanced surface wettability on nanocrystalline β Ti surface; the second one was that the strain energy stored by nanostructure

manufactured via severe plastic deformation were released by polishing procedure, then formed nano-roughness for cell attachment and proliferation. Gordin et al. [18] and Neacsu et al. [19] demonstrated some similar short-term *in vitro* MC3T3-E1 results based on conventionally manufactured Ti-Nb-X alloy by comparing with commercially pure (CP) titanium. They found that beta titanium alloys perform equally or even better than CP titanium in different types of cell-relevant assays (cytotoxicity, differentiation, etc.). Meanwhile, Miura et al. [181] and Ion et al. [182] compared the preosteoblast cell response of Ti-25Nb-11Sn and Ti-23Nb-0.7Ta-2Zr-0.5N alloy (wt. %) to Ti-6Al-4V. The two research groups both believed that a similar level preosteoblast attachment, spreading and proliferation obtained from these biomaterials.

Zhang et al. [183] performed Ti-24Nb-4Zr-8Sn and Ti-6Al-4V plugs implantation into dog and observed the bone remodeling changes around the implant using micro-CT. No adverse inflammatory reaction was found in both groups and there was no significant difference of newly formed bone around both screw stems. Matsuno et al. [184] demonstrated biocompatibility results of refractory metals, titanium, niobium, tantalum wires after 2-4 weeks implantation in subcutaneous tissue of the abdominal region and in femoral bone marrow of rats. Quantitative histological analysis of osteogenesis exhibited a slight decrease in the amount of new bone formation, and a remarkable increase in the percentage of bone in contact with metal implant from the second to the fourth week implantation. No dissolution of Ti, Nb, Ta in soft and hard tissue was detected by X-ray scanning analytical microscope (XSAM) and

electron probe microanalyser (EPMA), respectively.

2.5 Summary

This review has attempted to start from those characteristics of bone on the scope of tissue engineering (TE), which have been regarded to be crucial for bone replacement. Some major concerns for metallic load-bearing implants development have been summarised to show the challenges for this application. In addition, the author has reviewed SLM processing features (unlike conventional manufacturing) and the representative biomedical applications (cellular lattice structures & drug-delivery implant) fabricated by SLM. At the same time, those well-known post-SLM treatments e.g., HIP, CE were introduced for removing as-mentioned AM process-induced defects. As bio-friendly beta phase Ti-alloys have been received intense interests due to their relatively low Young's modulus and excellent biocompatibility, the author has performed a systematic review including material design, microstructural evolution, mechanical properties, wear and corrosion, *in vitro* and *in vivo* response, which provides a better understanding of the interplay between microstructure and the comprehensive properties of Ti-Nb-X, Ti-Mo-X, Ti-Ta-X alloys. It can be found that the aims of developing TNTZ β Ti-alloy via SLM are not only because the advantages of SLM technique, but also limited research have investigated the performance of SLMed TNTZ β Ti-alloy. The author believes that some attempts like introducing the advanced processing technique (e.g., SLM), biomaterial selection, post-SLM processing optimisation, structurally stable scaffolds design, etc. are helpful to improve the life-quality of patients who suffer from severe osteoarthritis or other orthopedic disorders.

3 THE INFLUENCE OF ZIRONIUM CONTENT ON THE MICROSTRUCTURE, MECHANICAL PROPERTIES, AND BIOCOMPATIBILITY OF *IN-SITU* ALLOYING TI-NB-TA BASED *β* ALLOYS PROCESSED BY SELECTIVE LASER MELTING

Paper Status: published

Weihuan Kong[a], Sophie C. Cox[b], Yu Lu[a], Victor Villapun[b], Xiaoling Xiao[c], Wenyou Ma[d], Min Liu[d*], Moataz M. Attallah[a*], **The Influence of Zirconium Content on the Microstructure, Mechanical Properties, and Biocompatibility of in-situ Alloying Ti-Nb-Ta Based β Alloys Processed by Selective Laser Melting**, Materials Science & Engineering C 131 (2021) 112486. https://doi.org/10.1016/j.msec.2021.112486.

Authorship contribution statement

Weihuan Kong conceived and designed the experiment, performed the experiment, interpreted the data, and wrote the manuscript. Sophie C. Cox assisted with designing the experiments. Yu Lu assisted micro-CT data analysis. Victor Villapun, Xiaoling Xiao performed cell-culture assays and TEM observations. Wenyu Ma and Min Liu involved resources and methodology. Moataz M. Attallah assisted with designing the experiments and revising the manuscript.

---

a. School of Metallurgy and Materials, University of Birmingham, Edgbaston, B15 2TT, UK

b. School of Chemical Engineering, University of Birmingham, Edgbaston, B15 2TT, UK

c. Guangdong Institute of Analysis, Guangzhou, 510651, PR China

d. National Engineering Laboratory for Modern Materials Surface Engineering Technology, The Key Lab of Guangdong for Modern Surface Engineering Technology, Guangdong Institute of New Materials, Guangzhou, 510651, PR China

Abstract

This chapter investigates Ti-Nb-Ta based β alloys with different zirconium additions (0, 5, 9 wt. %) manufactured by SLM. A low level of as-fabricated defects is obtained: the relative density of TNT(Z) alloys is >99.97% with the keyhole size in a range of 3—20 μm. BF-TEM images combining SAD patterns of TNT(Z) alloys show single β phase obtained inside the beta matrix; BF-STEM images reveal potential nano-scale grain boundary alpha phase precipitation. Zirconium functions as a neutral element in these high β-stabilized Ti-Nb-Ta based alloys. An increase in Vickers hardness and UTS caused by zirconium additions is observed, which is explained by beta grain refinement because higher degree of undercooling occurs. Corrosion ions of TNT(Z) alloys released from immersion testing at each time intervals show extremely small concentrations (<10 μg/L). It indicated that good biocompatibility during culture with the negligible corrosion ions. High strength-to-modulus ratio β Ti alloys together with excellent biological response show their prospect for biomedical applications.

3.1 Introduction

Osteoarthritis is the most common degenerative human joint disease worldwide and is characterised by the loss of joint cartilage leading to pain, and even loss of load-bearing function. It mainly occurs in the aged population, affecting 9.6% of men and 18% of women aged >60 years [39]. Traditionally, the end-stage pain cannot be removed by conservative modalities, like intra-articular injections, necessitating joint replacement surgery [41]. Among attractive candidate materials for total hip replacement (THR) and total knee replacement

(TKR), metallic orthopaedic implants play a predominant role mainly due to their mechanical stability [16]. As Ti-6Al-4V alloy has attractive mechanical properties and corrosion resistance, as well as good biocompatibility, it becomes a preferred material for load-bearing implant manufacturing to date [8]. However, there are still some doubts as to its functional reliability as a bimodal (α+β) alloy with a Young's modulus range of 100-120 GPa [185], which is much higher than that of cortical bone (10-30 GPa) [37]. Therefore, the "stress shielding" effect occurs after artificial prosthesis instalment in the long term. It is considered as a stiffer implant sustains the main load from the human body and causes a reduction in the stress level within bone, which leads to the detrimental remodelling of peri-prosthetic bone, thus the implant surrounding tissue resorption happens due to the change in the load transfer after total joint replacement (TJR) surgery [4–6,57]. Therefore, many researchers are investigating low-modulus Ti-6Al-4V lattice structure implants by additive manufacturing [90,186,187]. But a question mark surrounds their poor fatigue lifetime after subsequent artificial joint replacement. Another concern is that the metallic wear debris and *in vivo* corrosion products with vanadium may release potential cytotoxicity [8,51].

Beta titanium alloys can be described as any Ti alloys with the addition of enough beta stabilizers to retain up to 100% beta phase at room temperature upon cooling from above beta transus temperature [132]. Titanium alloys, combined with human-friendly β stabilizers such as niobium, molybdenum, and tantalum have been investigated for low-modulus bio-mechanical material applications [11–14]. Using the DV-Xα cluster method [140], Abdel-

Hady et al. [142] reported that Ti-29Nb-13Ta-4.6Zr alloy (approx. 2.88 $\overline{Bo}$ and 2.46 $\overline{Md}$) was measured with low elastic modulus at around 50 GPa. Based on molecular orbital calculation, $\overline{Bo}$ (average covalent bond strength between Ti and other alloying elements) and $\overline{Md}$ (average *d*-orbital energy level of the involved alloying elements) are used to predict mechanical properties of the specific Ti alloys. Most existing studies have focused on traditional processing, and mechanical properties of β Ti alloys. Among them, Sakaguchi et al. [188] investigated metastable as-forged and solution-treated Ti-Nb-Ta-Zr-O alloys with different niobium additions (20, 25, 30, 35 wt. %), demonstrating that all aforementioned alloys obtained ultimate tensile strength (UTS) of more than 700 MPa, and some of them possessed good elongation (more than 20%) with low Young's modulus. Besides that, Zhukova et al. [189] compared the electrochemical behaviour of Ti-22Nb-6Ta (at.%) with commercially pure (CP) titanium in simulated physiological medium (Hank's solution), reporting that the Ti-Nb-Ta β alloy possesses higher open circuit potential (OCP) values under cycling conditions. They also found that the oxide film exhibits superior resistance to the applied cyclic load when compared to CP titanium. Gordin et al. [18] and Neacsu et al. [19] reported short-term *in vitro* MC3T3-E1 preosteoblast results based on traditionally manufactured Ti-Nb-X β alloys. They found that the investigated β Ti alloys seemingly obtain equal or even better performance than CP titanium during different types of cell-relevant assays (cytotoxicity, differentiation, etc.).

Metal additive manufacturing (AM) is based on the principle of incremental layer-by-layer

material consolidation, facilitating the fabrication of complicated components through the controlled melting or sintering of feedstock materials with the aid of energy sources, e.g., lasers, electron beams, etc. [74,190,191]. Considering factors such as less feedstock consumption in manufacturing components, supply chain and assembly line simplification, customized complex-part fabrication, metal AM process is an attractive option for manufacturing high-end products when compared to traditional manufacturing techniques [20,81,192]. Among varieties of additive manufacturing techniques, powder bed fusion (PBF) techniques are typically suitable for manufacturing delicate, custom biomedical implants with high dimensional accuracy [96,109,193,194].

A limited amount of research on additive manufacturing β Ti alloys exists to date. Zhang et al. [21] and Liu et al. [22] investigated microstructure and mechanical properties of Ti-24Nb-4Zr-8Sn dense and lattice samples based on electron beam melting (EBM) and selective laser melting (SLM). Their studies illustrated keyhole defect (and its formation mechanism), which is caused by in-process tin vaporization because tin has the lowest boiling point among the evolved alloying elements. However, there does not appear to have publications which specifically demonstrate microstructure evolution of Ti-Nb-Ta-Zr alloys undergoing fast heating & cooling rates, and laser re-melting via PBF. The function of so-called neutral element Zr [195] on β phase stability is not confirmed in the aforementioned thermal history, and there is still some dispute about the function of Zr in Ti-Nb based β alloys manufactured by traditional manufacturing techniques. Hao et al. [196] mentioned the combined alloying

addition of Zr and Sn is effective in raising the beta transus temperatures of Ti–Nb based alloys, thus potentially narrowing beta phase region. Abdel-Hady et al. [142] concludes that zirconium works as a β stabilizing element in Ti-Zr-Nb β alloys over the wide range of Zr content in solution-treated and aged conditions. The present chapter investigates *in-situ* alloying Ti-Nb-Ta based β alloys with different zirconium additions (0, 5, 9 wt. %) manufactured by SLM. The as-fabricated parameter optimisation, microstructure evolution and process-induced defects distribution, tensile testing performance, ion release evaluation, and MC3T3-E1 preosteoblast cell viability of TNT(Z) alloys are sequentially characterised. We also introduce solution treating then water quenching aiming to reduce their Young's moduli, which is the starting point of decreasing the "stress shielding" effect based on its load-bearing application.

3.2 Materials and methods

3.2.1 Powder feedstock preparation

Pure element powder was chosen for as-designed materials powder mixing. The chemical composition of the three designed TNT(Z) alloys in this work (given in Table 3-1) are Ti-34Nb-13Ta, Ti-34Nb-13Ta-5Zr, Ti-34Nb-13Ta-9Zr, hereafter termed TNT, TNT5Zr and TNT9Zr

Table 3-1

As designed chemical composition of the three employed alloys (wt. %).

	TNT	**TNT5Zr**	**TNT9Zr**
Ti	Balance	Balance	Balance
Nb	34	34	34
Ta	13	13	13
Zr	0	5	9

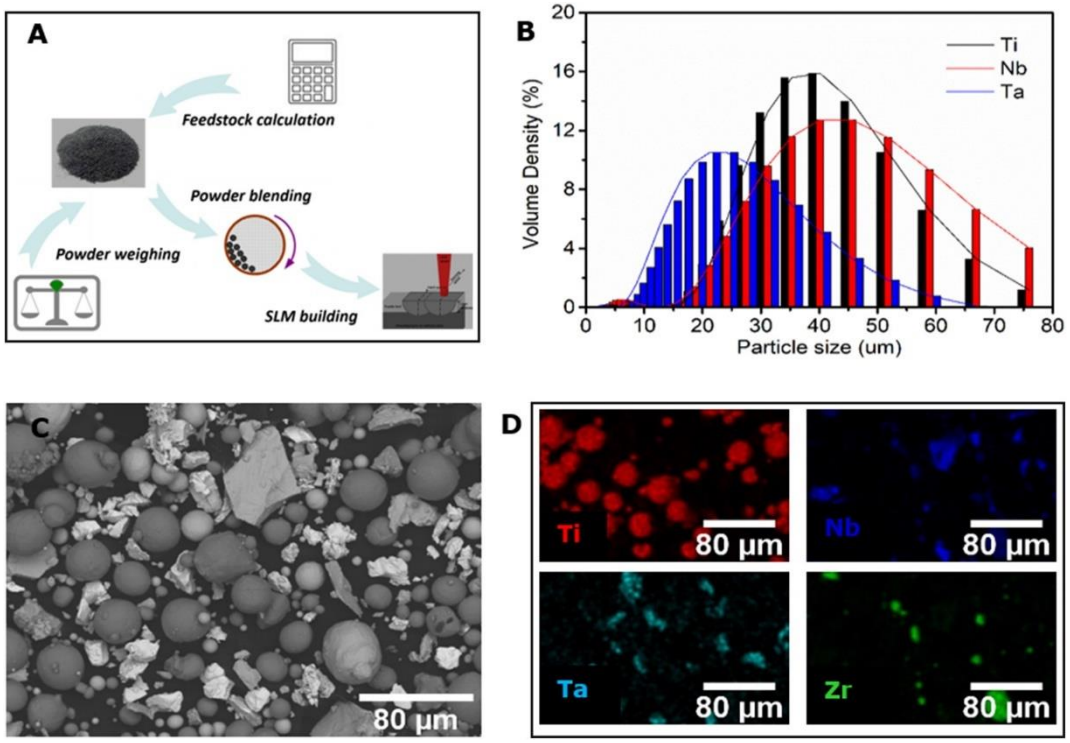

Fig. 3-1. (A) Schematic of the SLMed TNT(Z) alloys manufactured by in-situ alloying. Characteristic of feedstock powder: (B) particle size distribution (PSD) of as received pure Ti, Nb, Ta powder, (C) particle morphology of blended TNT9Zr (e.g.) powder, and (D) EDS map of the involved alloying elements. Note: the SLM process figure in panel A is sourced from article [197]. PSD of Zr powder is not listed as it is too reactive to be measured.

alloy, respectively. Spherical Ti, Zr powder (TLS, Germany) with nominal particle size distribution (15—83 μm) and (10—45 μm) were gas atomised in argon atmosphere. Rocky Nb (Elite, UK), Ta powder (H.C. Starck, Germany) with an average particle size (D_{50}) of 43.9 μm and 23.4 μm (Fig. 3-1B) was manufactured through a hydride-dehydride process. Powder weighing was finished in a glove box with an argon protective atmosphere. Following that, powder blending was performed for ten hours in a horizontal rotating drum, as-seen in Fig. 3-1A. The blended powder was characterised by energy-dispersive X-ray spectroscopy (EDS, Bruker) mapping, aiming to check blending performance before the SLM manufacturing

process (Fig. 3-1C-D).

3.2.2 Selective laser melting

An M2 Cusing SLM system (Concept Laser, GE Additive) was adopted to fabricate TNT, TNT5Zr and TNT9Zr samples on Ti alloy substrates. The machine was equipped with a 400 W Yb:YAG fibre laser at a wavelength of 1064 nm. The laser beam spot size was focused at approx. 63 μm. Considering the high oxidation risk of these pure elements, high purity protective argon (99.8%) was continually pumped into the process chamber until the as-fabricated parts thoroughly cooled down. The key SLM parameters investigated for manufacturing parameter optimisation were: laser power (240—300 W), scan speed (400—1000 mm/s), and scan spacing (35—65 μm). The chessboard scan strategy with scan vectors rotated by 90º in adjacent 5 x 5 mm blocks was used for building parts, and each successive layer was shifted by 1 mm in both the X and Y directions; the pre-set layer thickness was 20 μm. Based on SEM (TM3000, Hitachi) backscattered electron (BSE) images (nine low Mag. images for each parameter), area fraction of porosity, and un-melted Nb and Ta content through image processing software (Image J, Fiji), were analysed. All data were recorded as the mean ± standard deviation (SD). The manufactured parts were 7 x 7 x 7 mm cubes and sub-size

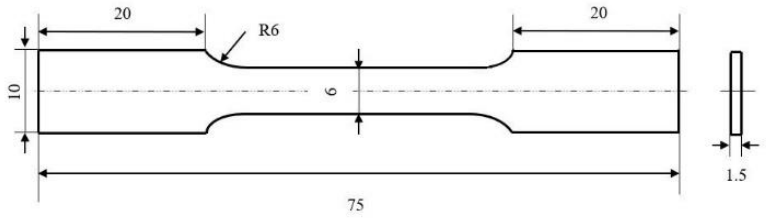

Fig. 3-2. Specimen geometry of dog-bone tensile test specimen in mm.

dog-bone tensile specimens with 75 mm total length. The sub-size tensile specimen dimension was designed according to the ASTM- E8/ E8M-13a standard [198]. The tailored cross-section parts were horizontally manufactured with a height of 10 mm, then sliced into 1.5 mm thickness dog-bone test-pieces (Fig. 3-2) with SLM original side surfaces using wire electron discharge machining (EDM, GF Machining Solutions).

3.2.3 Microstructure and micro-defects characterisation

Metallographic specimens were prepared using automatic grinding and polishing equipment (Tegramin 30, Struers), and then etched by Kroll's reagent (2% HF + 6% HNO_3 + 92% H_2O). The phase identification was performed by X-ray diffractometer (XRD) (AXRD, Proto) with Cu Kα radiation, and XRD spectra were collected by a fixed parameter of 0.02° step size and a 2s time/step. Electron backscatter diffraction (EBSD) mapping of samples were observed with a field-emission gun (FEG) SEM (NNS450, FEI) equipped with EBSD detector (EDAX, Ametek). The selected step size was 0.8 μm, aiming to maintain high EBSD indexing rate. A transmission electron microscope (JEM-2100, JEOL) operating at 200 kV was used to capture bright-field (BF) images and selected area diffraction (SAD) pattern, bright-field scanning transmission electron microscopy (BF-STEM) images. Thin foils for TEM were prepared through an argon ion milling technique (Gatan PIPS, Ametek), involving gradient milling by different Ar ion energy and sputter angle settings. The porosity and un-melted particles of cylinder specimens (D1.6 H7.5) were analysed with micro-CT (Skyscan, Bruker). The scan parameters were an accelerating voltage of 165 kV and a current of 75 μm for a 360º scan. A

total of 2,500 projections were collected on a charge-coupled device (CCD) detector using a 1s exposure time. The data was reconstructed and visualized using Nikon Pro 3D and Avizo software, respectively.

3.2.4 Differential scanning calorimetry and solution treatment

Differential scanning calorimetry (DSC) analysis was performed by heat-flux DSC cell (404 F1 Pegasus, Netzsch). As-fabricated TNT(Z) samples (approx. 20 mg each sample) were separately loaded in recrystallized alumina crucible, sealed with a lid using the same material. It ran with a constant heating and cooling rate of 10℃/min in argon atmosphere to predict the thermodynamic properties. The heating temperature was increased to a maximum temperature (1200℃), then cooled down to identify phase transformation characteristics of each alloy. Solution treatment specimens were encapsulated in evacuated quartz tubes, dwelled at 750℃ in an electric furnace for one hour, followed by quenching into water.

3.2.5 Micro-hardness and mechanical properties

Mirror-like specimens were mounted on a micro-hardness tester (Wilson VH1202, Buehler) for Vickers hardness measurement. The test for each sample was performed with a 100 g load and 10 times linearly, indented with recommended spacing according to the ASTM E384-17 standard [199]. The as-fabricated specimens in tensile testing were carried out perpendicularly build direction at room temperature. The stress-strain curves were measured at a crosshead speed of 0.5 mm/min at room temperature using a tensile testing machine (2500, Zwick/Roell).

Two specimens per alloy were tested to average tensile properties, and a clip-on extensometer was attached to the 15 mm gage length of specimen until rupture, then fracture morphology was observed using a SEM (NNS450, FEI).

3.2.6 Metallic ion release evaluation and cell viability

Metallic samples (two-side polished, 10 x 10 mm) were ultrasonically cleaned in pure ethanol for 10 minutes and then sterilized in autoclave for 90 minutes. For the ion release study, one sample per each metallic material was submerged for 7 days, 14 days, 21 days, and 30 days, 90 days, and 180 days in 20 mL of minimal essential medium (MEM) supplemented with 1% penicillin/streptomycin, and 0.5 g/L L-glutamine. Meanwhile, the control group for each time interval contained 20 mL aforementioned MEM medium without a metallic sample. These liquid samples were all kept in a cell incubator with 5% CO_2 at 37°C atmosphere. From these 20 mL after-immersion mediums, the 15 mL was used for metallic ion release evaluation, and the other 5 mL was a part of cell culture medium to perform MC3T3-E1 cell viability assays. The measurement of ion release after the immersion test was performed using inductively coupled plasma optical emission spectrometry (ICP-OES) (Optima 8000, PerkinElmer). Before the measurement of metallic ions in all samples, the calibration of standardised samples was conducted with the involved elements at a wavelength of Ti (334.940 nm), Nb (309.418 nm), Ta (226.230 nm), and Zr (343.823 nm). The correlate coefficients of these four calibrations were $\geqslant 0.999$. Two runs measurements were set up to demonstrate these element analysis results. After the longest time interval (180 days) immersion test, MC3T3-E1 preosteoblast was seeded and cultured in a flask with standard culture medium. The after cultured MC3T3-E1

cells were detached from the bottom surface of the flask using 0.25% trypsin-EDTA solution (5 minutes at 37°C), then seeded in each well (24-well plate) at a concentration of 2 x 10^4 cells/cm^2. The medium for cell culture was 0.5 mL medium after the immersion test, supplemented with 0.5 mL standard culture medium including serum (MEM, 10% foetal bovine serum, 1% penicillin/streptomycin, and 0.5g/L L-glutamine); alongside a control group containing standard supplemented medium was set up. The plate was then kept in the cell incubator for 24 hours. Alamar blue assay [200] in 96-well plate was performed using a spectrophotometer (Spark, Tecan) at a wavelength of 560 nm excitation and 590 nm emission. This assay was conducted in triplicate. The viability of cells after-immersion medium was analysed by staining with calcein-AM and propidium iondide. Stained cells were visualized using a microscope imaging system (EVOS M5000, Thermo Scientific). Analysis of Variance (ANOVA) and two-tailed t-tests were performed for Alamar blue results, with a p value < 0.05 considered as being statistically significant.

3.3 Results

3.3.1 Selective laser melting parameter optimisation

The relationships between un-melted particles, porosity and PBF key parameters, namely laser power, scan speed, scan spacing are presented in Fig. 3-3(A-C). Fig. 3-3A shows a clear tendency: the percentage of un-melted Nb decreases to a large extent from 4.55% to 1.93% when laser power rises from 240 W to the maxima (300 W); the variances of Y-values (un-melted Nb, Ta also porosity) become smaller when laser power increases. No ideal processing

window obtained inside this parameter group after considering the best sample with relatively high value of porosity (2.2%) and un-melted Ta (0.7%). The slow scan speed (500 mm/s) combining other preset parameters is considered an optional processing parameter with low defect level after conducting a batch of Y-values versus scan speed characterisation (Fig. 3-3B). The un-melted particles and porosity level is much higher in samples manufactured by high scan speed,

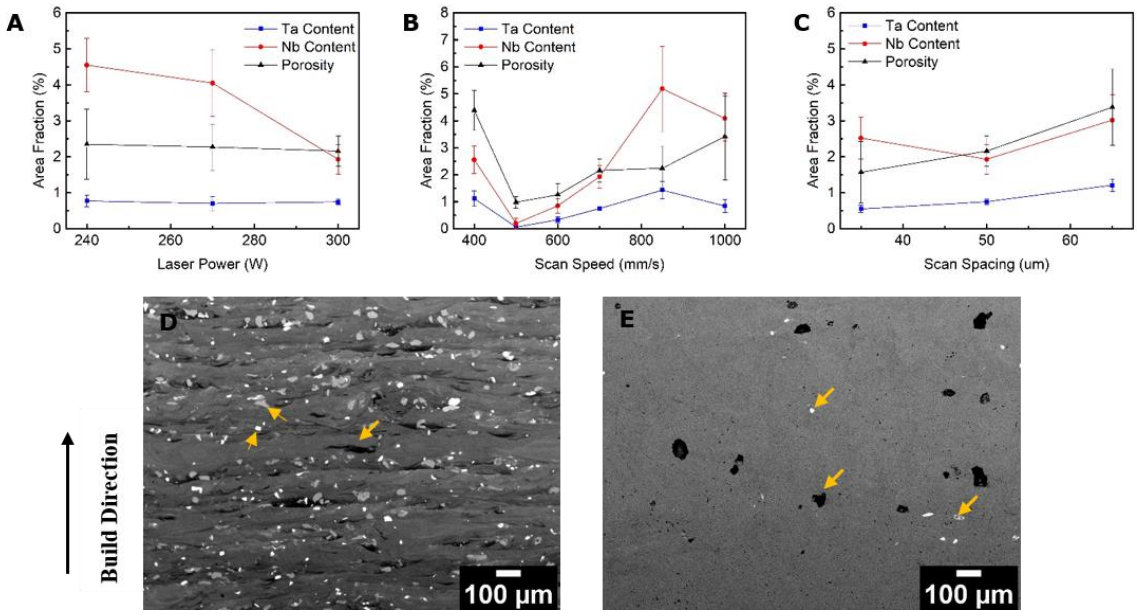

Fig. 3-3. (A) Un-melted Ta & Nb content and porosity versus laser power; the preset parameters are: 700 mm/s scan speed, 50 µm scan spacing. (B) Un-melted Ta & Nb content and porosity versus scan speed; the preset parameters are: 300 W laser power, 50 µm scan spacing. (C) Un-melted Ta & Nb content and porosity versus scan spacing; the preset parameters are: 300 W laser power, 700 mm/s scan speed. (D) Backscattered SEM image of as-built TNT specimen with low energy density, and (E) with high energy density. Note: arrows point out grey particle (Nb) and bright particle (Ta), and porosity features ((D) lack of fusion, (E) keyhole).

such as 850 mm/s, when compared to the counterpart manufactured by low scan speed (e.g., 500 mm/s). No obvious Y-values versus scan spacing fluctuation is found after increasing from 35 µm to 50 µm (Fig. 3-3C). Additionally, low energy density and high energy density as-built

TNT specimen SEM (BSE) images are provided in Fig. 3-3(D-E). The low energy density case could happen with low laser power (e.g., 240 W) or a high scan speed (e.g., 1000 mm/s); the porosity type is mainly a lack of fusion (arrows in Fig. 3-3D), and a high percentage of un-melted Nb & Ta disperses randomly in each layer. The high energy density case could happen in a low scan speed (e.g., 500 mm/s); the main porosity formation is keyhole [22,82] (arrows in (Fig. 3-3E), and an extremely low percentage of un-melted Nb & Ta appears in the specimen matrix. The same defect characterisation method was chosen for TNT5Zr and TNT9Zr alloy build parameter optimisation by changing laser scan speed, but the results were skipped due to the limited space.

3.3.2 Phase analysis and microstructure

Fig. 3-4 shows the XRD profiles of as-fabricated TNT samples with different Zr additions. As seen, these samples all obtained main β phase with the highest intensity peak (110). The diffraction angles for $(110)_{\beta}$ atomic arrangement plane in TNT, TNT5Zr, TNT9Zr alloys are 38.70º, 38.53º, and 38.43º respectively. There is a low intensity suspicious alpha peak at around 35º of the three alloys. IPF maps of as-fabricated TNT alloy (Fig. 3-5(A-B)) show equiaxed and columnar grain formation, and micro-pores randomly located in the material matrix. <001> fibre texture is observed by <001> IPF (Fig. 3-5C), and the phase distribution map (Fig. 3-5D) of TNT alloy indicates that beta phase matrix (red contrast) existence, and precipitates (green contrast) appear along grain boundary. The same type of grain formation and as-fabricated pore features are also observed in TNT5Zr (Fig. 3-6(A-B)) and TNT9Zr alloys (Fig. 3-7(A-B)). <001> fibre texture is kept in TNT alloys with zirconium additions, and the maximum texture

indices are between 1 and 3 (Fig. 3-6C & Fig. 3-7C). Additionally, Fig. 3-6D & Fig. 3-7D demonstrate phase distribution maps of TNT5Zr and TNT9Zr alloy with grain boundary precipitates. The grain size (Fig. 3-8A) and misorientation angle (Fig. 3-8B) of the three alloys prove that TNT5Zr, TNT9Zr alloys possess a higher percentage of fine grain size (<30 μm) grains than the TNT sample. The high-angle grain boundary (greater than 15°) is the main tilt boundary of the three alloys after misorientation angle quantification analysis. Fig. 3-9A shows a BF micrograph taken from the beta matrix of as-fabricated TNT alloy, together with a SAD pattern viewed along $[111]_{\beta}$ zone axis. It should be noted that no formation of metastable precipitates (e.g., ω or α'') inside beta matrix. Fig. 3-9B presents the BF-STEM image of as-fabricated TNT alloy, captured from a region close to grain boundary. It indicates the existence of nano-scale precipitates along the grain boundary.

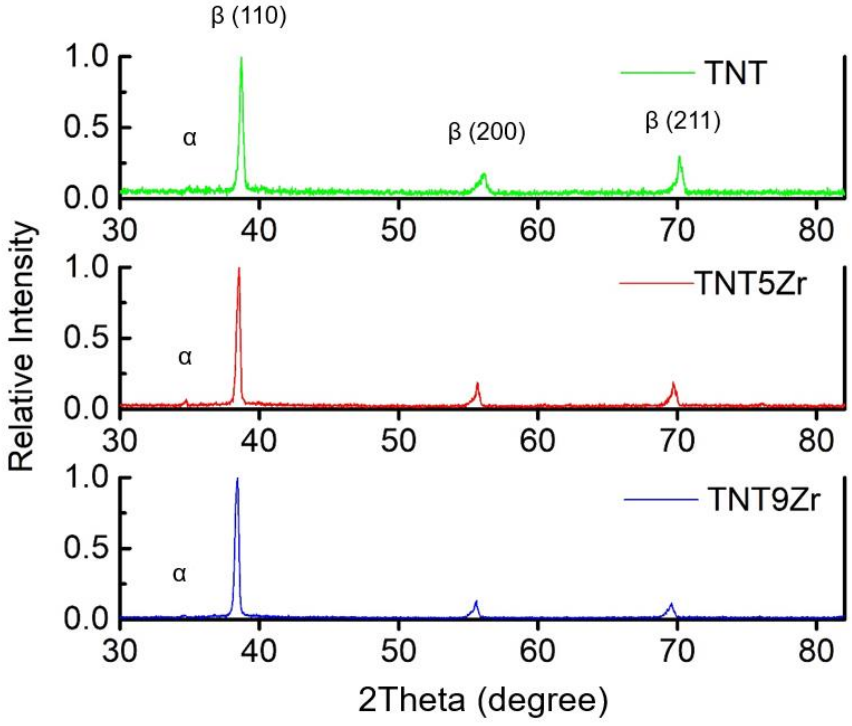

Fig. 3-4. X-ray diffraction patterns of as-fabricated TNT, TNT5Zr, TNT9Zr alloys.

The BF image and SAD pattern obtained from the beta matrix of as-fabricated TNT5Zr alloy are presented in Fig. 3-9C, which shows no precipitation in the beta matrix. The BF-STEM image (Fig. 3-9D) indicates dispersive nano-scale precipitates occur at the grain boundary. Similarly, a single beta phase microstructure is observed in the BF image and its SAD pattern (Fig. 3-9E) of as-fabricated TNT9Zr alloy. Meanwhile, potential precipitation is found along beta grain boundary (Fig. 3-9F).

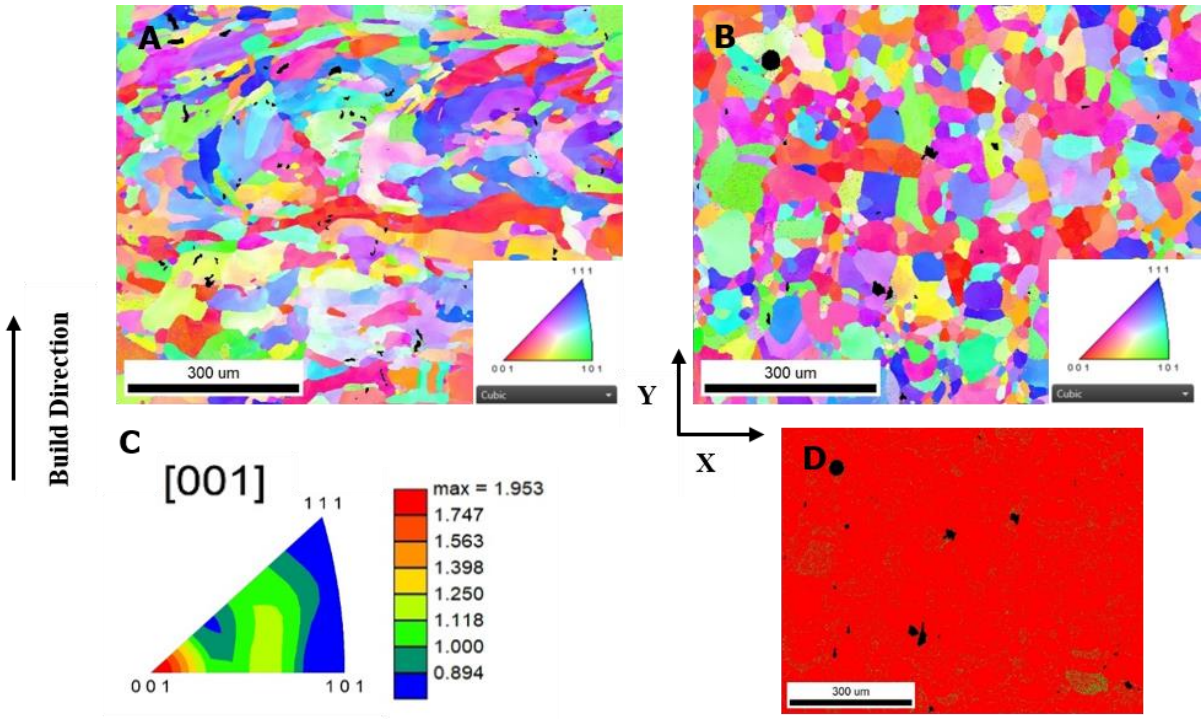

Fig. 3-5. EBSD results of SLM-processed TNT alloy: (A) inverse pole figure (IPF) map in parallel build direction, (B) inverse pole figure (IPF) map in perpendicular build direction, (C) <001> inverse pole figure (IPF) exported from the IPF map in parallel build direction, and (D) phase distribution map exported from the IPF map in perpendicular build direction. Note: red denotes beta Ti, green denotes precipitate phases.

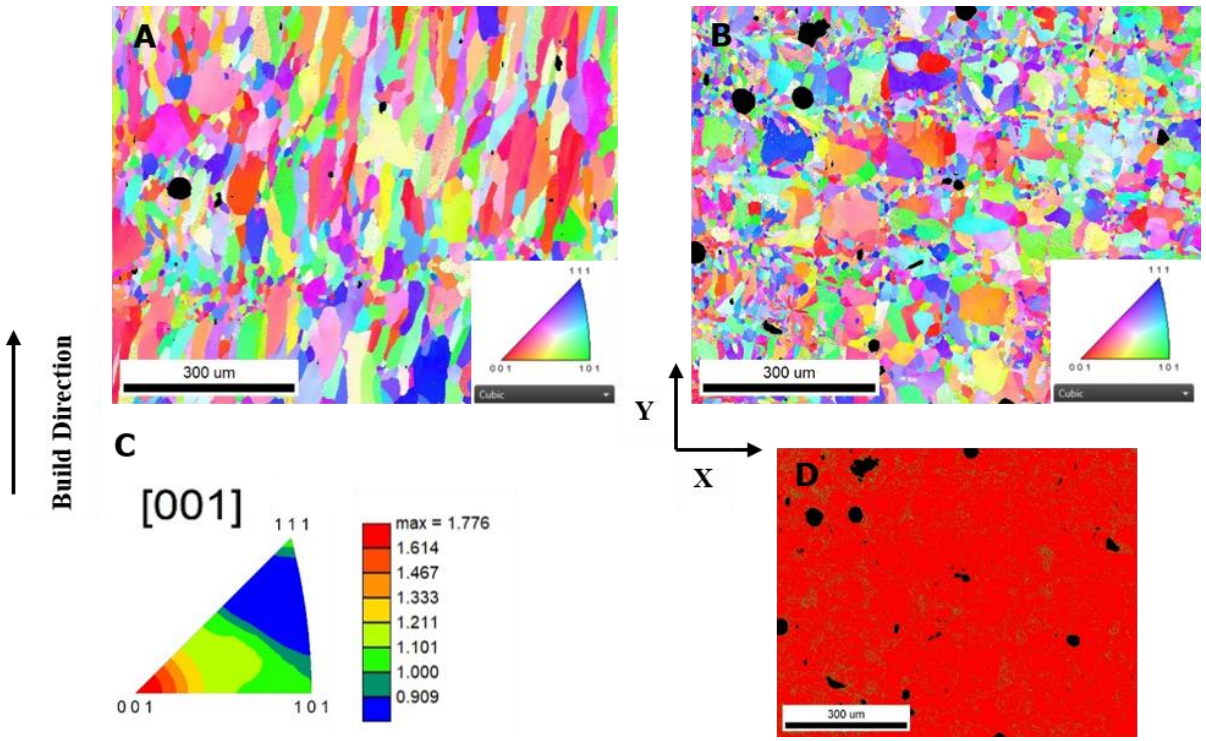

Fig. 3-6. EBSD results of SLM-processed TNT5Zr alloy: (A) inverse pole figure (IPF) map in parallel build direction, (B) inverse pole figure (IPF) map in perpendicular build direction, (C) <001> inverse pole figure (IPF) exported from the IPF map in parallel build direction, and (D) phase distribution map exported from the IPF map in perpendicular build direction. Note: red denotes beta Ti, green denotes precipitate phases.

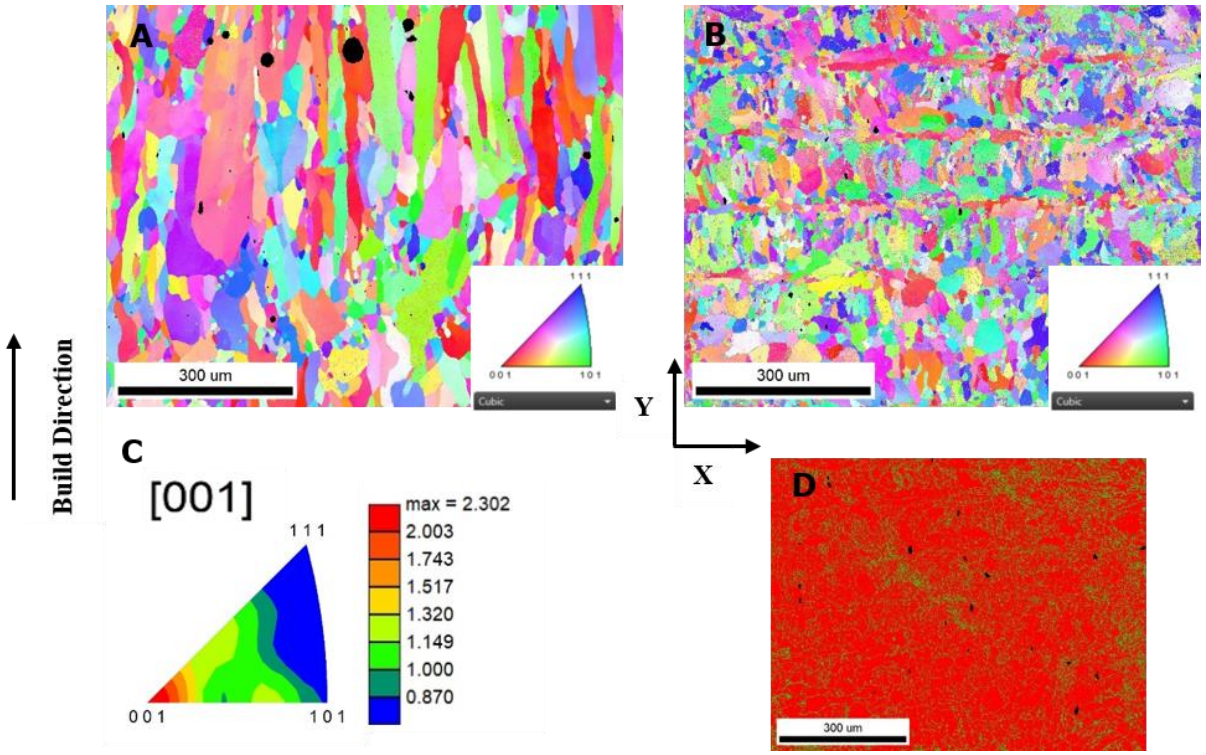

Fig. 3-7. EBSD results of SLM-processed TNT9Zr alloy: (A) inverse pole figure (IPF) map in parallel build direction, (B) inverse pole figure (IPF) map in perpendicular build direction, (C) <001> inverse pole figure (IPF) exported from the IPF map in parallel build direction, and (D) phase distribution map exported from the IPF map in perpendicular build direction. Note: red denotes beta Ti, green denotes precipitate phases.

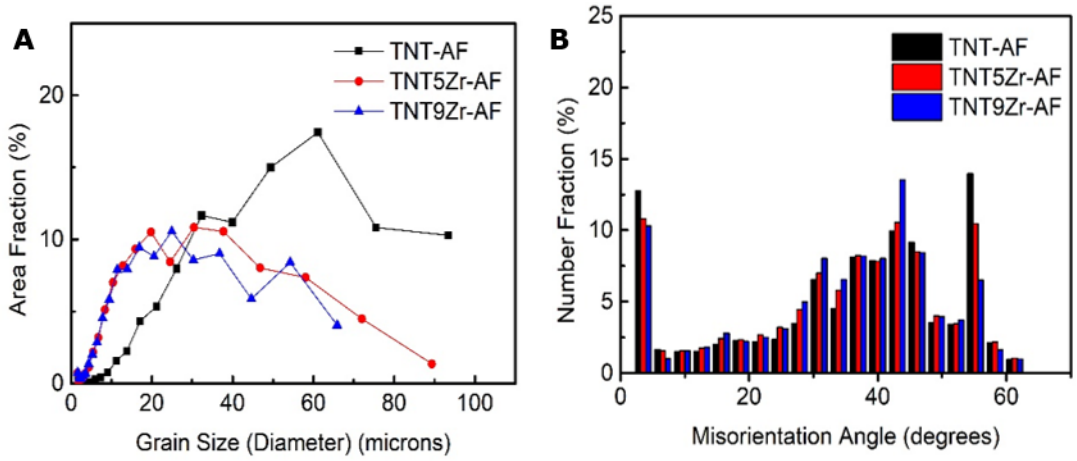

Fig. 3-8. EBSD quantitative results of SLM-processed TNT, TNT5Zr, TNT9Zr alloys: (A) grain size and (B) misorientation angle.

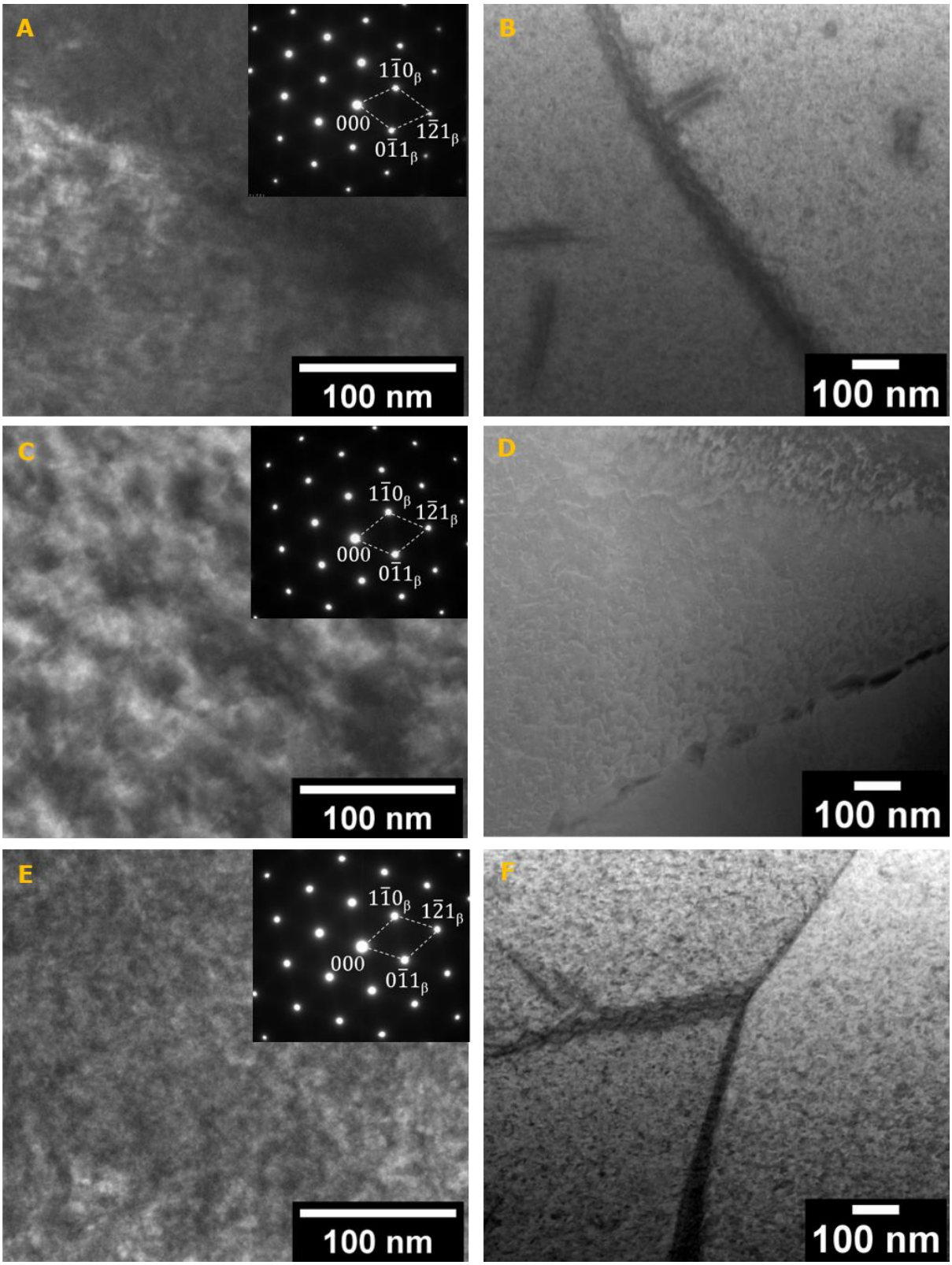

Fig. 3-9. (A) BF image with corresponding SAD pattern (inset) of as-fabricated TNT alloy, taken from the beta matrix region. (B) BF-STEM image of as-fabricated TNT alloy, taken from a region close to the grain boundary. (C) BF image with corresponding SAD pattern (inset) of as-fabricated TNT5Zr alloy in the beta matrix. (D) BF-STEM image of as-fabricated TNT5Zr alloy, taken from a region close to the grain boundary. (E) BF image with

corresponding SAD pattern (inset) of as-fabricated TNT9Zr alloy in the beta matrix. (F) BF-STEM image of ad-fabricated TNT9Zr alloy, taken from a region close to grain boundary. Note: the beam direction from each capture is parallel to the $[111]_{\beta}$ direction.

3.3.3 Micro-defects distribution and DSC thermal analysis

Fig. 3-10 demonstrates reconstructed 3D parts and the quantitative data of defects by the aid of micro-CT technique. Voids (yellow) are with an irregular shape and appear to be randomly distributed in SLM-processed TNT(Z) specimens. The total number of indexed un-melted particles (red) is smaller than voids in these three alloys. The main difference here is un-melted particles occupy slightly more sites in the TNT5Zr sample than the TNT and TNT9Zr samples. The size of two-type defects is mainly located in the range of 3—20 μm (Fig. 3-10B). Defects size (EqDiameter) here means the equivalent diameter of the spheres with the same volume as the measured defects. The relative density of as-fabricated TNT, TNT5Zr, TNT9Zr samples calculated based on the quantitative data are 99.98%, 99.99% and 99.97%, respectively. Meanwhile, the un-melted particle volume fracture of the TNT, TNT5Zr, TNT9Zr samples calculated based on the quantitative data are 0.0007%, 0.0030% and 0.0020%, respectively.

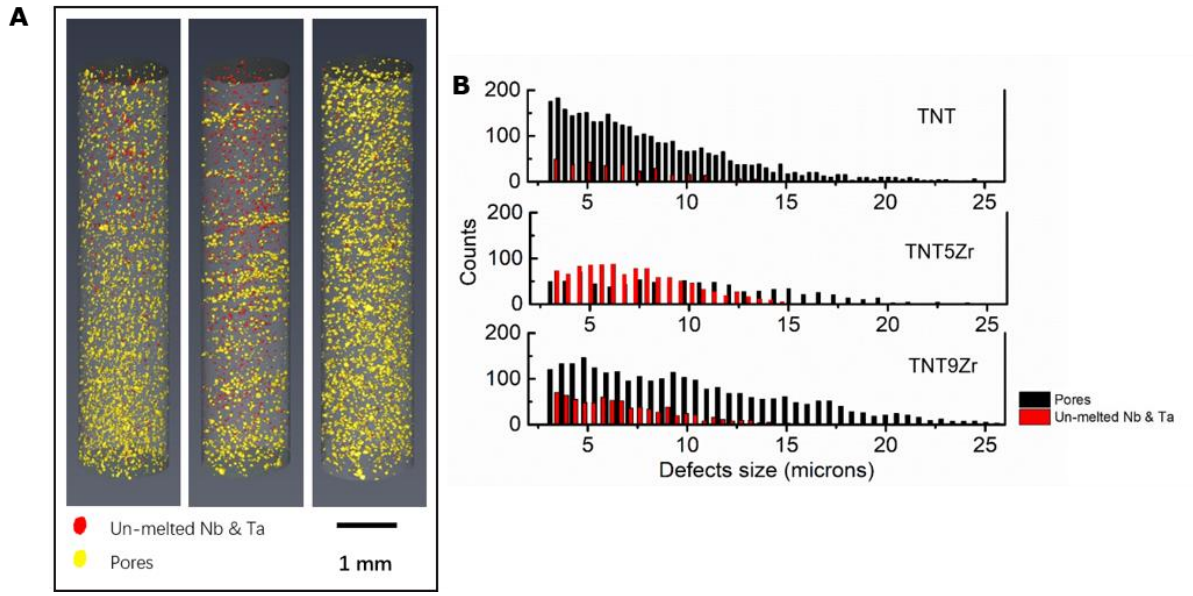

Fig. 3-10. (A) Un-melted particles and pore defects distribution of as-fabricated TNT (left), TNT5Zr (middle), TNT9Zr (right) alloy analysed by micro-CT, and (B) the size and counts of defects inside these samples.

High temperature DSC curves of the three TNT(Z) alloys are given in Fig. 3-11. During the heating process, from room temperature to the upper temperature limit (1200℃), there is an exothermic peak near 678℃ (TNT); the exothermic peaks of the TNT5Zr and TNT9Zr samples are observed near 765℃ and 848℃, respectively. The alpha → beta transus temperature was observed to increase with zirconium addition, and a wide range of no-clear exothermic peak lower than alpha → beta transus temperature was observed. Contrastively, no clear endothermic peaks were observed during the cooling process of the three alloys. The solution treating then water quenching was performed at a temperature (750℃) between the lowest alpha → beta transus temperature (678.6℃) and the highest counterpart temperature (848.3℃).

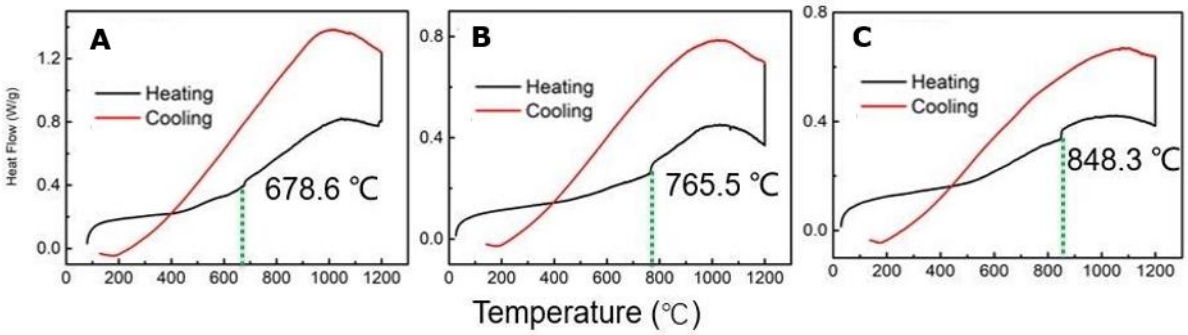

Fig. 3-11. The DSC heating & cooling curves of (A) TNT, (B) TNT5Zr, and (C) TNT9Zr alloys.

3.3.4 Vickers hardness and mechanical properties

The three designed alloys show Vickers hardness homogeneity for different planes and geometric positions (Fig. 3-12A). The micro-hardness of as-fabricated TNT (XOY plane) is 208.5 ± 5.5 HV0.1. The mean value of as-fabricated TNT5Zr (XOY plane) and TNT9Zr (XOY plane) are 232.0 ± 6.5 HV0.1 and 259.7 ± 3.9 HV0.1, respectively. The beta grain refinement made Vickers hardness of TNTZ as-fabricated samples higher than TNT alloy. The material's microhardness reduction in solution treated condition was observed due to grain growth when dwelling at 750℃ for one hour.

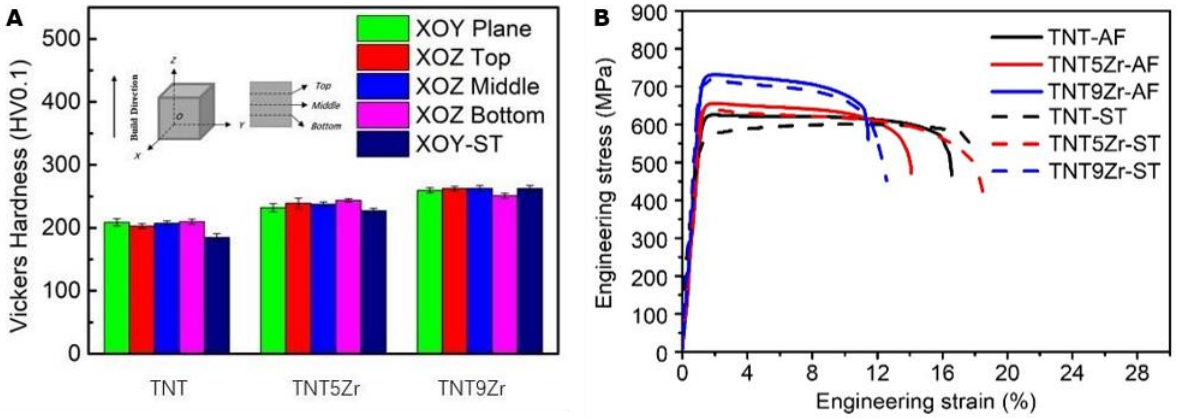

Fig. 3-12. (A) Vickers hardness of as-fabricated and solution heat treated TNT, TNT5Zr and TNT9Zr alloys, and (B) typical stress-strain curves of these alloys.

Typical stress–strain curves of the as-fabricated and solution-treated TNT, TNT5Zr, TNT9Zr alloys manufactured by SLM are shown in Fig. 3-12B. All samples exhibit an ultimate tensile strength (UTS) approx. above 600 MPa and an elongation exceeding 10%. Table 3-2 demonstrates tensile properties on the three as-mentioned alloys in both conditions. The elastic moduli of as-fabricated TNT(Z) alloys are all less than 70 GPa. Meanwhile, the elongation of as-fabricated TNT(Z) alloys ranges from 11.4% to 14.1%, showing their good ductility. The higher Young's modulus and UTS have been observed after the TNT alloy adding different percentage of zirconium. Meanwhile, the UTS slightly decreases after conducting solution treating then water quenching of these TNT(Z) alloys. Fig. 3-13A-F reveals typical ductile fractures of these alloys. The large shear-like oval dimple features in as-fabricated TNT specimen are more irregular than the counterpart of as-fabricated TNT5Zr and TNT9Zr. As-fabricated porosity is also found in both conditions of these alloys. The high magnification SEM images show the internal wall of keyhole from the as-fabricated TNT (Fig. 3-13G) and TNT5Zr alloys (Fig. 3-13H). It clearly shows the original un-deformed microstructural difference of the two alloys: cellular subgrain (TNT) and equiaxed/columnar mixed grain microstructure (TNT5Zr).

Table 3-2

Comparison of the tensile properties for the as-fabricated TNT(Z) alloys before and after solution treatment.

Material	E (GPa)	$\sigma_{0.2}$ (MPa)	σ_{UTS} (MPa)	δ (%)	σ_{UTS}/E
TNT-AF	52 ± 3	610 ± 5	681 ± 6	14.1 ± 1.2	12.9 ± 0.6
TNT5Zr-AF	57 ± 5	650 ± 8	698 ± 4	13.7 ± 0.6	12.1 ± 1.1
TNT9Zr-AF	66 ± 5	741 ± 8	772 ± 9	11.4 ± 0.4	11.9 ± 0.8
TNT-ST	47 ± 2	569 ± 2	597 ± 4	15.8 ± 1.8	12.7 ± 0.5
TNT5Zr-ST	56 ± 3	628 ± 3	639 ± 4	16.0 ± 2.6	11.3 ± 0.4
TNT9Zr-ST	66 ± 1	715 ± 2	722 ± 4	14.0 ± 1.4	10.9 ± 0.2

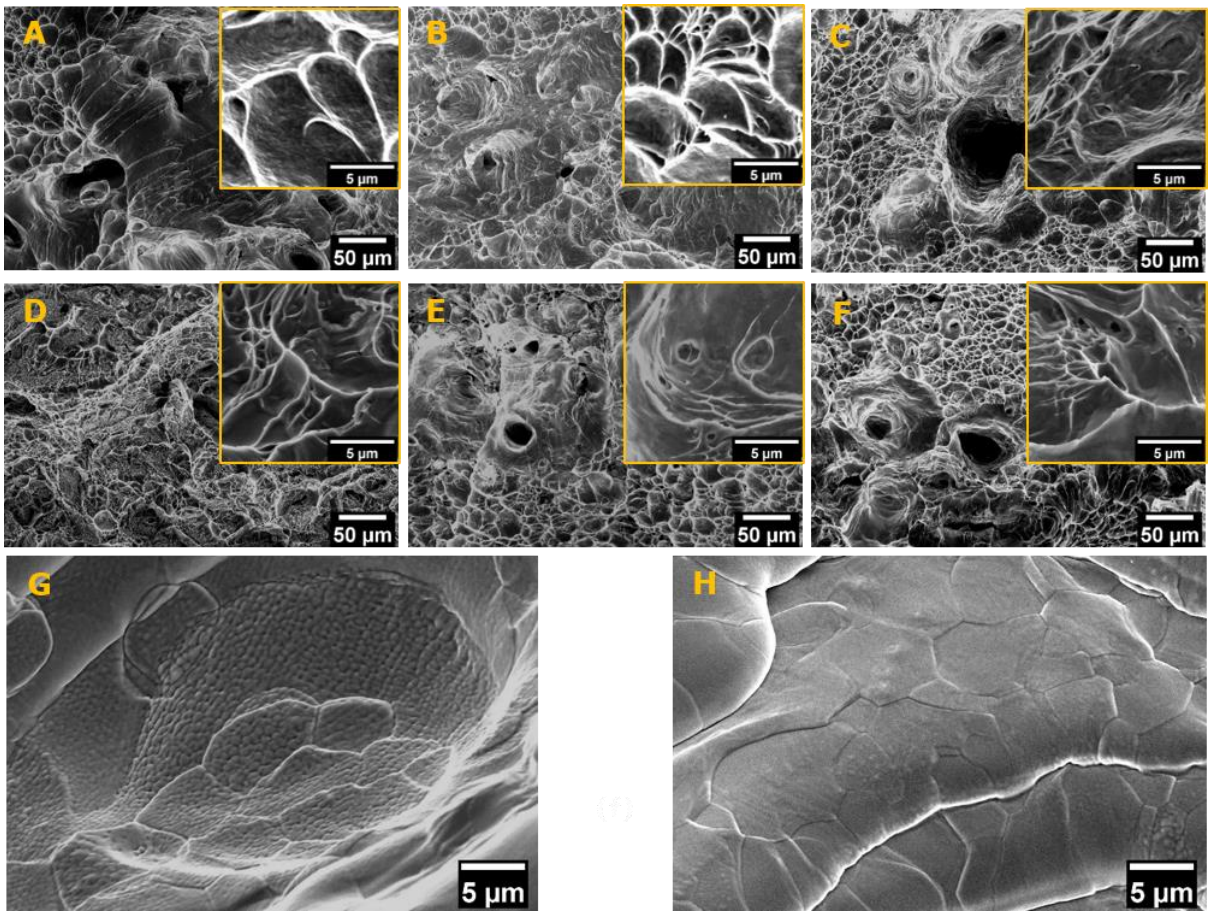

Fig. 3-13. Tensile fracture morphologies from the (A) as-fabricated TNT, (B) TNT5Zr and (C) TNT9Zr alloys, and (D) solution treated TNT, (E) TNT5Zr and (F) TNT9Zr alloys. (G) The internal wall feature of keyhole from

as-fabricated TNT alloy, and (H) from as-fabricated TNT5Zr alloy.

3.3.5 Ion release and in vitro preosteoblast response

The ion release rate of the three alloys after static immersion testing is shown in Fig. 3-14. Overall, the concentration of each metallic ion from TNT (Fig. 3-14A), TNT5Zr (Fig. 3-14B), TNT9Zr alloys (Fig. 3-14C) after immersion with MEM containing medium is no more than 10 μg/L. The TNT alloy ion release result seems show a tread that the concentration of the more detectable elements (Nb, Ta) in the initial stage decrease along with a longer time interval immersion (e.g., 180 days). Conversely, Ti ion concentration appears a slight rise with the growth of immersion time. By comparison, the concentration level of these four metallic ions in TNT5Zr alloy become even lower after Zr addition. Clearly, the mild ion concentration drops from Nb, Ta and no fluctuation from Ti, Zr is found when immersion time increased from 7 to 180 days. Overall, the TNT9Zr alloy ion release result was kept the tread as TNT5Zr alloy. However, a slight Ta ion fluctuation below 5 μg/L was observed in the range of relatively short-term immersion (≤30 days). The metabolic activity of MC3T3-E1 preosteoblast cells with the 7, 14, 21, 30, 90 and 180 days released ions and cell culture medium are shown in Fig. 3-14D. Similar Alamar blue reduction level of each alloy is found after immersion tests at different time intervals when compared to the corresponding control group (Fig. 3-14D). Noticeably, there happened a decrease in fluorescence of the control group after 180 days immersion by comparison with the other control groups. Osteoblast cells cultured with medium recovered from the ion release assays showcase a prevalence of intact membranes (green) with negligible cells marked as ruptured or damaged (red), see Fig. 3-15. Notably, it cannot find obvious

decrease of cell viability in the culture with metallic ion involved medium when compared to the control ones in each time points form 7 days to 180 days.

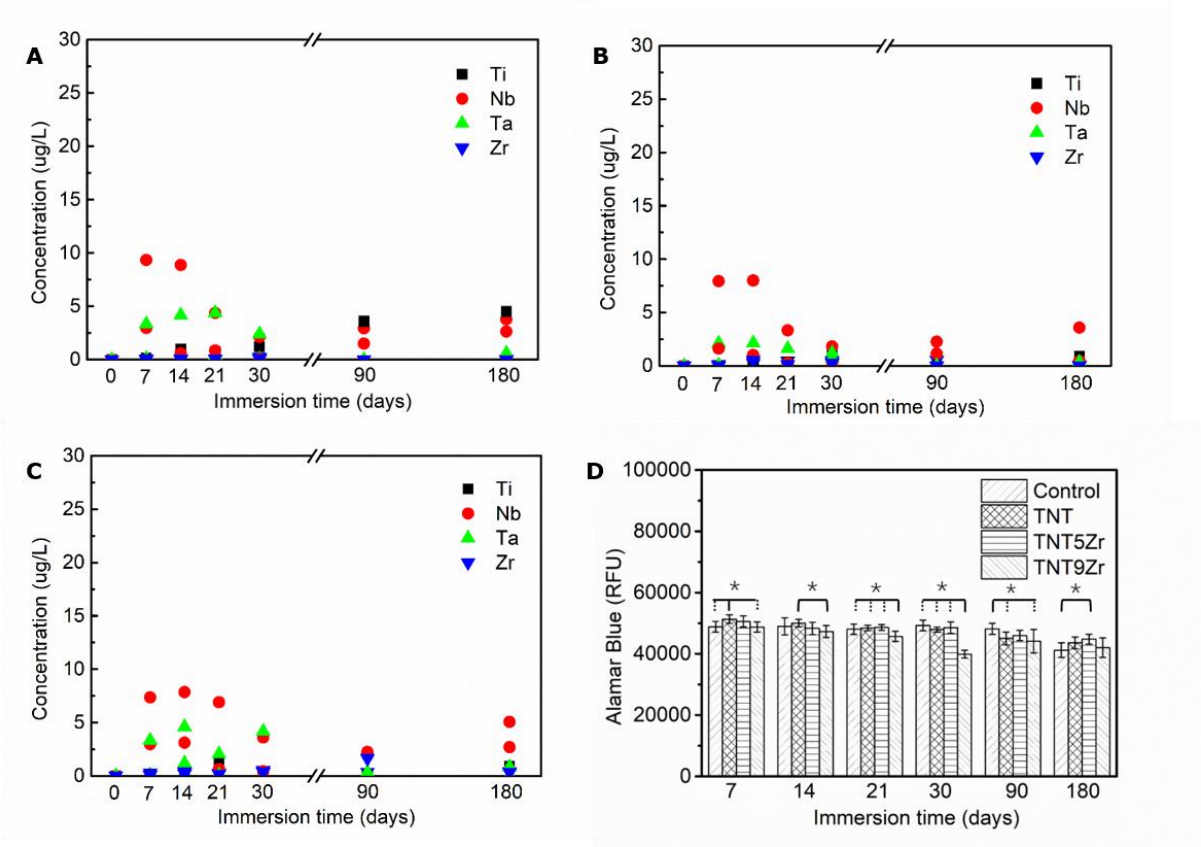

Fig. 3-14. Ion concentration of the involved elements in (A) TNT, (B) TNT5Zr, and (C) TNT9Zr alloys measured by ICP-OES, and (D) the metabolic activity of MC3T3-E1 preosteoblast cells seeded in after-immersion containing medium, where * signifies p value < 0.05 (where more than one pair is illustrated, the comparison between the group indicated with a solid line and any other groups indicated with dash lines).

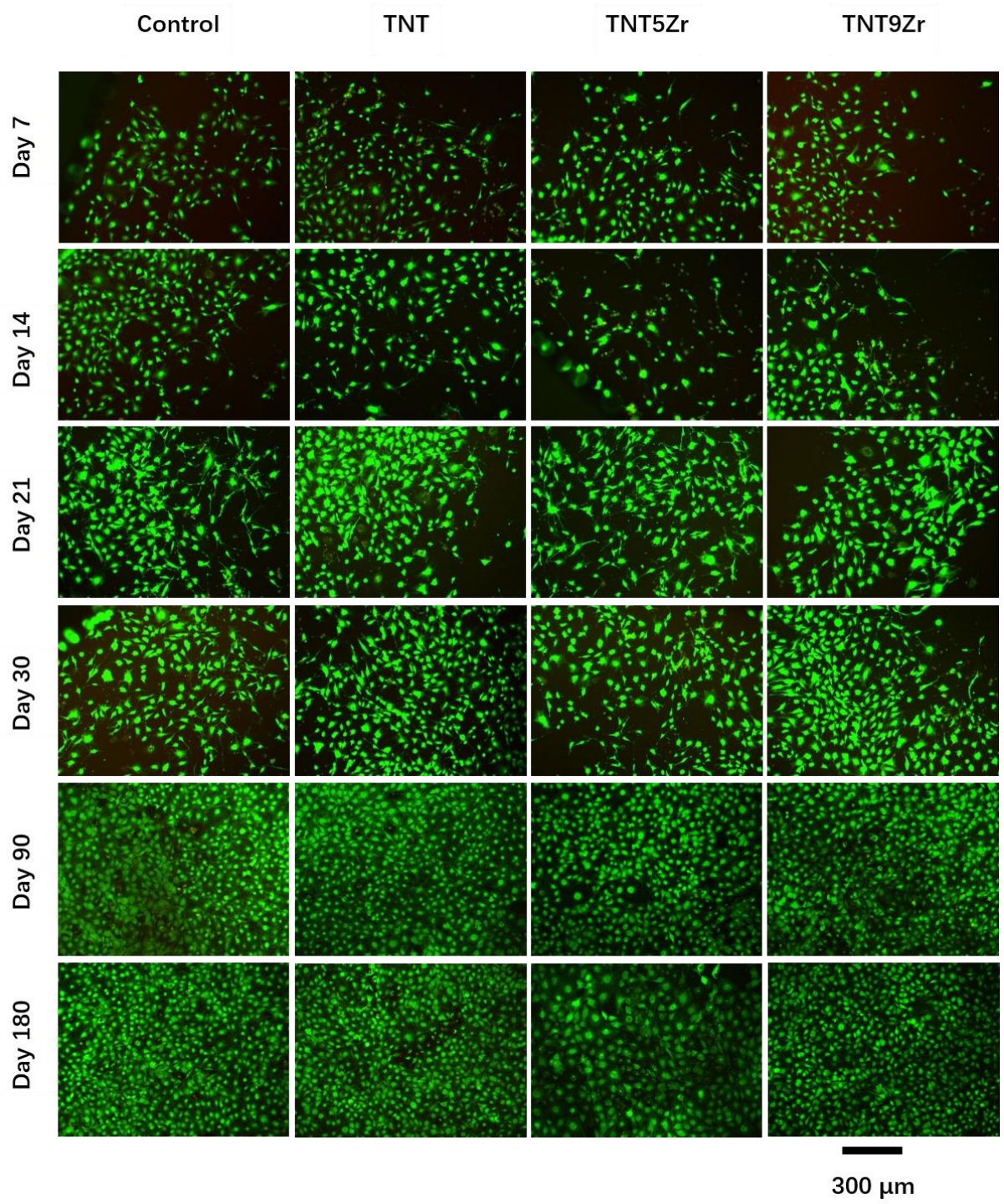

Fig. 3-15. Micrographs illustrating viability of cells with after-immersion containing medium. Note: live cells are stained in green and dead cells in red.

3.4 Discussion

3.4.1 Microstructure evolution and defects distribution

The weak peak (around 35º) found in XRD patterns of the three alloy (Fig. 3-4), which is suspected to be the peak of alpha phase obtained during rapid cooling from beta transus temperature in selective laser melting. As the chosen alloys consist of enough beta stabilizers (Nb, Ta), which increases the thermodynamic stability of the β phase in the alloy system. Therefore, martensitic transformation normally induced by high cooling rate is suppressed in these high β-stabilized Ti-Nb-Ta based β alloys, causing the three alloys retained main β phase at room temperature. The same trend that α'' martensite is depressed with the increase of Nb is reported by Hao et al. [201]. According to the former thermodynamic calculations [202], the classic microstructural evolution e.g., martensitic transformation, diffusionless transformation ($\beta \rightarrow \omega$) did not occur in high Nb composition Ti-Nb alloys during rapid cooling rate processing because the driving force for the metastable phases nucleation is not enough. Additionally, the Zr composition change in alloy chemistry generally produces a shift in the position of the diffraction peaks of the β phase. Zirconium has a calculated atomic radius (206 pm) larger than the replaced element titanium (176 pm) [203], which makes TNT9Zr alloy possess a slightly lower diffraction angle than TNT and TNT5Zr alloys [204]. A large number of grains were statistically analysed in EBSD mapping results (Figs. 3-(5-7)), and it found that a weak but typical <001> fibre texture was obtained in SLM-processed TNT(Z) alloys. The same preferred crystallographic orientation was observed in binary Ti–26Nb alloy manufactured by selective laser melting [23] and laser deposited quaternary Ti-34Nb-7Zr-7Ta alloy [159]. The majority

of grain growth direction is consistent with main thermal dissipation direction during layer-by-layer manufacturing in SLM. Also, it appears that the Zr addition induces the grain refinement of TNT5Zr and TNT9Zr alloys manufactured via SLM (Fig. 3-8A). It may relevant to the occurrence of greater undercooling [205] in melting TNTZ alloys than TNT alloy, which gives rise to more beta grain nucleation sites after Zr element addition. Except for the nucleation rate difference caused by alloying chemistry, short-time high temperature dwell and raid cooling in the selective laser melting process [206] restrict the growth of the nucleated grains.

Here, zirconium seems play the role of neutral element in this high β-stabilized Ti-Nb-Ta based alloy because there is no distinguishable precipitate intensity change when Zr weight percentage increasing from 0 to 5%, which is inconsistent with the descriptions as-mentioned before [142,196]. Noticeably, there is a study which attempts to explain the effects of Zr and Sn contents on α'' martensitic transformation of Ti-Nb based β Ti alloys, manufactured by plastically deformed techniques [201]. The conclusions referring to the alloying element effect on microstructural evolution of α'' precipitates should be drawn cautiously due to it may involve stress-induced martensitic transformation on material processing [25]. BF-TEM images (Fig. 3-9A, C, E) and XRD patterns (Fig. 3-4) of these as-fabricated TNT(Z) alloys further demonstrate no existence of athermal ω phase inside the beta matrix. These results are inconsistent with the results that nanometre-scale omega and alpha precipitation obtained inside beta matrix from Ti-34Nb-7Zr-7Ta alloy manufactured by direct laser deposition (DLD) [159]; while similar results without precipitation in the beta matrix were found after this as-

deposited alloy underwent solution treating then water quenching. We presume metastable precipitate phases probably still can be formed in some beta Ti alloys manufactured by rapid cooling rate processing (e.g., DLD), but they might be suppressed in relative slower cooling rate processing (e.g., quenching, and SLM). The latest microstructure analysis relevant to Ti-35Nb-7Zr-5Ta alloy manufactured by electron beam melting (EBM) reveals the existence of main β phase together with dispersed NbTi4 nanocrystalline intermetallic compound [207]. And these intermetallic precipitates transformed by β phase were also recorded by Li et al. [208] for Ti-10Nb-5Sn alloy heated and cooled repeatedly in the range of room temperature to 400K. Additionally, BF-STEM images of these three alloys show nano-scale grain boundary alpha phase precipitation, which agrees the former EBSD mapping and XRD results. The precipitation starts from beta transus temperature, and some embryos nucleate at grain boundary due to the β stabilizing element away from equilibrium in there. However, there is not enough time to grow up properly because of the still high cooling rate in the SLM process. From the DSC thermal characterisation results (Fig. 3-11) a wide range of no-clear exothermic peak lower than alpha → beta transus temperature was observed. This is consistent with DSC results of Ti-40Nb alloy [209], caused by the lack of athermal omega phase decomposition during heat up in these alloys. Meanwhile, no measurable sharp endothermic peak was observed during the slow furnace cooling process, probably because the material underwent smooth alpha phase growth along grain boundary [27].

Micro-CT provides a feasible characterisation thread to quantify the SLM-processed defects.

The results in Fig. 3-10 show the high relative density (≥99.97%) and extremely small amount of un-melted Nb & Ta particles of SLM-processed TNT(Z) specimens. The void shape tends to be irregular, which is regarded as the keyhole. The mechanism of its formation is due to local evaporation of the lowest boiling point element (titanium) when perform high-speed *in-situ* alloying by SLM, which appears similar to the findings from Liu et al. [22]. Meanwhile, the irregular-shaped pure powders (Nb, Ta) may increase the difficulty of evenly spreading the powder bed. Hence, the localized evaporation probably happens somewhere with a smaller amount of refractory element powder existence. The un-melted particles inside these SLM-processed materials may happen when performing *in-situ* alloying on the zones with relatively coarser refractory powder, the laser incident energy from scanning and remelting cannot thoroughly melt these particles. This is commonly found when *in-situ* alloying pure elements with different thermal physical properties [210], the percentage of un-melted particles can be minor after a systematic parameter optimisation.

3.4.2 Micro-hardness and tensile properties

There appears a small variation of as-measured Vickers hardness values (Fig. 3-12A) in different positions of the as-fabricated TNT(Z) specimens, which positively demonstrates that no obvious macro-structure inhomogeneity exists via *in-situ* alloying TNT(Z) alloys. The low Vickers hardness value (203-264 HV0.1) obtained here is at the same level of SLMed Ti-24Nb-4Zr-8Sn alloy, with a high relative density (>99%) [21]. This is mainly because of low critical resolved shear stress when slip happens in body-centred cubic (bcc) β Ti alloys. From stress-strain curves of as-fabricated TNT(Z) specimens (Fig. 3-12B), UTS of these as-fabricated β Ti

alloys is at the range from 681 ± 6 MPa to 772 ± 9 MPa. As-fabricated TNT alloy obtained the lowest UTS (681 ± 6 MPa), staying at the same UTS level of additive manufactured Ti-30Nb-5Ta-3Zr alloy [211] and Ti-24Nb-4Zr-8Sn alloy [21]. By comparing to cold rolling + solution treating then quenching beta alloys with enough β stabilizers, like Ti-35%Nb-4%Sn or Ti-35%Nb-7.9%Sn (approx. 500 MPa in UTS) [15], grain size difference is regarded as the main factor for the varying strength. Beta grain size refinement in AM-processed TNT(Z) alloys happens due to its rapid solidification from high temperature. Contrastively, beta grain of the aforementioned Ti-Nb-Sn alloys manufactured by traditional techniques may undergo a thorough growth when the long-time dwell above beta transus during solution treatment.

The UTS to modulus ratio is a crucial value to evaluate the mechanical stability of orthopaedic implants. In this work, all three alloys obtained a high strength-to-modulus ratio of approx. 12 (see in Table 3-2), while the recorded value of biomedical Ti-6Al-4V alloy was reported to variate between 8.1-8.8 [212]. To explain the UTS increase after zirconium additions in TNTZ alloys, as dislocations in one crystal pile up on the grain boundary, leading to a high stress concentration in the boundary and neighbouring grains. Hence, higher level grain refinement material (TNT9Zr) provides smaller stress multiplication in the next grain than the other two TNT(Z) alloys, thus a larger applied stress is needed to cause slip to pass through the boundary in fine-grained material [213]. Besides that, UTS, Young's modulus, and Vickers hardness experienced a weak reduction after solution treating then water quenching. This can be regarded as the grain growth after performing a dwell at solution treated temperature, and

probably no extra metastable precipitates were retained during water quenching process. After comparison with the fracture morphologies (Fig. 3-13(A-F)) of different alloys at both as-fabricated and solution treated conditions, these specimens all underwent dimple rupture with relatively high ductility (>10%). There exists nucleation, growth and coalescence of microvoids at grain boundary, and fracture happens after an accumulation of critical local strain for microvoids [214]. In particular, the irregular shear-like dimples obtained from as-fabricated TNT(Z) alloys turned into more regular equiaxed dimples (Fig. 3-13D-F) after conducting solution treating then water quenching. Fig. 3-13G-H presents the virgin microstructure of as-fabricated TNT and TNT5Zr alloy; the cellular subgrains inside the equiaxed beta grain structure are observed inside un-deformed pores of as-fabricated TNT alloy. The misorientation angle between these cells has been found in the range of 1-2º [215], which is the reason why as-fabricated TNT alloy obtains the highest percentage of low misorientation angle (≤5º) in these three alloys. However, the subgrain phenomenon disappears in as-fabricated TNT5Zr alloy, probably because it possesses enough grain growth time to form equiaxed grains during solidification.

3.4.3 Ion release and biocompatibility evaluation

This study has evaluated long-term ion release rate for the three defined alloys submerged in MEM containing medium and *in vitro* preosteoblast response to the after-immersion medium. Ion release results (Fig. 3-14(A-C)) confirmed that these investigated alloys possess good corrosion resistance because the highest metallic ion concentration is extremely small (<10 μg/L). The corrosion ions stemmed from uniform attack contain a higher concentration in the

first 14 days immersion than the other time interval immersion. It is assumed that the acid salts (e.g., $MgCl_2$, $CaCl_2$, etc.) from MEM containing medium generate a relatively higher extent of corrosion products when reacting with each alloy in the first stage (≤ 14 days). The corrosion product film on these TNT(Z) alloys became fairly stable after 30 days immersion, potentially further slowing down the overall corrosion rate. It indicated that good biocompatibility with respect to cytotoxicity during culture with corrosion ions was obtained in these TNT(Z) alloys. As the overall metallic ion concentration is small, no obvious cytotoxicity can be found after cell culture even though the highest time interval (6 months). The same positive results can be found in short-term (maximum 4 weeks) titanium, niobium, and tantalum wire implantation in soft and hard bone rat tissue [184]. No dissolution of Ti, Nb, Ta was detected in peri-implant tissues and no inflammatory response was observed around these implants. The literature [169] demonstrated that proteins in an *in vivo* environment can interplay with the corrosion reactions of metallic implants in several ways: proteins bind to metal ions and transport them away from the solid-liquid interface, thus accelerating further ion dissolution; the proteins may adhere to the alloy surface and restrict the diffusion of oxygen to the surface, potentially blocking the metal surface re-passivation. However, it is difficult to mimic a serum containing cell culture *in vitro* environment for long-term ion release evaluation due to its short shelf life when incubated in a 37°C atmosphere. Meanwhile, it should be noted that the quantification of released metallic ions from these three alloys is also challenging. The excellent corrosion resistant TNT(Z) alloys extract small concentration ions in MEM containing medium. If analysed using higher resolution facility (e.g., ICP-MS), proper dilution is needed due to a high

concentration background Ca^{2+} in MEM medium. However, the liquid samples should be a high percentage below the detection limit after that operation. Though the ion release rate can be increased by using strong acid or another corrosive medium, the chance to combine ion release test and cytotoxicity assays together will be lost.

3.5 Conclusions

This chapter investigated *in-situ* alloying Ti-Nb-Ta based β alloys with different zirconium additions (0, 5, 9 wt. %) manufactured by SLM for load-bearing implant development. The microstructure and defects, mechanical properties, and biocompatibility were systematically analysed, and the following main conclusions are drawn:

1 The slow scan speed (e.g., 500 mm/s) with high laser power (e.g., 300 W) is accepted as being an optional parameter combination to manufacture TNT(Z) alloys at a low defects level. Micro-CT results show that the size of un-melted particles (Nb & Ta) and keyhole of after-optimisation TNT(Z) alloys is mainly located in a range of 3—20 μm, and the relative density of as-fabricated TNT(Z) alloys is >99.97%.

2 Martensitic transformation normally caused by high cooling is suppressed in the high β-stabilized Ti-Nb-Ta based alloys, making these three SLMed alloys obtain main β phase at room temperature. No existence of athermal ω or α'' phase inside the beta matrix and potential nano-scale grain boundary alpha phase precipitation is observed in TNT(Z) alloys, which agrees the relevant EBSD mapping and XRD results. Additionally, zirconium is regarded as a neutral element in this high β-stabilized Ti-Nb-Ta based alloy

when performing SLM manufacturing.

3 Tensile testing shows that the UTS of these as-fabricated β Ti alloys ranges from 681 ± 6 MPa to 772 ± 9 MPa. Here, the Vickers hardness and UTS increase caused by zirconium addition is explained by grain refinement. A weak UTS reduction after solution treating then water quenching is regarded as grain growth when dwell at solution treated temperature. Notably, the UTS to modulus ratio of as-designed TNT(Z) alloys is approx. 12, which is much higher than the recorded value (8.1-8.8) of biomedical Ti-6Al-4V.

4 Corrosion ions released from uniform attack in MEM containing medium at each time interval have an extremely small concentration (<10 μg/L). The corrosion product film on these TNT(Z) alloys, presumably to be fairly stable after 30 days immersion. It indicated that good biocompatibility with respect to cytotoxicity during culture with corrosion ions is obtained in these TNT(Z) alloys.

4 MICROSTRUCTURAL EVOLUTION, MECHANICAL PROPERTIES, AND PREOSTEOBLAST CELL RESPONSE OF POST-PROCESSING TREATED TNT5ZR β TI ALLOY MANUFACTURED BY SELECTIVE LASER MELTING

Paper Status: published

Weihuan Kong[a], Sophie C. Cox[b], Yu Lu[a], Victor Villapun[b], Xiaoling Xiao[c], Wenyou Ma[d], Min Liu[d*], Moataz M. Attallah[a*], **Microstructural Evolution, Mechanical Properties, and Preosteoblast Cell Response of Post-processing Treated TNT5Zr β Ti Alloy Manufactured by Selective Laser Melting**, ACS Biomaterials Science & Engineering. https://doi.org/10.1021/acsbiomaterials.1c01277

Authorship contribution statement

Weihuan Kong conceived and designed the experiment, performed the experiment, interpreted the data, and wrote the manuscript. Sophie C. Cox assisted with designing the experiments. Yu Lu assisted micro-CT data analysis. Victor Villapun, Xiaoling Xiao performed cell-culture assays and TEM observations. Wenyu Ma and Min Liu involved resources and methodology. Moataz M. Attallah assisted with designing the experiments and revising the manuscript.

---

a. School of Metallurgy and Materials, University of Birmingham, Edgbaston, B15 2TT, UK

b. School of Chemical Engineering, University of Birmingham, Edgbaston, B15 2TT, UK

c. Guangdong Institute of Analysis, Guangzhou, 510651, PR China

d. Guangdong Institute of New Materials, Guangzhou, 510651, PR China

Abstract

A Ti-34Nb-13Ta-5Zr (TNT5Zr) β Ti alloy with high strength-to-modulus ratio has been developed, showing its potential to become another candidate material in load-bearing implant applications. This work mainly investigates the microstructural evolution, mechanical properties, and biocompatibility of post-processing treated TNT5Zr alloy manufactured by selective laser melting (SLM). TEM observation shows the existence of single beta grain matrix and alpha precipitates along grain boundary in SLM+HIP manufactured TNT5Zr alloy (TNT5Zr-AF+HIP), and ellipsoidal nano-sized intragranular α'' precipitates (approx. 5~10 nm) were introduced after subsequent low temperature aging treatment. The precipitation strengthening makes SLM+HIP+aging manufactured TNT5Zr (TNT5Zr-AF+HIPA) alloy obtained a comparable ultimate tensile strength (853 ± 9 MPa) to the reference material (Ti64-AF+HIP, 926 ± 23 MPa). Including the inferior notch-like surface of the test-pieces, slip-band cracking occurs in this ductile TNT5Zr-AF+HIPA alloy are regarded as the main factors to determinate its fatigue strength (170 MPa). *In vitro* short-term biocompatibility evaluation reveals that almost no significant difference of preosteoblast viability, differentiation, and mineralization between TNT5Zr-AF+HIPA and the reference biomaterial (Ti64-AF+HIP).

4.1 Introduction

Some snapshots in the scope of bone mechanics provide significant guidance in bone replacement research and development. Bone is a lightweight composite with combination of collagen, mineral and non-collagenous proteins [34]. As one extraordinary multifunctional hard

tissue, bone is responsible to mechanical support, aiding in mineral homeostasis, and haematopoiesis [35]. Young's modulus is one of the crucial mechanical properties of human bone. It shows that the elastic modulus of diaphyseal cortical bone ranging from 53 to 93-year-old measured by nano-indentation test was 20.1 ± 5.4 GPa and that of cancellous bone was 11.4 ± 5.4 GPa [37]. Osteoblasts, which are responsible for bone formation, they are recognized by the site of bone surface with exhibiting high levels of alkaline phosphatase (ALP) and osteocalcin.

There has high percentage of aging people suffer severe osteoarthritis worldwide. Therefore, it's necessary to develop satisfactory implant materials to replace malfunctioned load-bearing human joints. Historically, many series of material such as cobalt based alloy, stainless steel and titanium alloys have been developed for joint replacement. For example, Co-Cr-Mo alloys containing sufficient C (>0.20%) have been designed for implant material because wear-resistant carbides (e.g., M23C6-type) existence [67]. SS 316L stainless steel due to its low cost, availability, good weldability has been regarded as an attractive candidate for joint replacement [54]. When comparing Young's moduli of these alloys to that of natural bone, there exists a massive mismatch between them. It has demonstrated that high stiffness implants caused bone resorption due to "stress shielding" effect [4]. Meanwhile, some tissue reaction cases have been documented after cobalt based or nickel involved alloys implantation. Released Cr and Co ions in Co-Cr-Mo alloys have been considered to increase *in vivo* carcinogenic potential [49,216]. It also has been mentioned nickel ion released from stainless steel implant caused a loss of cell

viability [217].

In the field of low Young's modulus alloys designed for load-bearing implants, some research have been conducted on Ti-Nb based β Ti alloys manufactured by traditional manufacturing techniques. Hanada et al. [15] showed the feasibility to obtain low elastic modulus (approx. 40 GPa) after performing Ti-Nb-Sn β Ti alloys composition optimisation. They regarded that Sn addition retards ω precipitates transformation, thereby reducing its Young's modulus. Laheurte et al. [143] designed β Ti alloys with biofriendly elements (e.g., Nb, Ta, Zr) using the DV-Xα electronic approach. They concluded that incipient modulus of β Ti alloys can be reduced to the value as low as 30 GPa, which is extremely close to the counterpart of cortical bone. Panigrahi et al. [173] demonstrated mechanical properties, microstructure and texture evolution of Ti-45Nb alloy manufactured by severe plastic deformation (SPD). They found that elastic moduli of samples after hydrostatic extrusion (HE) and high pressure torsion (HPT) kept the same as initial ingot at the level of 65 GPa, hypothesizing that the volume fraction of ω phase induced by deformation is too small to influence its elastic modulus.

Besides the material's elastic modulus, biocompatibility is another important factor in load-bearing implant development. Gordin et al. [18] and Neacsu et al. [19] demonstrated Ti-Nb-X alloys possess equal or even better short-term *in vitro* MC3T3-E1 preosteoblast response when compared with commercially pure (CP) titanium. Miura et al. [181] and Ion et al. [182] evaluated preosteoblast cell response of Ti-25Nb-11Sn, Ti-23Nb-0.7Ta-2Zr-0.5N alloy (wt. %) and Ti-6Al-4V. The two research groups both observed a same level of preosteoblast

attachment, spreading and proliferation in these biomaterials.

Powder bed fusion (PBF) has become capable of manufacturing tailored parts with dimensional accuracy after several decades of technological development [96,109]. It also shows relative lower feedstock consumption than other manufacturing techniques. It may make implant more affordable if manufacture biofriendly β Ti alloys consisted by expensive elements (e.g., Nb, Ta, Zr). Combining the aforementioned benefits of Ti-Nb based β Ti alloys (e.g., narrow elastic modulus mismatch to natural bone, excellent biocompatibility), it is necessary to consider what are the main disadvantages of additive manufacturing Ti-Nb based β Ti alloys? The first concern arises from the relatively low ultimate tensile strength (UTS) caused by main beta phase matrix with body-centered cubic (bcc) lattice arrangement, which is observed in high β-stabilized Ti alloys underwent relatively high cooling rate. Recently, Ummethala et al. [218] and Kong et al. [219] SLM manufactured single β phase Ti-35Nb-7Zr-5Ta (wt. %) and main β phase Ti-34Nb-13Ta-5Zr (wt. %), the UTS collected from tensile test were 631 MPa and 694~702 MPa, respectively. Therefore, it increases the risk of implant early-stage failure in service. Another concern is that the existence of as-fabricated keyhole due to localized element evaporation may deteriorate material's mechanical properties [22,23]. Hot isostatic pressing (HIP) is a technique involves simultaneous function of elevated temperature and high pressure applied with inert argon gas in a specific vessel. Argon atoms are pressed every surface of a component in a normal direction like "hot forge", then densification is fulfilled due to a surface energy reduction of the pores [119]. In this study, we investigated the microstructural evolution,

defects distribution, mechanical properties of Ti-34Nb-13Ta-5Zr β Ti alloy before and after post-processing treatment, such as traditional HIP, low temperature aging treatment. In addition, we investigated the short term *in vitro* MC3T3-E1 preosteoblast response of the post-processed β Ti alloy. Ti-6Al-4V alloy was inserted as a benchmark to compare tensile properties and cell culture results, which is commonly found in load-bearing biomedical implants.

4.2 Materials and methods

4.2.1 Powder feedstock

Pure element (Ti, Nb, Ta, Zr) powders were used for mixing the as-designed material powder feedstock. The chemical composition and particle size of the Ti-34Nb-13Ta-5Zr alloy is given in Table 4-1, hereafter it was termed TNT5Zr alloy. The spherical Ti, Zr powder (TLS, Germany) with a particle size range (15-83 μm) and (10-45 μm) were gas atomised in argon atmosphere. The rocky Nb (Elite, UK), Ta powder (H.C. Starck, Germany) with a particle size range (5-86 μm) and (8-52 μm) (Fig. 4-1B) were manufactured by hydride-dehydride process. The mass of each elemental powder was measured using a top pan balance (Kern EMB2000, 0.01g accuracy) inside a glove box (Saffron, UK) with an argon protective atmosphere (≤0.005% O2). Then the powder was mixed for ten hours in a horizontal rotating drum (Kimber-Allen, UK). The blended powder was characterised by energy-dispersive X-ray spectroscopy (EDS, Bruker) map for checking mixing performance before manufacturing process (Fig. 4-1A, C). The pre-alloyed Ti-6Al-4V powder with a particle size range (20-65 μm) manufactured by gas atomisation was used for building the reference specimens (Fig. 4-1D).

Table 4-1

The chemical composition of TNT5Zr alloy and particle size of the involved pure element powders for selective laser melting.

	Ti	Nb	Ta	Zr
Composition (wt. %)	Bal	34	13	5
Particle size (μm)	15-83	5-86	8-52	10-45

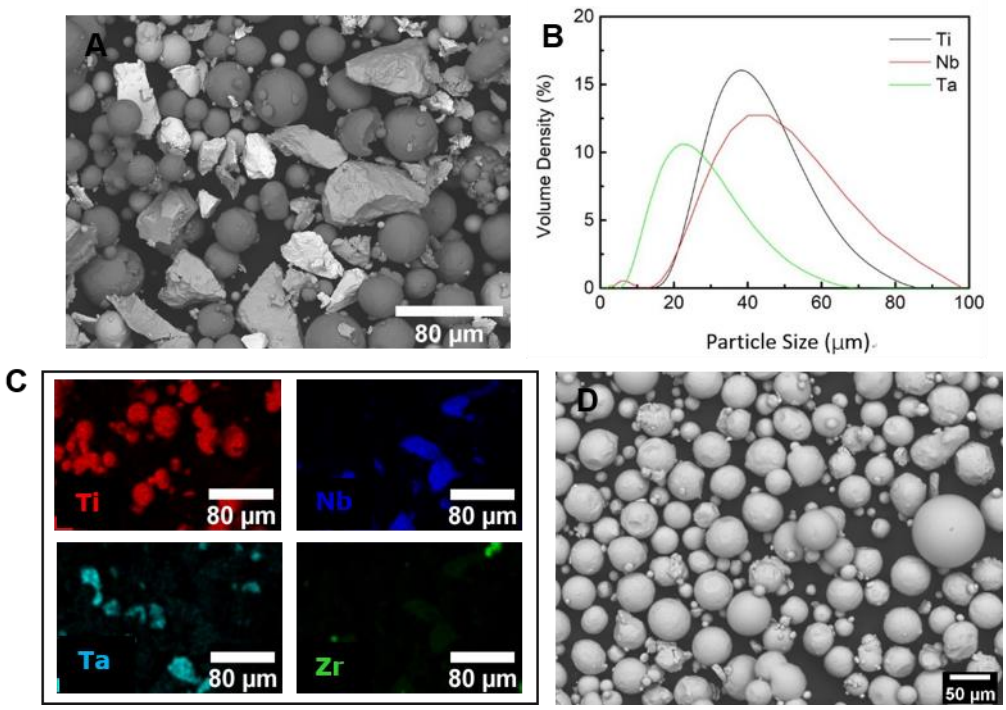

Fig. 4-1. (A) The morphology of the TNT5Zr powder after blending, (B) particle size distribution of the as-received pure element powders, and (C) EDS map after blending. (D) The morphology of Ti-6Al-4V pre-alloyed powder. Note: PSD of Zr powder is not listed as it is too reactive to be measured.

4.2.2 Selective laser melting

An M2 Cusing SLM system (Concept Laser, GE Additive) was adopted to fabricate TNT5Zr samples on Ti-alloy substrates. The machine was equipped with 400 W Yb:YAG fibre laser at a wavelength of 1064 nm. The laser beam spot size was focused approx. 63 μm. Because high

oxidation risk caused by these pure element powders, high-purity protective argon was continually supplied inside the SLM build module till components were thoroughly cooling down. The optimized SLM parameter for manufacturing specimens were: 300 W laser power, 500 mm/s scan speed, and 50 μm hatch spacing. Scan strategy (chessboard) with scan vectors rotated by 90º in adjacent 5 x 5 mm blocks and each successive layer was designed by shifting 1 mm in both X and Y directions; the preset layer thickness was 20 μm. The manufactured parts were 7 x 7 x 7 mm cubes and sub-size dog-bone tensile and fatigue specimens with 75 mm total length. Tensile specimen dimension was designed according to ASTM-E8/ E8M-13a standard [198]; fatigue specimen was designed with tangentially blending fillets between the uniform test section and the ends according to ASTM-E466-15 standard [220]. The tensile and fatigue parts (10 mm in height) were horizontally manufactured with SLMed original side surface then sliced into dog-bone test-pieces (1.5 mm in height) by a wire electron discharge machining (EDM, GF Machining Solutions) system. Manual grinding kit (8220, Dremel) was used to reduce surface roughness of side surfaces from fatigue test-pieces.

4.2.3 Post processing heat treatment and porosity distribution

Traditional hot isostatic pressing (HIP, EPSI) was used to close pores induced by SLM. The process parameter were: 3 hours dwell at 1000℃ in the container filled with 120 MPa pressurized argon atmosphere, followed by furnace cooling with 10℃/min cooling rate. Low temperature (300℃) aging treatment with different aging time (1, 4, 7, 10, 13, 24, 48, 64, 72 hours) was investigated to strengthen TNT5Zr alloy. The finalized aging time (48 hours) for microstructure evaluation, mechanical tests, *in vitro* tests was decided by the microhardness-

aging time results. The porosity and un-melted particle of samples (1.1 x 1.1 x 7.5 mm) before and after HIP treatment were analysed by Micro-CT (Skyscan, Bruker). The scan parameters were: accelerating voltage of 165 kV and current of 75 μA for 360º scan. A total of 2,500 projections were collected on a charge-coupled device (CCD) detector using a 1s exposure time. The data was reconstructed and visualized using Nikon Pro 3D and Avizo software, respectively.

4.2.4 Microstructure characterisation

Metallographic specimens were prepared using automatic grinding and polishing machine (Tegramin 30, Struers), and then etched by Kroll's solution (2% HF + 6% HNO_3 + 92% H_2O). A field-emission gun (FEG) SEM (JSF-7000F, JEOL) was employed for observing the microstructure. The phase identification was performed by X-ray diffractometer (XRD) (AXRD, Proto) with Cu Kα radiation, and XRD spectra were collected by a fixed parameter of 0.02º step size and a 2s time/step. To reveal the evolution of texture, the samples before and after HIP were examined by electron backscatter diffraction (EBSD) using a SEM (NNS450, FEI). The step size was 0.4 μm aiming to obtain high EBSD indexing rate for the characterisation of texture and grain size. A transmission electron microscope (JEM-2100, JEOL) operating at 200 kV was used to capture bright-field (BF) images and selected area diffraction (SAD) patterns, bright-field scanning transmission electron microscopy (BF-STEM) images, and high-resolution TEM (HRTEM) images. Thin foils for TEM were prepared through an argon ion milling technique (Gatan PIPS, Ametek), involving gradient milling by different Ar ion energy and sputter angle settings.

4.2.5 Mechanical test

Mirror-like specimens were mounted on micro-hardness tester (Wilson VH1202, Buehler) for Vickers hardness measurement. The test for each sample was performed with 100g load and 10 times linearly indented with recommended spacing according to ASTM E384-17 [199]. Specimens (1.6 x 6 mm rectangular cross-section, SLM-processed original side surface) in tensile testing were carried out perpendicularly to the build direction at room temperature. The stress-strain curves were measured at a crosshead speed of 0.5 mm/min at room temperature using a tensile testing machine (2500, Zwick/Roell). Two specimens per alloy were tested in order to average tensile properties, and a clip-on extensometer was attached to 15 mm gage length of specimen until rupture. Fatigue test with a rectangular cross-section of 1.5 x 6 mm specimens were tested perpendicularly to the build direction. Axial high cycle fatigue testing was performed on a fatigue testing machine (Vibraphore Resonant), using magnetic resonance to deliver low constant amplitude, load ratio of R = 0.1, and high frequency (usually in a range of 50-100Hz, decided by the specimen geometry and stiffness). The testing with a maximum stress (up to 250 MPa) inside the elastic region was performed at room temperature. Tensile and fatigue fracture morphology was observed using a SEM (JSF-7000F, JEOL).

4.2.6 In vitro MC3T3-E1 performance

MC3T3-E1 preosteoblasts were selected to evaluate cell response of TNT5Zr and Ti-6Al-4V alloy. All metallic specimens were grinded using 1200 Grit SiC sandpaper for 10 mins. Then they were ultrasonically cleaned in pure ethanol for 10 minutes and then autoclaved at 121°C

for 90 minutes before cell seeding. All metallic substrates (10 x 5 mm) and polyester plastic coverslip controls (ThermoFisher, D13 mm) were placed in a 24-well plate and seeded with preosteoblast cells with a density of 2 x 10^4 cells/cm^2. Samples were incubated at 37°C in humidified atmosphere with 5% CO_2. The cell culture medium was minimal essential medium (MEM) supplemented with 10% foetal bovine serum, 1% penicillin/streptomycin, and 0.5g/L L-glutamine. The medium was changed every two days during the specific culture periods. Cell viability was evaluated by Alamar blue staining after 1 day, 7 days, 14 days culture using spectrophotometer (Spark, Tecan) at a wavelength of 560 nm excitation and 590 nm emission. Calcein-AM and propidium iodide (PI) solution was chosen to evaluate the viability of MC3T3-E1 cell after 7 days culture on the metallic and control substrates. Stained cells were visualized using a microscope imaging system (EVOS M5000, Thermo Scientific). Nine optical microscope images were captured using a 4X low magnification objective, and live cell coverage on each substrate was analysed by image processing software (Image J, Fiji). Alkaline Phosphatase (ALP) was measured using a SensoLyte® pNPP ALP Assay Kit (AnaSpec Inc., US) for the 7 and 14 cultured substrates, absorbance read at a wavelength of 405 nm (Spark, Tecan). Total calcium deposits after 28 days of culture was studied by Alizarin red staining (ARS) assay. Samples were fixed with 10% paraformaldehyde solution for 30 minutes and washed with deionized water three times. Then, 1mL of cetylpyridinium chloride (CPC) was added and samples cultivated for 1 hour at 37 °C. The resulting elution was collected in a 96 well plate and absorbance read at a wavelength of 570 nm (Spark, Tecan). The aforementioned assays were conducted in triplicate. All involved data were recorded as the mean ± standard deviation

(SD). Analysis of Variance (ANOVA) and two-tailed t-tests were performed for as-mentioned assays, with a p value <0.05 considered as being statistically significant.

4.3 Results

4.3.1 Porosity and un-melted particle distribution

Fig. 4-2(A-B) shows the reconstructed SLM-manufactured 3D parts before and after HIP by the aid of micro-CT technique. Micro pores (yellow) with irregular shape were randomly distributed in as-fabricated TNT5Zr specimen (Fig. 4-2A), hereafter termed TNT5Zr-AF. Fig. 4-2B shows that no micro-pores can be detected in the sample after HIP treatment (hereafter termed TNT5Zr-AF+HIP). The low volume percentage of un-melted particles (red) can be found distributed in the scanned volume of both TNT5Zr-AF and TNT5Zr-AF+HIP specimens. Fig. 4-2(C-D) show the 2D cross-section micrographs of TNT5Zr in both conditions. Comparing with the TNT5Zr-AF sample, the pores were disappeared, and low percentage of un-melted particles (Ta, Nb) were kept in the sample after HIP.

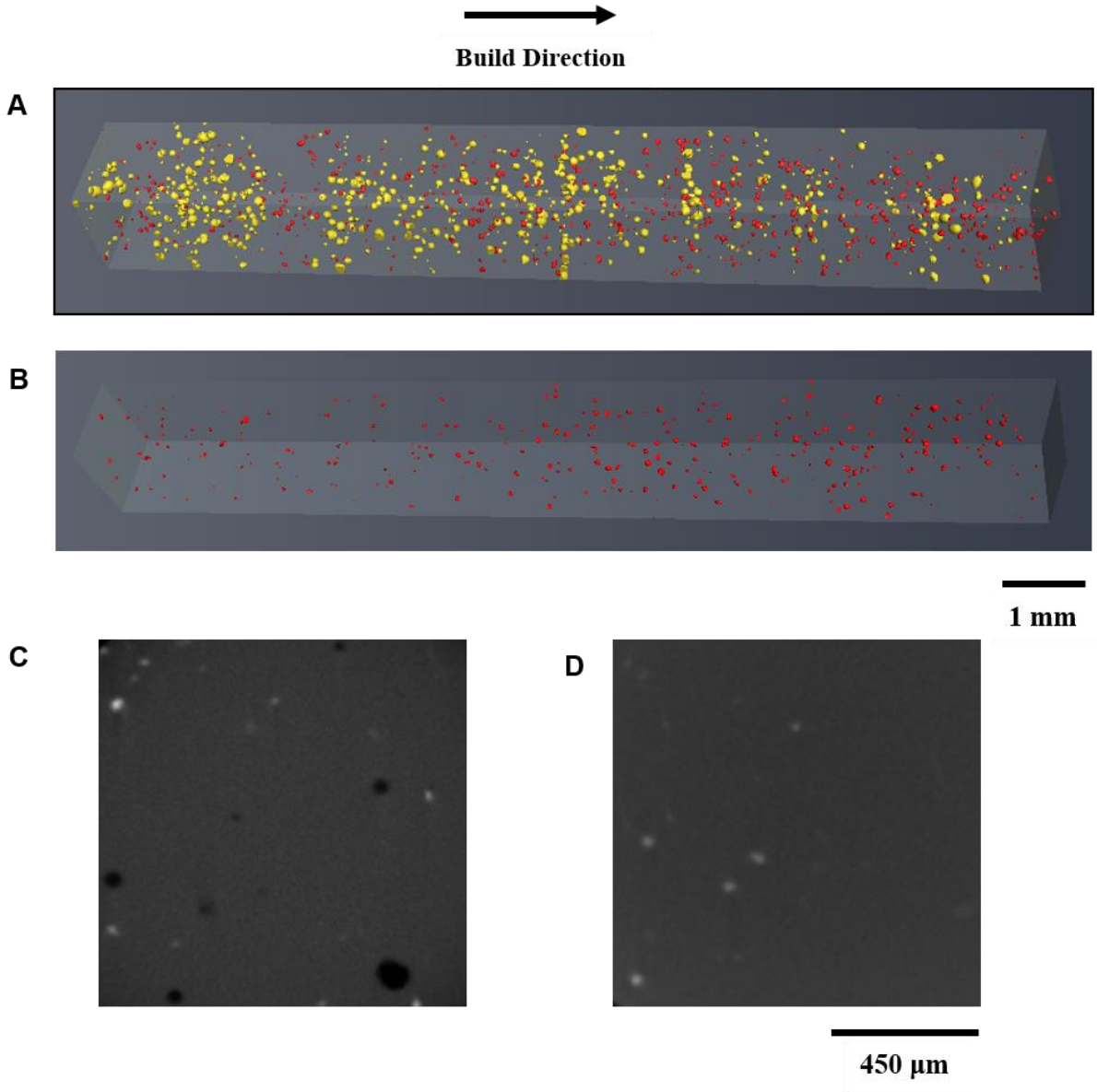

Fig. 4-2. 3D tomography of the un-melted Ta, Nb particles (red) and porosity (yellow) of the TNT5Zr samples: (A) as-fabricated, and (B) after HIP at 1000℃ for 3h. 2D reconstructed cross sections of (C) as-fabricated and (D) as-HIPed TNT5Zr samples. The dark regions indicate pores, while the brighter regions indicate un-melted particles.

4.3.2 Microstructure characteristics

The EBSD inverse pole figure (IPF) results of TNT5Zr-AF from the parallel and perpendicular build direction are shown in Fig. 4-3(A-B). It can be found that the columnar and equiaxed beta grains were obtained during SLM. Additionally, keyholes were observed in TNT5Zr alloy

manufactured via *in-situ* alloying. The <001> fibre texture (Fig. 4-3C) was formed because the grains grew preferentially along <001> orientation, which is consistent with the main heat dissipation direction of layer-by-layer SLM technique. The IPFs of TNT5Zr-AF+HIP from the parallel and perpendicular build direction (Fig. 4-3(D-E)) show the same grain type and a phenomenon of grain growth when compared with the as-fabricated samples. The extent of <001> preferred crystallographic orientation in HIP-manufactured sample is much weaker than the counterpart of TNT5Zr-AF, see in Fig. 4-3F.

The XRD profiles of different types of manufactured TNT5Zr are shown in Fig. 4-4A. XRD patterns at diffraction angle range (36-72º) demonstrate the main diffraction peaks of beta phase. Fig. 4-4B reveals that the SLM+HIP+aging manufactured TNT5Zr alloy (hereafter termed TNT5Zr-AF+HIPA) appears peak splitting along beta phase (200), due to the precipitation during low-temperature aging. The diffraction angle shift observed in post-processed TNT5Zr alloys may be relevant to the grain growth in thermal treatments. The corresponding SEM micrographs of TNT5Zr alloys are shown in Fig. 4-5. The equiaxed beta grains were obtained in high β-stabilized TNT5Zr alloys without a presence of acicular α' precipitates in the beta matrix.

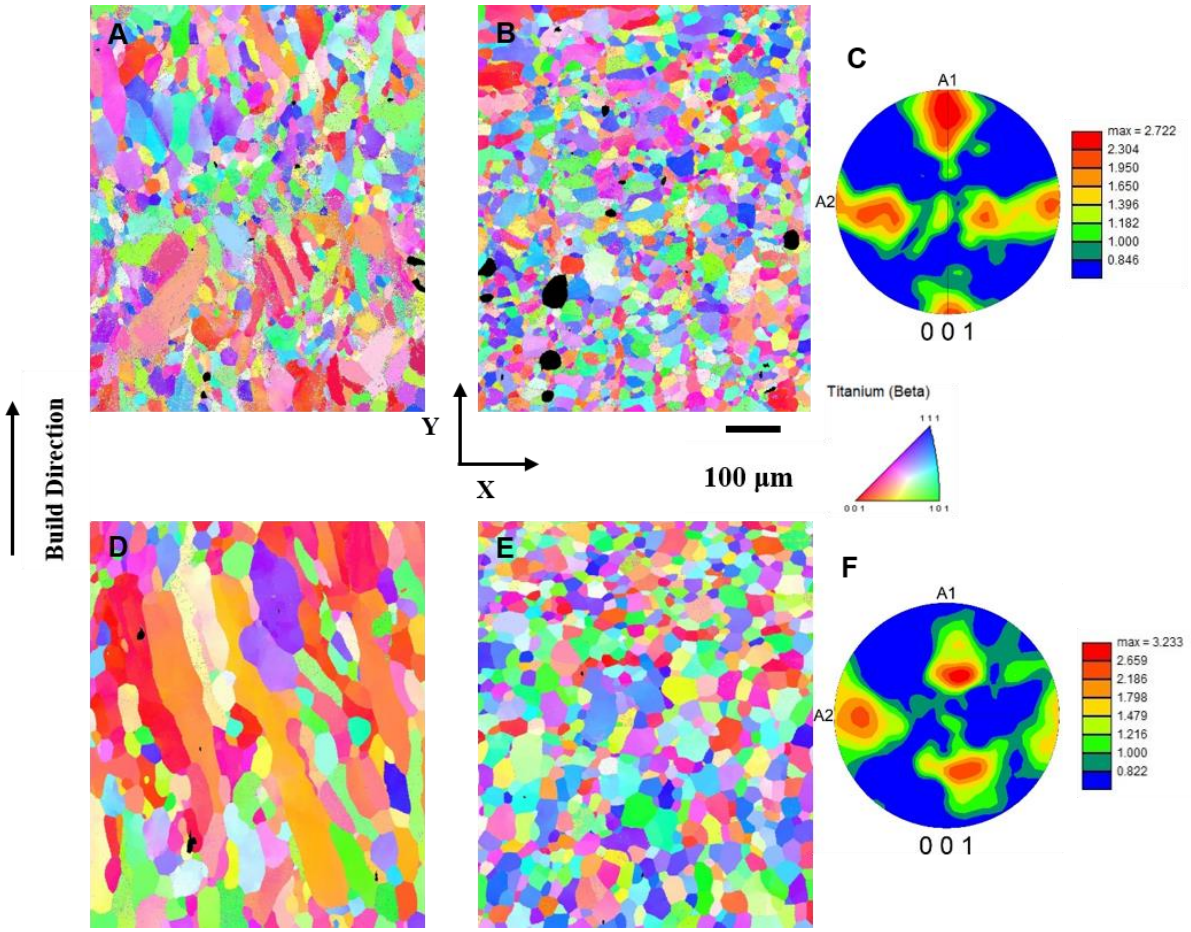

Fig. 4-3. The inverse pole figure (IPF) map of TNT5Zr-AF (A) along build direction; (B) perpendicular build direction, and (C) its pole figure (PF). The inverse pole figure (IPF) map of TNT5Zr-AF+HIP (D) along build direction; (E) perpendicular build direction and (F) its pole figure (PF).

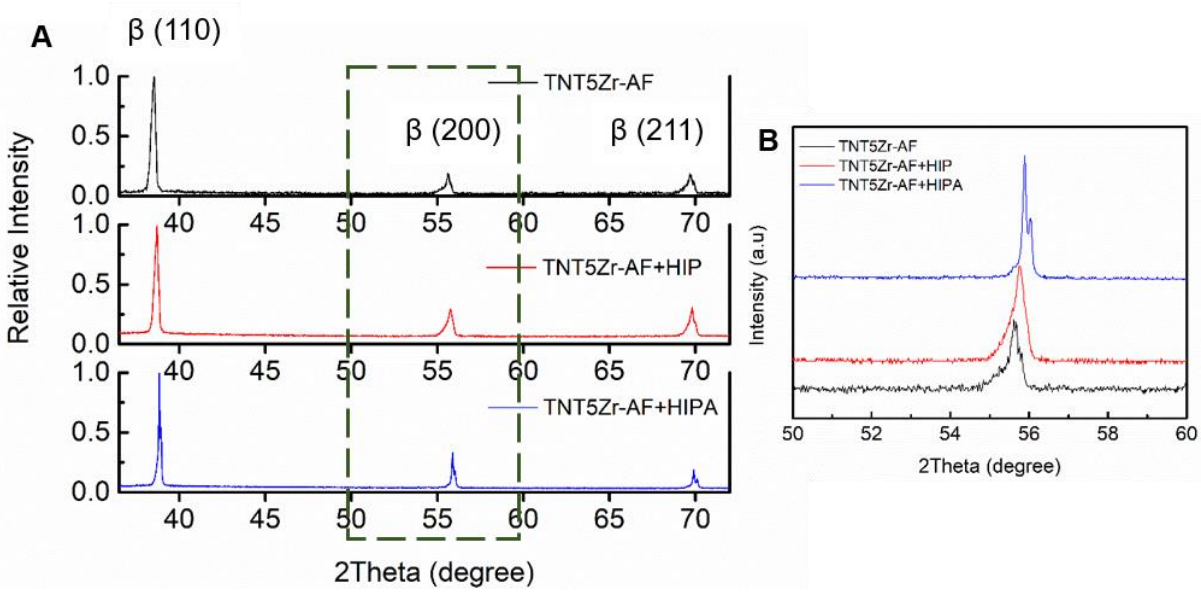

Fig. 4-4. (A) XRD spectra of SLM manufactured TNT5Zr (TNT5Zr-AF), SLM+HIP manufactured TNT5Zr

(TNT5Zr-AF+HIP), SLM+HIP+aging manufactured TNT5Zr (TNT5Zr-AF+HIPA). (B) XRD profiles of as-mentioned specimens, 2θ located between 50º and 60º.

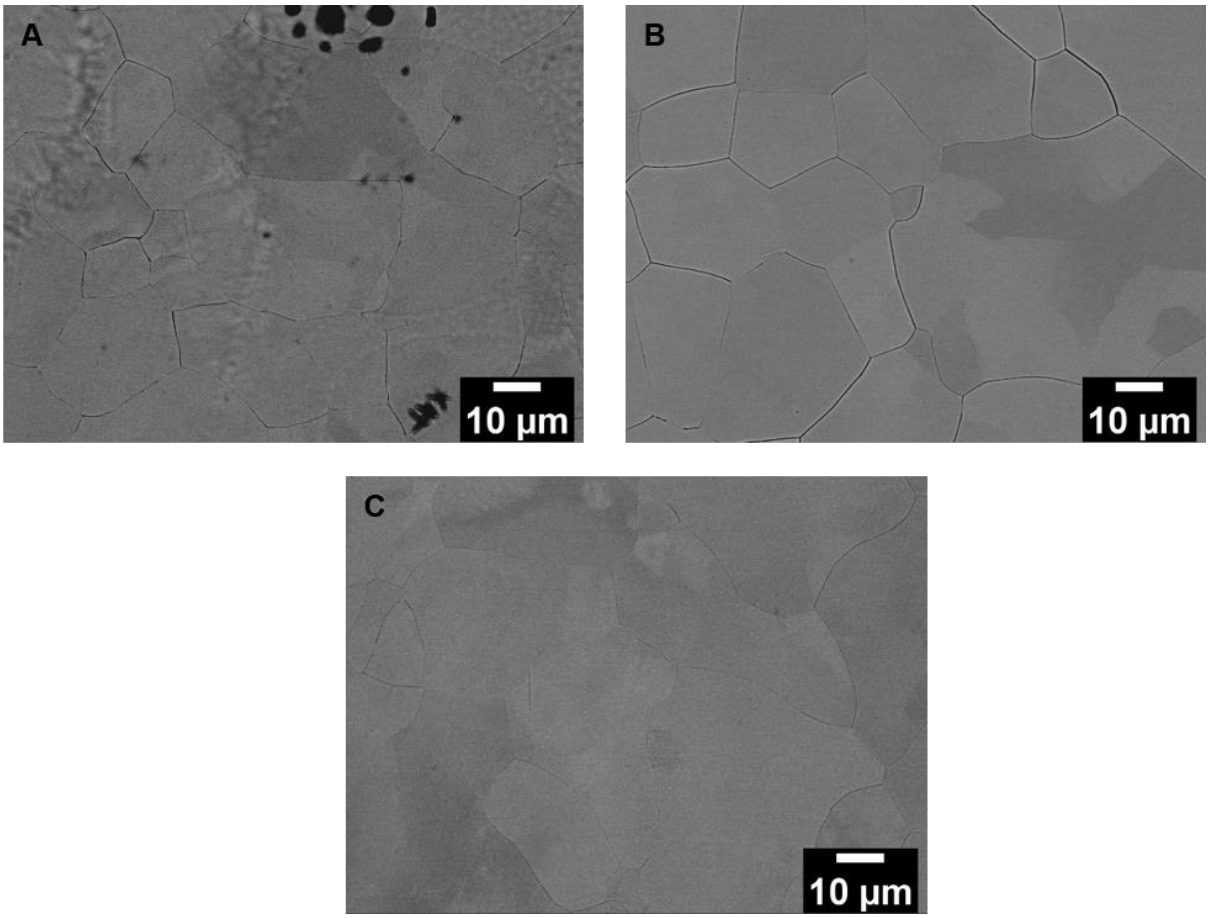

Fig. 4-5. The SEM micrographs of (A) TNT5Zr-AF, (B) TNT5Zr-AF+HIP, and (C) TNT5Zr-AF+HIPA.

The BF image (Fig. 4-6A) of TNT5Zr-AF+HIP sample taken from $[110]_{\beta}$ zone axis reveals the single beta phase with bcc reflection. Fig. 4-6B showcases the presence of distinguishable ellipsoidal nano-sized precipitates (about 5~10 nm) and a weak reflection from TNT5Zr-AF+HIPA alloy. It reveals the orientation relationship between α'' particles and beta phase can be achieved: $(001)_{\alpha''} \parallel (110)_{\beta}$. Fig. 4-6C and Fig. 4-6D present BF-STEM images of TNT5Zr-AF+HIP and TNT5Zr-AF+HIPA alloy, which captured from a region close to the grain boundary. The presence of heterogeneous alpha precipitates can be observed along grain

boundary in the two post-processed TNT5Zr specimens. HRTEM image taken from $[110]_{\beta}$ zone axis (Fig. 4-6E) of as-fabricated TNT5Zr alloy reveals the presence of main beta domain (e.g., dashed rectangle) with some in-homogeneously distorted areas (e.g., dashed circle). Inverse fast Fourier transform (IFFT) images show the crystallographic plane difference of as-mentioned domains without or with partial shear (Fig. 4-6(F-G)). A similar observation can be seen in the TNT5Zr-AF+HIP alloy (Fig. 4-6H). HRTEM image and IFFT analysis (Fig. 4-6I) indicates that there exist nanoscale local domains with α'' orthorhombic lattice arrangement in TNT5Zr-AF+HIPA alloy. The corresponding *d*-spacing calculations suggest that the lattice mismatch between the β and α'' phases is small.

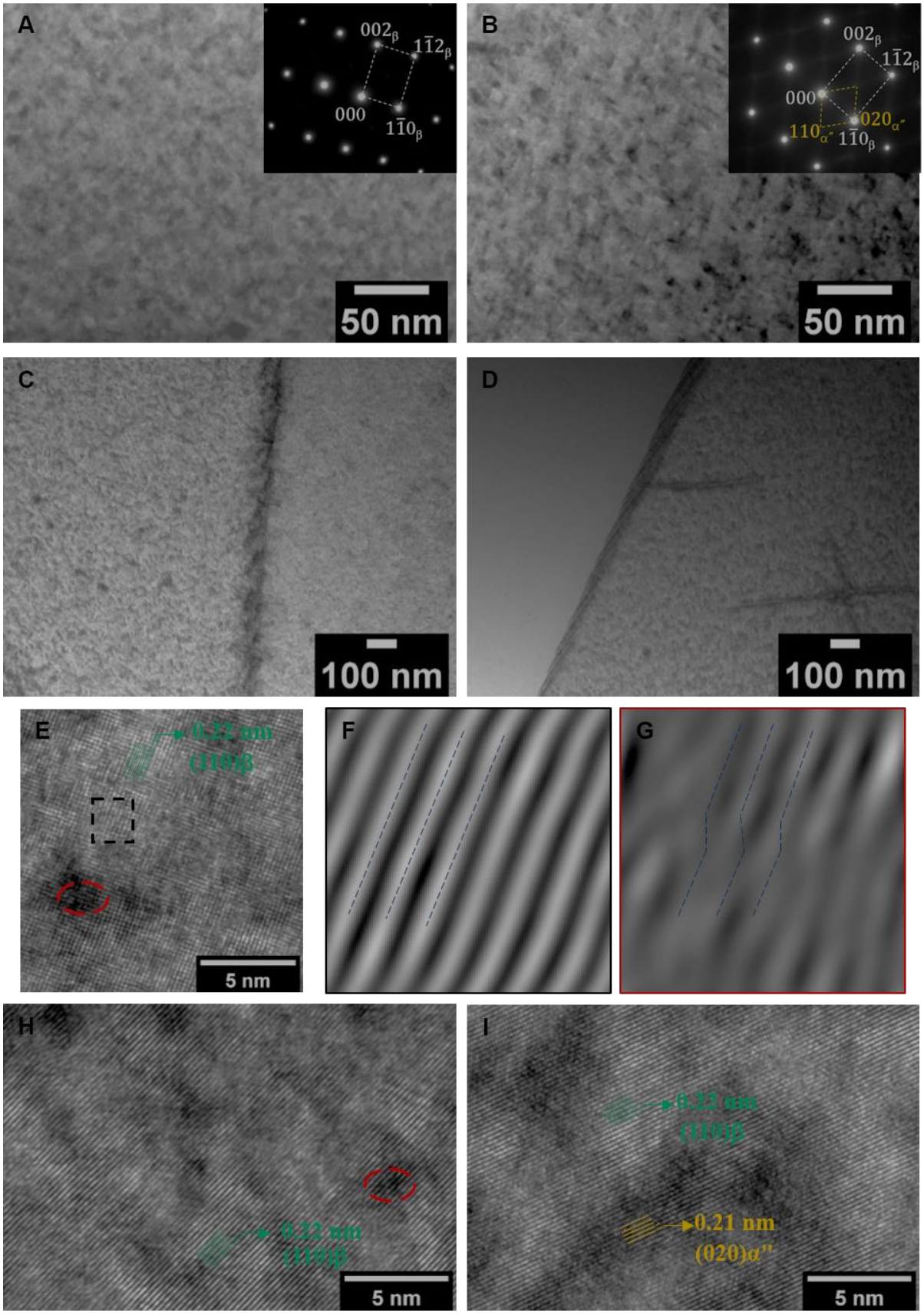

Fig. 4-6. BF image with corresponding SAD pattern (inset) of (A) TNT5Zr-AF+HIP and (B) TNT5Zr-AF+HIPA, taken from the beta matrix region, viewing from $[110]_{\beta}$ zone axis. BF-STEM image of (C) TNT5Zr-

AF+HIP and (D) TNT5Zr-AF+HIPA, taken from a region close to the grain boundary. HRTEM image of (E) as-fabricated TNT5Zr alloy, inverse FFT image from the region (F) squared by black dash lines and (G) circled by red dashed lines. HRTEM image of (H) TNT5Zr-AF+HIP and (I) TNT5Zr-AF+HIPA. Note: the HRTEM images are taken from $[110]_{\beta}$ zone axis.

4.3.3 Mechanical test

Fig. 4-7A shows Vickers hardness versus aging time result of TNT5Zr sample. Overall, the microhardness increase is not severe in the range of 64-hour aging time interval, increasing from 232 ± 6.5 HV0.1 to the maxima (301.3 ± 6.8 HV0.1). It rapidly reached 376.7 ± 10.3 HV0.1 after applying 72-hour aging treatment. Average beta grain size of SLM-manufactured TNT5Zr before and after HIP treatment measured by EBSD quantification are demonstrated in Fig. 4-7B. It can be clearly found beta grain size growth after HIP at the temperature above β-transus. Fig. 4-7C reveals microhardness homogeneity in both planes sectioned from different types of manufactured TNT5Zr alloys. It also can be found a slight crystallographic orientation induced microhardness variation between XOZ and XOY plane (e.g., 267.7 ± 3.4 HV0.1, and 232.0 ± 6.5 HV0.1 in TNT5Zr-AF). The Vickers hardness of TNT5Zr-AF+HIP sample almost kept at the same level of TNT5Zr-AF alloy. TNT5Zr-AF+HIPA obtained by HIP and 48-hour aging experienced a slight increase (70.1 HV0.1 in XOY plane) in microhardness than the counterpart of TNT5Zr-AF.

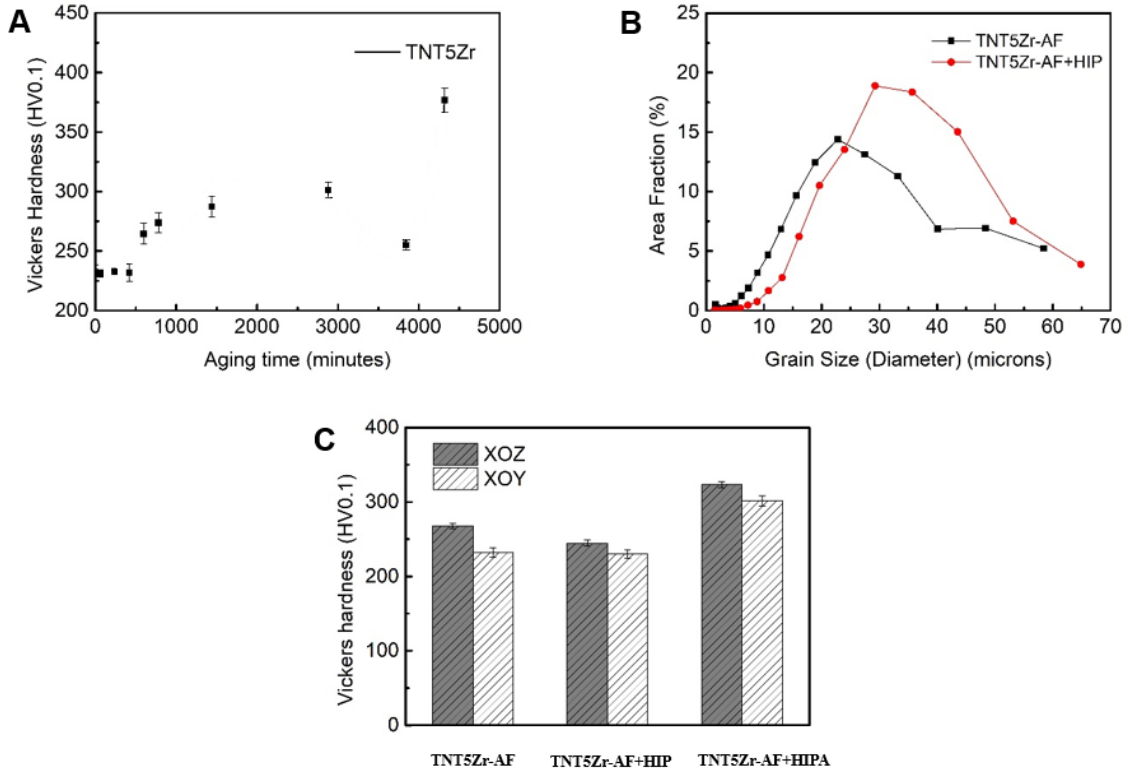

Fig. 4-7. (A) The Vickers hardness of TNT5Zr alloy with different aging time intervals. Note: the specimens are sectioned from XOY plane. (B) Beta titanium grain size of SLM-manufactured TNT5Zr before and after HIP measured by EBSD. (C) The Vickers hardness of different types of manufactured TNT5Zr alloys.

The engineering stress-strain curves of post-processing treated SLMed Ti alloys are revealed in Fig. 4-8A. Table 4-2 integrates values of tensile properties of the involved materials. The most ductile material is TNT5Zr-AF with a lowest ultimate tensile strength (UTS) of 698 ± 4 MPa, and highest elongation of 13.7% ± 0.6%. TNT5Zr-AF+HIP shows a slightly higher UTS (760 ± 5 MPa) and lower elongation (11.4% ± 0.7%). The TNT5Zr alloy after HIP and aging duplex treatment has the highest UTS (853 ± 9 MPa) but sacrifices the material's plasticity (7.3% ± 1.1%). When comparing tensile properties of TNT5Zr-AF+HIPA and the reference material (Ti64-AF+HIP), it showcases TNT5Zr alloy after duplex treatment has a roughly

comparable UTS with Ti64-AF+HIP (926 ± 23 MPa). It is noteworthy that TNT5Zr -HIPA still maintains the low Young's modulus (57 ± 5 GPa), which remains approx. half of the reference material (Ti64-AF+HIP). Fig. 4-8(B-E) demonstrates tensile fractures of different types of manufactured TNT5Zr alloy and the reference material. Fig. 4-8B shows ductile fracture with as-fabricated pores in TNT5Zr-AF specimen, large irregular shear-like oval dimple features can be observed in the high magnification SEM micrograph. Regular shape dimples without SLM induced pores appear in TNT5Zr-AF+HIP (Fig. 4-8C) and TNT5Zr-AF+HIPA (Fig. 4-8D). By comparison, the dimple size is smaller in Ti64-AF+HIP alloy (Fig. 4-8E) than the counterpart of TNT5Zr-AF and TNT5Zr-AF+HIP.

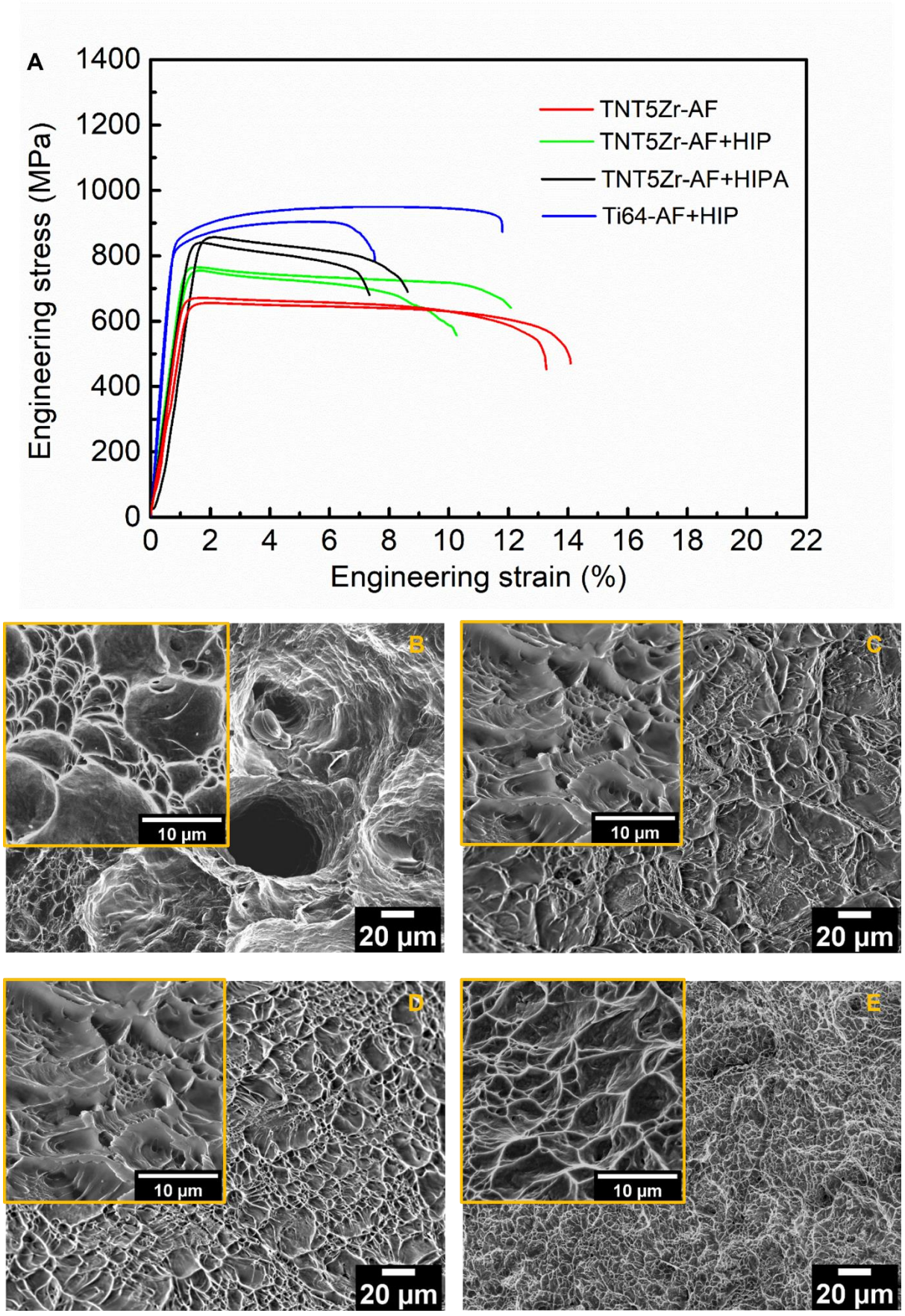

Fig. 4-8. (A) Typical stress-strain curves of different types of manufactured TNT5Zrs and post-processed Ti64

specimens. The tensile fracture morphologies for (B) TNT5Zr-AF, (C) TNT5Zr-AF+HIP, (D) TNT5Zr-AF+HIPA, (E) Ti64-AF+HIP. Note: 1. here Ti64 is short for Ti-6Al-4V due to limited space in the graph. 2. High magnification SEM images inset the corresponding fracture micrographs.

Table 4-2

Comparison of the tensile properties for different types of manufactured TNT5Zr alloys and Ti64-AF+HIP alloy.

Material	E (GPa)	$\sigma_{0.2}$ (MPa)	σ_{UTS} (MPa)	δ (%)	σ_{UTS}/E
TNT5Zr-AF	57 ± 5	650 ± 8	698 ± 4	13.7 ± 0.6	12.1 ± 1.1
TNT5Zr-AF+HIP	63 ± 4	734 ± 8	760 ± 5	11.4 ± 0.7	12.2 ± 0.8
TNT5Zr-AF+HIPA	57 ± 5	831 ± 9	853 ± 9	7.3 ± 1.1	15.2 ± 1.4
Ti64-AF+HIP	107 ± 1	842 ± 9	926 ± 23	9.7 ± 2.1	8.7 ± 0.3
TNTZ [143,186,221]	46-80	447-900	545-950	--	--

Fatigue test was performed using TNT5Zr alloy in the condition with the highest UTS, namely TNT5Zr-AF+HIPA. Fatigue test results of TNT5Zr-AF+HIPA alloy are demonstrated in Fig. 4-9. Low magnification SEM image (Fig. 4-9A) shows relatively flat fracture surfaces, it roughly partitions three fatigues regions, namely, fatigue source, extension, and fracture zone. Multi-source cracks originated from the specimen surface, then expanded radially towards the inside of specimen, finally formed a fast fracture region. The S-N curve (Fig. 4-9B) indicates that TNT5Zr-AF+HIPA alloy possessed low fatigue life when loading at the level of 230-250 MPa maximum stress. The maximum stress (170 MPa) did not fail at $1x10^7$ cycles, was defined as the fatigue limit of TNT5Zr-AF+HIPA alloy. Fig. 4-9C reveals its SEM micrograph with fine extruded ribbon-like formation near the crack initiation site; Fig. 4-9D demonstrates

obviously coarser slip-band cracks propagate along the stable fatigue extension region. Intergranular cracks occur in coarse grain distributed zones, which suffer from cyclic stress are found at fast fracture zone (Fig. 4-9E). Fine dimples and micro-cleavage facets are also observed, and no river pattern is formed accordingly.

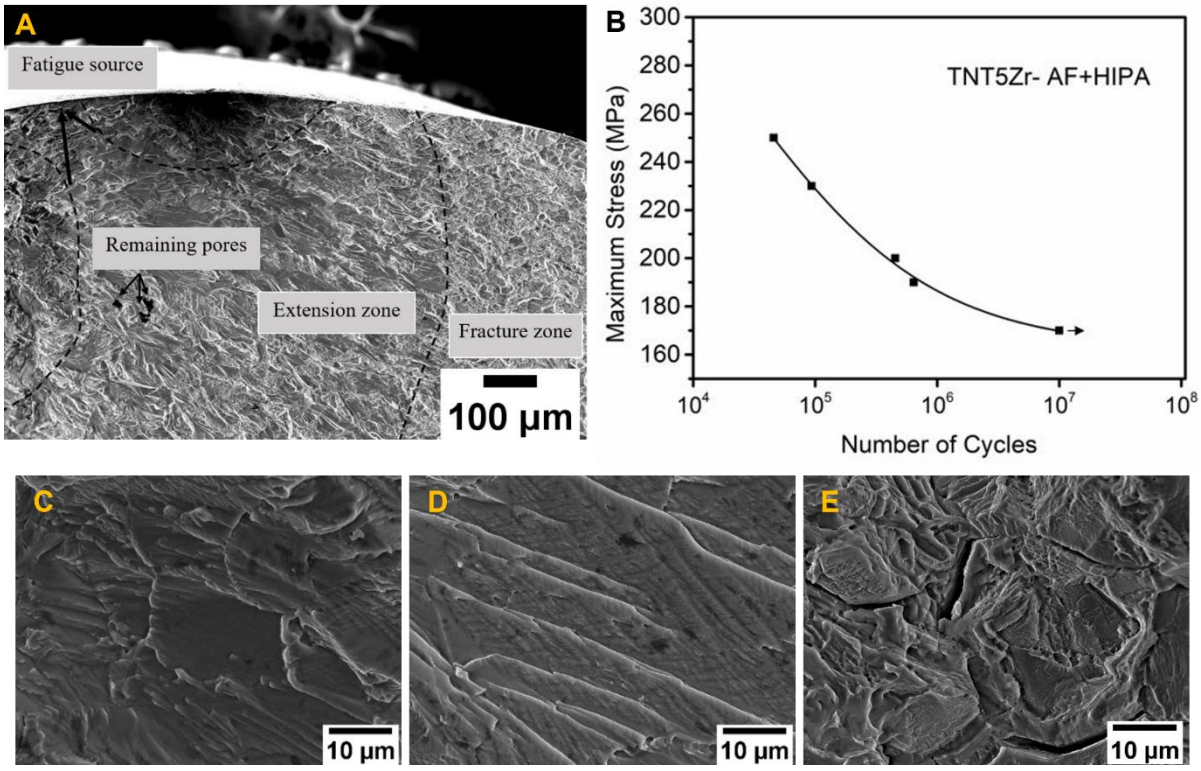

Fig. 4-9. (A) Fatigue fracture with different zones taken from TNT5Zr-AF+HIPA, and its (B) S-N curve. SEM morphology of (C) crack initiation in fatigue source zone, (D) crack extension zone and (E) final fast fracture zone. Note: fatigue fracture was obtained from maximum stress of 200 MPa, N=453900.

4.3.4 Biocompatibility evaluation

Metabolic activity of MC3T3-E1 preosteoblast cells after 1, 7, and 14 days of incubation within Ti alloys substrates and plastic control is shown in Fig. 4-10A. Similar metabolic activity was observed after culturing with TNT5Zr-AF+HIPA and Ti64-AF+HIP substrates in these time intervals. In addition, no obvious Alamar blue reduction difference in these groups was

observed when the incubation time increased from 1 day to 14 days. 7-day cell viability fluorescence imaging (Fig. 4-10B) reveals that both metallic surfaces and plastic control displayed confluent cell growth with no visible damaged membranes. The quantitative values of cell adhesion area on these substrates appear no significant difference after 7-day of culture, and the highest cell coverage was observed in control group. Fig. 4-10C shows short-term mineralization after 7 and 14 days culture with different substrates. Fluorescent intensity after 7-day of culture with the two metallic substrates remain at a similar level in comparison with the control group. According to 14-day ALP activity results, there exhibited an increase of MC3T3-E1 cells differentiation level on both metallic substrates than the counterpart of 7-day, and the ALP activity values of two Ti alloys were significantly lower than the value in control group. Alizarin red staining was used for examination of long-term (28 days) mineralization deposited on Ti alloys substrates. As shown in Fig. 4-10D, levels of calcium deposits are not statistically different between TNT5Zr-AF+HIPA and Ti64-AF+HIP alloy, but significantly lower than the counterpart collected from the plastic control.

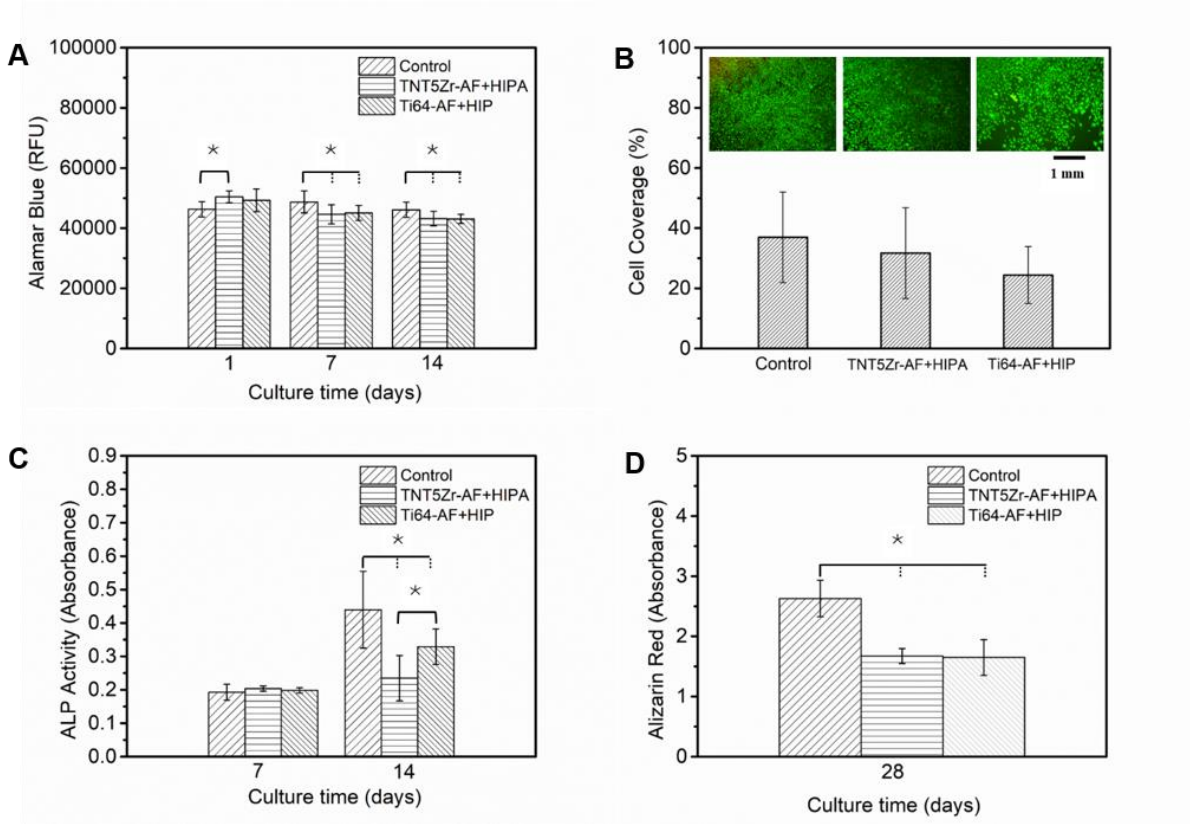

Fig. 4-10. (A) Metabolic activity of MC3T3-E1 preosteoblasts seeded on different substrates. (B) Live cell coverage quantification values and viability staining images after 7 days culture. (C) Levels of ALP activity measured after different culture time intervals. (D) ARS absorbance values at 28 days post-seeding. Where signifies p value < 0.05 (where more than one pair is illustrated, the comparison between the group indicated with a solid line and any other groups indicated with dash lines).

4.4 Discussion

4.4.1 Microstructural evolution, defects distribution of SLM-manufactured TNTZ alloys before and after post-processing

According to the results of TNT5Zr-AF alloy, the microstructure of columnar and equiaxed fine grains with single phase (bcc structure) was retained at room temperature. The EBSD results (Fig. 4-3) have shown that these fine grains possessed <001> fibre texture. As component coined by layer-by-layer consolidation manner, decided that grains prefer to grow

along the main heat dissipation direction (build direction). No obvious metastable phase peaks such as α'' or ω are observed in XRD pattern (Fig. 4-4). Meanwhile, no distinguishable acicular α' phases are observed in its SEM micrograph (Fig. 4-5). The same XRD patterns and SEM micrographs were also observed in Ti-Nb based beta titanium alloy with enough β stabilizing elements manufactured by solution and quenching treatment [209,222]. Dominant bcc β phase without metastable phases retained in grain matrix of TNT5Zr-AF alloy even though it underwent a high cooling rate in SLM [77,223], which demonstrates the commonly found cooling rate dependent martensitic transformation is suppressed in our high β-stabilized Ti alloy. HRTEM image (Fig. 4-6E) taken from TNT5Zr-AF alloy reveals the lattice spacing of 0.22 nm corresponding to {110} planes of the bcc β phase. The IFFT analysis confirms that no existence of α'' or ω phases, which normally form by moving small distances relative to the unit cell dimensions of β phase or collapsing of two {111} planes of parent phase into one plane at an intermediate position [224,225]. As shown in TNT5Zr-AF HRTEM observations (Fig. 4-6(E-G)), the planar nano-sized areas of partial plastic shear is considered as nanodisturbances where has been found in low resistance-to-shear planes in deformed Gum metal [226].

The HIP treatment broke up the as-fabricated <001> fibre texture and produced the coarser beta grains caused by grain boundary migration when a dwell occurred at the temperature above β-transus. TEM results (Fig. 4-6(A, C)) indicate the existence of single beta matrix and alpha precipitates along the grain boundary in TNT5Zr-AF+HIP alloy. The similar microstructure can be found in homogenized and furnace cooled TNTZ alloys consisting of the

β phase and grain boundary α precipitates [11,227]. The diffusion-controlled coarsening [228] of precipitates located at grain boundary in TNT5Zr-AF+HIP alloy is due to β stabilizer solute-lean in that zone, thus forms intergranular α precipitates. These particles undergo a further particle size increase after a relative long time furnace cooling.

The TEM investigation of TNT5Zr-AF+HIPA alloy has shown that ellipsoidal nano-sized α'' precipitates obtained in beta matrix, along with intergranular alpha precipitates (Fig. 4-6(B, D)). The similar microstructure with fine-scale intragranular α'' precipitation was also observed in Ti-32Nb-(2, 4) Sn alloy after low temperature aging at 400℃ for 2 hours [152]. The nano-sized α'' precipitates formation is accompanied by diffusion controlled local solute compositional fluctuation at low temperature, which is regarded as the same thermally activated formation mechanism with isothermal ω phases [138]. According to the fundamental basis of spinodal decomposition [225], localized fluctuations in composition can be triggered in the supersaturated stage and spontaneously grow in the vicinity "critical nuclei" by the continuous low-amplitude composition fluctuations, then gradually evolves into a distinct two-phase mixture. In our case, combining the results that microhardness values did not experience a large increase in the first 48 hours aging treatment (Fig. 4-7A) and ultrafine nano-sized precipitates (approx. 5~10 nm) were obtained in beta phase matrix (Fig. 4-6B), we presume the activation energy for the thermally activated diffusional jumps from the parent phase to the critical nucleus during isothermal aging is high in this high β-stabilized Ti alloy.

Reconstructed 3D visualization of keyhole (Fig. 4-2A) from as-fabricated TNT5Zr alloy is

observed by Micro-CT. The mechanism of keyhole formation was mentioned like that rear part of molten pool bears with intensive local evaporation due to incident beam function, then dynamic recoil pressure of vapor jet and surface tension pressure dent the adjacent wall for keyhole formation [22,82]. As TNT5Zr alloy possesses narrow temperature gap between the highest melting point Ta (3017°C) and lowest boiling point element Ti (3287°C), therefore the keyhole formation risk could be high due to local element evaporation happens inside the molten pool. It is noteworthy that HIP thoroughly closed these as-fabricated pores. This has been explained by Atkinson et al. [119] that the surrounding matter is transported to fill internal pores by the aid of high pressure argon atmosphere. However, in order to fulfill the pore closure at high temperature, the cooling rate dependent microstructural evolution inevitably occurred in this alloy. In our former work [219], micro-CT evaluation showcased an extremely low volume fraction (0.0030%) of un-melted particles (Nb, Ta) in as-fabricated TNT5Zr alloy. Additionally, there is no diffraction peak belonging to these un-melted particles can be detected in this alloy (Fig. 4-4). We consider that microstructural inhomogeneity caused by these negligible particles were not formed due to a high energy input and remelting effect in laser scanning.

4.4.2 Mechanical properties

The low Vickers hardness value obtained from as-fabricated TNT5Zr (Fig. 4-7C) is consistent with Ti–24Nb–4Zr–8Sn alloy manufactured by SLM [21]. Similarly, tensile test data (Table 4-2) reveals that lowest UTS (698 ± 4 MPa) and Young's modulus (57 ± 5 MPa) was obtained in the as-fabricated TNT5Zr specimen. Slip has been reported in bcc polycrystalline materials on

various planes, e.g., {110}, {123}, and {112} containing the <111> direction of close packing [229], which makes the as-fabricated TNT5Zr alloy possessed a relative low critical resolved shear stress. Grain size decided by Hall-Petch relationship is another factor to explain the flow stress difference of polycrystalline β Ti alloy under plastic deformation. Available literatures [211,230] show that a comparable UTS (~680 MPa) is found in fine-grained Ti-30Nb-5Ta-3Zr alloy manufactured by SLM, and even lower UTS (449 MPa) is obtained in coarse-grained Ti-30Nb alloy after cold rolling then solution treatment at 750°C. In addition, it has been found that nanoscale imperfections caused by nanodisturbances play a crucial role in the formation of unique mechanical properties of Gum Metal [226]. The theory involves that elastic interaction between the nanodisturbances and provides for the softening of Gum Metal where they carry plastic flow, which is assumed to be another factor to explain the good plasticity of the as-fabricated TNT5Zr alloy.

By comparison with the mechanical properties results of TNT5Zr-AF alloy, it retains the same microhardness level but slightly higher UTS after HIP treatment (Table 4-2). The HIP treated material obtained a microstructure with coarser beta grains and grain boundary α precipitates. The strengthening induced by grain boundary precipitation and the change of grain orientation, together with material softening caused by grain growth after HIP treatment, dominate the resulting flow stress of TNT5Zr-AF+HIP. By comparison with the morphology and size difference of dimples in TNT5Zr-AF and TNT5Zr-HIP alloys, large irregular shear-like and smaller regular shape dimples were obtained accordingly. The regular shape dimples were

observed in the latter alloy because a higher extent of micro-void coalescence occurred in the heterogeneous microstructure of relatively coarse grains with a weaker preferred orientation, and grain boundary precipitates. It is noteworthy that no obvious improvement of plasticity of TNT5Zr-AF+HIP alloy was obtained after pores closure, suggesting that microstructure is potentially regarded as the more crucial factor than porosity to determine the plasticity of it.

HIP & aging duplex treatment further strengthens TNT5Zr alloy by introducing ellipsoidal nano-sized secondary alpha precipitates in beta matrix (Fig. 4-6B). The nanoscale particles inevitably cause lattice distortions and impede the dislocation movement through a lattice containing precipitate particles. Therefore, the as-mentioned microstructural evolution after duplex treatment make TNT5Zr-HIPA alloy obtain a comparable UTS (853 ± 9 MPa) than the counterpart of Ti64-AF+HIP (926 ± 23 MPa). Moreover, Young's modulus of TNT5Zr-HIPA alloy is kept as low as TNT5Zr-AF alloy (57 ± 5 GPa). This is inconsistent with the Young's modulus increases after aging treatment commonly reported in the literatures [150,186]. The authors suspected that the strengthening induced by fine nano-sized α'' precipitates (about 5~10 nm) in beta matrix is not severe. In addition, the existence of coarse intercrystallite alpha phases makes grain boundaries probably undergo fast collapse as a result of crack propagation paths during tension. Overall, the highest ratio of σ_{UTS}/E (15.2 ± 1.4) of TNT5Zr-AF+HIPA alloy among the involved materials demonstrates the potential for load-bearing implant application. This strengthened beta Ti alloy possesses an advantage on "stress shielding" effect reduction than the high elastic modulus biomedical Ti-6Al-4V [212].

After studying the fractographic characteristics of different regions (Fig. 4-9) in TNT5Zr-AF+HIPA alloy, inferior notch-like surface irregularities are regarded as fatigue cracks initiation sites. Meanwhile, slip-band cracking has been widely observed in this ductile alloy caused by cyclic stressing close to the fatigue limit (170 MPa). The ribbon-like extrusion along slip bands normally starts after small number of loading cycles. The phenomenon of intrusions and extrusions is a result of persistent slip bands beneath the surface. Smaller crack spacing in the crack initiation region demonstrates that the crack growth rate is smaller than crack propagation zone. After crack further aggregating inside the extension region, the crack spacing becomes wider as an indication of local plastic deformation [231]. When cracks migrate to the final fast fracture region, it occurs two crack growth mechanisms. Micro-cleavage involves facture along grain, which describes like that coarse intergranular precipitates impede the gliding and thus provide the crack paths. Due to the stress level of cracks propagation along boundaries is probably lower than slip-band cracking within grains, therefore destructive cyclic stress promptly peels off grain boundaries. Moreover, microvoid coalescence takes place during plastic deformation can be attributed to the microstructure of nano-sized precipitation inside beta matrix.

S-N curve (Fig. 4-9B) shows intermediate fatigue limit of 170 MPa in the condition of TNT5Zr-AF+HIPA. According to the results from literatures, the measured fatigue limit is lower than the counterpart of as-forged + solution treated Ti-29Nb-13Ta-4.6Zr (320 MPa) [150], but remains on the same level of SLMed Ti–30Nb–5Ta–3Zr (140 MPa) using pre-alloyed feedstock

[211]. Here the improvement of fatigue limit of TNT5Zr alloy manufactured by SLM is discussed. First, microstructure tailoring to enhance strength and ductility of the material can be considered. From the aforementioned tensile testing results, heterogeneous intergranular second-phase (alpha precipitates) induced from high temperature HIP treatment deteriorated the ductility of TNT5Zr-HIPA, making cracks preferably propagate along grain boundary. These precipitates should be suppressed by post-processing treatments undergoing a higher cooling rate. In addition, a proper longer aging time is supposed to increase the content and size of isothermal precipitates inside beta matrix, making dislocation bowing dominate around particles during plastic deformation. Second, as the nature of sample surface strongly affects the fatigue initiation and propagation behaviour, test-pieces with a better surface finish for fatigue test can significantly enhance the fatigue strength. Unlike the aforementioned fatigue test in the former work [150,211] via using as-machined test-pieces, the authors in this study measured the fatigue limit of the as-grinded samples to better reveal the real surface imperfections fabricated via additive manufacturing (AM). Surface roughness modification (e.g., chemical polishing) [122,127] can be introduced to decrease surface discontinuities of complex-shape AMed components, which helps to reduce stress concentrators and further lower crack initiation risk from the surface. At the same time, recorded data [231] also revealed that square cross-section caused a large decrease in fatigue limit than circular ones; ultimate tensile strength enhancement caused by specimen cross-sectional area increasing was observed in as-built Ti-6Al-4V for both cylindrical and rectangular-shaped specimen types [232]. It means that the types of test-pieces and the amount of surface area manufactured by SLM should

be well considered.

4.4.3 In vitro performance

The biocompatibility investigation (Fig. 4-10) according to quantitative results has shown that almost no significant difference between cell-substrate (metallic ones) interactions, referring to viability, differentiation, and mineralization. Similarly, it has shown the same level of MC3T3-E1 preosteoblasts attachment, spreading and proliferation between Ti-23Nb-7Ta-2Zr-0.5N alloy and Ti-6Al-4V control samples [182]. The passive oxide films formed from TNT5Zr and Ti-6Al-4V alloy presumably exhibit subtle chemistry differences in these short-term cultures, thus negligible toxicity was observed due to the protection of various oxides (Fig. 4-10A). Available literature [233] found that the quantities of alloying elements (Ti, Al, and V) released from Ti-6Al-4V alloy and alloying elements (Ti, Zr, Nb, and Ta) from Ti-15Zr-4Nb-4Ta alloy were negligible after immersion in cell culture medium for one week. However, the metallic ion concentration as function of *in vivo* implantation period (0~48 weeks) result revealed a metallic ion level increase in Ti-6Al-4V but much lower released ion level in the latter alloy. As cytotoxicity induced from released metallic ions is crucial for long-term implantation of any biomaterial [18], the more noble corrosion-resistant TNTZ alloy maybe become an advantageous Ti alloy for use, which is also reported in Atapour et al. [17] 14-day ALP content and 30-day calcium deposits quantification suggest a significant lower level of cell differentiation than the counterpart of control group. These results without normalization ignored the surface area of substrates. Because preosteoblasts cultured in plastic control substrate possessed 2.5 times larger surface area than the counterpart of the two Ti alloy

substrates, thus a comparable level of the mineralization results can be obtained after a proper normalization. During *in vitro* MC3T3-E1 tests, the authors consider that the SLM manufactured TNT5Zr can be worked as a biomaterial like the well-accepted bio-friendly Ti-6Al-V.

4.5 Conclusions

This chapter investigated the microstructural evolution, defects distribution, mechanical properties of SLM-manufactured TNT5Zr β Ti alloy before and after post-processing treatment. In addition, we evaluated short-term *in vitro* MC3T3-E1 preosteoblast response of the post-processed β Ti alloy and Ti-6Al-4V alloy. The main conclusions are drawn:

1 HIP treatment closes the as-fabricated keyhole pores in TNT5Zr alloy due to densification caused by the pressured and high-temperature argon atmosphere. Meanwhile, the grain growth and slighter extent of preferred crystallographic orientation is observed in specimen after HIP. BF image & SAD pattern together with BF-STEM observation shows the existence of single beta matrix and alpha precipitates along the grain boundary in TNT5Zr-AF+HIP alloy. The same microstructure included ellipsoidal nano-sized α'' precipitates (about 5~10 nm) in the β matrix is obtained in TNT5Zr-AF+HIPA alloy.

2 By comparison with the mechanical properties of TNT5Zr-AF alloy, it remains the slightly higher UTS (760 ± 5 MPa) after HIP treatment. HIP & aging duplex treatment further strengthens the ductile TNT5Zr alloy by precipitation strengthening, making it obtained a comparable UTS (853 ± 9 MPa) to Ti64-AF+HIP (926 ± 23 MPa).

3 Inferior notch-like surface irregularities are regarded as fatigue cracks initiation sites in TNT5Zr-AF+HIPA alloy. Slip-band cracking has been widely observed in this alloy caused by cyclic stressing close to the fatigue limit (170 MPa). Both crack growth mechanisms, namely micro-cleavage and microvoid coalescence take place when cracks migrate to final fast fracture region.

4 *In vitro* biocompatibility investigation of both Ti alloys has shown similar metabolic activity and long-term mineralisation. The high strength-to-modulus ratio (15.2 ± 1.4) together with excellent biological *in vitro* behaviour, demonstrating TNT5Zr-AF+HIPA alloy can be a good candidate for load-bearing implant.

5 THE INFLUENCE OF ADVANCED HOT ISOSTATIC PRESSING ON PHASE TRANSFORMATIONS, MECHANICAL PROPERTIES OF TI-34NB-13TA-5ZR-0.2O ALLOY MANUFACTURED BY *IN-SITU* ALLOYING VIA SELECTIVE LASER MELTING

Paper Status: published

Weihuan Kong[a], Elisabeth M. Francis[b], Qi Shi[c], Sophie C. Cox[d], Feng Wang[a], Min Kuang[c], Moataz M. Attallah[a*], **The Influence of Advanced Hot Isostatic Pressing on Phase Transformations, Mechanical Properties of Ti-34Nb-13Ta-5Zr-0.2O Alloy Manufactured by In-situ Alloying Via Selective Laser Melting**, Journal of Alloys and Compounds 903 (2022) 163974.

https://doi.org/10.1016/j.jallcom.2022.163974.

Authorship contribution statement

Weihuan Kong conceived and designed the experiment, performed the experiment, interpreted the data, and wrote the manuscript. Elisabeth M. Francis and Feng Wang conducted TEM observations. Qi Shi provided the support for material post-processing. Sophie C. Cox and Min Kuang assisted with designing the experiments. Moataz M. Attallah assisted with revising the manuscript.

---

a. School of Metallurgy and Materials, University of Birmingham, Edgbaston, B15 2TT, UK
b. Manchester Materials Science Centre, The University of Manchester, Grosvenor Street, Manchester, M1 7HS, UK
c. Guangdong Institute of New Materials, Guangdong Academy of Science, Guangzhou, 510651, PR China
d. School of Chemical Engineering, University of Birmingham, Edgbaston, B15 2TT, UK

Abstract

In this chapter, advanced hot isostatic pressing (HIP) subjected to high and intermediate cooling rate (HCR & ICR) were exploited to close keyholes and tune the microstructure of SLMed Ti-34Nb-13Ta-5Zr-0.2O alloys (TNT5Zr-0.2O, wt. %). XRD analysis along with SEM and TEM micrographs reveal single beta phase in grain matrix of as-fabricated TNT5Zr-0.2O (TNT5Zr-0.2O-AF), TNT5Zr-0.2O-HCR, TNT5Zr-0.2O-ICR alloys. Additionally, high-angle annular dark-field (HAADF) micrographs show discrete large Ti-rich α grain boundary precipitates in TNT5Zr-0.2O-ICR alloy. Tensile properties show that TNT5Zr-0.2O-AF alloy possessed high UTS of 975 ± 12 MPa, and elongation of 4.9% ± 0.3%; the TNT5Zr-0.2O-ICR alloy obtained slightly higher UTS (1036 ± 26 MPa) and lower elongation (3.0% ± 0.3%). S-N curves demonstrate fatigue limit of TNT5Zr-0.2O-ICR alloy (150 MPa) is slightly higher than the counterpart of TNT5Zr-0.2O-AF alloy (130 MPa), and slip-band cracking phenomenon was observed in both alloys. Advanced HIP subjected to intermediate cooling rate functions well to close SLM-processed keyholes but the resistance to fatigue is not markedly enhanced; the addition of proper amount oxygen interstitial solutes in TNTZ-O alloy is regarded as an inexpensive, effective strengthening technique for load-bearing biomedical applications.

5.1 Introduction

Ti-Nb-Ta-Zr (TNTZ) alloy possesses excellent mechanical properties, such as ultralow Young's modulus, relatively high strength and good plasticity, which exhibits its potential to be the next generation load-bearing implant material [54]. However, there still have some controversial

microstructural evolution mechanisms in TNTZ alloys manufacturing. For example, the mechanism of oxygen effect on the phase transformation in TNTZ-O alloy (Gum Metal) is not commonly accepted. Some researchers believe that oxygen addition retards the formation of athermal ω and α'' phases in Gum Metal. Tane et al. [30,31] manufactured solution treated single crystal samples of Ti-36Nb-2Ta-3Zr alloys containing 0.09, 0.36, 0.51 wt. % oxygen and the cold-worked same metallic element composition alloy containing 0.06, 0.30, 0.47 wt. % oxygen, and observed the microstructures with a TEM equipped with cooling stage. They concluded that higher oxygen addition in different-method prepared alloys variously suppresses the formation of athermal ω and α'' phases cooling from room temperature to a fairly low temperature of ~ 13 K. Wei et al. [234] carried out TEM investigations of solution treated Ti-23Nb-2Zr-0.7Ta-(0.6~1.8)O (at. %) alloys and observed SAD patterns belonging to athermal ω phases in the aforementioned three alloys. The researchers insisted that the intensity of these diffraction spots corresponding to athermal ω phases decreased with increasing oxygen concentration, which agrees with the conclusion drew from the former work. In addition, Saito et al. [32] asserted that oxygen function as interstitial atoms in Ti-23Nb-0.7Ta-2Zr-(0.5~2.5)O (at. %) alloys, then tend to form extremely short-range atom clusters around zirconium atoms, which could effectively inhibit dislocation activity. Moreover, Yokota et al. [235] observed gradient tensile strength increase in water-quenched Ti-35Ta-O alloys (at. %) when oxygen content was increased from 1.5% to 4.6%. The oxygen solid solution strengthening was supported by first-principles calculations due to the existence of O atoms at the octahedral interstitial sites in the bcc structures. Similarly, the interstitial oxygen in water-quenched Ti-

(15~34)Nb-O (wt. %) alloys was believed to produce a strong influence on strength and micro-hardness increase [236,237]. Miinomi et al. [33] questioned the conventionally accepted understanding that oxygen destabilizes the omega phase in Gum Metal. In their study, they prepared Ti-29Nb-13Ta-4.6Zr alloys containing 0.1 and 0.4 wt. % oxygen using two-step aging treatment. After performing TEM characterisation, clear diffraction patterns of isothermal α'' in the former alloy and additional ω also α'' in the latter alloy were revealed. Additionally, reconstructed APT data showed that oxygen content was significantly higher in ω or α'' particle than β phase in TNTZ-0.4O alloy. Thus, the high concentration of oxygen within that alloy was considered as the potential driving force for $\beta \rightarrow$ isothermal ω phase transformation during aging at 723 K.

The prior investigations have shown that the microstructure of high β stabilized TNT(Z) alloys is sensitive to cooling rate after the homogenization treatment. Tang et al. [227] exhibited the TEM micrographs of Ti-23.2Nb-22.0Ta alloy (wt. %), which homogenized at 1000℃ for 2 hours followed by water quenching and air cooling, respectively. According to BF-TEM image and its SAD pattern, the authors asserted that martensite phases with an acicular morphology and indistinguishable embryo ω precipitates were retained in beta grain matrix after water quenching. By comparison, TEM observation indicated that the ω phase underwent a significantly growth during the slower air-cooling process. In addition to microstructure difference in the beta grain matrix caused by cooling rate, grain boundary is also regarded as a preferred site to form cooling rate dependent microstructure. Banerjee et al. [11], Nag et al. [27]

both observed relatively large beta grains with grain boundary α precipitates in Ti-34Nb-9Zr-8Ta alloy (wt. %), which was homogenized at 1100℃ for 7 days then furnace cooled. Microstructural evolution and mechanical properties of Ti-29Nb-13Ta-4.6Zr alloy (wt. %) experienced solution treatment and cooling procedure via different mediums e.g., water, static air, vacuum furnace, etc was preliminarily investigated by Najdahmadi et al. [238]. Based on the measured elongation values, the furnace cooled specimen possessed the lowest ductility. The authors concluded that the formation of intergranular and intragranular precipitates in the furnace cooled TNTZ alloy leads to an inhomogeneous deformation and easier crack initiation.

In this chapter, we investigated the microstructural evolution, mechanical properties of SLMed Ti-34Nb-13Ta-5Zr-0.2O alloy (wt. %) before and after advanced HIP subjected to high and intermediate cooling rate. The effect of oxygen on the microstructure, tensile and fatigue characteristics of the SLMed Ti-34Nb-13Ta-5Zr-0.2O alloy was studied. Furthermore, advanced HIP technique was exploited aiming to close the as-fabricated pores and tune the microstructure of the β Ti alloy cooled from the temperature above beta transus to room temperature.

5.2 Materials and methods

5.2.1 Powder feedstock preparation

Pure element powder was used to blend the as-designed Ti-34Nb-13Ta-5Zr alloy (TNT5Zr, wt. %) for *in-situ* alloying via SLM. Spherical Ti and Zr powders (TLS, Germany) with nominal particle size distribution of 15—83 μm and 10—45 μm, respectively were gas

atomized in an argon atmosphere. Irregular-shaped Nb (Elite, UK), Ta powder (H.C. Starck, Germany) with an average particle size (D50) of 43.9 μm and 23.4 μm, respectively were manufactured through hydride-dehydride technique (Fig. 5-1A). The mass of each elemental powder was measured using a top pan balance (Kern EMB2000, 0.01g accuracy) inside a glove box (Saffron, UK) with an argon protective atmosphere (≤0.005% O_2). Then the powder was mixed for ten hours in a horizontal rotating drum (Kimber-Allen, UK), and the blended powder was demonstrated by benchtop SEM (TM3030, Hitachi) (Fig. 5-1B).

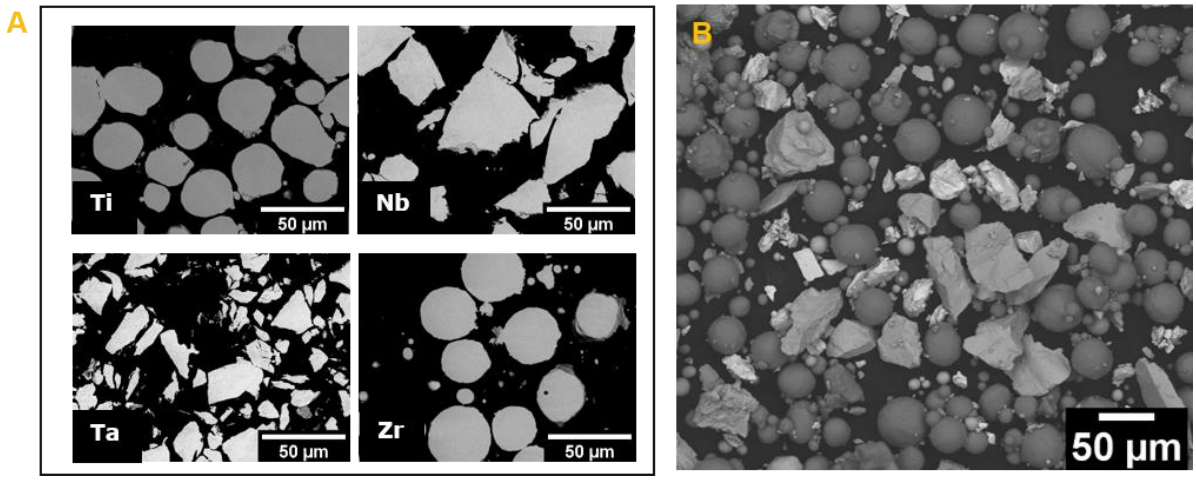

Fig. 5-1. (A) Cross-section micrographs of different pure element powders. (B) Particle morphology of blended TNT5Zr powder.

5.2.2 Selective laser melting

An M2 Cusing SLM system (Concept Laser, GE Additive) was used to fabricate TNT5Zr samples on Ti-alloy substrates. This machine was equipped with a 400 W Yb:YAG fiber laser at a wavelength of 1064 nm with a spot size of approx. 63 μm. After a batch of SLM parameter optimization, parameters for manufacturing specimens were: 300 W laser power, 500 mm/s scanning speed, 50 μm hatch spacing and 20 μm layer thickness. A chessboard scan strategy

was employed with scan vectors rotated by 90º in adjacent 5 x 5 mm blocks and successive layers shifted by 1 mm in both X and Y direction. TNT5Zr-0.2O alloy was obtained when perform *in-situ* alloying TNT5Zr due to the deteriorated seal in SLM system. The oxygen level in the SLM-manufactured alloy was measured using inert gas fusion standard test [239]. Among those as-fabricated samples, tensile specimen dimension was designed according to ASTM-E8/E8M-13a [198]; fatigue specimen was designed with tangentially blending fillets between the uniform test section and the ends according to ASTM-E466-15 [220]. The tensile and fatigue parts (10 mm in height) were horizontally manufactured with SLMed original side surface then sliced into dog-bone test-pieces (1.5 mm in height) by a wire electron discharge machining (EDM, GF Machining Solutions). Manual grinding kit (8220, Dremel) was used to reduce surface roughness of side surfaces from fatigue test-pieces.

5.2.3 Advanced hot isostatic pressing

Besides achieving SLMed pores closure, advanced HIP (Quintus, Sweden) was used to tune the microstructure of TNT5Zr-0.2O alloy. The investigated process parameters were: 3 hours dwell at 1000℃ in a container filled with 120 MPa pressurized argon atmosphere, followed by different cooling processes, namely high cooling rate (1000℃/min) and intermediate cooling rate (100℃/min). The samples supplied for the advanced HIP treatment were three forms: cuboidal, tensile and fatigue test specimens.

5.2.4 Microstructure characterisation

Metallographic specimens were prepared using automatic grinding and polishing (Tegramin

30, Struers), and then etched by Kroll's solution (2% HF + 6% HNO_3 + 92% H_2O). A field-emission gun (FEG) SEM (JSF-7000F, JEOL) was used for observing the as-etched microstructure. The phase identification was performed by X-ray diffractometer (XRD) (AXRD, Proto) with Cu Kα radiation, and XRD spectra were collected by a fixed parameter of 0.02º step size and a 2s time/step. Transmission electron microscopes (Talos F200X, FEI; Tecnai G2 F30, FEI) operating at 200 kV and 300 kV were used to capture bright-field (BF) TEM images & selected area diffraction (SAD) patterns, bright-field scanning transmission electron microscopy (BF-STEM) images, and high-angle annular dark-field (HAADF) images. Thin foils for TEM were prepared through an argon ion milling technique (Gatan PIPS, Ametek), involving gradient milling by different Ar ion energy and sputter angle settings.

5.2.5 Mechanical test

SLM-processed original side surface specimens (1.6 x 6 mm rectangular central cross-section) were used in tensile testing. And the tests were carried out perpendicularly to the build direction of as-fabricated samples at room temperature. The stress-strain curves were measured at a crosshead speed of 0.5 mm/min at room temperature using a tensile testing machine (2500, Zwick/Roell). Two specimens per alloy were tested to compare tensile properties difference, and a clip-on extensometer was attached to 15 mm gauge length of specimen for strain measurement until rupture. Fatigue testing with rectangular central cross-section (1.5 x 6 mm) specimens were tested perpendicularly to the build direction. Axial high cycle fatigue testing was performed on a fatigue testing machine (Vibraphore Resonant), using magnetic resonance to deliver low constant amplitude (load ratio of R = 0.1), and 53Hz high frequency (decided by

the specimen geometry and stiffness). The testing with a maximum stress (up to 250 MPa) inside the elastic region was performed at room temperature. Tensile and fatigue fracture morphologies were observed using SEM (XL-30, Philips).

5.3 Results

5.3.1 Microstructure characterisation

The XRD results for as-fabricated and as-HIPed TNT5Zr-0.2O specimens are presented in Fig. 5-2. Single beta phase with $(110)_{\beta}$, $(200)_{\beta}$, and $(211)_{\beta}$ peaks were obtained in as-fabricated TNT5Zr-0.2O alloy at room temperature. A profile of primary beta phase peaks along with low intensity α phase peak is revealed in TNT5Zr-0.2O-ICR alloy, whereas TNT5Zr-0.2O-HCR alloy only contains single β phase (Fig. 5-2).

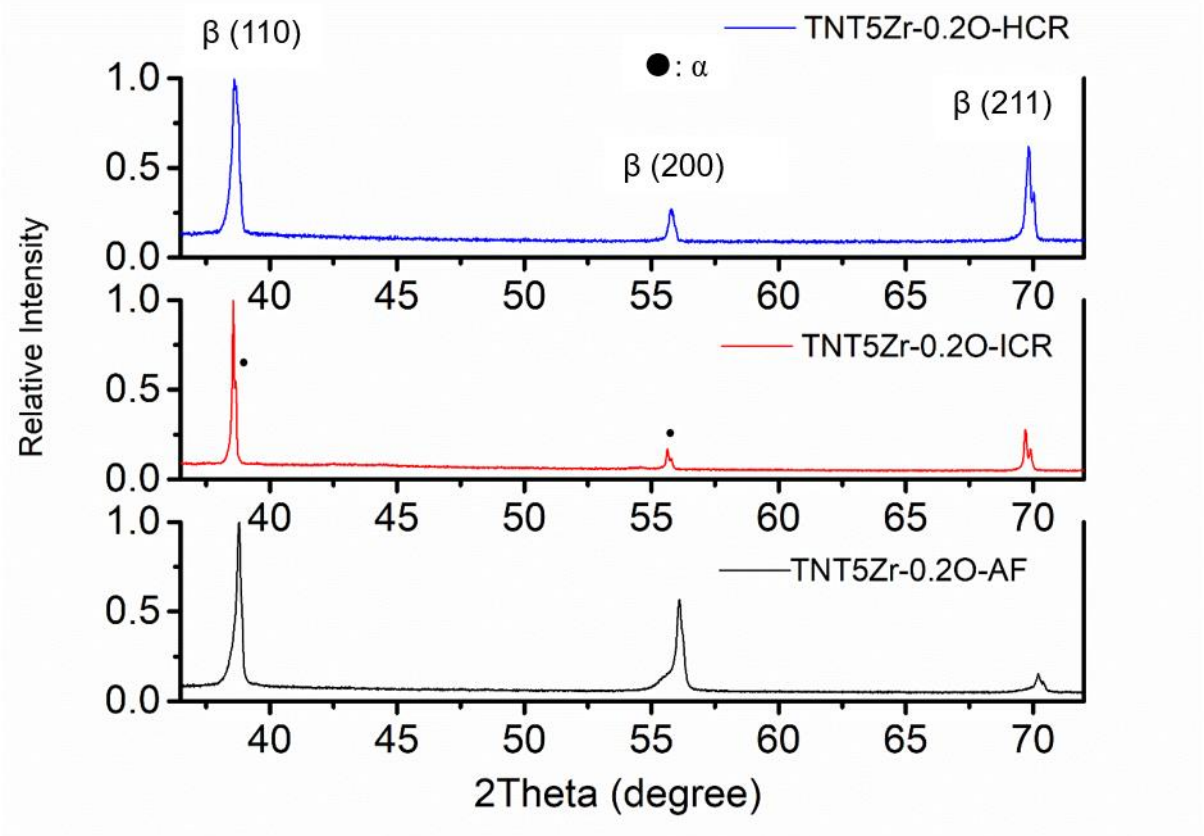

Fig. 5-2. X-ray diffraction patterns of the as-fabricated, as-HIPed (ICR), as-HIPed (HCR) TNT5Zr-0.2O alloys.

Note: $K_{\alpha 1}$ and $K_{\alpha 2}$ peak doublets are observed at high 2Theta angle.

Fig. 5-3 shows SEM images of microstructure captured from the as-fabricated, as-HIPed (ICR), as-HIPed (HCR) TNT5Zr-0.2O alloys. Equiaxed β grains were obtained in TNT5Zr-0.2O-AF alloy after performing *in-situ* alloying via SLM (Fig. 5-3A). The suspicious grain boundary alpha phase is observed in its high magnification (mag.) SEM micrograph (Fig. 5-3B). The same equiaxed grain type was kept in TNT5Zr-0.2O-ICR alloy (Fig. 5-3C). At the same time, nucleation with discrete precipitates occurred at grain boundaries when the alloy was intermediately cooled from the 1000℃ HIP temperature (Fig. 5-3D). By comparison, TNT5Zr-0.2O-HCR alloy retained equiaxed β grains in a manner without intragranular plate-like or acicular metastable precipitates after rapid cooling (Fig. 5-3E). In addition, no intergranular precipitates are seen in the corresponding high mag. SEM image (Fig. 5-3F).

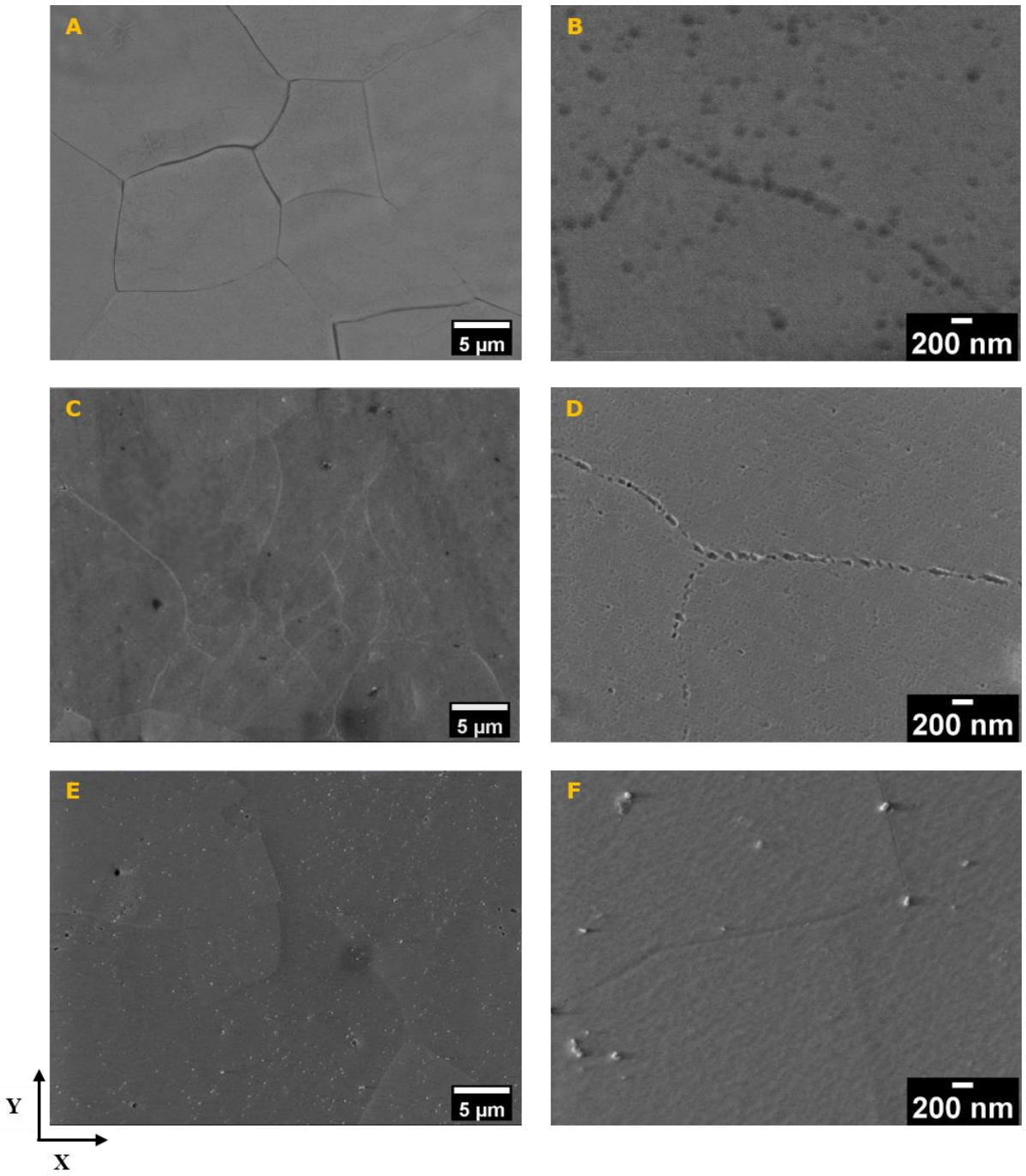

Fig. 5-3. (A) Low and (B) high mag. SEM micrographs illustrating the microstructure of as-fabricated TNT5Zr-0.2O alloy; (C) low and (D) high mag. SEM micrographs illustrating the microstructure of TNT5Zr-0.2O-ICR alloy; (E) low and (F) high mag. SEM micrographs illustrating the microstructure of TNT5Zr-0.2O-HCR alloy.

TEM examination reveals grain matrices in TNT5Zr-0.2O-AF and TNT5Zr-0.2O-ICR alloy, as shown in the BF-TEM images (Fig. 5-4(A-B)); the corresponding SAD patterns (inset) taken

from $[110]_{\beta}$ zone axis confirms the presence of single beta phase in grain matrices of both alloys. Similarly, BF-TEM micrograph taken from the beta grain matrix of TNT5Zr-0.2O-HCR alloy, together with SAD pattern (Fig. 5-4C) reveals single beta phase without formation of metastable athermal precipitates. Fig. 5-4D demonstrates a BF-STEM image collected from grain boundary sites of TNT5Zr-0.2O-ICR alloy. Clearly, heterogeneous discrete large plate-like precipitates nucleated and grew on grain boundaries. The corresponding grain boundary HAADF image and EDS maps of the involved elements (Ti, Nb, Ta, Zr, O) in TNT5Zr-0.2O-ICR alloy are presented in Fig. 5-4E. The TEM-EDS analysis indicated the presence of second-phase enriched in Ti element, leaned in Nb and Ta along grain boundary. Notably, parent beta phase appeared a uniform distribution of all the involved elements, and the existence of oxygen element were found in both two phases.

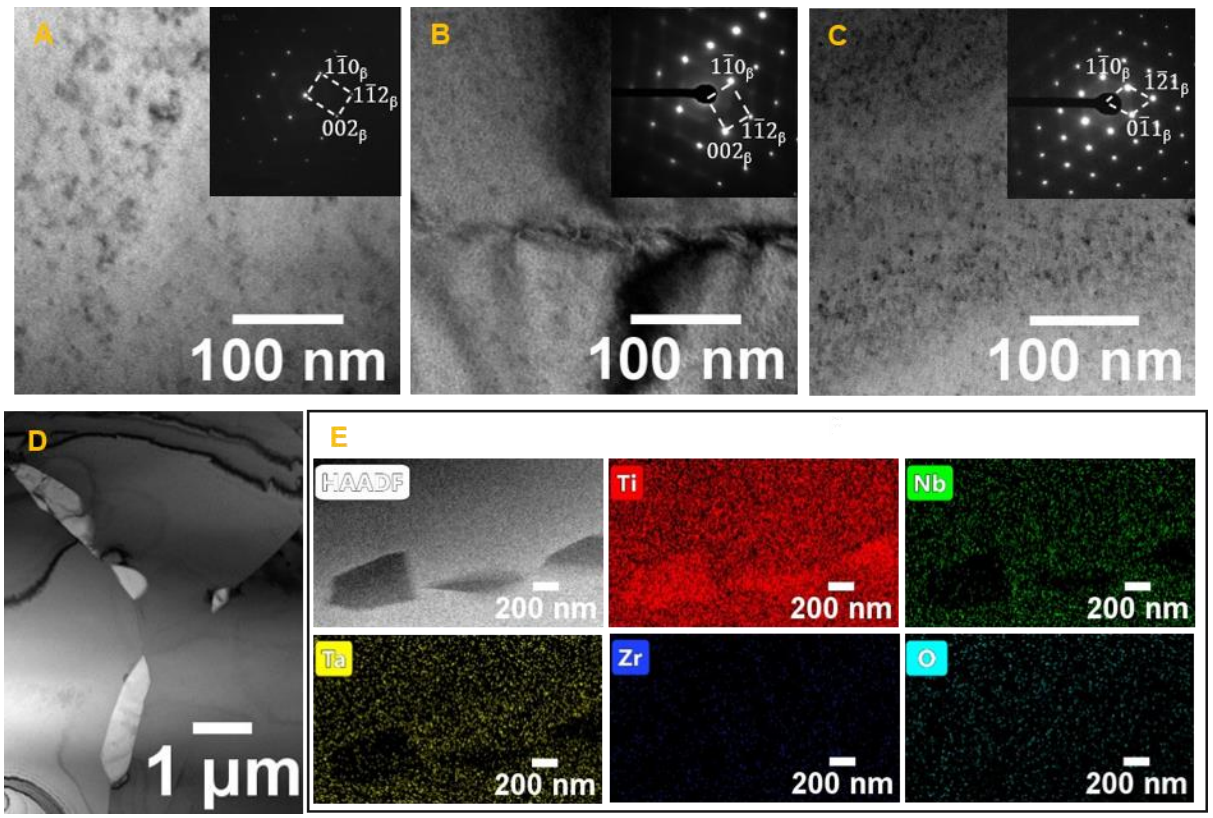

Fig. 5-4. (A) BF-TEM image collected from grain matrix with corresponding SAD pattern (inset) of TNT5Zr-0.2O-AF, (B) TNT5Zr-0.2O-ICR alloy, viewing from $[110]_{\beta}$ zone axis. (C) TNT5Zr-0.2O-HCR alloy, viewing from $[111]_{\beta}$ zone axis. BF-STEM image of (D) TNT5Zr-0.2O-ICR, taken from a region close to the grain boundary. (E) HAADF image captured from TNT5Zr-0.2O-ICR grain boundary region and TEM-EDS distribution maps of Ti, Nb, Ta, Zr, O element.

5.3.2 Tensile properties

The engineering stress-strain curves of as-fabricated and as-HIPed TNT5Zr-0.2O alloys are given in Fig. 5-5. Table 5-1 summarizes the as-measured tensile properties including the former collected as-fabricated TNT5Zr alloy data (without oxygen pick-up) using the same testing method. Fig. 5-5 presents both the as-fabricated and as-HIPed (ICR) TNT5Zr-0.2O alloy underwent elastic and plastic deformation till rupture. However, the as-HIPed (HCR) TNT5Zr-0.2O alloy broke at the initial linear elastic region (682 ± 75 MPa) without yielding phenomenon. In the comparison with the obtained mechanical data (Table 5-1), TNT5Zr-0.2O-AF alloy possessed high ultimate tensile strength (UTS) of 975 ± 12 MPa, and elongation of 4.9% ± 0.3%; the TNT5Zr-0.2O-ICR alloy obtained a slightly higher UTS (1036 ± 26 MPa) and lower elongation (3.0% ± 0.3%). When comparing tensile properties of TNT5Zr-0.2O-AF and TNT5Zr-AF alloy, an obvious material strengthening with >250 MPa UTS increase happened after oxygen pick-up during *in-situ* alloying via SLM. There appeared a slight elastic modulus (3 GPa in mean value) increase after absorption of oxygen in the as-fabricated alloy, and a further elastic modulus (9~15 GPa in mean value) rise after conducting two types of HIP treatment. Among these alloys, TNT5Zr-0.2O-AF alloy obtained the highest σ_{UTS}/E ratio (16.3

± 1.1) after the reinforcement effect caused by oxygen interstitial solutes and still maintained the low Young's modulus (60 ± 5 GPa).

Table 5-1

Tensile properties of the SLM processed TNT5Zr, and TNT5Zr-0.2O alloys subjected to different cooling rate HIP treatment.

Material	E (GPa)	$\sigma_{0.2}$ (MPa)	σ_{UTS} (MPa)	δ (%)	σ_{UTS}/E
TNT5Zr-0.2O-AF	60 ± 5	938 ± 8	975 ± 12	4.9 ± 0.3	16.3 ± 1.1
TNT5Zr-0.2O-ICR	69 ± 1	982 ± 6	1036 ± 26	3.0 ± 0.3	14.9 ± 0.7
TNT5Zr-0.2O-HCR	75 ± 5	--	682 ± 75	0.9 ± 0.1	9.1 ± 0.4
TNT5Zr-AF [240]	57 ± 5	650 ± 8	698 ± 4	13.7 ± 0.6	12.1 ± 1.1
TNTZ [143,186,221]	46-80	447-900	545-950	--	--

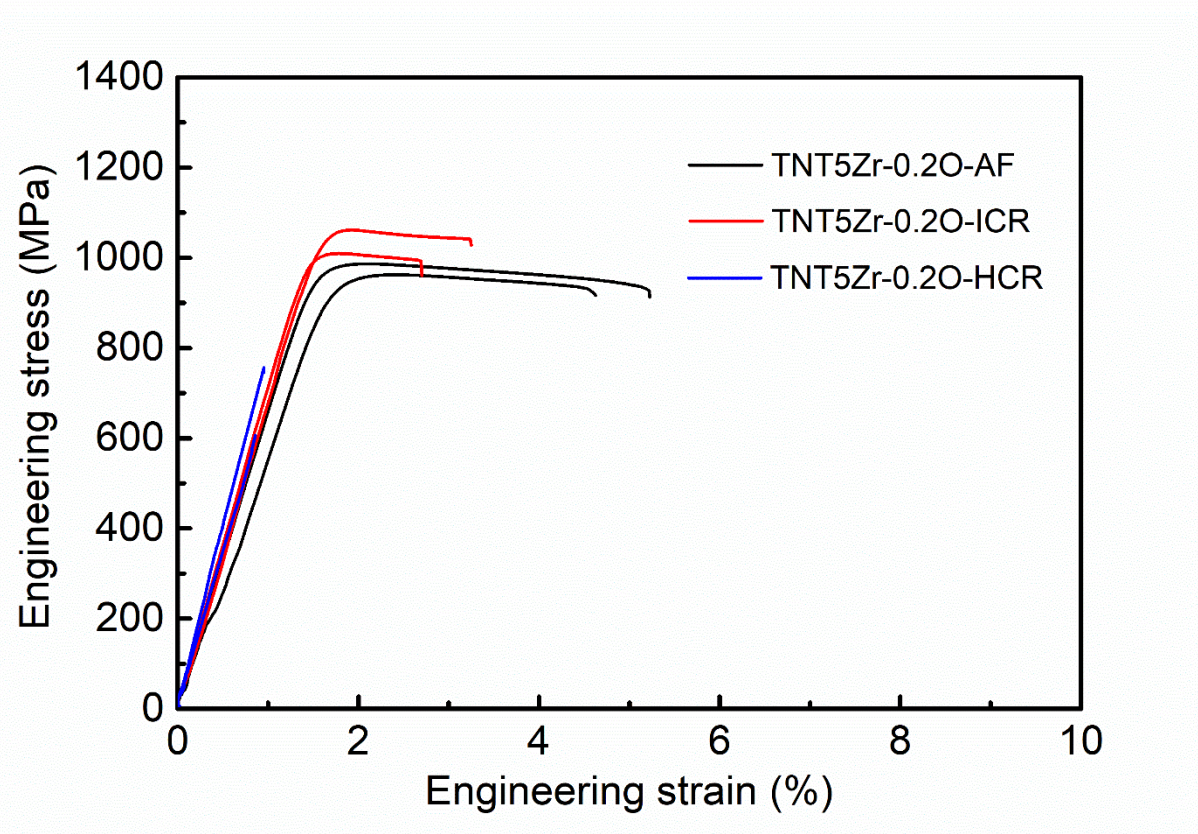

Fig. 5-5. Engineering stress-strain curves of as-fabricated and as-HIPed TNT5Zr-0.2O alloys.

Fig. 5-6 demonstrates representative fracture surfaces of TNT5Zr-0.2O alloy at different conditions. The low mag. (Fig. 5-6A) and intermediate mag. (Fig. 5-6B) SEM images show that the mixed surface of intergranular fracture together with intragranular fracture was found in TNT5Zr-0.2O-AF alloy under tension. Meanwhile, high mag. (Fig. 5-6C) fractograph reveals fine dimples at the central region of the ductile fracture. SEM images (Fig. 5-6(D-E)) of TNT5Zr-0.2O-ICR alloy fracture reveal a mixture of terrace-like intergranular fracture and matrix fracture formed by coalescence of voids; SEM fracture images (Fig. 5-6(G-H)) of TNT5Zr-0.2O-HCR alloy demonstrates the flattest surface with intergranular/intragranular fracture. It is clearly found that low mag. fractographs (Fig. 5-6(D, G)) show the absence of keyholes in the two as-HIPed TNT5Zr-0.2O alloys; high mag. fractographs (Fig. 5-6(F, I))

show the two as-HIPed TNT5Zr-0.2O alloys obtained the same dimple feature as TNT5Zr-0.2O-AF alloy (Fig. 5-6C) under tension.

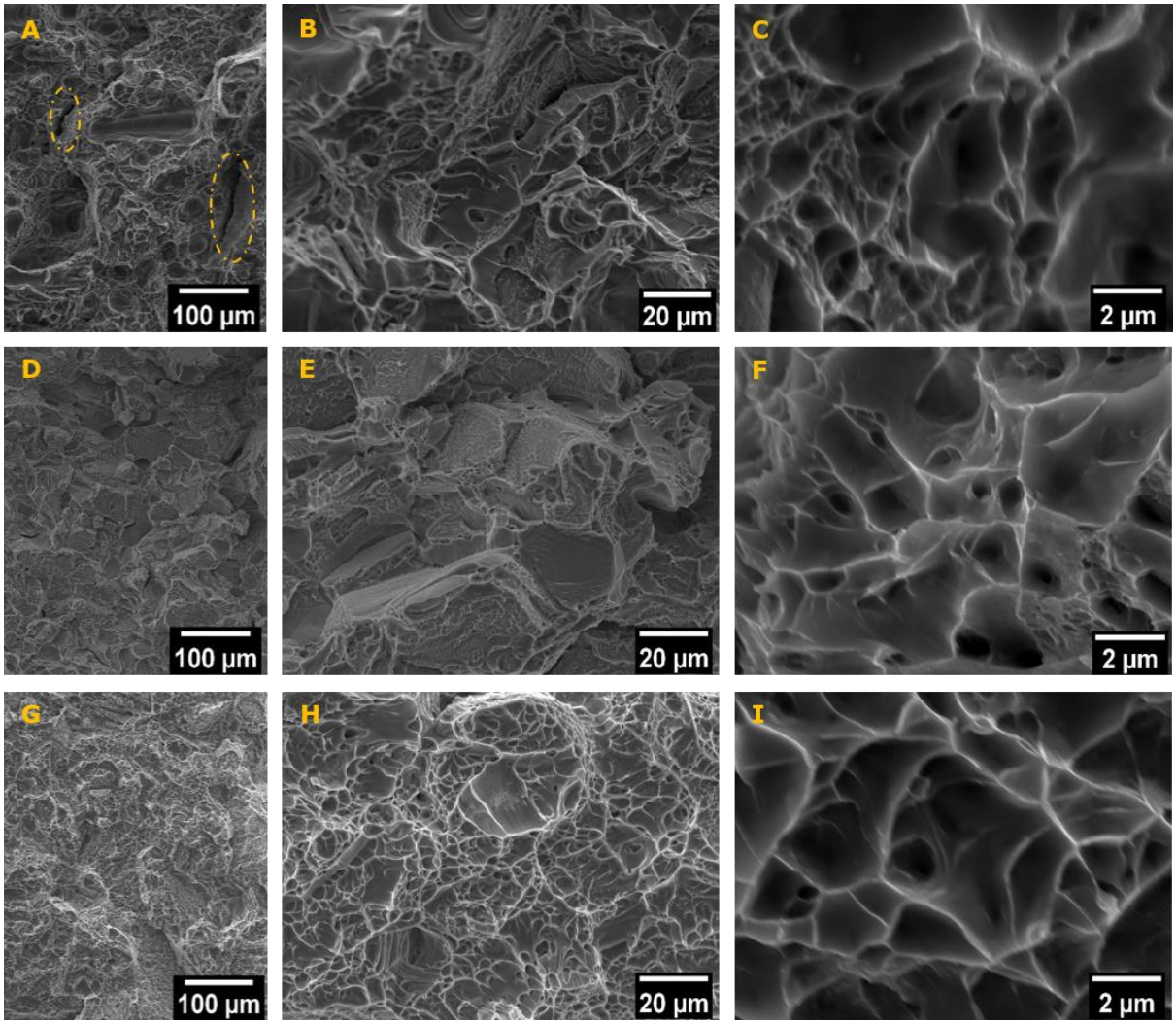

Fig. 5-6. (A), (B) and (C) increasing mag. SEM fractographs of as-fabricated TNT5Zr-0.2O alloy; (D), (E) and (F) increasing mag. SEM fractographs of TNT5Zr-0.2O-ICR alloy; (G), (H) and (I) increasing mag. SEM fractographs of TNT5Zr-0.2O-HCR alloy. Note: the dash line zones in (A) show the deformed region located in keyhole.

5.3.3 Fatigue properties

Fig. 5-7A shows the S-N curves of TNT5Zr-0.2O-AF and TNT5Zr-0.2O-ICR alloys obtained

from plain fatigue testing. Clearly, the fatigue limit of TNT5Zr-0.2O-ICR alloy (150 MPa) is slightly higher than the counterpart of TNT5Zr-0.2O-AF alloy (130 MPa). The number of cycles to failure in both alloys was almost the same in the maximum stress region (170-250 MPa). Low mag. SEM fractographs show fatigue crack preferably initiates from voids located in the surface of specimen in both alloys (Fig. 5-7(B-C)). These voids were kept after HIP treatment due to surface-connected pores cannot be removed if component is not coated or encapsulated, similarly reported by Atkinson et al. [119] and Williams et al. [241]. Three typical zones in TNT5Zr-0.2O-AF alloy fatigue fracture surface, namely crack initiation, crack propagation and final fracture are revealed in Fig. 5-7(D-F). Under the uniaxial cyclic tensile stress, slip occurred on favourably orientated nearby planes in crack initiation site leads to the formation of crevices or intrusions and extrusions (Fig. 5-7D). Coarse slip band cracks combining appreciable striations are observed in the crack propagation zone (Fig. 5-7E) and fine dimples appear in the final fast fracture zone (Fig. 5-7F), which demonstrates good ductility of the alloy. By comparison, slip-band cracking phenomenon with development of extrusion/intrusion pair is also observed in TNT5Zr-0.2O-ICR alloy under cyclic loading (Fig. 5-7(G-H)). Unlike the typical fine cellular dimples found in the final fracture zone of TNT5Zr-0.2O-AF (Fig. 5-7F), intergranular and intragranular mixed fracture appears in TNT5Zr-0.2O-ICR alloy (Fig. 5-7I). The discrete nano-sized grain boundary precipitates strengthened grain boundaries but at the same time locally high stress made there become the preferably fracture paths.

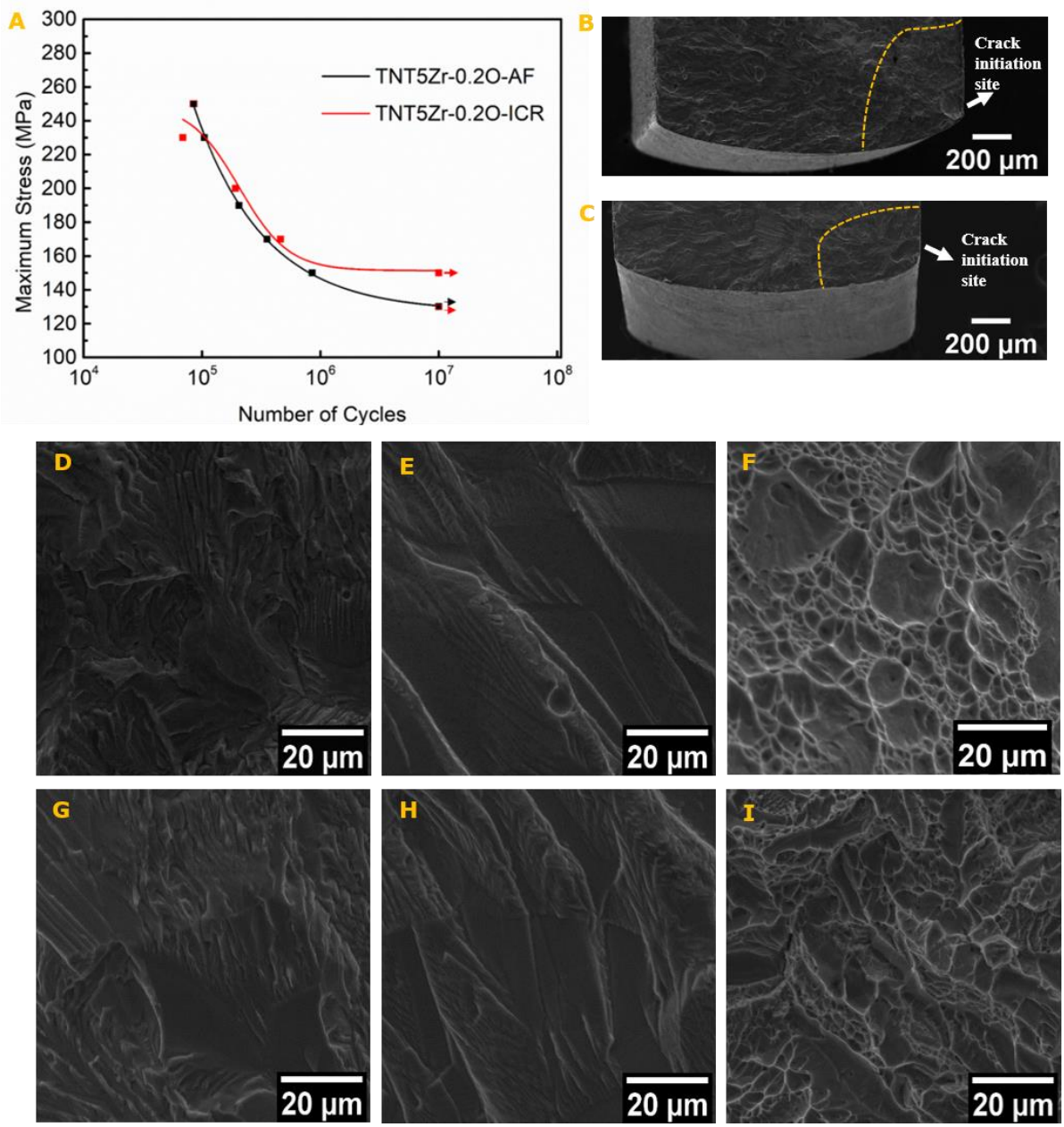

Fig. 5-7. (A) S-N curves of the as-fabricated and as-HIPed (ICR) TNT5Zr-0.2O alloy. (B) Fatigue fracture illustrating both fatigue source and fatigue propagation zones taken from TNT5Zr-0.2O-AF alloy, and (C) TNT5Zr-0.2O-ICR alloy. SEM morphology of (D) crack initiation area, (E) crack propagation area and (F) final fast fracture area of TNT5Zr-0.2O-AF alloy. SEM morphology of (G) crack initiation area, (H) crack propagation area and (I) final fast fracture area of TNT5Zr-0.2O-ICR alloy. Note: fatigue fracture surfaces were obtained from the maximum stress of 170 MPa. TNT5Zr-0.2O-AF alloy failed at N=354900; and TNT5Zr-0.2O-ICR alloy, N=460500.

5.4 Discussion

5.4.1 Microstructural evolution of the as-fabricated and as-HIPed *β* Ti alloys

Very small volume (below XRD detection limit) of nano-sized grain boundary alpha phases but no distinguishable precipitates within beta grain matrix probably retained in the as-fabricated TNT5Zr-0.2O alloy after performing XRD, SEM and conventional TEM characterisation. As oxygen concentration in Ti alloys has been found to raise the *β* transus temperature [242], which might provide more thermodynamic driving force and make precipitates more easily nucleate and grow along grain boundaries during TNT5Zr-0.2O alloy solidification. In contrast to the prior work, similar XRD and TEM diffraction pattern belonging to single *β* phases were revealed in hot processing & solution treating, then quenching treated Ti-35Nb-7Zr-5Ta-(0.06-0.68)O (wt. %) alloys [154]. In TNT5Zr-0.2O *in-situ* alloying, due to this *β* titanium alloy is constituted by enough *β* stabilizing elements (Nb, Ta), it obtained single beta grain matrix without formation of athermal ω and α'' phases even though the alloy underwent rapid cooling process in SLM. Therefore, the mechanism of oxygen suppressing athermal precipitates formation mentioned in introduction section is not applicable to clarify findings in our work. Here, oxygen atoms occupied in the interstices of bcc *β* phase at sufficient concentration (0.8 at. %) can well explain similar microstructure but pronounced tensile properties difference between the TNT5Zr-AF and TNT5Zr-0.2O-AF alloys. The oxygen solid solute strengthening mechanism will be discussed later in section 5.4.2.

TEM observation demonstrated the same single β phase within grain matrix in two as-HIPed TNT5Zr-0.2O and as-fabricated TNT5Zr-0.2O alloy (Fig. 5-4(A-C)). It observed that discrete large precipitates form along some grain boundaries in TNT5Zr-0.2O alloy when subjected to intermediate cooling rate (100℃/min) HIP treatment, captured by SEM (Fig. 5-3(C-D)). TEM characterisation further confirmed that the presence of large Ti-rich grain boundary secondary-phase (Fig. 5-4(D-E)), which is consistent with the element distribution in α phase found in Niinomi et al. [33] work. In the thermodynamic aspect of view, the usually heterogeneous formation of second-phase nucleus is favoured at grain boundary sites of the parent phase. Because the energy barrier for heterogeneous nucleation is well lower than homogeneous nucleation, and the total Gibbs free energy is reduced by an increase of the nucleus size [213]. In our work, the magnitude of solute redistribution of Ti atoms from the matrix towards grain boundaries is moderately high at the HIP temperature (1000℃). At the step of intermediate cooling , the intergranular precipitates possessed an ensuring solute concentration gradients and grain boundary diffusion coefficient for growth [243]. At the same time, second-phase particles tend to coalesce at high temperatures and form fewer large particles (Fig. 5-4D). Therefore, long-time high temperature HT followed by slow cooling rate should be avoided due to the formation of detrimental coarse grain-boundary particles. By comparison, grain boundary alpha precipitates are fully suppressed in TNT5Zr-0.2O-HCR alloy (Fig. 5-3(E-F)) as a result of much lower Ti element diffusion (from the matrix to grain boundary) and nucleus growth rate when underwent high cooling rate (1000℃/min) HIP.

5.4.2 Tensile properties of the studied alloys

Unlike the oxygen concentration control technique based on dissolution of titanium dioxide in conventional processing, deteriorated seal, and high oxygen-affinity of the involved elements (Zr, Ta, Nb, Ti) in SLM system make oxidation unavoidably occur at alloy melting and solidification stage. The strength enhancement after oxygen pick-up during TNT5Zr *in-situ* alloying is found in our work (Table 5-1). A similar phenomenon was observed in solution treated Ti-35Nb-7Zr-5Ta and Ti-24Nb β-Ti alloys containing oxygen fabricated by conventional manufacturing [244,245]. The solution-hardening by oxygen was also found and clarified in pure α-Ti, Yu et al. [246] proposed that interstitial oxygen atoms move from the original sites into Ti basal planes due to the shear pronounced decreases the volume of hcp octahedral site. Additionally, the presence of oxygen atoms near the screw dislocation core may force part of dislocation to cross slip to the neighbouring prismatic plane. Therefore, three factors, namely strong repulsion for oxygen and dislocation, large barriers for the “mechanical shuffle” of interstitial atoms in the core, and the local cross slip induced by oxygen atoms produce a strong pinning effect on screw dislocations. The scenario that cross-slip event induced by interstitial oxygen atom create two jogs on the screw dislocation is also seen in Zr-O alloys [247]. In addition, low Young’s modulus (60 ± 5 GPa) was retained in our TNT5Zr-0.2O-AF alloy due to its elastic deformation associated with bcc lattice structure stretching, which represents a big perturbation about the equilibrium spacing (more than 1% strain). We agree with the standpoint in Yang et al. work [248], the proper introduction of oxygen interstitial solutes in TNTZ-O alloy is an inexpensive, effective

strengthening method for load-bearing implants manufactured by SLM. However, it will sacrifice materials' ductility if forms coarse grain boundary alpha precipitates.

Besides oxygen solid solute strengthening mechanism in TNT5Zr-0.2O-ICR alloy, the nano-sized particles impede grain boundary migration and pin dislocation motion within the grain boundary. Normally, these particles preferentially appear at low-energy grain boundaries form pileup caused by interactions of the dislocations [249]. As a slightly higher UTS increase is observed in TNT5Zr-0.2O alloy after HIP followed by 100℃/min cooling, we presume that the pinning of planar dislocation has minor contribution on strength due to volume and size factor of the particles. Simultaneously, the UTS value of TNT5Zr-0.2O-ICR alloy is also affected by the grain growth softening when it underwent 3 hours dwell at 1000℃. After comparing its fracture images (Fig. 5-6(D-F)) with the prior work, the mixed morphology in appearance of dimple-like transgranular fracture and brittle intergranular fracture is also found in Ti-28Nb-13Zr-0.5Fe (wt. %) specimen aged at 450℃ with the presence of grain boundary α precipitates [250].

The embrittlement phenomenon is seen in TNT5Zr-0.2O alloy after HIP followed by 1000℃/min cooling. Both residual stress and strain incompatibilities in anisotropic grains or grain boundaries may be relevant to brittleness of the alloy. As temperature of the surface and core of components is distinct in rapid cooling process, thermal residual stress may attain at room temperature [251]. The internal residual stress combining with the external loading make cracks proceed rapidly. At the same time, the strain incompatibilities in adjacent

anisotropic grains produce locally high stresses near grain boundaries that could lead to crack initiation along boundaries under tension [252]. Moreover, the microvoids nucleate near the relatively weakened grain boundaries [253] without precipitation, then grow and coalesce into larger cavities when align with the low applied stress. It is noteworthy that unlike the conventional fracture of brittle material without significant plastic deformation, the dimpled intergranular fracture surfaces of TNT5Zr-0.2O-HCR alloy (Fig. 5-6(G-I)) exhibit localized plasticity of the solute-strengthened beta grain matrix but a rapid collapse of grain boundary sites.

5.4.3 Fatigue characteristics of TNTZ-(O) alloys

Both TNT5Zr-0.2O-ICR and TNT5Zr-0.2O-AF alloy possessed low fatigue limit, namely 150 MPa and 130 MPa. Considering the porosity factor, the resistance to fatigue is not markedly enhanced by removing the most of voids via HIP treatment. Due to the fatigue failure of the two alloys is determined by slip-band cracking mode, the cracks associated with slip band may take slightly shorter to propagate across the test-piece with voids. After a review of limited TNTZ alloy fatigue test results, many variable differences like material, geometry, testing condition (environment, frequency, etc.) can be found when making comparison with the as-measured values by Niimomi et al. [178] and Li et al. [179]. In the former study [178], the lowest fatigue limit (solution treated, mirror-like, 320 MPa) of the various heat-treated Ti-29Nb-13Ta-4.6Zr alloys measured using rectangular-shaped flat plate test-pieces is much higher than our highest fatigue limit (ICR HIPed, grinded, 150 MPa) TNT5Zr-0.2O alloy. Without considering microstructure difference, we presume that

specimen surface finish, and geometry are the main factors to explain the marked gap of fatigue limits of these investigated TNTZ-(O) alloys. The notches like surface irregularities have been greatly eliminated after final polishing in Niimomi et al. [178] work, which reduced the fatigue crack initiation sites. At the same time, the rectangular-shaped (unlike dog-bone) geometry leads to less concentration of stress at the central region and provide a more uniform stress distribution along specimen. Both two advantages make the Ti-29Nb-13Ta-4.6Zr alloys possessed much lower crack growth rate under cyclic deformation than TNT5Zr-0.2O alloy.

5.5 Conclusions

This chapter investigated the microstructural evolution, mechanical properties of SLMed Ti-34Nb-13Ta-5Zr-0.2O alloy (TNT5Zr-0.2O, wt. %) before and after advanced HIP subjected to high and intermediate cooling rate (HCR & ICR). The main conclusions about the influence of oxygen concentration and cooling rate on microstructure and overall properties are drawn:

1 XRD analysis along with SEM and TEM micrographs reveal single beta phase in grain matrix of TNT5Zr-0.2O-AF, TNT5Zr-0.2O-ICR, TNT5Zr-0.2O-HCR alloys. BF-STEM and HAADF micrographs show discrete large Ti-rich α precipitates formed along grain boundaries in TNT5Zr-0.2O-ICR alloy. By comparison, grain boundary α particles are fully suppressed in TNT5Zr-0.2O-HCR alloy.

2 TNT5Zr-0.2O-AF alloy possessed high UTS of 975 ± 12 MPa, and elongation of 4.9% ± 0.3%; the TNT5Zr-0.2O-ICR alloy shows slightly higher UTS (1036 ± 26 MPa) and lower

elongation (3.0% ± 0.3%). However, TNT5Zr-0.2O alloy breaks at the initial linear elastic region (682 ± 75 MPa) without yielding phenomenon, the brittleness may be caused by residual stress and strain incompatibilities in anisotropic grains or grain boundaries. The mixed surfaces of intergranular fracture together with intragranular fracture are observed in these three alloys but appear an obvious grain boundary fracture morphology difference. Notably, TNT5Zr-0.2O-AF alloy obtains the highest σ_{UTS}/E ratio (16.3 ± 1.1) and still maintains the low Young's modulus (60 ± 5 GPa).

3 S-N curves obtained from plain fatigue test show fatigue limit of TNT5Zr-0.2O-ICR alloy (150 MPa) is slightly higher than the counterpart of TNT5Zr-0.2O-AF alloy (130 MPa). SEM fractographs demonstrate fatigue crack preferably initiates from voids located in the surface of specimen, and slip-band cracking phenomenon with development of extrusion/intrusion pair is observed in both alloys.

4 The oxygen atoms occupied in the interstices of bcc β phase at sufficient concentration (0.8 at. %), probably produce a strong pinning effect on screw dislocations. Therefore, the addition of proper amount oxygen interstitial solutes in TNTZ-O alloy is regarded as an inexpensive, effective strengthening technique for load-bearing biomedical applications.

6 THE INFLUENCE OF THERMAL OXIDATION ON THE MICROSTRUCTURE, FATIGUE PROPERTIES, TRIBOLOGICAL AND *IN VITRO* BEHAVIOUR OF SLM-MANUFACTURED TI-34NB-13TA-5ZR-0.2O ALLOY

Paper Status: ready for submission

Weihuan Kong[a*], Victor M. Villapun[b], Yu Lu[a], Luke N. Carter[b], Min Kuang[c], Sophie Cox[b*], Moataz M. Attallah[a*], **The Influence of Thermal Oxidation on the Microstructure, Fatigue Properties, Tribological and In vitro Behaviour of SLM-manufactured Ti-34Nb-13Ta-5Zr-0.2O Alloy**, Journal of Alloys and Compounds.

Authorship contribution statement

Weihuan Kong conceived and designed the experiment, performed the experiment, interpreted the data, and wrote the manuscript. Victor M. Villapun assisted with the collection of biocompatibility results and manuscript revision. Yu Lu performed EDX mappings to reveal the gradient microstructures after thermal oxidation. Luke N. Carter and Sophie Cox assisted with revising the manuscript. Min Kuang and Moataz M. Attallah involved resources and methodology.

a. School of Metallurgy and Materials, University of Birmingham, Edgbaston, B15 2TT, UK
b. School of Chemical Engineering, University of Birmingham, Edgbaston, B15 2TT, UK
c. Guangdong Institute of New Materials, Guangdong Academy of Science, Guangzhou, 510651, PR China

Abstract

This chapter innovatively investigates the feasibility of thermal oxidation (TO) for improving the wear and fatigue properties of TNT5Zr-0.2O alloys manufactured by selective laser melting (SLM). Static chemical etching (CE) as a pre-treatment for TO successfully removed the SLM-induced surface adhered powders. A mixture of rutile, Nb_2O_5, Ta_2O_5, and ZrO phases were formed as an oxide layer after TO. It can be found a better wear resistance was retained in this β-titanium alloy after TO, as demonstrated by the wear scar features with ploughing grooves changing into brittle peeling of oxides. Plain fatigue strength of CE treated alloy (150 MPa) was 1.5 times higher than the value of CE+TO treated alloy (60 MPa), as a result of multiple premature fatigue cracks possibly developing in the compounds region after TO. *In vitro* biocompatibility results showed no significant differences in metabolic activity of pre-osteoblasts seeded on the treated surfaces. In addition, early and late mineralisation assays revealed similar levels of 14-day ALP activity, and 28-day mineral deposits formed on the two biocompatible TNT5Zr-0.2O alloy surfaces. Overall, though the oxide layer is corrosion-resistant in the aggressive environment (3M HCl solution), showing potential application of TO in additively manufactured titanium medical devices. TO should be cautiously exploited due to the mechanical properties deterioration.

6.1 Introduction

The demand for durable artificial joints is on the rise due to a relatively high utilization rate of revision hip replacement, which has been reported in the range of 16 to 23 per 100,000

population between 2007 and 2017 [254]. Since metallic materials usually possess high static/dynamic strength and good biological compatibility, they are widely used in the development of load bearing medical devices to date [16,192,255,256]. From these materials, Ti-6Al-4V is a well-established alloy utilised in metallic implants combining excellent mechanical performance with good biocompatibility. However, it is commonly accepted that Ti-6Al-4V suffers from fairly poor tribological performance [257]. The disruption of the protective oxide film under fretting and sliding in an *in vivo* corrosive environment will form wear debris and raise metal ion release, which accelerates the degradation of the alloy [258,259]. This may also have adverse effects on patients, with some studies highlighting increases in vanadium concentrations after approximately 5 years with a Ti-6Al-4V implant [51]. Specifically, it has been shown that vanadium and aluminium ions may inhibit preosteoblast and fibroblast cell growth [52].

Based on the aforementioned concerns of Ti-6Al-4V, various surface hardening methods have been investigated for improving the tribological properties and corrosion resistance of this widely used alloy. The most common of these techniques are nitrogen ion implantation, plasma nitriding and thermal oxidation. Nitrogen ion implantation is regarded as an effective method to improve the performance of Ti-6Al-4V, and prevent distortion and a loss of substrate properties [260,261]. In the work of Schmidt et al. [262], interstitial solid solutions as well as TiN compounds were formed during nitrogen implantation, raising the micro-hardness from 3 to approximately 8 GPa at the near-surface region and strongly reducing the wear volume.

Budzynski et al. [263] confirmed that the improvement in the wear resistance after implantation is correlated with a decrease in friction coefficient and increase of hardness. In contrast to nitrogen ion implantation, plasma nitriding treatment uses an external voltage, applied between the furnace (anode) and the workpiece (cathode) for ionizing the nitriding gas, providing active nitrogen flux for surface modification [264,265]. Filemonowicz et al. [266] demonstrated better wear resistance of glow-discharge nitrided Ti-6Al-4V compared with an untreated control. This was attributed to the presence of nanocrystalline δ-TiN in the outermost sublayers, and top sublayers composed of Ti_2N and some Ti_2AlN phases. Thermal oxidation (TO) is a method to grow titanium oxide layer on Ti-6Al-4V via exposure to an oxygen-rich atmosphere [267], improving both tribological and corrosion properties. Dong et al. [257] observed an improvement in wear resistance of more than two orders of magnitude in TO-treated Ti-6Al-4V compared with untreated material due to tough and adherent rutile oxide film formation. Güleryüz et al. [259] carried out corrosion test in 5 M HCl acidic solution and found the most corrosion resistant surface were structures containing anatase and rutile TiO_2 formed after Ti-6Al-4V oxidation at 600°C for 60 hours.

Beta titanium alloys when alloyed with human-friendly β stabilizers such as niobium, molybdenum, and tantalum, have been reported with low elastic moduli at around 50 GPa [268]. The excellent biocompatibility of beta titanium alloys make them become attractive candidate materials for biomedical applications [18,182,212]. Moreover, the low elastic moduli can result in a decrease of “stress shielding” effect, which is regarded as the reason for implant

surrounding tissue resorption [4]. However, it has been found that the wear resistance of beta titanium alloys is generally inferior compared to the Co based alloys [269]. Only limited research has been performed to investigate the influence of surface hardening treatment on microstructural and comprehensive properties of the conventionally manufactured β-titanium alloys. Nakai et al. [270] observed that a titanium nitride layer along with acicular α precipitates below the top surface layer resulted in a significant surface hardness increase after performing gas nitriding of Ti-29Nb-13Ta-4.6Zr (TNTZ) alloy at 750–950°C. Akahori et al. [269] further reported that gas nitriding of the TNTZ alloy enhanced its wear resistance in Ringer's solution compared to solution treated samples. Additionally, they concluded that elongation reduction was due to diffusion of nitrogen into the centre of the specimen, which make the material matrix more brittle.

Considering factors such as less feedstock consumption in manufacturing components and customized complex-part fabrication, metal AM processes are an attractive option for producing high-end products compared to traditional manufacturing techniques [20,81]. Analysis of the available literature shows that there is no relevant research on surface hardening treatment of additively manufactured β-titanium alloys. In this work, static chemical etching (CE) in aqueous HF/HNO_3 solution was used as a pre-treatment for thermal oxidation (TO) to remove the surface adhered powder from Ti-34Nb-13Ta-5Zr-0.2O alloy (hereafter termed TNT5Zr-0.2O alloy) specimens manufactured by SLM. The surface morphology and microstructural changes in the TO processed surface were investigated by X-ray diffraction

and SEM-EDS characterisation. In addition, the wear resistance, plain/chemical-interfering fatigue properties, and *in vitro* cytocompatibility were compared before and after treatment. The results obtained in this manuscript provide one of the first evaluations of TO as a potential treatment to enhance the native wear and chemical-interfering fatigue properties of TNT5Zr-0.2O alloys for biomedical applications.

6.2 Materials and methods

6.2.1 Powder feedstock preparation

Pure element powder was used to blend the as-designed Ti-34Nb-13Ta-5Zr alloy (wt. %) for SLM *in-situ* alloying. Spherical Ti and Zr powders (TLS, Germany) with nominal particle size distribution of 15—83 μm and 10—45 μm, respectively were gas atomized in an argon atmosphere. Irregular-shaped Nb (Elite, UK), Ta powder (H.C. Starck, Germany) with an average particle size (D50) of 43.9 μm and 23.4 μm, respectively were manufactured through hydride-dehydride technique. The mass of each elemental powder was measured using a top pan balance (Kern EMB2000, 0.01g accuracy) inside a glove box (Saffron, UK) with an argon protective atmosphere (≤0.005% O_2). Then the powder was mixed for ten hours in a horizontal rotating drum (Kimber-Allen, UK).

6.2.2 Selective laser melting

An M2 Cusing SLM system (Concept Laser, GE Additive) was used to fabricate TNT5Zr samples on Ti-alloy substrates. This machine was equipped with a 400 W Yb:YAG fiber laser at a wavelength of 1064 nm with a spot size of approx. 63 μm. After a batch of SLM parameter

optimization, parameters for manufacturing specimens were: 300 W laser power, 500 mm/s scanning speed, 50 μm hatch spacing and 20 μm layer thickness. A chessboard scan strategy was employed with scan vectors rotated by 90º in adjacent 5 x 5 mm blocks and successive layers shifted by 1 mm in both X and Y direction. TNT5Zr-0.2O alloy was obtained when perform *in-situ* alloying TNT5Zr due to the deteriorated seal in SLM system. The oxygen level in the SLM-manufactured alloy was measured using inert gas fusion standard test [239]. Among those as-fabricated samples, fatigue specimens were designed with tangentially blending fillets between the uniform test section and the ends according to ASTM-E466-15 [220]. The fatigue specimens (75mm in length, 10 mm in height) were horizontally manufactured and then sliced into 1.5 mm-high dog-bone test-pieces by a wire electrical discharge machining (EDM, GF Machining Solutions).

6.2.3 Chemical etching and thermal oxidation treatment

Before chemical etching (CE), as-fabricated TNT5Zr-0.2O cuboidal and fatigue testing samples were cleaned in an ultrasonic cleaner using ethanol for 10 minutes. The CE procedure was designed for preparing a powder free surface as a pre-treatment, aiming to provide a better adhesion site when undergoing thermal oxidation (TO). The concentration of aqueous HF/HNO_3 bath for etching was selected based on the ASTM E407-07 [126], with consideration of the excellent corrosion resistance of this β-titanium alloy. Samples were statically immersed in etching solution (10% HF + 15% HNO_3 + 75% H_2O) for 16 hours with the immersion time optimised through scanning electron microscopy (SEM, TM3030, Hitachi) observation. Then samples were cleaned in distilled water for ten minutes to thoroughly remove the remnant acid.

A group of TO samples were prepared in an air containing muffle furnace at 1000℃ for 15, 30, 60 minutes. After oxidation, the cuboidal samples were cooled down in air after a step of 2 minute initial intermediate finance cooling (50℃/min). Subsequently the thickness of the oxide layer as well as its morphology were characterised by SEM (BSE imaging, TM3030, Hitachi). The designated TO treatment time (15 minutes) was decided by the results: satisfactory oxide film thickness at approximately 10 μm and oxide film without delamination from substrate. This finalized TO treatment was used for manufacturing the wear and plain/chemical interfering fatigue specimens.

6.2.4 Surface and microstructure analysis

For clarity purposes, surface treated β-titanium alloys will be referred to as CE and CE+TO treated TNT5Zr-0.2O alloys. The phase identification for both CE and CE+TO treated samples was performed by X-ray diffractometer (XRD) (AXRD, Proto) with Cu Kα radiation with spectra collected between 30-80° by a fixed parameter of 0.02° step size and a 2s time/step. Surface morphology after the two treatments was observed by SEM (SE imaging, XL-30, Philips). Mirror-like specimens were prepared using automatic grinding and polishing (Tegramin 30, Struers). A final polishing was undertaken using H_2O_2 activated OP-S colloidal silica suspension with an average particle size of 0.25 μm (Struers, UK). The mirror-like surfaces were prepared for the evaluation of cross-sectional oxide layer and matrix microstructure via SEM (SE imaging, JSF-7000F, JEOL)/EDS (Oxford Instruments).

6.2.5 Wear test

Wear test in reciprocating mode was used to investigate properties before and after TO treated TNT5Zr-0.2O alloy. The surfaces of samples were cleaned ultrasonically in ethanol for 10 minutes before testing. A wear test machine (TE79 multi-axis tribology machine) was performed at room temperature in air under dry sliding conditions using an Al_2O_3 ball of 10 mm in diameter as the counterface material. The wear test was carried out at a load of 10 N with a reciprocating sliding distance of 5 mm, for 1,000 cycles at a sliding speed of 10 mm/s. Wear tracks were evaluated using InfiniteFocus microscope (G5 plus, Alicona) and SEM (SE imaging, JSM-6060, JEOL).

6.2.6 Plain/chemical-interfering fatigue testing

The CE treated TNT5Zr-0.2O fatigue test-pieces without and with TO treatment were immersed in 3M HCl solution for 16 hours in order to form a different level of chemically induced notches. Then fatigue properties after HCl immersion specimens were evaluated. At the same time, S-N curves of CE and CE+TO treated TNT5Zr-0.2O fatigue test-pieces (without HCl immersion) were collected as benchmark conditions to investigate the fatigue strength difference. Fatigue testing with rectangular central cross-section specimens were performed perpendicular to the build direction. Axial high cycle fatigue testing was carried out on a fatigue testing machine (Vibraphore Resonant), using magnetic resonance to deliver low constant amplitude, load ratio of R = 0.1, and high frequency (usually in a range of 50-100Hz, decided by the specimen geometry and stiffness). The testing with a maximum stress (up to 250 MPa) inside the elastic region was performed at room temperature.

6.2.7 In vitro cytocompatibility study

MC3T3-E1 preosteoblasts were used to evaluate the cytocompatibility of CE and CE+TO treated TNT5Zr-0.2O alloys. All specimens were ultrasonically cleaned in pure ethanol for 10 minutes and then autoclaved at 121°C for 90 minutes before cell seeding. The samples were placed in 24-well plates and were seeded at a density of 2 x 10^4 cells/cm^2 onto the surface treated substrates and tissue culture plastic as a positive control. The samples were then incubated at 37 °C in a humidified atmosphere with 5% CO_2. Dulbecco's Modified Eagle Medium (10% fetal bovine serum, 12% L-Glutamine and 1% penicillin/streptomycin) was used during the cytotoxicity tests, while this was substituted with DMEM modified with 50 μg/ml ascorbic acid, 10 mM β-glycerophosphate and 10-7M dexamethasone (Sigma Aldrich) with further changes in media every two to three days for the mineralisation assays. Cell viability was evaluated by Alamar blue staining after 1, 3 and 7 days of culture using a spectrophotometer (Spark, Tecan) at a wavelength of 560 nm excitation and 590 nm emission. A Calcein-AM and propidium iodide (PI) solution was selected to evaluate the viability of MC3T3-E1 cell after 7 days of culture on the surface treated substrates. Stained cells were visualized using a microscope imaging system (EVOS M5000, Thermo Scientific). All involved data were recorded as the mean ± standard deviation (SD), and we performed the same as-shown Analysis of Variance (ANOVA).

To assess if the treatment had any effect on early mineralisation alkaline phosphatase activity was quantified after 7 and 14 days of seeding using a SensoLyte® pNPP Alkaline Phosphatase

kit (Anaspec, UK). Total calcium deposits after 28 days of culture were also analysed using Alizarin red S (ARS) staining. Surfaces were fixed in 0.4% Paraformaldehyde for 30 min, rinsed in 10mM DPBS and stained with a 2% ARS in phosphate buffered saline (PBS) for 20 minutes. Excess staining was removed by washing 3 times in PBS and ARS was retained by immersion in a 10% cetylpyridinium chloride (CPC) solution for 1 hour. For both mineralisation assays, absorbance was measured with a TECAN Spark plate reader (Tecan Trading AG, Switzerland) using 405 nm and 570 nm wavelengths for ALP and ARS, respectively.

6.3 Results

6.3.1 Microstructural characteristics of thermal oxide layer and matrix

Fig. 6-1A shows the XRD spectra obtained from the surface of TNT5Zr-0.2O alloy after CE, along with the surface and matrix of the alloy after CE+TO. A profile with main β-Ti peaks alongside low intensity α-Ti is observed in the alloy after CE. For comparison, nearly the same XRD profile is found in the matrix of the alloy after CE+TO. In the XRD pattern of the CE+TO treated surface, a mixture of main phases of TiO_2 (rutile), Nb_2O_5, and minor phases of Ta_2O_5, ZrO was detected. The matrix microstructure of the alloy after CE+TO treatment is shown in Fig. 6-1B. Equiaxed β grains were obtained and alpha precipitates (black arrows) were heterogeneously nucleated at grain boundaries when the alloy was cooled from 1000°C for the TO treatment. The surface morphology of chemical etched TNT5Zr-0.2O alloy (Fig. 6-1C) clearly revealed the removal of surface adhered particles, which is regarded as a typical feature

formed on the external surface of SLM components [87,271]. In addition, uneven groove-shaped structures and cracks were visible after long-time intercrystalline corrosion with 3M HCl solution. Surface examination of the CE+TO treated sample (Fig. 6-1D) illustrated micro-scale oxide islands grown on the outward CE treated surface in a manner of relatively dense oxide agglomeration and growth.

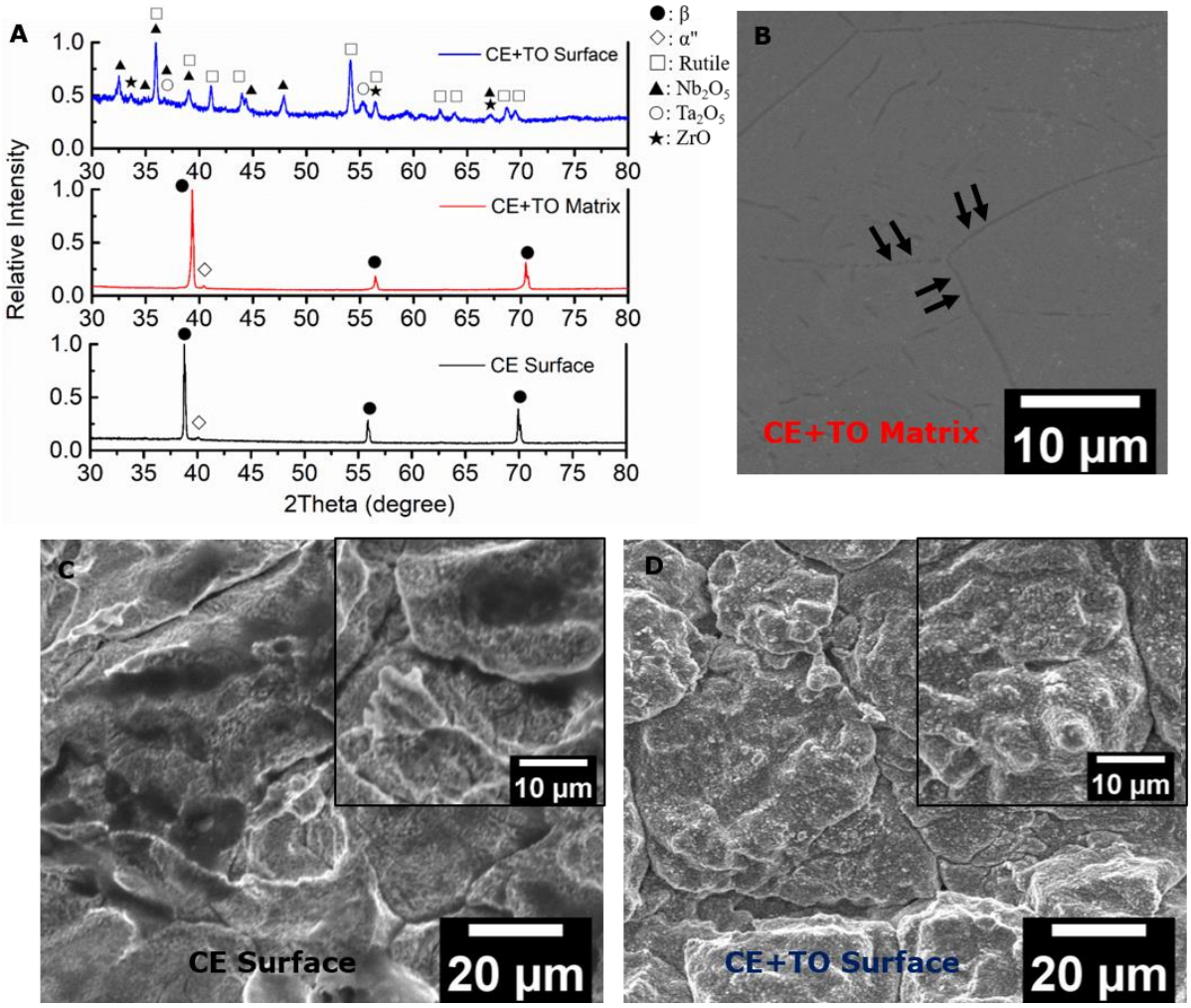

Fig. 6-1. (A) X-ray diffraction patterns obtained from the surface of CE+TO, CE treated TNT5Zr-0.2O alloys, and the matrix of CE+TO treated alloy. (B) The microstructure of the matrix for the CE+TO treated alloy and surface morphology of (C) CE treated, and (D) CE+TO treated TNT5Zr-0.2O alloys.

Fig. 6-2A presents the cross-sectional SEM-EDS results of SLM-manufactured TNT5Zr-0.2O

alloy after CE+TO. In the SEM micrograph, an adherent layer of metallic oxides with a thickness of approx. 13 μm was formed on the top surface, followed by a region with fine acicular precipitates on the inner side, and a mixture of equiaxed grains and grain boundary alpha particles in the innermost region. EDS mapping detected the presence of Ti, Nb, Ta, Zr, O elements in the three distinct zones. It clearly revealed that the content of metallic elements (Ti, Nb, Ta, Zr) in the oxide layer is lower than the material's matrix. Additionally, it showcased a decrease in oxygen concentration from the outer to the inner side. Fig. 6-2B shows the localized SEM-EDS results in the inner zone marked in Fig. 6-2A. Grain boundary and transgranular acicular alpha precipitates at submicron scale were observed via SEM. The two types of phases showed a common elemental distribution: both are enriched in Ti, leaned in Nb, Ta, Zr element, and O is uniformly distributed. Further elemental analysis corresponding to an EDS line scan analysis of the cross-section of CE+TO treated TNT5Zr-0.2O alloy is shown in Fig. 6-2C. The results showed a homogenous distribution of Ti, Nb, Ta, Zr, O element inside the equiaxed beta grain matrix, with a substantial increase of Ti and slight increase of O through the grain boundary. There appeared to be a significant precipitation of acicular α-phase, and obvious Ti and β-stabilizer (Nb, Ta) element fluctuation in the β-depleted zone. The line scan results showed that the content of all metallic elements (Ti, Nb, Ta, Zr) in the outermost layer is lower than the counterparts of the base material. In contrast, there was no distinct fluctuation of oxygen content in the inner diffusion regions until a remarkable increase was observed in the oxide layer.

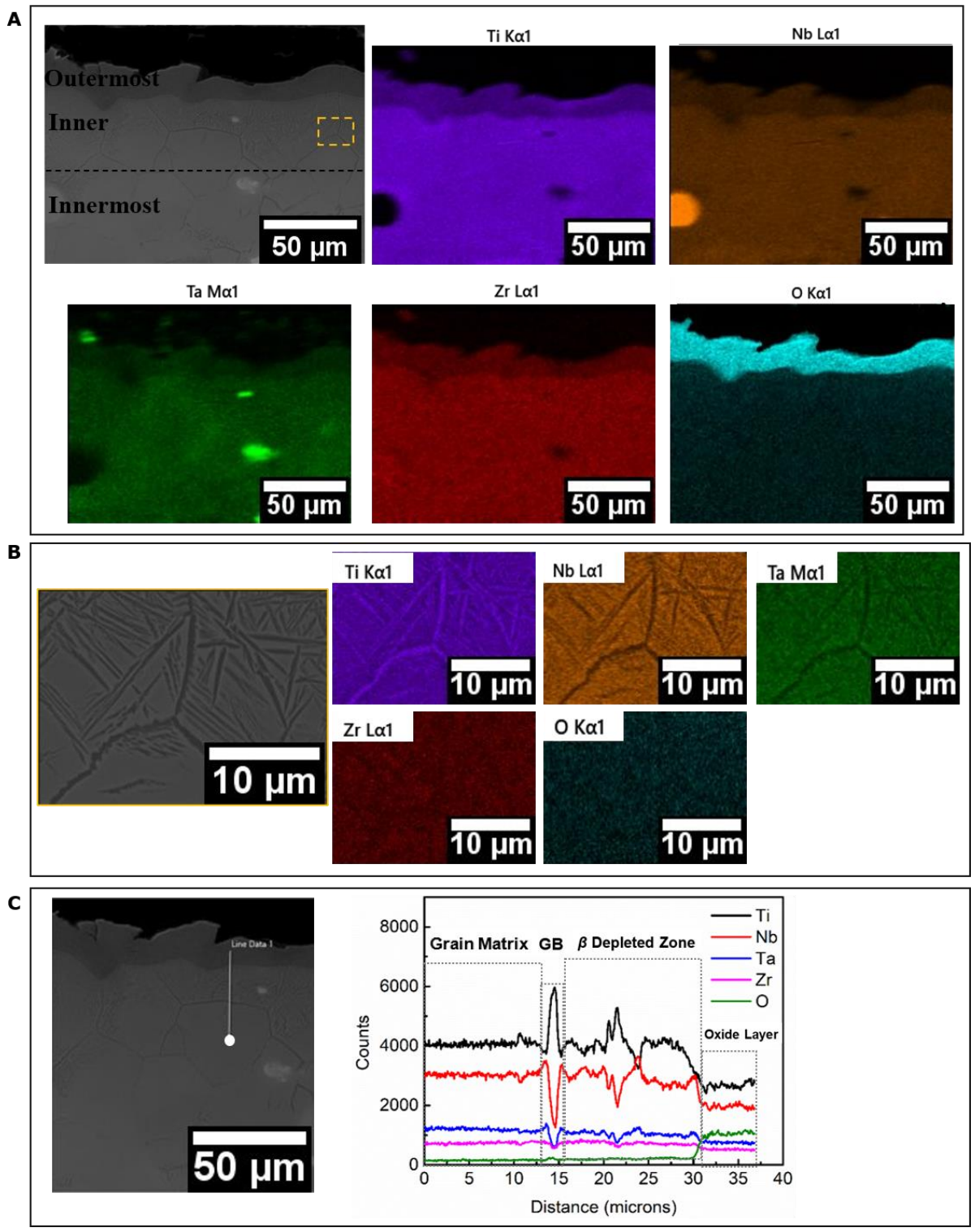

Fig. 6-2. (A) Cross-sectional SEM micrograph after CE+TO treatment including EDS element mapping for Ti, Nb, Ta, Zr, and O. (B) SEM-EDS mapping obtained from the dotted line rectangle region in Fig. 6-2A. (C) SEM image and the corresponding EDS line scan elemental profiles. Notes: 1. Bright spots in Fig. 6-2A belong to the un-melted particles (Nb, Ta). 2. White dot in Fig. 6-2C is the starting point of scan trace.

6.3.2 Wear properties

Fig. 6-3(A-B) presents the 2D profilograms of the wear tracks obtained from CE and CE+TO treated TNT5Zr-0.2O alloys under a load of 10 N. The wear scar of the CE treated sample was shallow and wide, and the wear track of the CE+TO treated sample was at the same depth level but much narrower after 1,000 cycles of friction tests. SEM micrographs in Fig. 6-3C show that the worn surface in the sample without TO treatment were dominated by adhesive wear with narrow and smooth ploughing grooves in the sliding direction. On the other hand, the wear morphology on the CE+TO (Fig. 6-3D) sample is relatively smooth in contact areas between the treated alloy and the Al_2O_3 ball. Peeling of brittle metallic oxides occurs in some uneven groove-shaped sites induced by chemical etching treatment. The corresponding high magnification SEM micrograph reveals the existence of wear debris with extremely fine oxide particles found in the XRD analysis (Fig. 6-1A).

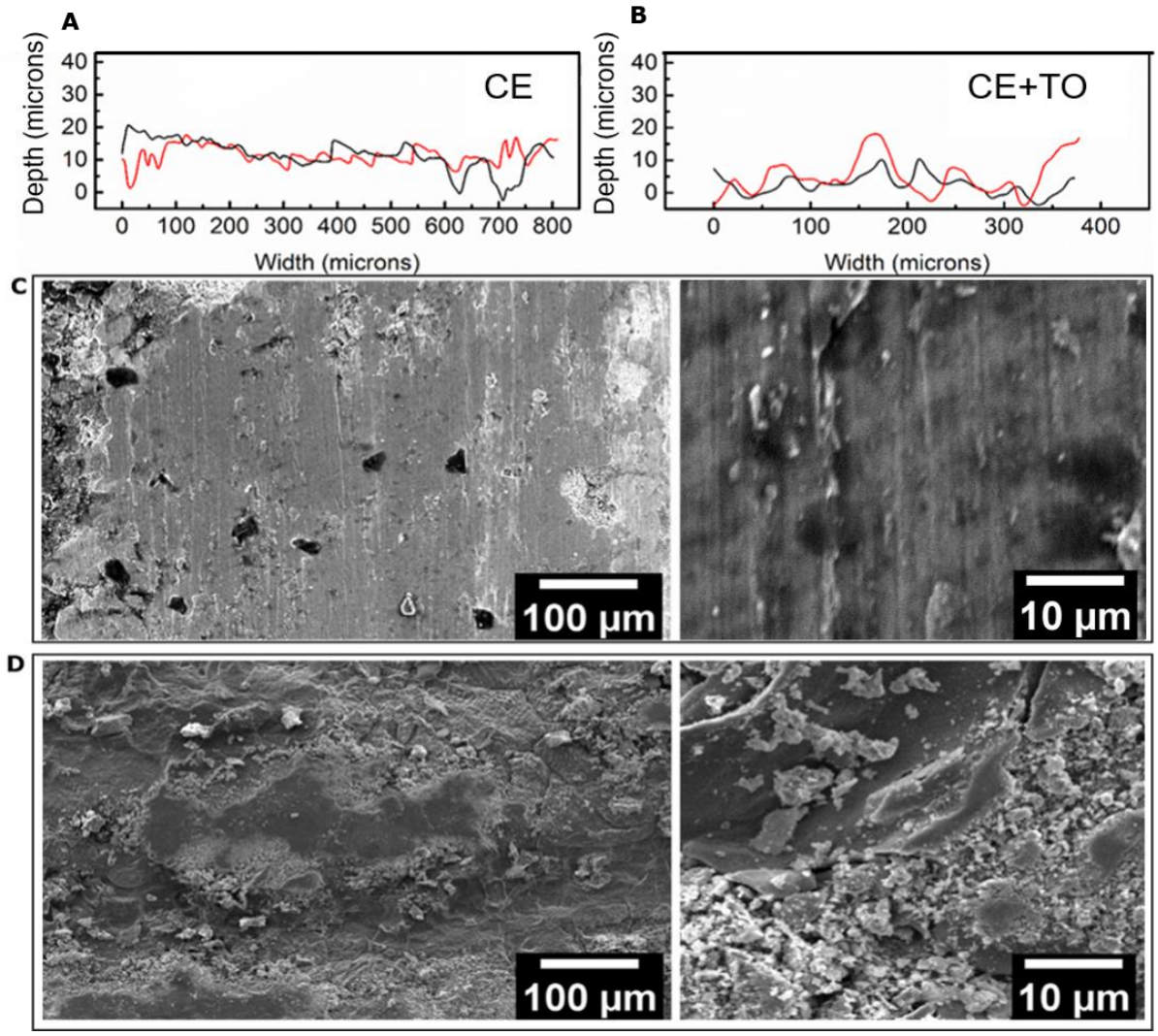

Fig. 6-3. Two-dimensional wear track profiles of (A) CE and (B) CE+TO treated TNT5Zr-0.2O alloys under a load of 10 N. Low and high magnification SEM micrographs showing wear morphology of worn surface of (C) CE and (D) CE+TO treated specimens.

6.3.3 Plain/chemical-interfering fatigue study

Fig. 6-4A shows stress-life (S-N) curves of CE, and CE+TO treated TNT5Zr-0.2O alloys when conduct plain and chemical-interfering fatigue testing. The 10^7 cycle HCF plain fatigue strength of CE and CE+TO treated alloys were 150 MPa and 60 MPa, respectively. In order to better mimic the mechanical behaviour of the biomedical alloys after long-term implantation, aggressive 3M HCl solution was used for immersion to form chemically induced notches. The

chemical-interfering fatigue S-N curves showed a slight decrease in fatigue limit (130 MPa) in the CE treated alloy, while a similar fatigue limit was maintained for the CE+TO treated alloy (70 MPa). Fig. 6-4B shows that crack initiation in all the analysed alloys started at the surface. After observation of the morphologies from the former two surfaces, cracks seem to be preferentially initiated on the chemically induced notches generated after the immersion with aqueous HF/HNO_3 or additional 3M HCl solution. No morphology difference of the latter two surfaces was seen due to the oxide film protection against the aggressive 3M HCl solution. Detailed SEM examination of fatigue fracture surfaces of the CE treated alloy (Fig. 6-4C) indicated that microcracks are faceted with cleavage-like appearance near the initiation zone. Slip band cracks combining appreciable striations can be observed after extensive micro cracks join, and reach a macroscopic size in the crack propagation zone, and intergranular and transgranular mixed fracture appears in the final fracture zone. By comparison, chemical-interfering fatigue fracture surfaces of the CE treated alloy (Fig. 6-4D) showed slightly larger fracture facets caused by intense shear in stage I portion, followed by slip band cracks with wider arrays of ridges during fast crack growth in stage II portion, and similar fracture features in the final fracture portion. For the crack initiation regions of fatigue and chemical-interfering fracture surfaces of the CE+TO treated alloy, the transgranular cleavage of β phase with coarse facet morphology was found to be the main mechanism of fracture (Fig. 6-4(E-F)). Images of crack propagation regions obtained from the two fatigue tests exhibit predominantly crack-path features and the typical chevron patterns are observed in Fig. 6-4E (middle). The two SEM fractographs in the zone of final fast fracture appear to be a mixture of intergranular facets

covered by fine dimples and transgranular fractures.

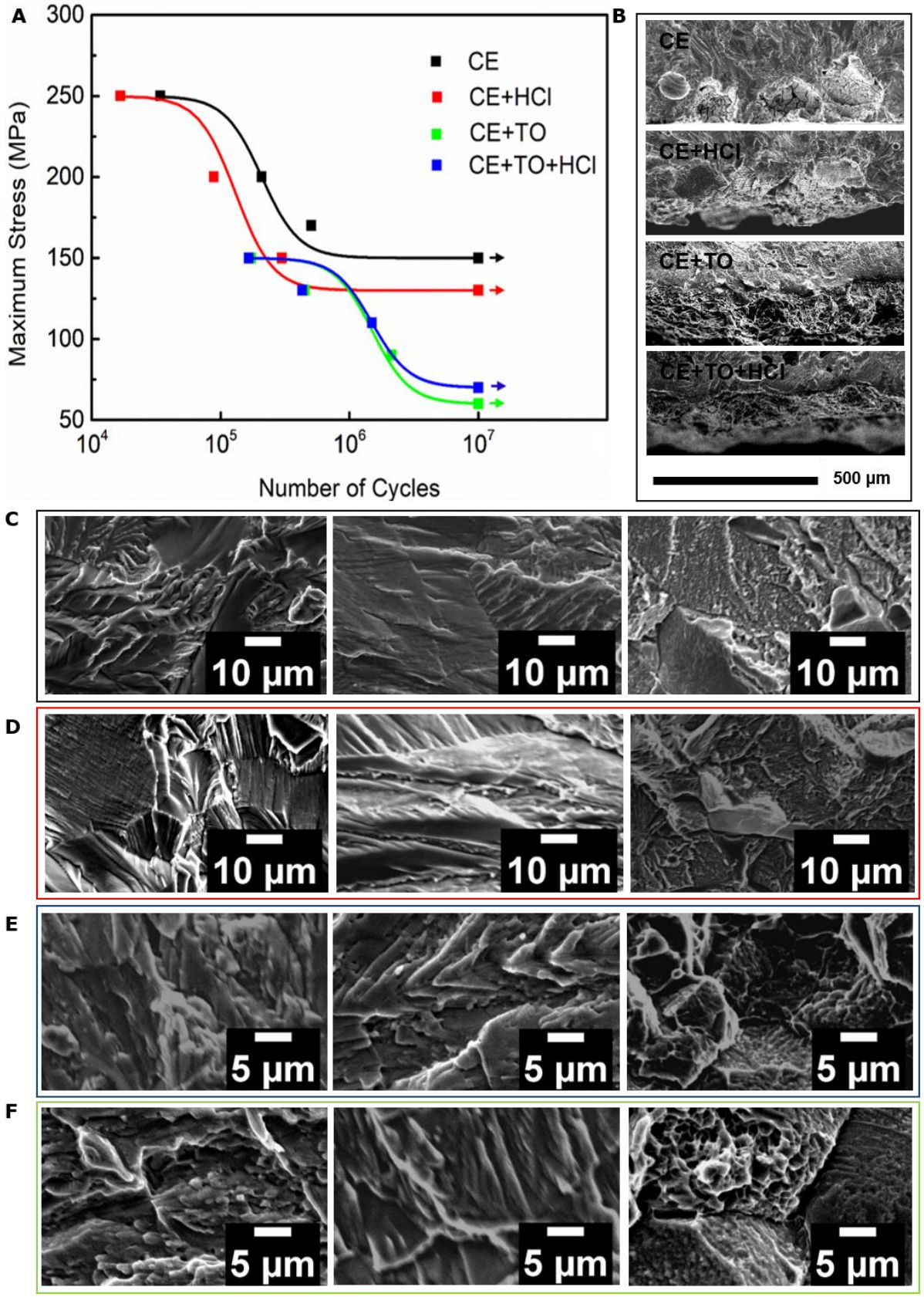

Fig. 6-4. (A) S-N curves of the two alloys collected using plain and chemical-interfering fatigue testing. (B) Fatigue fractures illustrating fatigue source of the four specimens. (C) Fatigue fracture of crack initiation (left), crack propagation (middle), and final fast fracture (right) area of CE treated specimen. (D) Chemical-interfering fatigue fractures of the three zones of CE treated specimen. (E) Plain and (F) chemical-interfering fatigue fractures of the corresponding three zones of CE+TO treated specimen. Note: both fatigue fracture surfaces of CE and CE+TO treated specimens were obtained from the maximum stress of 200 MPa and 150 MPa accordingly.

6.3.4 Cytocompatibility of specimens before and after thermal oxidation

Fig. 6-5A shows MC3T3-E1 preosteoblast cell proliferation assessed by Alamar blue assay after 1, 3, and 7 days of incubation with surface treated and the control substrates. Similar metabolic activity was observed compared with the control group for the selected time intervals. In contrast, the metabolic activity of cells cultured on the surface treated substrates slightly declined as culture time increased from day 1 to day 7. In addition, no statistically significant ($p < 0.05$) difference in Alamar blue reduction could be observed between CE and CE+TO treated samples on day 1, 3, and day 7. Live-dead fluorescence micrographs obtained after 7-days of culture (Fig. 6-5B) revealed that both CE and CE+TO treated surfaces exhibit an almost confluent cell growth with negligible number of dead cells, which appeared to show no substantial difference compared against the plastic control group.

Fig. 6-5C shows the normalized ALP activities after 7 and 14 days of culture on different substrates. According to the 7-day ALP measurements, the amount of recovered enzyme was significantly ($p < 0.05$) smaller for the CE+TO surface than both control and CE treated surfaces. On day 14, the ALP activity presented on the control group was significantly higher

than the values measured in surface treated groups. Additionally, an ALP activity drop in CE group could be observed between the two studied time frames, while a slight increase in CE+TO group was observed. ARS staining was used for examination of long-term (28 days) mineralisation on the aforementioned substrates (Fig. 6-5D). The normalized ARS results indicated a slight increase in calcium deposits in metallic substrates compared to the control substrate, although only statistical significance ($p<0.05$) was found between CE treated and the control surface.

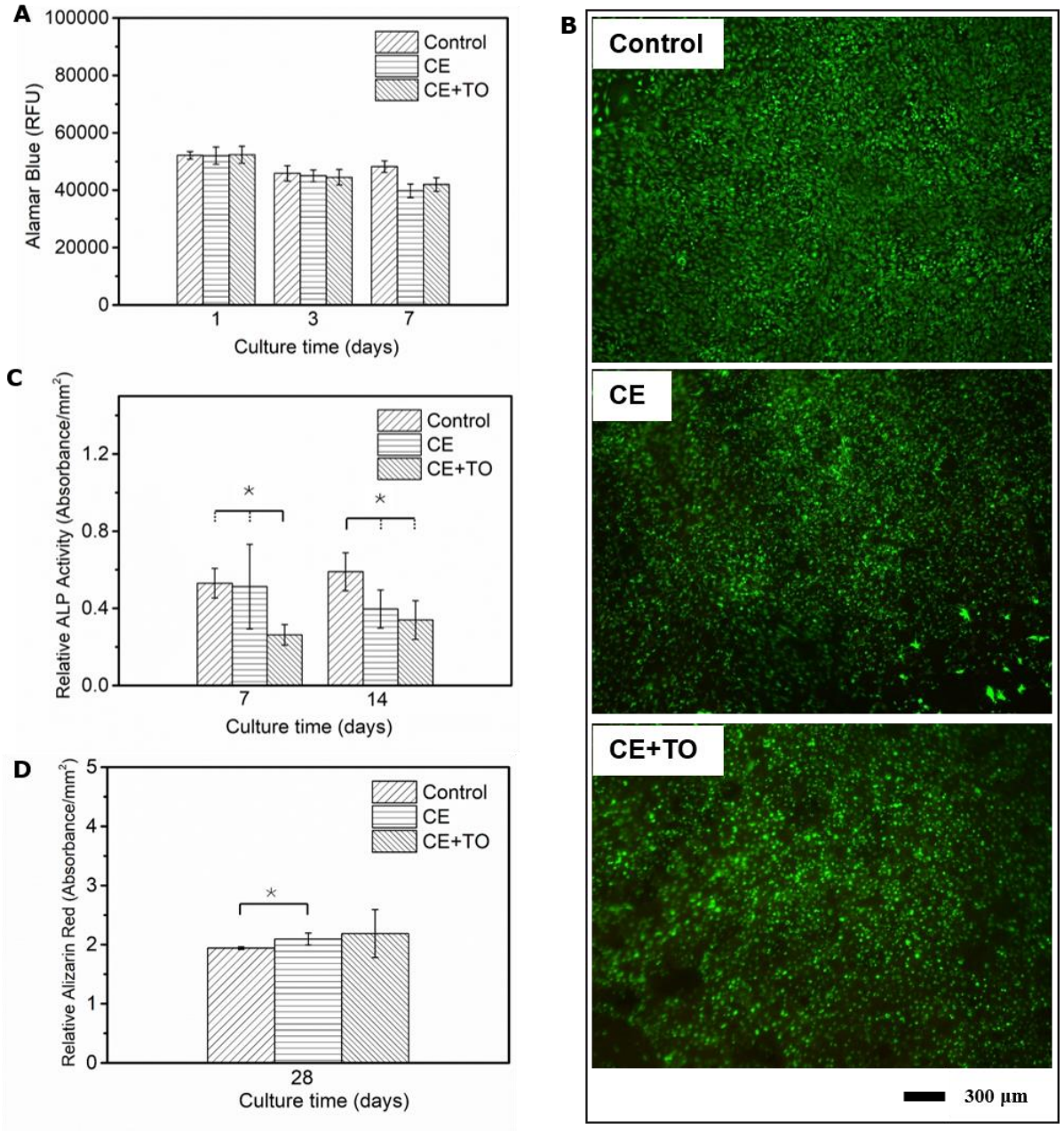

Fig. 6-5. (A) Metabolic activity of MC3T3-E1 preosteoblast cells seeded on different substrates, including (B) Live/dead epifluorescence images after 7 days culture. (C) Levels of relative ALP activity measured after different incubation periods and (D) Relative Alizarin red S staining absorbance values at 28 days post-seeding. Where signifies p value < 0.05 (where more than one pair is illustrated, the comparison between the group indicated with a solid line and any other groups indicated with dash lines).

6.4 Discussion

6.4.1 Microstructural evolution and chemical kinetics in thermal oxidation

After the β-titanium alloy is exposed to an oxidizing atmosphere at elevated temperatures, the following processes simultaneously take place: (i) various oxidation reactions at the oxide/atmosphere interface, (ii) oxygen atom penetration through the oxide film to the matrix, and (iii) diffusion of metal (Ti, Nb, Ta, Zr) ions from the matrix to the oxide film. It is clear that the prerequisite for the oxidation reaction occurrence is the standard Gibbs free energy change of the reaction must be negative [272]. As these reactions at 1000℃ are spontaneous and relatively rapid, a variety of thermodynamically stable metallic oxides (e.g., rutile, Nb_2O_5, ZrO) were formed and detected in the top layer (Fig. 6-1A) after TO. As mentioned by Kofstad et al. [273], temperature-dependent rate laws of oxidation have been presented associated with CP titanium TO work. A cubic and parabolic rate law is found in the temperature region 300-600℃ and 600-850℃ respectively, while the oxidation behaviour above 850℃ is unclear.

In the oxygen penetration process, oxygen can diffuse through the compact outermost layer after a consumption for oxide generation at high temperature [274]. Similar to the findings from Shamblen et al. [275], oxygen further diffuses inward from the oxide-metal interface into the base alloy due to the high solid solubility of interstitial oxygen in the constituent phases (e.g., α or β) of TNT5Zr-0.2O alloy. The assumption of oxygen penetration was verified by SEM-EDX mapping (Fig. 6-2(A, C)) demonstrated by the presence of oxygen in different cross-sectional regions. At the same time, metal (Ti, Nb, Ta, Zr) ions are capable to transfer

through the matrix to the oxide film, which was also confirmed by the EDX line scan results in Fig. 6-2C. As a consequence of beta stabilising element (Nb, Ta) migration into the oxide layer, the beta stabilizer-lean grain boundary and transgranular acicular alpha precipitates were nucleated in the β-depleted zone upon cooling, as shown in Fig. 6-2B. Moreover, it seems that no substantial oxygen intensity difference exists between alpha precipitates and matrix beta phase. Other studies [269,276] indicate that the precipitation of the needle-like α phase could also be observed neighbouring the outermost layer in nitriding or TO treated β-titanium alloys. Unlike our assertion of acicular alpha mainly caused by the beta stabilizer migration, Akahori et al. [269] and Park et al. [276] considered that the interstitial atoms (e.g., oxygen, nitrogen) thoroughly stabilize the α–phase until at least saturated. After the comparison with processes of oxygen penetration and metal ions diffusion, it appears to be a common temperature-dependent feature. The influence of temperature on the rates of oxygen and metal ion diffusion can both be interpreted in terms of the Arrhenius equation [277].

$$D_T = D_o e^{-Q/RT} \tag{6-1}$$

where D_T is the diffusion coefficient at temperature T, R is the gas constant, D_0 is the frequency factor, and Q is the activation energy. As the depth of detectable oxygen is higher than the metallic element fluctuation counterpart shown in Fig. 6-2C, the inward oxygen penetration is probably facilitated at a higher rate than the outward metallic ion diffusion from the matrix, also reported by Kofstad et al. [273].

6.4.2 Tribological behaviour in air

Adhesive wear occurred when Al_2O_3 counterface slide on the CE treated TNT5Zr-0.2O alloy

under unlubricated sliding conditions (Fig. 6-3C). When each surface slides against each other, plastic deformation results in mechanical damage to the β-titanium alloy at the asperity level [278]. As described by Dong et al. [257,279], titanium and its alloys possess a high ductility, which gives rise to strong adhesion during wear. A growth of continuous junction takes place during motion, followed by junction shearing and rupture within the weaker asperities, associated with the detachment of fragments. It can be found that the wear scar of TO treated alloy is narrower than the CE treated sample, as shown in Fig. 6-3(A-D). Unlike the wear mechanism of CE treated sample, delaminated metallic oxide debris particles are generated during the period when contact between the rubbing surfaces takes place, which is consistent with frictional features of nickel-base alloys at elevated temperatures reported by Jiang et al. [280]. They presented that the considerable number of fine oxides form a relatively higher resistance when contacting between the two sliding surfaces. In addition, these agglomerated clusters of particles are subjected to compression and compaction during further sliding, and sinter to form a smooth and durable surface layer [278]. Therefore, the oxide layer formed by thermal oxidation can reduce metal-to-metal contact and decrease the wear loss. In addition, Dong et al. [257] have shown that adhesive wear in TO treated titanium alloys can be effectively eliminated due to the metallurgical nature of the contact materials (ceramic, metal). They also mentioned the rutile oxide layer possesses a much lower ratio of modulus to hardness than the untreated titanium alloy, which promotes elastic deformation and induces a reduction in adhesion wear.

6.4.3 Plain/chemical-interfering fatigue properties

As measured in plain fatigue testing, the fatigue strength of CE treated TNT5Zr-0.2O alloy is 1.5 times higher than the value of CE+TO treated alloy (Fig. 6-4A). It can be observed that deterioration in fatigue limit of titanium alloys using gas/plasma nitriding or thermal oxidation techniques have been previously reported [281–283]. These results suggest that the top compound layer and the solid solution hardened layer below the surface are considered to be strongly related to the decrease in fatigue strength [284]. The explanation for the differences of fatigue characteristics before & after TO in TNT5Zr-0.2O alloy is most likely relevant to crack initiation sites and microstructural factors.

The notches induced by aggressive aqueous HF/HNO_3 immersion are regarded as the preferable crack initiation sites in CE treated TNT5Zr-0.2O alloy (Fig. 6-4B) because the cyclic stress at the notch boundary is higher than the remote sites. Similar to the observations from the near fracture surface by Long et al. [285], slip is initiated in the notch neighbouring grains as the resolved shearing stress reaches the critical value [286]. Additionally, fatigue cracks in CE treated alloy also initiate at the intrusions, which are regarded as the result of slip on one set of planes during cycles subjected to different cyclic stresses under tension [229]. The reason for intergranular and transgranular mixed fracture surfaces in final fracture zone (Fig. 6-4C) highly lies in oxygen pick-up of the β-titanium alloy. Yu et al. [246] reported strong solution-hardening as a result of oxygen atoms producing a pinning effect on screw dislocations in pure α-Ti. Thus, dislocations move via a local cross slip that creates immobile dislocation segments.

As high localized strain occur along grain boundaries without enough pinning by precipitates, intergranular fracture surfaces appear because preferential nucleation, growth, and coalescence of micro-voids takes place along grain boundaries [252]. By comparison, fatigue cracks start on the outermost surface where valleys of the CE+TO treated alloy surface might act as stress concentrators. Similar to the work of Li et al. [282], as the Young's moduli of the metallic oxides and inward acicular alpha precipitates are much higher than the matrix material, multiple premature fatigue cracks might develop in the complex compounded region. Moreover, other studies [287–289] have suggested that nucleated cracks mainly occur across colonies in the acicular alpha structure obtained in various near α-titanium alloys, and another type of stage I crack at a relatively large size initiates along α/β interfaces. Unlike the cracking found in CE treated alloy, these microstructural related fatigue cracking processes probably appear when passing through the β-depleted zone in CE+TO treated alloy. It presents chevron marks in the region of crack propagation (Fig. 6-4E), which shows the fact that many small cracks have initiated from a common location then joined together, and pointed towards the slow-growth zone [290]. As pointed by Vasudévan et al. [291], the presence of non-deformable intergranular precipitates (obtained from TO) that differ in their elastic moduli with respect to the neighbouring beta grain matrix will form stress and strain incompatibilities, which seems to cause grain boundaries to become crack paths in final fracture zone.

As a result of the superior corrosion resistance of the various metallic oxides, most of the protective passive thin film seemed to remain relatively stable during the entire 3M HCl

immersion period. However, the area of notches generated after the immersion with aqueous HF/HNO_3 is likely enlarged (Fig. 6-4B). Since titanium alloys are moderately resistant to chemical attacks, a dissolution of the passive layer may occur in high concentrations of hydrochloric acid solutions [292]. Therefore, the fatigue limit of CE treated TNT5Zr-0.2O alloy obtained in chemical-interfering fatigue testing (130 MPa) is slightly lower than the counterpart in plain fatigue testing (150 MPa). Fractographic features (Fig. 6-4D) in the three typical zones of chemical-interfering fatigue are like the features seen in Fig. 6-4C. In contrast, it has been widely reported that the thermally oxidised surface layers are highly inert and effective in protecting titanium and its alloys against aggressive environments [259,267]. This could be the reason behind the limited deterioration of fatigue strength after the aggressive acid treatment with similar fracture characteristics in the corresponding regions (Fig. 6-4(E-F)).

6.4.4 Cell response of CE and CE+TO treated samples

The osteoblast cell viability results show that no significant ($p < 0.05$) Alamar blue reduction and similar epifluorescence coverage between the two surface treated TNT5Zr-0.2O alloys and the control substrate (Fig. 6-5(A-B)). The limited influence in metabolic activity of the CE treated alloy can be likely explained by the excellent corrosion behaviour and negligible released ions from the thermodynamic stable film containing various metallic oxides (e.g., TiO_2, Nb_2O_5, Ta_2O_5) in simulated body fluid [17,219,293]. Considering the presence of a thick bioinert oxide film in CE+TO treated alloy, it will not impair the excellent cell viability due to the function of protective oxides as mentioned before.

The 7-day normalized ALP activity collected from the CE+TO group was significantly ($p < 0.05$) smaller than the control and CE counterparts. After prolonging the culture time to 14 days, ALP content of cells seeded on the CE+TO substrate was slightly lower than that of the CE treated sample (Fig. 6-5C). These findings appear to imply that chemically etched surfaces had greater ALP-specific activity than CE+TO surface, suggesting that differentiation of MC3T3 cells takes place earlier in CE surface. A former *in-vitro* study on Ti-6Al-4V with different surface roughness demonstrated that ALP-specific activity was similarly expressed with differences becoming smaller between rough and smooth titanium groups for increased time intervals [294]. Other work [295] has suggested that the roughened surfaces possesses higher surface energy, thus it probably forms more surface hydroxyl groups resulting in more favourable attachment and differentiation of the osteoblasts. Additionally, as shown by Wang et al. [296], the hollow structure observed on CE treated surfaces, and particle-like structure observed on CE+TO treated surfaces at high magnification (Fig. 6-1(C-D)) may introduce different surface wettability, which is believed as another important factor to determine cell surface interactions. Moreover, excellent long-term mineralisation was observed with extracellular calcium deposits remaining similar between groups (Fig. 6-5D). Similar to the superior osteogenic activity found in the two surface treated groups, a prior research reported that acid etched CP titanium implants achieved an improved osteointegration after implantation in rabbit femur [297]. In addition, an enhancement of *in vivo* bone regeneration and mineralisation has been observed in CP titanium after 6 hour TO [296]. The investigators all mentioned the surface characteristics may attributed to the enhanced osteointegration, however,

the detailed complex cell surface interactions are still unknown.

6.5 Conclusions

This chapter investigated the surface morphology, and microstructural changes in thermal oxidation (TO) processed TNT5Zr-0.2O alloy. In addition, the wear, plain/chemical-interfering fatigue properties, and osteoblast cell response to the alloy before & after TO treatment were also investigated. The main conclusions of this work are as follow:

1 Chemical etching (CE) as a pre-treatment for thermal oxidation successfully removed surface adhered powders from the SLM-manufactured TNT5Zr-0.2O alloy. A mixture of main phases of TiO_2 (rutile), Nb_2O_5, and minor phases of Ta_2O_5, ZrO was obtained in the oxide layer after the subsequent TO treatment. Additionally, beta stabilizer-lean acicular alpha precipitates were observed in the β-depleted zone is mainly due to these elements (Nb, Ta) migration into the oxide layer.

2 Higher wear resistance was obtained after TO treatment as suggested by the wider wear track of the CE treated sample. Adhesive wear features with ploughing grooves were found in the former alloy; while the wear scar was relatively smooth in real contact areas between the CE+TO treated sample and the ceramic counterpart, with brittle metallic oxides peeling.

3 The HCl plain fatigue strength of CE and CE+TO treated TNT5Zr-0.2O alloy were 150 MPa and 60 MPa, respectively. The higher Young's moduli of the metallic oxides and precipitates in the inner zone caused multiple premature fatigue cracks to develop in the

compounded region deteriorating the fatigue properties. Moreover, a slight decrease in fatigue limit (130 MPa) was observed in the CE treated alloy, while a same level fatigue limit (70 MPa) was retained in CE+TO treated alloy after chemical-interfering fatigue testing. Though the thick oxide layer brings a positive effect against the aggressive HCl solution, the described TO should be cautiously exploited as a fatigue limit deterioration caused by the complex compound system.

4 No statistically significant ($p < 0.05$) difference in metabolic activity between the CE and CE+TO treated groups was observed with 7-day live-dead fluorescence micrographs indicating similar cell confluence negligible damaged cell membranes. Early and late mineralisation assays revealed similar levels of 14-day ALP activity, and 28-day mineral deposits formed on the two biocompatible TNT5Zr-0.2O alloy surfaces. These indicate the potential use of these surface treatments for additively manufactured medical devices.

7 COMPRESSION BEHAVIOUR, DEFORMATION MECHANISM, AND PREOSTEOBLAST CELL RESPONSE OF SELECTIVE LASER MELTED TI-34NB-13TA-5Zr-0.2O SCAFFOLDS WITH TRIPLY PERIODIC MINIMAL SURFACES FOR LOAD-BEARING APPLICATIONS

Paper Status: ready for submission

Weihuan Kong[a*], Luke N. Carter[b], Victor M. Villapun[b], Kenny Man[b], Sophie Cox[b*], Moataz M. Attallah[a*], **Compression Behaviour, Deformation Mechanism, and Preosteoblast Cell Response of Selective Laser Melted Ti-34Nb-13Ta-5Zr-0.2O Scaffolds with Triply Periodic Minimal Surfaces for Load-bearing Implant Applications**, Additive Manufacturing.

Authorship contribution statement

Weihuan Kong conceived and designed the experiment, performed the experiment, interpreted the data, and wrote the manuscript. Victor M. Villapun and Kenny Man assisted with the collection of biocompatibility results. Luke N. Carter and Sophie Cox assisted with revising the manuscript. Moataz M. Attallah involved resources and methodology.

a. School of Metallurgy and Materials, University of Birmingham, Edgbaston, B15 2TT, UK
b. School of Chemical Engineering, University of Birmingham, Edgbaston, B15 2TT, UK

Abstract

Three-dimensional (3D) porous structures have been receiving more attention for orthopedic implant development mainly due to their lower elastic moduli to prevent aseptic loosening, however, their low yield strengths may increase failure risk in load-bearing implants. Here, Ti-34Nb-13Ta-5Zr-0.2O scaffolds infilled with sheet-based triply periodic minimal surface (TPMS) unit cells, namely diamond, gyroid, splitP, were manufactured with different design porosity (50%, 35%, 18%) via selective laser melting (SLM). Quasi-static compression tests showed that low elastic moduli (10~22 GPa) and high yield strengths (358~1045 MPa) were obtained in the varying TPMS cylindrical specimens, with both elastic modulus and yield strength increasing with density in each type of scaffolds. Metabolic activity and epifluorescence microscopy revealed lower osteoblastic cell adhesion and proliferation in denser scaffolds, possibly resulting from lower available area and limited transport into the inner pores. A good balance of high strength and low modulus is obtained in low-porosity TNT5Zr-0.2O TPMS scaffold implants, which potentially work well in human body and provides long service time.

7.1 Introduction

Human joints are prone to degenerative and inflammatory diseases that result in severe pain in elderly people [54]. Over centuries, degenerated joints have been preferentially replaced with dense high-strength metallic prostheses, but the bone is weakened after implant's long-term service due to "stress shielding" effect [4,16]. At present, three-dimensional (3D) lattice

structures have been receiving more attention for orthopedic implant development. Available studies show that a highly porous and interconnected structure can enhance cell migration, proliferation, differentiation and nutrient-waste transportation [298,299].

It is well known that porous structures can reduce the stiffness of biomaterials and narrow the elastic moduli mismatch between them and human cortical bone (10~30 GPa) [16], but the trade-off is a lower level of mechanical strength. To understand this correlation, numerous researchers have studied different selective laser melting (SLM) manufactured structural configurations in Ti-6Al-4V which due to its high strength, corrosion resistance and biocompatibility is considered the gold standard in medical devices. Traxel et al. [300] designed unique Ti-6Al-4V lattice structures with 53-65% theoretical porosity based on natural crystal structures: hexagonal closed packed (HCP) and body-centred cubic (BCC). Through modification of design factors including strut sizes (diameter of 0.4-0.7 mm), unit cells (HCP, BCC) and symmetric thin walls (thickness of 0.125-0.25 mm), the highest-performance column-layered lattice structures obtained yield strengths (511.1 ± 125.5 MPa) but still high elastic moduli (76.5 ± 20.5 GPa) under compression. In addition, Alomar et al. [301] manufactured Ti-6Al-4V lattice structures with circular-based constituent cells and assessed their compression behaviour. They found that the circular lattice structures provided low elastic moduli (1~3 GPa) but failed under low load (≤ 100 MPa) in a layer-wise crushing manner without exhibiting any plateau region. Some researchers also have evaluated the *in vitro* osseointegration responses of Ti-6Al-4V porous structures. Hollander et al. [302] investigated

human osteoblast cell ingrowth into different pore diameter (500~1000 μm) lattices after 14 days of culture, and observed a circular-shaped growth pattern along the rims of the largest pores (1000 μm) via scanning electron microscopy (SEM) imaging. In addition, high magnification micrographs revealed a partially confluent layer in the region of smallest pore size (200 μm) in gradient mesh structure due to a less extent of cell-to-material interaction than the counterpart in larger pore sites (400~600 μm) [105]. Except for the evaluation of comprehensive properties of Ti-6Al-4V lattice structures, some bio-morphic architectures recently have been gaining interest as additive manufacturing (AM) technologies have enabled the fabrication of these complex architectures with good precision [303].

Triply periodic minimal surfaces (TPMS) are the structures that locally minimize surface area for a given boundary such that the mean curvature at each point on the surface is zero [304,305]. The geometry possesses a continuous through space, which is divided into pore and non-pore by a non-intersecting two-sided surface [306]. Al-Ketan et al. [307] evaluated the mechanical behaviour of sheet-based and beam-based TPMS micro-architected polymeric materials via experimental and numerical methods. They concluded that TPMS sheet-based microlattices exhibit superior mechanical properties because they undergo more stretching-dominated deformation and less plastic strain localization compared with TPMS beam-based microlattices. Also, the surface area to volume ratio of the sheet-networks is higher than strut-based structures, which makes the material is more distributed within unit cells and more effective in carrying the applied load.

Alongside variations in design, microstructural and chemical modifications to the base alloys can enhance the mechanical and biological behaviour of medical implants. In titanium based alloys, the low modulus [15] and excellent biocompatibility [18] of beta titanium has led to a preference of these systems for bone replacement applications. However, limited research has been conducted to fabricate porous β titanium alloys with an elastic modulus matching natural bone. Ti-24Nb-4Zr-8Sn (wt. %) porous meshes (75% design porosity) with rhombic dodecahedron unit cell were manufactured via electron beam melting (EBM) and SLM by Liu et al. [22]. Uniaxial compression testing results showed promising low elastic moduli (0.9~1.4 GPa), nevertheless, both as-fabricated samples exhibited low compressive strength (<55 MPa) and extremely reduced fatigue strength (~ 6 MPa). Similarly, Luo et al. [308] successfully manufactured scaffolds with different unit cells but similar design porosity levels using Ti-30Nb-5Ta-8Zr (wt. %) via SLM. Their results indicated comparable yield strengths (13~67 MPa) to those previously reported by Liu et al. [22]. However, those high design porosity structures probably cannot satisfy the requirements of mechanical properties for load-bearing orthopaedic implants during long-term service.

In this study, the authors SLM processed and heat-treated different design porosity Ti-34Nb-13Ta-5Zr-0.2O (wt. %) scaffolds via a selection of three sheet-based TPMS surfaces including diamond, gyroid, splitP. Young's modulus and compressive offset stress were determined by performing quasi-static compression tests. In addition, *in vitro* tests showed the viability of osteoblast cells seeded on the representative gyroid lattices.

7.2 Materials and methods

7.2.1 Design of TPMS sheet-based scaffolds

Cylindrical compression test specimen geometries with overall dimensions (10 mm in diameter, 15 mm in height) were generated by a specialised software (nTopology 2.20). Using the TPMS module, the lattice structures, namely diamond, gyroid, and splitP were applied to these geometries. Table 7-1 lists the detailed parameters for designing the scaffolds using different unit cells (Fig. 7-1A). Fig. 7-1(B-D) shows the porosity-dependent and height-dependent cross-sectional CAD geometries of these prototypes. Geometries of the cylindrical specimens were exported in *.stl format, and the volume of scaffolds was determined by mesh volume in a commercial software (Magics V24.0, Materialise). Note that design porosity of each lattice was calculated by dividing the mesh volume by the overall cylinder volume.

Table 7-1

Design parameters of unit cells for forming various TMPS sheet-based scaffolds.

Scaffold type	Design porosity (%)	Unit cell dimension (mm)	Unit cell bias length (mm)	Unit cell wall thickness (mm)
Diamond 50	50	4 × 4 × 4	1.5	3.0
Diamond 35	35	4 × 4 × 4	1.5	3.5
Diamond 18	18	4 × 4 × 4	1.5	4.1
Gyroid 50	50	4 × 4 × 4	1.5	3.0
Gyroid 35	35	4 × 4 × 4	1.5	3.6
Gyroid 18	18	4 × 4 × 4	1.5	4.3
SplitP 50	50	4 × 4 × 4	1.5	3.1
SplitP 35	35	4 × 4 × 4	1.5	3.5
SplitP 18	18	4 × 4 × 4	1.5	4.0

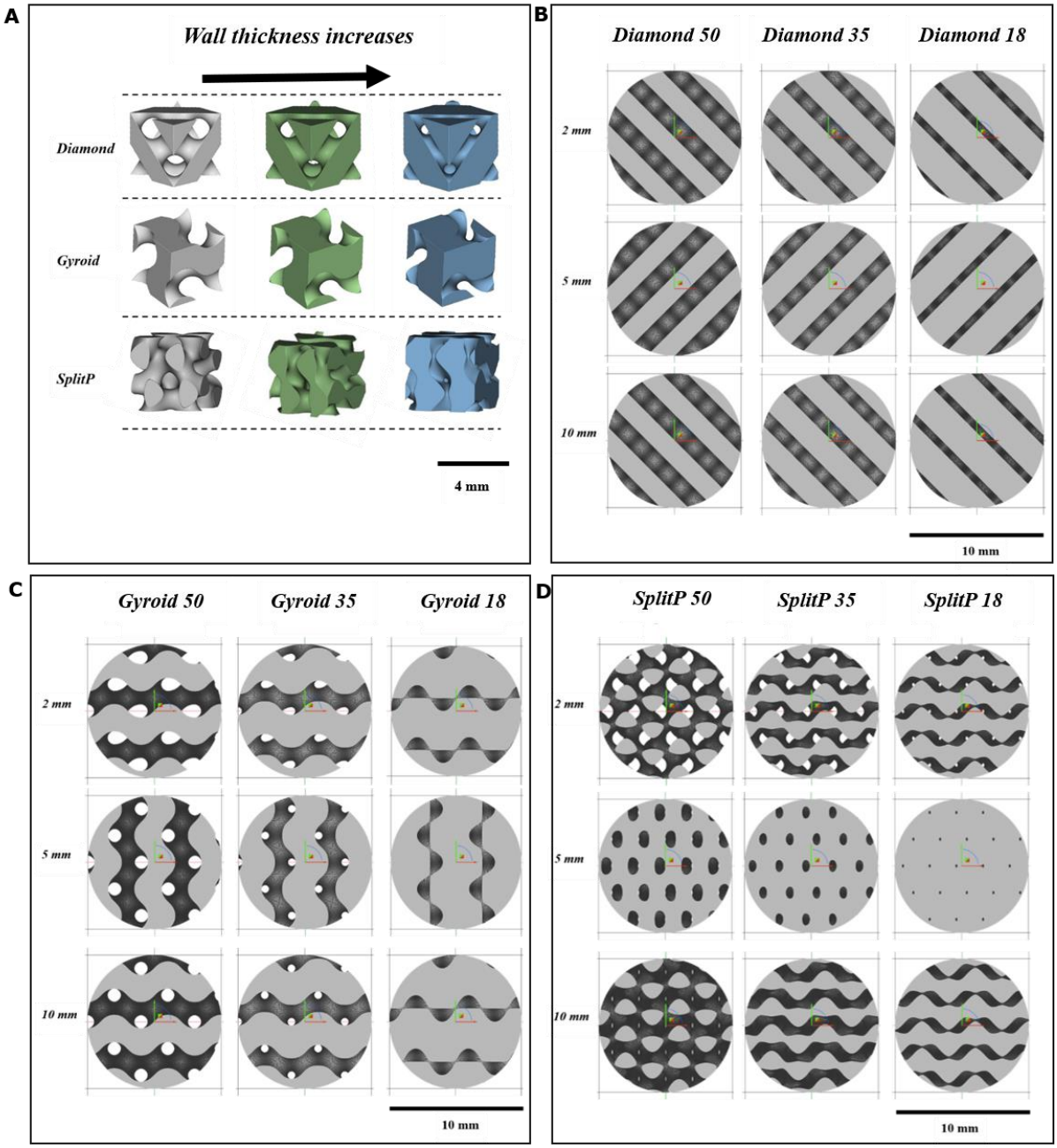

Fig. 7-1. (A) Schematic of unit cells used for the as-fabricated scaffolds. Top view images illustrating (B) diamond, (C) gyroid, and (D) splitP lattice structures for compression testing, captured from 2 mm, 5mm, 10 mm in height.

7.2.2 Powder feedstock preparation

Elemental powders were used to blend the as-designed Ti-34Nb-13Ta-5Zr alloy (TNT5Zr,

wt. %) for SLM *in-situ* alloying. Spherical Ti and Zr powders (TLS) were gas atomized with nominal particle size distribution of 15~83 μm and 10~45 μm, respectively. Irregular-shaped Nb (Elite), Ta powder (H.C. Starck) with an average particle size (D50) of 43.9 μm and 23.4 μm, respectively were manufactured through hydride-dehydride technique. The mass of each elemental powder was measured using a top pan balance (Kern EMB2000, 0.01g accuracy) inside a glove box (Saffron) with an argon protective atmosphere (≤0.005% O_2) and mixed for ten hours in a horizontal rotating drum (Kimber-Allen).

7.2.3 Selective laser melting and vacuum heat treatment

An M2 Cusing SLM system (Concept Laser, GE Additive) was used to fabricate TNT5Zr samples on a Ti-alloy substrate. The machine was equipped with a 400 W Yb:YAG fibre laser at a wavelength of 1064 nm with a spot size of ~ 63 μm. The authors conducted a SLM parameter optimisation, which screened from laser power (240–300 W), scan speed (400–1000 mm/s), and hatch spacing (35–65 μm). According to the results of defects (un-melted particles, keyholes) in the region away from TPMS pores quantified using the same SEM imaging like before [219], the processing conditions for the current study were selected: 300 W laser power, 500 mm/s scanning speed, 50 μm hatch spacing and 20 μm layer thickness. A chessboard scan strategy was employed with scan vectors rotated by 90º in adjacent 5 x 5 mm blocks and successive layers shifted by 1 mm in both X and Y direction.

Oxygen content in the SLM-manufactured alloy was measured using inert gas fusion standard test [239], yielding a final composition of Ti-34Nb-13Ta-5Zr-0.2O alloy (hereafter named as

TNT5Zr-0.2O). A vacuum furnace (TPF 60, TAV Engineering) was used to tune the microstructure of SLM-manufactured TNT5Zr-0.2O alloy. The heat treatment (HT) parameters were: 3 hours dwell at 1000℃, followed by intermediate cooling rate (100℃/min). For clarity purposes, SLM+ HT treated β titanium alloy will be referred to SLM+HTed TNT5Zr-0.2O alloy.

7.2.4 Build porosity density measurement and microstructure

Archimedes method was used to determine the manufactured material density of the post-processed TNT5Zr-0.2O lattice structures. The mass of each part was measured in air and ethanol using a top pan balance and density kit (Ohaus ax223) with a measuring accuracy of ± 0.1 mg. The volume of each scaffold was calculated by dividing the mass value in air by the measured material density; build porosity of each lattice was calculated by dividing the volume of each scaffold by the solid cylinder one. Measurements were repeated three times and reported with mean values and standard deviations of lattice build porosity.

The specimens with cross-sectional struts and pores were sectioned from the bottom position of TPMS sheet-based scaffolds using wire electron discharge machining (EDM, GF Machining Solutions). Specimens were prepared using automatic grinding and polishing (Tegramin 30, Struers). A final polishing to a mirror finish was undertaken using a H_2O_2 activated OP-S colloidal silica suspension with an average particle size of 0.25 μm (Struers). The struts and pores in each scaffold were observed by SEM (BSE imaging, TM3000, Hitachi). To reveal the microstructure, the polished SLM+HTed TNT5Zr-0.2O surface was etched with Kroll's reagent

(2% HF + 6% HNO_3 + 92% H_2O) following SEM analysis (SE imaging, XL-30, Philips).

7.2.5 Compression testing

All heat-treated TNT5Zr-0.2O scaffolds were studied under uniaxial compression using an universal testing machine (ESH Testing 200), according to ISO 13314 [309]. Compression testing of the lattice samples was performed at a constant crosshead speed of 2 mm/min using a 100 kN load cell for two samples per condition analysed at room temperature. The strain was obtained as the ratio of crosshead displacement to the initial specimen height while the stress was calculated as the compressive force divided by the initial cross-sectional area without consideration of surface area from the TPMS pores. From this curve, the quasi-elastic gradient, regarded as the slope of the compressive stress-strain curve in the linear elastic region, and the compressive offset stress determined as the stress at a plastic strain of 0.2%, which can be used as an alternative for compressive yield strength [309] were calculated. For a comparison, compression testing of the SLM+HTed TNT5Zr-0.2O solid material was also performed.

7.2.6 In vitro experiments

MC3T3-E1 preosteoblasts were used to evaluate the cell response of representative TNT5Zr-0.2O lattices, namely Gyroid 50, Gyroid 35, Gyroid 18. Lattice samples (3.5 mm in diameter, 2 mm in height) were ultrasonically cleaned in pure ethanol for 10 minutes and then autoclaved at 121°C for 90 minutes before cell seeding. The lattices were placed in 1.5mL Eppendorfs with punctured caps covered with a filter (AeraSeal^{TM}, Sigma-Aldrich) to enable gas exchange. The samples were statically seeded at a density of 2 x 10^5 cells/mL for 1 hour followed by

dynamical culturing overnight at 8 rpm 37 °C with 5% CO_2. Dulbecco's Modified Eagle Medium (10% foetal bovine serum, 12% L-Glutamine and 1% penicillin/streptomycin) was continuously used for the cytotoxicity tests with changes performed every two to three days. Cell viability was evaluated by Alamar blue staining after 1, 3 and 7 days of culture, using a spectrophotometer (Spark, Tecan) at a wavelength of 560 nm excitation and 590 nm emission. A Calcein-AM and propidium iodide (PI) solution was used to analyse the viability of MC3T3-E1 cells after 7 days of culture into varying porosity scaffolds. Stained cells were visualized using a microscope imaging system (EVOS M5000, Thermo Scientific). All involved data was recorded as the mean ± standard deviation (SD). Analysis of Variance (ANOVA) and two-tailed t-tests were performed, with a p value <0.05 considered as being statistically significant.

7.3 Results

7.3.1 Morphological and microstructural characterisation

Fig. 7-2A shows macrographs of the corresponding SLM+HIPed compression testing specimens from different views (top, side, and bottom). The build porosity (Fig. 7-2B) varied between 16.7% and 38.6% in diamond models while the values in the gyroid and splitP models were in the range of 15.9%~34.8% and 17.7%~41.4%. In addition, variations between design and build porosity became the smallest for the densest scaffolds achieving values of 1.3%, 2.1% and 0.3% for the Diamond 18, Gyroid 18 and SplitP 18, respectively. A representative microstructure of the SLM+HTed TNT5Zr-0.2O alloy is shown in Fig. 7-2C. Equiaxed β grains were obtained and nucleation of discrete alpha precipitates occurred at grain boundaries when

the alloy was intermediately cooled from the HT temperature (1000℃), which are into agreement with our previous results [310].

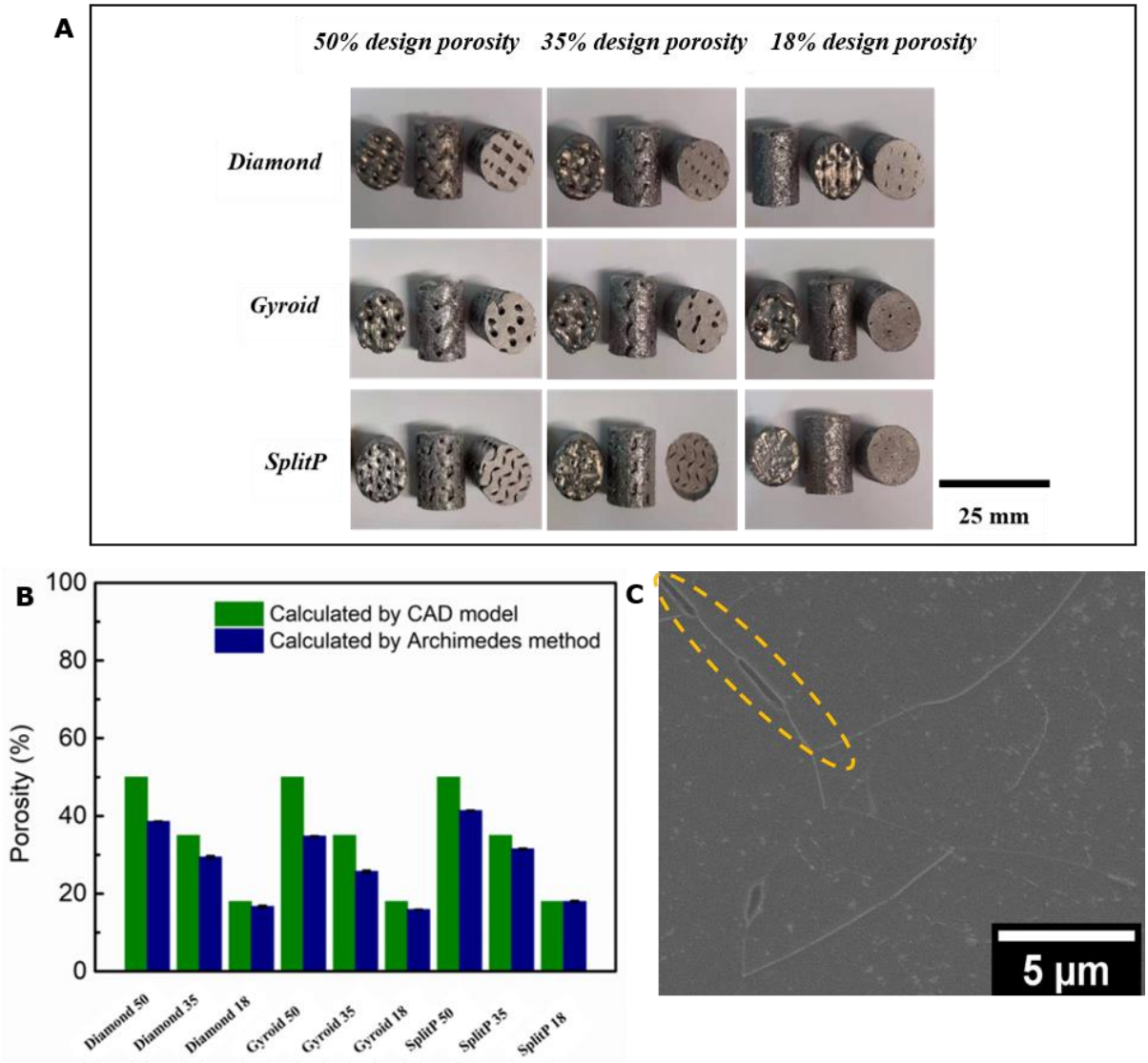

Fig. 7-2. (A) Macrographs illustrating diamond, gyroid, splitP lattices with different porosity. (B) Bar chart showing the porosity obtained by Archimedes method compared to the corresponding design values. (C) The microstructure of SLM+HTed TNT5Zr-0.2O alloy captured by SEM (SE imaging), grain boundary precipitates were pointed by dashed line.

SEM images of the bottom of the lattices with different porosity levels are presented in Fig. 7-3, clearly indicating the decrease in pore size as the wall thickness of scaffolds increases. In

addition, the SLM and material induced defects including un-melted niobium, tantalum particles (yellow arrows) mainly occurred in the region (pointed by round-cornered rectangle) close to the TPMS pores in each SLM manufactured scaffold. By comparison, keyholes (red arrows) seem to preferably distribute in the regions away from the TPMS pores in these components.

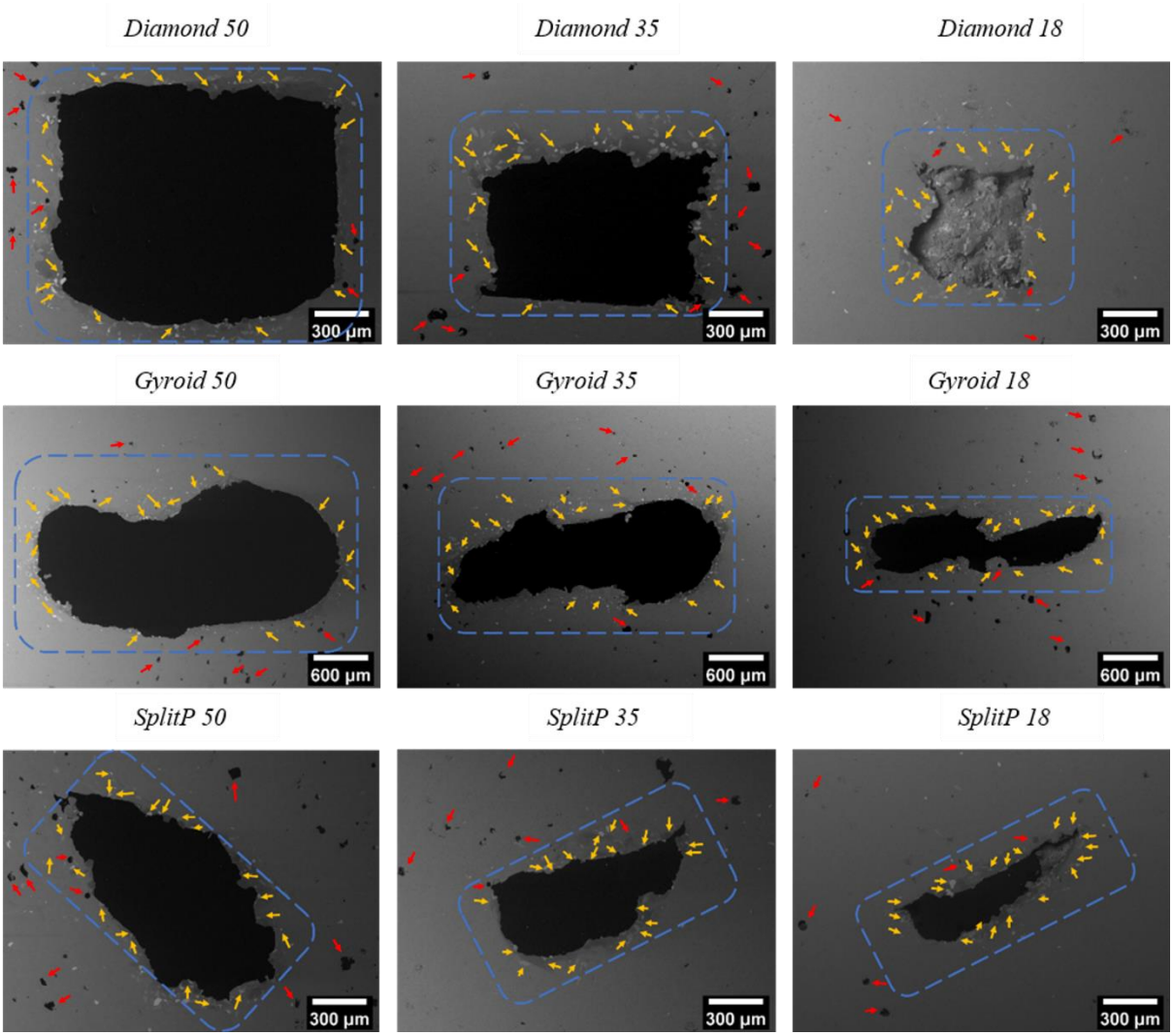

Fig. 7-3. Representative micrographs (BSE imaging) taken from the bottom of the compression testing specimens showing the TPMS pores with defects, either un-melted elements or keyholes, highlights with yellow and red arrows, respectively.

7.3.2 Lattices performance under compression testing

The quasi-static stress-strain curves of the various unit-cell infilled specimens are shown in Fig. 7-4(A-C). Compressive stress-strain curves reveal that all scaffolds experienced initial linear-elastic deformation, followed by a rapid rise in stress under loading. After a certain amount of scaffold compaction, the stress began to rise steeply caused by the densification under loading with stiffness more akin to the solid material. In all case considered, it is clearly observed that the elastoplastic transition takes place earlier in the high porosity samples. It is noted that every curve ended at 1275 MPa where the universal testing machine reached the maximum load (100 kN). Fig. 7-4D depicts the compression properties including quasi-elastic gradients and compressive offset stress for the nine cellular structures. The mean values show that low quasi-elastic gradients (12~18 GPa) and high compressive offset stress (395~995 MPa) were obtained in the varying porosity diamond scaffolds. Similarly, quasi-elastic gradients were in the range of 10 to 18 GPa and compressive offset stress were between 358 and 974 MPa in gyroid lattices. Data revealed that the splitP scaffolds obtained a higher level of compressive offset stress (618~1045 MPa) and quasi-elastic gradient (15~22 GPa).

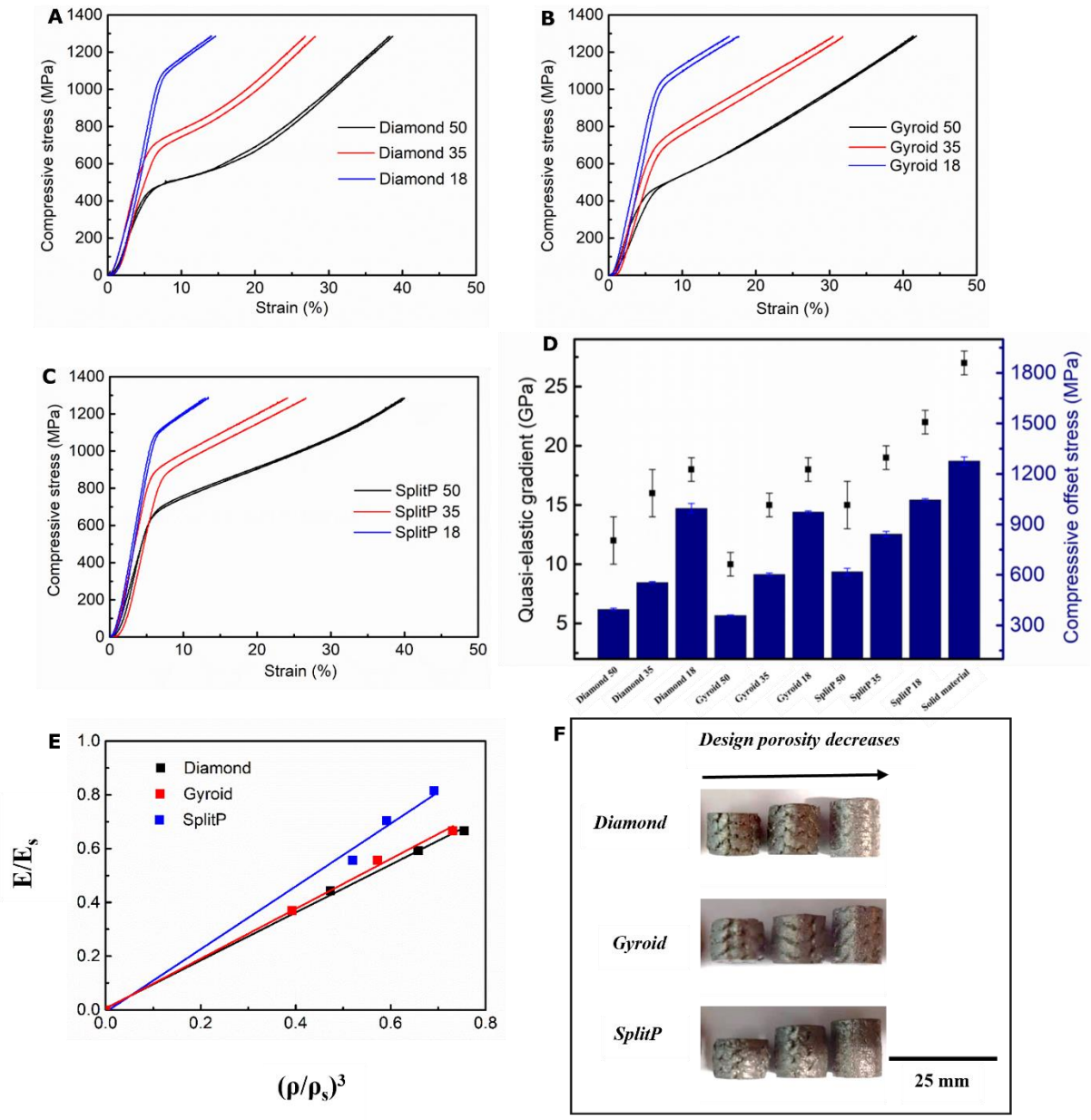

Fig. 7-4. Compressive stress-strain curves of the SLM+HTed (A) diamond, (B) gyroid and (C) splitP specimens with 50%, 35%, 18% design porosity (D)Bar chart showing the mechanical properties of the tested lattice and solid structures. (E) Gibson-Ashby model presents the relative modulus as a linear dependence of the $(\rho/\rho_s)^3$ value. (F) Macrographs of different unit cell infilled scaffolds after compression.

Fig. 7-3E presents the linear relationships of relative modulus and relative as-built density cubed in three in these TPMS scaffold arrays. The corresponding relative modulus was the experimental modulus from each lattice structure divided by the solid counterpart. According

to the classic Gibson & Ashby closed cell model [91], the experimental results were well fitted to a first degree polynomial with varying proportional coefficients (0.89, 0.93, 1.17) and R^2 values (0.997, 0.996 and 0.990) for diamond, gyroid and splitP, respectively. This implies that the relationship between relative modulus and relative as-built density differs in various TPMS sheet-based porous structures. Fig. 7-4F demonstrates the macrographs of the nine scaffolds after quasi-elastic compression testing. No holistic breaking is found in each test-piece when it suffered a continuous deformation up to the maximum load.

7.3.3 In vitro cell behaviour

MC3T3-E1 preosteoblast cell viability results after 1, 3, and 7 days of incubation within varying porosity gyroid scaffolds are shown in Fig. 7-5A. Similar metabolic activity levels were observed after 1 and 3 days of culture for Gyroid 50 and Gyroid 35, however, Gyroid 18 presented significantly lower metabolism. After 7 days of culturing, a slight drop in metabolic activity was observed in the three groups albeit Gyroid 50 maintained a significantly higher activity between groups. Live-dead fluorescence images (Fig. 7-5B) viewed from the side of each localized pore site apparently show that preosteoblasts are preferably spread and grow in the pores rather than in the external surface. Additionally, more dead cells (red contrast) can be observed in the pores of Gyroid 18 than in the other two groups.

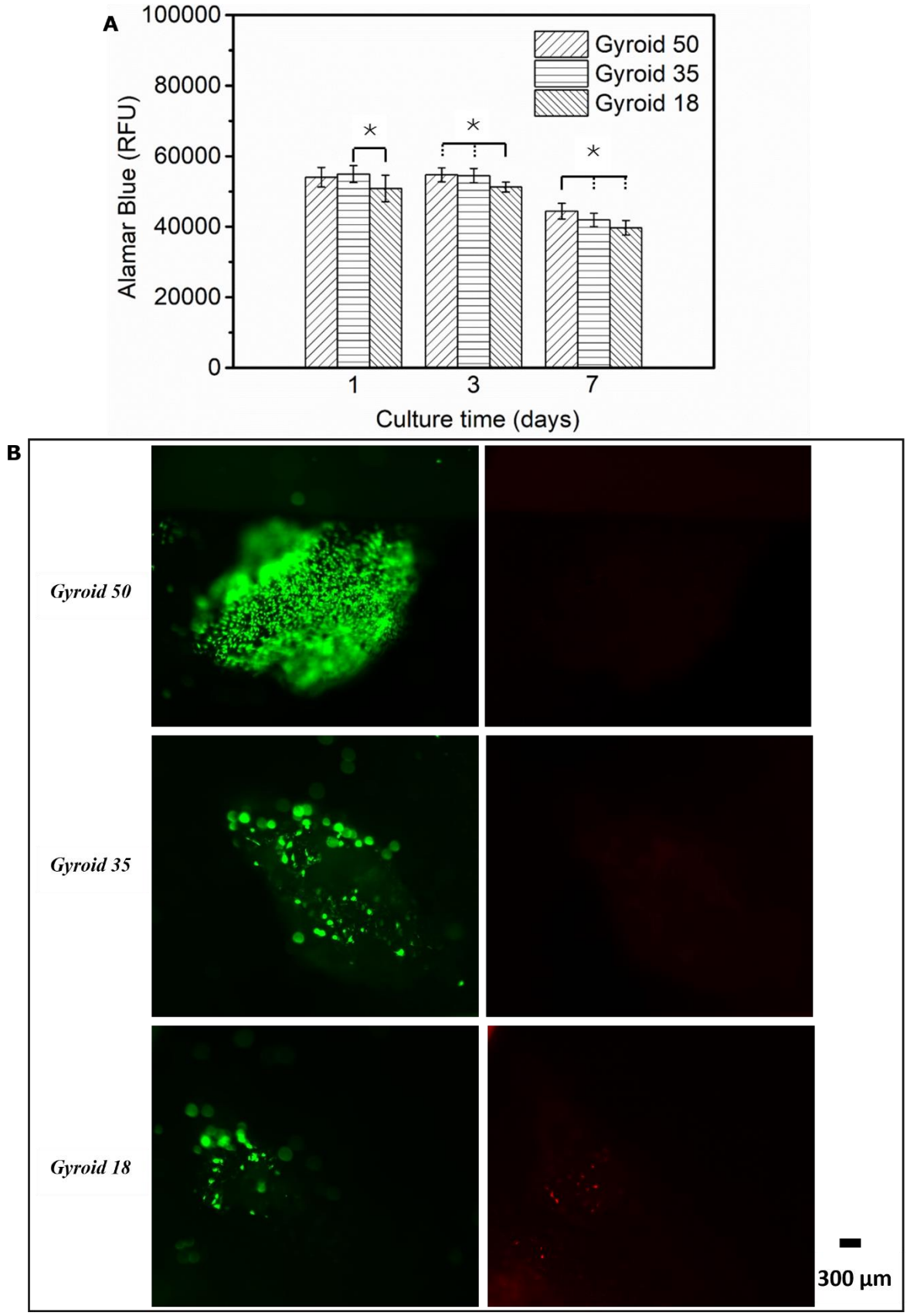

Fig. 7-5. (A) Metabolic activity of MC3T3-E1 preosteoblast cells seeded into different Gyroid lattices after 1, 3 and 7 days of culture. (B) Viability staining images after 7 days of culture with GFP channel in the left, and TX

Red channel in the right panel. signifies p value < 0.05 (when more than one pair is illustrated, pairwise comparisons refer to those between the group indicated with a solid line and any other groups indicated with dash lines).

7.4 Discussion

7.4.1 TPMS sheet-based architectures manufacturing and characterisation

Imperfections such as keyholes, and un-melted particles can unavoidably occur in TNT5Zr-0.2O TPMS sheet-based scaffolds when performing high energy density *in-situ* alloying via SLM (see Fig. 7-3). Available literature [82] shows that keyholes with high aspect ratio are formed owing to the intense recoil pressure of local element evaporation inside the molten pool, which are commonly reported in alloys with low boiling point elements [22]. In addition, un-melted particles have been observed for melting alloys without enough laser energy input [21,311]; the phenomenon is evident when *in-situ* alloying powders with big differences in melting point or average particle size. In our former study, Kong et al. [240] successfully manufactured TNT5Zr cubical components at a low defect level, namely 99.99% relative density and 0.0030% un-melted particles (Nb & Ta) in the range of 3–20 μm. However, the typical un-melted particles phenomenon appeared to be more severe when manufacturing TPMS sheet-based lattices than cubical component (Fig. 7-3), even though the final build was developed after a systematic parameter optimisation. This resulted from continuous manufacturing in SLM process which provides lower remelting of previous layers during laser scan of complex struts than uniform cross-section structures. Therefore, the lack of enough energy input in regions close to the pores probably makes un-melted particles form easily, and

keyhole defect formation more difficult.

The Archimedes method is commonly selected to measure and calculate as-built porosity/relative density of scaffolds as it considers the volume of whole sample. To explain the difference of design and build porosity, the accumulation of un-melted Nb and Ta particles in whole scaffold caused by insufficient laser energy input is regarded as one factor. These heavy particles occupied the space that should be infilled by homogenous β titanium alloy, thus increasing the total mass of each scaffold than the ideal counterpart, then probably further raising as-built volume and lowering its build porosity. As 50% design porosity scaffolds obtained much higher design and build porosity differences (9.6%~15.2%) than their 18% counterparts (0.3%~2.1%), it is suggested that un-melted particle phenomenon is more severe in the outskirts of pores in larger porous structures. On the other hand, the molten pool conserves enough heat to partially melt the powder surrounding the scaffold contour, forming metal agglomerates during low scan speeds (500 mm/s). Therefore, the dimensional deviation obtained from the internal pores and external profile of these scaffolds is regarded as another factor leading to a higher relative density than the design. In comparison with the open-cell Ti-6Al-4V lattice work by Chen et al. [98], the measured as-built porosity is similar to the CAD design porosity when manufacturing scaffolds with 40~70% design porosity. However, the mismatch of porosity (9%) appears to increase dramatically with increasing design porosity level (80%). They considered laser beam broadening and melting edge effects would make powders attach to the pore edges, and result in the smaller pore sizes and larger strut width, thus increasing relative density of scaffolds.

7.4.2 Experimental compression properties of Ti-alloy cellular structures

The measured compression properties indicated that the TNT5Zr-0.2O TPMS sheet-based structures possess low Young's modulus (9~23 GPa) and high compressive strength (355~1052 MPa). Microstructural characteristics depicted in Fig. 7-2C should be considered to explain the experimental mechanical values of the scaffolds. Low Young's moduli are retained due to material elastic deformation associated with body-centred cubic lattice structure stretching, which represents a bigger perturbation from the equilibrium spacing than that of hexagonal close-packed lattice structures commonly found in other titanium alloys. Additionally, a larger strain is measured in the more porous structure (50% design porosity) than other structures (35% and 18% design porosity) when loading at the same stress level, thus resulting in a further decrease in elastic moduli of TNT5Zr-0.2O lattice structures (e.g., Diamond 50, Gyroid 50, SplitP 50). On the other hand, oxygen solid solute strengthening mechanism [246,247] is introduced to explain the scaffolds' high strength. Three causes, namely strong repulsion for oxygen and dislocation, large barriers for the "mechanical shuffle" of interstitial atoms in the core, and the local cross slip induced by oxygen atoms produce a strong pinning effect on screw dislocations of the material. Additionally, the nano-sized particles also impede grain boundary migration and pin dislocation motion within grain boundaries to a certain extent. The highest strengths were obtained in 18% design porosity lattices because strength is proportional to as-built density in these TPMS scaffold arrays.

The compressive stress-strain curves measured in the TPMS sheet-based scaffolds (Fig. 7-4(A-C)) exhibit entirely different morphologies when compared to the typical stress-strain curves found in other beam-based scaffolds. The latter compressive stress strain curves show that lattice specimens normally experience a linear elastic deformation, followed by dramatic fluctuations before approaching the final densification stage [312]. The struts yielding in the plateau stage result in a sudden loss of load-bearing capability, displaying the characteristic failure behaviour of brittle materials [313]. For TNT5Zr-0.2O sheet-based scaffolds, a continuous and rapid rise in stress is observed after the elastic deformation. Except for scaffold densification and the oxygen solid solute strengthening, the rapidly enhanced strength is also caused by strain-hardening effect, which is explained by the pinning or tangling of dislocations occurring after the scaffold densification.

From the former work of Ti-6Al-4V scaffolds fabricated via AM, highly porous structures were preferably designed to lower their monolithic elastic moduli for biomedical applications. For example, Yavari et al. [187] successfully manufactured lattice structures with porosity level in the range of 68%~88% using dodecahedron unit cells. However, the manufactured porous structures provided low yield strengths (varied between 16 and 92 MPa) and compressive stresses (varied between 19 and 117 MPa) under static compression testing. Unlike the high elastic modulus measured from Ti-6Al-4V (approx. 110 GPa), beta titanium alloys with much lower elastic moduli can be used for manufacturing higher-level density scaffolds. In our work, the high-density scaffolds infilled by TPMS based unit cells with large wall thickness achieved a good balance of high strength and low modulus, which improves the reliability of lattice

implants during long-term service.

7.4.3 In vitro cell proliferation within different porosity Gyroid sheet-based lattices

The metabolic activity measurements (Fig. 7-5A) suggested that variations in porosity influence cell proliferation. Clearly, it can be seen that lower Alamar blue content was obtained for the densest gyroid lattice (Gyroid 18). This is consistent with previous findings by Balla et al. [314] and Bael et al. [104] where *in vitro* metabolic activity was significantly higher in Ti-6Al-4V and pure Ta scaffolds with larger pore sizes. This linkage between metabolism and lattice porosity has been commonly ascribed to potential area for cell adhesion and permeability [104,105,315]. As described by Bael et al. [104], larger space for cell adhesion, higher diffusivity and less pore occlusion for growth is available in the more porous scaffolds. Despite there exists interconnections between the pores in these gyroid scaffold architectures, the pathway (channel) for the flow of media is much narrower in Gyroid 18, which may affect osteoblastic permeability, adhesion, and proliferation. The subsequent 7-day culture live-dead staining result (Fig. 7-5B) possibly confirms the explanation as more dead cells were found within Gyroid 18 lattice.

7.5 Conclusions

In this chapter, the authors SLM manufactured and heat-treated diamond, gyroid, splitP TNT5Zr-0.2O scaffolds with different design porosity (50%, 35%, 18%). Both morphological and mechanical characteristics were studied experimentally and numerically, followed by *in vitro* cytotoxicity tests. The main conclusions of this work are as follow:

1 In these scaffolds, the porosity of build scaffolds determined by the Archimedes method were lower than the design porosity, possibly caused by the accumulation of un-melted heavy Nb and Ta particles during laser scan of complex struts and dimensional deviation as a result of metal agglomerates. Additionally, heterogenous nucleation of alpha precipitates at beta grain boundaries occurred when the alloy underwent intermediate cooling from 1000℃.

2 Low elastic moduli (12~18 GPa) and high yield strengths (395~995 MPa) were obtained in the varying porosity diamond scaffolds due to their high density, large wall thickness of the scaffolds, and the inherent low elastic modulus of the β titanium alloy. Similarly, elastic moduli were in the range of 10 to 18 GPa and yield strengths were between 358 and 974 MPa in gyroid lattices. SplitP scaffolds possessed the highest level of elastic moduli (15~22 GPa) yield strengths (618~1045 MPa).

3 Lower metabolic activity of osteoblasts was obtained in the densest gyroid lattice group, which could have resulted from the lower available adhesion area and permeability within the pores.

It has been shown that a good balance between high strength and low modulus can be obtained with TNT5Zr-0.2O TPMS sheet-based scaffolds. These results showcase that through both structural and alloying strategies TPMS beta titanium scaffolds can provide enhanced devices which improve the reliability of lattice implants during long-term service.

8 CONCLUSIONS AND FUTURE WORK

8.1 Conclusions

The TNT and TNTZ alloy design chapter investigated *in-situ* alloying Ti-Nb-Ta based β alloys with different zirconium additions (0, 5, 9 wt. %) manufactured by SLM for load-bearing implant development. The microstructure and defects, mechanical properties, and biocompatibility were systematically analysed, and the following main conclusions are drawn:

1 The slow scan speed (e.g., 500 mm/s) with high laser power (e.g., 300 W) is accepted as being an optional parameter combination to manufacture TNT(Z) alloys at a low defects level. Micro-CT results show that the size of un-melted particles (Nb & Ta) and keyhole of after-optimisation TNT(Z) alloys is mainly located in a range of 3—20 μm, and the relative density of as-fabricated TNT(Z) alloys is >99.97%.

2 Martensitic transformation normally caused by high cooling is suppressed in the high β-stabilized Ti-Nb-Ta based alloys, making these three SLMed alloys obtain main β phase at room temperature. No existence of athermal ω or α'' phase inside the beta matrix and potential nano-scale grain boundary alpha phase precipitation is observed in TNT(Z) alloys, which agrees the relevant EBSD mapping and XRD results. Additionally, zirconium is regarded as a neutral element in this high β-stabilized Ti-Nb-Ta based alloy when performing SLM manufacturing.

3 Tensile testing shows that the UTS of these as-fabricated β Ti alloys ranges from 681 ± 6 MPa to 772 ± 9 MPa. Here, the Vickers hardness and UTS increase caused by zirconium addition is explained by grain refinement. A weak UTS reduction after solution treating then water quenching is regarded as grain growth when dwell at solution treated temperature. Notably, the UTS to modulus ratio of as-designed TNT(Z) alloys is approx. 12, which is much higher than the recorded value (8.1-8.8) of biomedical Ti-6Al-4V.

4 Corrosion ions released from uniform attack in MEM containing medium at each time interval have an extremely small concentration (<10 μg/L). The corrosion product film on these TNT(Z) alloys, presumably to be fairly stable after 30 days immersion. It indicated that good biocompatibility with respect to cytotoxicity during culture with corrosion ions is obtained in these TNT(Z) alloys.

The TNT5Zr post-processing treatment chapter investigated the microstructural evolution, defects distribution, mechanical properties of SLM-manufactured TNT5Zr β Ti alloy before and after post-processing treatment. In addition, we evaluated short-term *in vitro* MC3T3-E1 preosteoblast response of the post-processed β Ti alloy and Ti-6Al-4V alloy. The main conclusions are drawn:

1 HIP treatment closes the as-fabricated keyhole pores in TNT5Zr alloy due to densification caused by the pressured and high-temperature argon atmosphere. Meanwhile, the grain growth and slighter extent of preferred crystallographic orientation is observed in specimen

after HIP. BF image & SAD pattern together with BF-STEM observation shows the existence of single beta matrix and alpha precipitates along the grain boundary in TNT5Zr-AF+HIP alloy. The same microstructure included ellipsoidal nano-sized α'' precipitates (about 5~10 nm) in the β matrix is obtained in TNT5Zr-AF+HIPA alloy.

2 By comparison with the mechanical properties of TNT5Zr-AF alloy, it remains the slightly higher UTS (760 ± 5 MPa) after HIP treatment. HIP & aging duplex treatment further strengthens the ductile TNT5Zr alloy by precipitation strengthening, making it obtained a comparable UTS (853 ± 9 MPa) to Ti64-AF+HIP (926 ± 23 MPa).

3 Inferior notch-like surface irregularities are regarded as fatigue cracks initiation sites in TNT5Zr-AF+HIPA alloy. Slip-band cracking has been widely observed in this alloy caused by cyclic stressing close to the fatigue limit (170 MPa). Both crack growth mechanisms, namely micro-cleavage and microvoid coalescence take place when cracks migrate to final fast fracture region.

4 *In vitro* biocompatibility investigation of both Ti alloys has shown similar metabolic activity and long-term mineralisation. The high strength-to-modulus ratio (15.2 ± 1.4) together with excellent biological *in vitro* behaviour, demonstrating TNT5Zr-AF+HIPA alloy can be a good candidate for load-bearing implant.

The TNT5Zr-0.2O post-processing treatment chapter investigated the microstructural evolution, mechanical properties of SLMed Ti-34Nb-13Ta-5Zr-0.2O alloy (TNT5Zr-0.2O,

wt. %) before and after advanced HIP subjected to high and intermediate cooling rate (HCR & ICR). The main conclusions about the influence of oxygen concentration and cooling rate on microstructure and overall properties are drawn:

1 XRD analysis along with SEM and TEM micrographs reveal single beta phase in grain matrix of TNT5Zr-0.2O-AF, TNT5Zr-0.2O-ICR, TNT5Zr-0.2O-HCR alloys. BF-STEM and HAADF micrographs show discrete large Ti-rich α precipitates formed along grain boundaries in TNT5Zr-0.2O-ICR alloy. By comparison, grain boundary α particles are fully suppressed in TNT5Zr-0.2O-HCR alloy.

2 TNT5Zr-0.2O-AF alloy possessed high UTS of 975 ± 12 MPa, and elongation of 4.9% ± 0.3%; the TNT5Zr-0.2O-ICR alloy shows slightly higher UTS (1036 ± 26 MPa) and lower elongation (3.0% ± 0.3%). However, TNT5Zr-0.2O alloy breaks at the initial linear elastic region (682 ± 75 MPa) without yielding phenomenon, the brittleness may be caused by residual stress and strain incompatibilities in anisotropic grains or grain boundaries. The mixed surfaces of intergranular fracture together with intragranular fracture are observed in these three alloys but appear an obvious grain boundary fracture morphology difference. Notably, TNT5Zr-0.2O-AF alloy obtains the highest σ_{UTS}/E ratio (16.3 ± 1.1) and still maintains the low Young's modulus (60 ± 5 GPa).

3 S-N curves obtained from plain fatigue test show fatigue limit of TNT5Zr-0.2O-ICR alloy (150 MPa) is slightly higher than the counterpart of TNT5Zr-0.2O-AF alloy (130 MPa). SEM fractographs demonstrate fatigue crack preferably initiates from voids located in the

surface of specimen, and slip-band cracking phenomenon with development of extrusion/intrusion pair is observed in both alloys.

4 The oxygen atoms occupied in the interstices of bcc β phase at sufficient concentration (0.8 at. %), probably produce a strong pinning effect on screw dislocations. Therefore, the addition of proper amount oxygen interstitial solutes in TNTZ-O alloy is regarded as an inexpensive, effective strengthening technique for load-bearing biomedical applications.

The TNT5Zr-0.2O surface treatment chapter investigated the surface morphology, and microstructural changes in thermal oxidation (TO) processed TNT5Zr-0.2O alloy. In addition, the wear, plain/chemical-interfering fatigue properties, and osteoblast cell response to the alloy before & after TO treatment were also investigated. The main conclusions of this work are as follow:

1 Chemical etching (CE) as a pre-treatment for thermal oxidation successfully removed surface adhered powders from the SLM-manufactured TNT5Zr-0.2O alloy. A mixture of main phases of TiO_2 (rutile), Nb_2O_5, and minor phases of Ta_2O_5, ZrO was obtained in the oxide layer after the subsequent TO treatment. Additionally, beta stabilizer-lean acicular alpha precipitates were observed in the β-depleted zone due to these elements (Nb, Ta) migration into the oxide layer.

2 Higher wear resistance was obtained after TO treatment as suggested by the wider wear track of the CE treated sample. Adhesive wear features with ploughing grooves were found

in the former alloy; while the wear scar was relatively smooth in real contact areas between the CE+TO treated sample and the ceramic counterpart, with brittle metallic oxides peeling.

3 The HCl plain fatigue strength of CE and CE+TO treated TNT5Zr-0.2O alloy were 150 MPa and 60 MPa, respectively. The higher Young's moduli of the metallic oxides and precipitates in the inner zone caused multiple premature fatigue cracks to develop in the compounded region deteriorating the fatigue properties. Moreover, a slight decrease in fatigue limit (130 MPa) was observed in the CE treated alloy, while a same level fatigue limit (70 MPa) was retained in CE+TO treated alloy after chemical-interfering fatigue testing. Though the thick oxide layer brings a positive effect against the aggressive HCl solution, the described TO should be cautiously exploited as a fatigue limit deterioration caused by the complex compound system.

4 No statistically significant ($p < 0.05$) difference in metabolic activity between the CE and CE+TO treated groups was observed with 7-day live-dead fluorescence micrographs indicating similar cell confluence negligible damaged cell membranes. Early and late mineralisation assays revealed similar levels of 14-day ALP activity, and 28-day mineral deposits formed on the two biocompatible TNT5Zr-0.2O alloy surfaces. These indicate the potential use of these surface treatments for additively manufactured medical devices.

In the TNT5Zr-0.2O lattice design and manufacturing chapter, the authors SLM manufactured and heat-treated diamond, gyroid, splitP TNT5Zr-0.2O scaffolds with different design porosity

(50%, 35%, 18%). Both morphological and mechanical characteristics were studied experimentally and numerically, followed by *in vitro* cytotoxicity tests. The main conclusions of this work are as follow:

1 In these scaffolds, the porosity of build scaffolds determined by the Archimedes method were lower than the design porosity, possibly caused by the accumulation of un-melted heavy Nb and Ta particles during laser scan of complex struts and dimensional deviation as a result of metal agglomerates. Additionally, heterogenous nucleation of alpha precipitates at beta grain boundaries occurred when the alloy underwent intermediate cooling from 1000℃.

2 Low elastic moduli (12~18 GPa) and high yield strengths (395~995 MPa) were obtained in the varying porosity diamond scaffolds due to their high density, large wall thickness of the scaffolds, and the inherent low elastic modulus of the β titanium alloy. Similarly, elastic moduli were in the range of 10 to 18 GPa and yield strengths were between 358 and 974 MPa in gyroid lattices. SplitP scaffolds possessed the highest level of elastic moduli (15~22 GPa) yield strengths (618~1045 MPa).

3 Lower metabolic activity of osteoblasts was obtained in the densest gyroid lattice group, which could have resulted from the lower available adhesion area and permeability within the pores.

It has been shown that a good balance between high strength and low modulus can be obtained

with TNT5Zr-0.2O TPMS sheet-based scaffolds. These results showcase that through both structural and alloying strategies TPMS beta titanium scaffolds can provide enhanced devices which improve the reliability of lattice implants during long-term service.

8.2 Future work

8.2.1 TNTZ-(O) alloy manufacturing via selective laser melting

The external adhered powder inevitably occurred when building components using high-speed *in-situ* alloying. Because pure elemental powders were used in this study, it increased the difficulty to remove the corrosion-resistant powders (Nb, Ta, Zr) via chemical etching technique. In section 6.2.6, samples were statically immersed in etching solution (10% HF + 15% HNO_3 + 75% H_2O) for 16 hours, then obtained a powder-free surface. However, surface notches induced by aggressive aqueous HF/HNO_3 immersion can be preferable crack initiation sites in fatigue testing, reported in section 6.3.3. The chemical etching procedure should be more efficient to remove the adhered pre-alloyed powder of components due to an inferior corrosion resistance. In TNTZ-(O) lattice scaffold manufacturing, the removed powder can further decrease the gap between as-built and as-designed porosity. On the other hand, powder measurement and blending in laboratory for *in-situ* alloying lowers the build efficiency. Pre-alloyed TNTZ powder can be used for manufacturing specimens in future. Note that the feedstock should possess a good particle size distribution (PSD) for AM, which guarantees the build quality of samples. The author has been found an enhancement of UTS in SLM manufactured TNTZ after oxygen pick-up, reported in section 5.3.2. Therefore,

oxygen level in powder processing is another important factor to determine the properties of SLM-manufactured components.

8.2.2 Microstructural evolutions of TNTZ-(O) during SLM in-situ alloying and post-processing heat treatment

TEM characterisation is necessary for clarifying the complicated microstructural evolutions of the AM and post-processed TNTZ-(O) alloys, however, the preparation of thin foils has been found to be very difficult. Twin jet electropolishing was not successfully to thin the specimens with low applied voltages in an electrolyte (5% perchloric acid, 68% methanol, 27% n-butanol), the not thin enough foils with a presence of large holes were not satisfactory for TEM observation. Argon ion milling technique managed to prepare couple of thin foils for demonstration the TEM & HRTEM results of these alloys. However, the materials were physically damaged in the thinning process to some extent, it increased the difficulty to distinguish nanoscale precipitates from the BF images with milling defects. According to the former experience, it took a long time (16 hours) for preparing TNT5Zr-0.2O thin foils because of oxygen solid solution strengthening effect. Focused-ion beam (FIB) approach can be used in future studies to investigate if a higher efficiency can be maintained in TNTZ-O thin foils preparation, and a better quality of micrographs during observation.

8.2.3 Mechanical properties of TNTZ-(O) manufactured by SLM in-situ alloying and post-processing heat treatment

In this study, the author did not investigate deformation mechanisms of polycrystalline SLM manufactured TNTZ-(O) alloys. The deformation markings belonging to slip or twin planes need to be confirmed in future studies during the observation of morphologies of bands. If twin bands are observed, crystallographic analysis will be performed to identify the twinning type. Additionally, the occurrence of well-known stress-induced β to α'' martensitic transformation [316] in Gum metal need to be analysed in SLM-manufactured TNTZ-(O) alloys via tensile test and DP characterisation. Note that micro-pillar compression tests can be involved in future studies to investigate the deformation behaviour and strengthening mechanisms of oxygen containing TNTZ alloys. Moreover, fatigue properties of the highest-strength splitP scaffolds can be evaluated in future research.

8.2.4 Biocompatibility evaluation of TNTZ-(O) manufactured by SLM in-situ alloying and post-processing heat treatment

In this study, no SEM imaging has been conducted to reveal morphology and spatial distributions of cells onto various surface treated and lattice structure TNTZ-0.2O. Therefore, the extent and uniformity of cell ingrowth within specimens can be analysed in future. Besides that, long-term cell mineralisation within 3D scaffolds can be visualised via micro-CT technique. Even though the *in vitro* investigations showcased excellent cell response of the as-built β titanium alloys, it is noteworthy that the biggest limitation is lack of *in vivo*

evaluation to confirm the superb osseointegration. The long-term *in vivo* tests within TNTZ-(O) implants can be considered in future studies.

Overall, the author has performed systematic research including material design, microstructural evolution, mechanical properties, wear, *in vitro* and *in vivo* response of SLM-manufactured TNTZ-(O) alloys. In future, some challenging research regarding to electro-chemical testing and drug-delivery system design can be carried out to evaluate the reliability and functionality of the TNTZ-(O) implants in long-term service.

REFERENCES

[1] J.A. Planell, M. Navarro, Challenges of bone repair, in: Bone Repair Biomater., 2009. https://doi.org/10.1533/9781845696610.1.3.

[2] C.H. MacLean, K. Knight, H. Paulus, R.H. Brook, P.G. Shekelle, Costs attributable to osteoarthritis, J. Rheumatol. (1998).

[3] D. Jahoda, Clinical strategy for the treatment of deep infection of hip arthroplasty, in: Infected Implant, 2009. https://doi.org/10.1007/978-3-540-92836-2_7.

[4] R. Huiskes, H. Weinans, B. Van Rietbergen, The relationship between stress shielding and bone resorption around total hip stems and the effects of flexible materials, Clin. Orthop. Relat. Res. (1992). https://doi.org/10.1097/00003086-199201000-00014.

[5] J.P. Paul, Strength requirements for internal and external prostheses, J. Biomech. (1999). https://doi.org/10.1016/S0021-9290(98)00190-0.

[6] W.D. Bugbee, W.J. Culpepper, C. a Engh, Long-term clinical consequences of stress-shielding after total hip arthroplasty without cement., J. Bone Joint Surg. Am. (1997).

[7] T. Hanawa, Metal ion release from metal implants, in: Mater. Sci. Eng. C, 2004. https://doi.org/10.1016/j.msec.2004.08.018.

[8] T.M. Sridhar, S.P. Vinodhini, U. Kamachi Mudali, B. Venkatachalapathy, Load-bearing metallic implants: electrochemical characterisation of corrosion phenomena, Mater. Technol. (2016). https://doi.org/10.1080/10667857.2016.1220752.

[9] G.C. McKay, R. Macnair, C. MacDonald, M.H. Grant, Interactions of orthopaedic metals with an immortalized rat osteoblast cell line, Biomaterials. (1996). https://doi.org/10.1016/0142-9612(96)88681-9.

[10] Y. Okazaki, S. Rao, Y. Ito, T. Tateishi, Corrosion resistance, mechanical properties: corrosion fatigue strength and cytocompatibility of new Ti alloys without A1 and V, Biomaterials. (1998). https://doi.org/10.1016/S0142-9612(97)00235-4.

[11] R. Banerjee, Strengthening mechanisms in Ti-Nb-Zr-Ta and Ti-Mo-Zr-Fe orthopaedic alloys, Biomaterials. (2004). https://doi.org/10.1016/j.biomaterials.2003.10.041.

[12] Y. Al-Zain, H.Y. Kim, H. Hosoda, Miyazaki, Shape memory properties of Ti-Nb-Mo biomedical alloys, Acta Mater. (2010). https://doi.org/10.1016/j.actamat.2010.04.013.

[13] W.T. Huo, L.Z. Zhao, S. Yu, Z.T. Yu, P.X. Zhang, Y.S. Zhang, Significantly enhanced osteoblast response to nano-grained pure tantalum, Sci. Rep. (2017). https://doi.org/10.1038/srep40868.

[14] L. Trentani, F. Pelillo, F.C. Pavesi, Forlino, Evaluation of the TiMo12Zr6Fe2 alloy for orthopaedic implants: In vitro biocompatibility study by using primary human fibroblasts and osteoblasts, Biomaterials. (2002). https://doi.org/10.1016/S0142-9612(01)00413-6.

[15] S. Hanada, H. Matsumoto, S. Watanabe, Mechanical compatibility of titanium implants in hard tissues, Int. Congr. Ser. (2005). https://doi.org/10.1016/j.ics.2005.06.084.

[16] Q. Chen, G.A. Thouas, Metallic implant biomaterials, Mater. Sci. Eng. R Reports. (2015). https://doi.org/10.1016/j.mser.2014.10.001.

[17] M. Atapour, A.L. Pilchak, G.S. Frankel, J.C. Williams, Corrosion behavior of β titanium alloys for biomedical applications, Mater. Sci. Eng. C. (2011). https://doi.org/10.1016/j.msec.2011.02.005.

[18] D.M. Gordin, R. Ion, C. Vasilescu, S.I. Drob, A. Cimpean, T. Gloriant, Potentiality of the “gum Metal” titanium-based alloy for biomedical applications, Mater. Sci. Eng. C. (2014). https://doi.org/10.1016/j.msec.2014.08.003.

[19] P. Neacsu, D.M. Gordin, V. Mitran, T. Gloriant, M. Costache, A. Cimpean, In vitro performance assessment of new beta Ti-Mo-Nb alloy compositions, Mater. Sci. Eng. C. (2015). https://doi.org/10.1016/j.msec.2014.11.023.

[20] S.H. Huang, P. Liu, A. Mokasdar, L. Hou, Additive manufacturing and its societal impact: A literature review, Int. J. Adv. Manuf. Technol. (2013). https://doi.org/10.1007/s00170-012-4558-5.

[21] L.C. Zhang, D. Klemm, J. Eckert, Y.L. Hao, T.B. Sercombe, Manufacture by selective laser melting and mechanical behavior of a biomedical Ti-24Nb-4Zr-8Sn alloy, Scr. Mater. (2011). https://doi.org/10.1016/j.scriptamat.2011.03.024.

[22] Y.J. Liu, S.J. Li, H.L. Wang, W.T. Hou, Y.L. Hao, R. Yang, T.B. Sercombe, L.C. Zhang, Microstructure, defects and mechanical behavior of beta-type titanium porous structures manufactured by electron beam melting and selective laser melting, Acta Mater. (2016). https://doi.org/10.1016/j.actamat.2016.04.029.

[23] M. Fischer, D. Joguet, G. Robin, L. Peltier, P. Laheurte, In situ elaboration of a binary Ti-26Nb alloy by selective laser melting of elemental titanium and niobium mixed

powders, Mater. Sci. Eng. C. (2016). https://doi.org/10.1016/j.msec.2016.02.033.

[24] L. Wang, W. Lu, J. Qin, F. Zhang, D. Zhang, Change in microstructures and mechanical properties of biomedical Ti-Nb-Ta-Zr system alloy through cross-rolling, Mater. Trans. (2008). https://doi.org/10.2320/matertrans.MRA2008040.

[25] Y.L. Hao, S.J. Li, Elastic deformation behaviour of Ti-24Nb-4Zr-7.9Sn for biomedical applications, Acta Biomater. (2007). https://doi.org/10.1016/j.actbio.2006.11.002.

[26] T. Furuta, S. Kuramoto, J. Hwang, K. Nishino, T. Saito, M. Niinomi, Mechanical properties and phase stability of Ti-Nb-Ta-Zr-O alloys, in: Mater. Trans., 2007. https://doi.org/10.2320/matertrans.48.1124.

[27] S. Nag, R. Banerjee, H.L. Fraser, Microstructural evolution and strengthening mechanisms in Ti-Nb-Zr-Ta, Ti-Mo-Zr-Fe and Ti-15Mo biocompatible alloys, in: Mater. Sci. Eng. C, 2005. https://doi.org/10.1016/j.msec.2004.12.013.

[28] Y. Mantani, M. Tajima, Effect of ageing on internal friction and elastic modulus of Ti-Nb alloys, Mater. Sci. Eng. A. (2006). https://doi.org/10.1016/j.msea.2006.03.124.

[29] R.J. Talling, R.J. Dashwood, M. Jackson, D. Dye, Compositional variability in gum metal, Scr. Mater. (2009). https://doi.org/10.1016/j.scriptamat.2009.02.044.

[30] M. Tane, T. Nakano, S. Kuramoto, M. Hara, M. Niinomi, N. Takesue, T. Yano, H. Nakajima, Low Young's modulus in Ti-Nb-Ta-Zr-O alloys: Cold working and oxygen effects, Acta Mater. (2011). https://doi.org/10.1016/j.actamat.2011.07.050.

[31] M. Tane, T. Nakano, S. Kuramoto, M. Niinomi, N. Takesue, H. Nakajima, ω Transformation in cold-worked Ti-Nb-Ta-Zr-O alloys with low body-centered cubic phase stability and its correlation with their elastic properties, Acta Mater. (2013). https://doi.org/10.1016/j.actamat.2012.09.041.

[32] T. Saito, T. Furuta, J.H. Hwang, S. Kuramoto, K. Nishino, N. Suzuki, R. Chen, A. Yamada, K. Ito, Y. Seno, T. Nonaka, H. Ikehata, N. Nagasako, C. Iwamoto, Y. Ikuhara, T. Sakuma, Multifunctional alloys obtained via a dislocation-free plastic deformation mechanism, Science (80-.). (2003). https://doi.org/10.1126/science.1081957.

[33] M. Niinomi, M. Nakai, M. Hendrickson, P. Nandwana, T. Alam, D. Choudhuri, R. Banerjee, Influence of oxygen on omega phase stability in the Ti-29Nb-13Ta-4.6Zr alloy, Scr. Mater. (2016). https://doi.org/10.1016/j.scriptamat.2016.06.027.

[34] S.C. Cowin, Bone Mechanics Handbook, 2001. https://doi.org/10.1115/1.1579463.

[35] D.B. Burr, Basic and Applied Bone Biology, 2013. https://doi.org/10.1016/C2011-0-05817-9.

[36] P. Haghighi, Structure, function and adaptation of compact bone, Skeletal Radiol. (1989). https://doi.org/10.1007/bf00351748.

[37] P.K. Zysset, X. Edward Guo, Elastic modulus and hardness of cortical and trabecular bone lamellae measured by nanoindentation in the human femur, J. Biomech. (1999). https://doi.org/10.1016/S0021-9290(99)00111-6.

[38] C.M. Serre, D. Farlay, P.D. Delmas, C. Chenu, Evidence for a dense and intimate innervation of the bone tissue, including glutamate-containing fibers, Bone. (1999). https://doi.org/10.1016/S8756-3282(99)00215-X.

[39] A.D. Woolf, B. Pfleger, Burden of major musculoskeletal conditions, Bull. World Health Organ. (2003). https://doi.org/10.1590/S0042-96862003000900007.

[40] V. Mouriño, Bone tissue engineering therapeutics: Controlled drug delivery in three-dimensional scaffolds, J. R. Soc. Interface. https://doi.org/10.1098/rsif.2009.0379.

[41] D.J. Hunter, Osteoarthritis, Lancet. https://doi.org/10.1016/S0140-6736(19)30417-9.

[42] P.A. Revell, Joint Replacement Technology. https://doi.org/10.1201/9781439833063.

[43] D.F. Williams, Definitions in biomaterials: proceedings of a consensus conference of the European Society for Biomaterials, Chester, England, March 3-5, 1986, Defin. Biomater. Proc. a Consens. Conf. Eur. Soc. Biomater. Chester, England, March 3-5, 1986,. (1987).

[44] US FDA, Biological Responses to Metal Implants, Food Drug Admistration. (2019).

[45] P. Balakrishnan, M.S. Sreekala, S. Thomas, Fundamental biomaterials: Metals, 2018. https://doi.org/10.1016/C2016-0-03502-7.

[46] J.C. Heath, M.A.R. Freeman, Carcinogenic Properties of wear particels from prostheses made in cobalt-chromium alloy, Lancet. (1971). https://doi.org/10.1016/S0140-6736(71)91162-7.

[47] C. Delaunay, I. Petit, I.D. Learmonth, P. Oger, P.A. Vendittoli, Metal-on-metal bearings total hip arthroplasty: The cobalt and chromium ions release concern, Orthop. Traumatol. Surg. Res. (2010). https://doi.org/10.1016/j.otsr.2010.05.008.

[48] H.S. Gill, G. Grammatopoulos, S. Adshead, E. Tsialogiannis, E. Tsiridis, Molecular and

immune toxicity of CoCr nanoparticles in MoM hip arthroplasty, Trends Mol. Med. (2012). https://doi.org/10.1016/j.molmed.2011.12.002.

[49] A. Katzer, S. Hockertz, G.H. Buchhorn, J.F. Loehr, In vitro toxicity and mutagenicity of CoCrMo and Ti6Al wear particles, Toxicology. (2003). https://doi.org/10.1016/S0300-483X(03)00147-1.

[50] M. Akbar, Effect of chromium and cobalt ions on primary human lymphocytes in vitro, J. Immunotoxicol. https://doi.org/10.3109/1547691X.2011.553845.

[51] S. Catalani, S. Stea, A. Beraudi, M.E. Gilberti , Vanadium release in whole blood, serum and urine of patients implanted with a titanium alloy hip prosthesis, Clin. Toxicol. (2013). https://doi.org/10.3109/15563650.2013.818682.

[52] Y. Okazaki, S. Rao, S. Asao, T. Tateishi, Effects of Ti, Al and V concentrations on cell viability, Mater. Trans. JIM. (1998). https://doi.org/10.2320/matertrans1989.39.1053.

[53] J. Davis, Handbook of Materials for Medical Devices, ASM Int. (2003). https://doi.org/10.1361/hmmd2003p001.

[54] M. Long, H.J. Rack, Titanium alloys in total joint replacement - A materials science perspective, Biomaterials. (1998). https://doi.org/10.1016/S0142-9612(97)00146-4.

[55] M. Burke, S. Goodman, Failure mechanisms in joint replacement, in: Jt. Replace. Technol., 2008. https://doi.org/10.1533/9781845694807.2.264.

[56] M.I.Z. Ridzwan, S. Shuib, A.Y. Hassan, A.A. Shokri, M.N. Mohammad Ibrahim, Problem of stress shielding and improvement to the hip implant designs: A review, J. Med. Sci. (2007). https://doi.org/10.3923/jms.2007.460.467.

[57] J.D. Bobyn, E.S. Mortimer, Producing and Avoiding Stress Shielding, Clin. Orthop. Relat. Res. (1992). https://doi.org/10.1097/00003086-199201000-00010.

[58] A.J. Smith, P. Dieppe, P.W. Howard, A.W. Blom, Failure rates of metal-on-metal hip resurfacings: Analysis of data from the National Joint Registry for England and Wales, Lancet. (2012). https://doi.org/10.1016/S0140-6736(12)60989-1.

[59] D.R. Sumner, T.M. Turner, R. Igloria, R.M. Urban, J.O. Galante, Functional adaptation and ingrowth of bone vary as a function of hip implant stiffness, in: J. Biomech., 1998. https://doi.org/10.1016/S0021-9290(98)00096-7.

[60] C.M. Rimnac, T.M. Wright, D.L. Bartel, R.W. Klein, A.A. Petko, Failure of orthopedic

implants: Three case histories, Mater. Charact. (1991). https://doi.org/10.1016/1044-5803(91)90012-S.

[61] S.S.M. Tavares, F.B. Mainier, F. Zimmerman, R. Freitas, C.M.I. Ajus, Characterization of prematurely failed stainless steel orthopedic implants, Eng. Fail. Anal. (2010). https://doi.org/10.1016/j.engfailanal.2010.02.003.

[62] ASTM, F 1801-97 Standard Practice for Corrosion Fatigue Testing of Metallic Implant Materials, ASTM Int. Conshohocken, PA, Www.Astm.Org. (2014).

[63] International Standard Organisation, ISO 14801:2007 Dentistry. Implants. Dynamic fatigue test for endosseous dental implants, Geneva ISO. (2007).

[64] J. Black, Systemic effects of biomaterials, in: Biomater. Silver Jubil. Compend., 1984. https://doi.org/10.1016/B978-008045154-1.50005-8.

[65] K.R. Trethewey, J. Chamberlain, The theory of aqueous corrosion., (1988).

[66] G. Manivasagam, U. Kamachi Mudali, B. Rajb, R. Asokamani, Corrosion and Microstructural Aspects of Titanium and its Alloys as Orthopaedic Devices, Corros. Rev. (2003). https://doi.org/10.1515/CORRREV.2003.21.2-3.125.

[67] R.M. Pilliar, Modern metal processing for improved load-bearing surgical implants, Biomaterials. (1991). https://doi.org/10.1016/0142-9612(91)90185-D.

[68] R. Dieckmann, T. Schmidt-Braekling, G. Gosheger, C. Theil, J. Hardes, B. Moellenbeck, Two stage revision with a proximal femur replacement, BMC Musculoskelet. Disord. (2019). https://doi.org/10.1186/s12891-019-2442-2.

[69] H.J. Cooper, C.J. Della Valle, The two-stage standard in revision total hip replacement, Bone Joint J. (2013). https://doi.org/10.1302/0301-620X.95B11.32906.

[70] B.H. Kapadia, R.A. Berg, J.A. Daley, J. Fritz, A. Bhave, M.A. Mont, Periprosthetic joint infection, Lancet. (2016). https://doi.org/10.1016/S0140-6736(14)61798-0.

[71] R. Trebse, Treatment of infected retained implants, J. Bone Jt. Surg. - Br. Vol. (2005). https://doi.org/10.1302/0301-620X.87B2.15618.

[72] E.M. Hetrick, M.H. Schoenfisch, Reducing implant-related infections: Active release strategies, Chem. Soc. Rev. (2006). https://doi.org/10.1039/b515219b.

[73] Y. Kok, X.P. Tan, P. Wang, M.L.S. Nai, N.H. Loh, E. Liu, S.B. Tor, Anisotropy and

heterogeneity of microstructure and mechanical properties in metal additive manufacturing: A critical review, Mater. Des. (2018).

[74] A. Basak, S. Das, Epitaxy and Microstructure Evolution in Metal Additive Manufacturing, Annu. Rev. Mater. Res. (2016). https://doi.org/10.1146/annurev-matsci-070115-031728.

[75] T. Majumdar, N. Eisenstein, J.E. Frith, S.C. Cox, N. Birbilis, Additive Manufacturing of Titanium Alloys for Orthopedic Applications: A Materials Science Viewpoint, Adv. Eng. Mater. (2018). https://doi.org/10.1002/adem.201800172.

[76] A. Razavykia, E. Brusa, C. Delprete, R. Yavari, An overview of additive manufacturing technologies-A review to technical synthesis in numerical study of selective laser melting, Materials (Basel). (2020). https://doi.org/10.3390/ma13173895.

[77] T. DebRoy, H.L. Wei, J.S. Zuback, T. Mukherjee, J.W. Elmer, J.O. Milewski, Additive manufacturing of metallic components – Process, structure and properties, Prog. Mater. Sci. (2018). https://doi.org/10.1016/j.pmatsci.2017.10.001.

[78] W.E. King, A.T. Anderson, R.M. Ferencz, N.E. Hodge, Laser powder bed fusion additive manufacturing of metals; physics, computational, and materials challenges, Appl. Phys. Rev. (2015). https://doi.org/10.1063/1.4937809.

[79] X.C. Wang, T. Laoui, J. Bonse, J.P. Kruth, B. Lauwers, L. Froyen, Direct selective laser sintering of hard metal powders: Experimental study and simulation, Int. J. Adv. Manuf. Technol. (2002). https://doi.org/10.1007/s001700200024.

[80] M. Markl, C. Körner, Multiscale Modeling of Powder Bed-Based Additive Manufacturing, Annu. Rev. Mater. Res. (2016). https://doi.org/10.1146/annurev-matsci-070115-032158.

[81] C. Körner, Additive manufacturing of metallic components by selective electron beam melting - A review, Int. Mater. Rev. https://doi.org/10.1080/09506608.2016.1176289.

[82] A. Matsunawa, J.-D. Kim, N. Seto, Dynamics of keyhole and molten pool in laser welding, J. Laser Appl. (1998). https://doi.org/10.2351/1.521858.

[83] T. Mukherjee, J.S. Zuback, A. De, T. DebRoy, Printability of alloys for additive manufacturing, Sci. Rep. (2016). https://doi.org/10.1038/srep19717.

[84] K. Darvish, Z.W. Chen, T. Pasang, Reducing lack of fusion during selective laser melting of CoCrMo alloy: Effect of laser power on geometrical features of tracks, Mater. Des.

(2016). https://doi.org/10.1016/j.matdes.2016.09.086.

[85] B. Zhang, Y. Li, Q. Bai, Defect Formation Mechanisms in Selective Laser Melting: A Review, Chinese J. Mech. Eng. (English Ed. (2017). https://doi.org/10.1007/s10033-017-0121-5.

[86] D. Zhao, C. Han, In situ fabrication of a titanium-niobium alloy with tailored microstructures, enhanced mechanical properties and biocompatibility by using selective laser melting, Mater. Sci. Eng. C. https://doi.org/10.1016/j.msec.2020.110784.

[87] D. Gu, Y. Shen, Balling phenomena in direct laser sintering of stainless steel powder: Metallurgical mechanisms and control methods, Mater. Des. (2009). https://doi.org/10.1016/j.matdes.2009.01.013.

[88] J.J. Lewandowski, M. Seifi, Metal Additive Manufacturing: A Review of Mechanical Properties, Annu. Rev. Mater. Res. (2016). https://doi.org/10.1146/annurev-matsci-070115-032024.

[89] A.D. Lantada, Rapid Prototyping for Biomedical Engineering: Current Capabilities and Challenges, Annu. Rev. Biomed. Eng. (2012). https://doi.org/10.1146/annurev-bioeng-071811-150112.

[90] B. Van Hooreweder, Y. Apers, K. Lietaert, J.P. Kruth, Improving the fatigue performance of porous metallic biomaterials produced by Selective Laser Melting, Acta Biomater. (2017). https://doi.org/10.1016/j.actbio.2016.10.005.

[91] L.J. Gibson, M.F. Ashby, Mechanic of three-dimensional cellular materials, Proc. R. Soc. London, Ser. A Math. Phys. Sci. (1982). https://doi.org/10.1098/rspa.1982.0088.

[92] M. Benedetti, A. du Plessis, R.O. Ritchie, M. Dallago, S.M.J. Razavi, F. Berto, Architected cellular materials: A review on their mechanical properties towards fatigue-tolerant design and fabrication, Mater. Sci. Eng. R Reports. (2021). https://doi.org/10.1016/j.mser.2021.100606.

[93] E. Hernández-Nava, C.J. Smith, F. Derguti, S. Tammas-Williams, F. Léonard, P.J. Withers, I. Todd, R. Goodall, The effect of density and feature size on mechanical properties of isostructural metallic foams produced by additive manufacturing, Acta Mater. (2015). https://doi.org/10.1016/j.actamat.2014.10.058.

[94] C. Yan, L. Hao, A. Hussein, P. Young, Ti-6Al-4V triply periodic minimal surface structures for bone implants fabricated via selective laser melting, J. Mech. Behav. Biomed. Mater. (2015). https://doi.org/10.1016/j.jmbbm.2015.06.024.

[95] J. Kadkhodapour, H. Montazerian, A.C. Darabi, A.P. Anaraki, S.M. Ahmadi, A.A. Zadpoor, S. Schmauder, Failure mechanisms of additively manufactured porous biomaterials: Effects of porosity and type of unit cell, J. Mech. Behav. Biomed. Mater. (2015). https://doi.org/10.1016/j.jmbbm.2015.06.012.

[96] H.E. Burton, N.M. Eisenstein, B.M. Lawless, P. Jamshidi, M.A. Segarra, O. Addison, D.E.T. Shepherd, M.M. Attallah, L.M. Grover, S.C. Cox, The design of additively manufactured lattices to increase the functionality of medical implants, Mater. Sci. Eng. C. (2019). https://doi.org/10.1016/j.msec.2018.10.052.

[97] M. Dallago, V. Fontanari, E. Torresani, M. Leoni, C. Pederzolli, C. Potrich, M. Benedetti, Fatigue and biological properties of Ti-6Al-4V ELI cellular structures with variously arranged cubic cells made by selective laser melting, J. Mech. Behav. Biomed. Mater. (2018). https://doi.org/10.1016/j.jmbbm.2017.11.044.

[98] S.Y. Chen, J.C. Huang, C.T. Pan, C.H. Lin, T.L. Yang, Y.S. Huang, C.H. Ou, L.Y. Chen, D.Y. Lin, H.K. Lin, T.H. Li, J.S.C. Jang, C.C. Yang, Microstructure and mechanical properties of open-cell porous Ti-6Al-4V fabricated by selective laser melting, J. Alloys Compd. (2017). https://doi.org/10.1016/j.jallcom.2017.04.190.

[99] V. Weißmann, R. Bader, H. Hansmann, N. Laufer, Influence of the structural orientation on the mechanical properties of selective laser melted Ti6Al4V open-porous scaffolds, Mater. Des. (2016). https://doi.org/10.1016/j.matdes.2016.01.095.

[100] L. Bai, J. Zhang, Y. Xiong, X. Chen, Y. Sun, Influence of unit cell pose on the mechanical properties of Ti6Al4V lattice structures manufactured by selective laser melting, Addit. Manuf. (2020). https://doi.org/10.1016/j.addma.2020.101222.

[101] S.J. Li, L.E. Murr, X.Y. Cheng, Z.B. Zhang, Y.L. Hao, R. Yang, F. Medina, R.B. Wicker, Compression fatigue behavior of Ti-6Al-4V mesh arrays fabricated by electron beam melting, Acta Mater. (2012). https://doi.org/10.1016/j.actamat.2011.10.051.

[102] Y.J. Liu, D.C. Ren, S.J. Li, H. Wang, L.C. Zhang, T.B. Sercombe, Enhanced fatigue characteristics of a topology-optimized porous titanium structure produced by selective laser melting, Addit. Manuf. (2020). https://doi.org/10.1016/j.addma.2020.101060.

[103] M.W. Wu, J.K. Chen, B.H. Lin, P.H. Chiang, M.K. Tsai, Compressive fatigue properties of additive-manufactured Ti-6Al-4V cellular material with different porosities, Mater. Sci. Eng. A. (2020). https://doi.org/10.1016/j.msea.2020.139695.

[104] S. Van Bael, Y.C. Chai, S. Truscello, M. Moesen, G. Kerckhofs, H. Van Oosterwyck, J.P. Kruth, J. Schrooten, The effect of pore geometry on the in vitro biological behavior of

human periosteum-derived cells seeded on selective laser-melted Ti6Al4V bone scaffolds, Acta Biomater. (2012). https://doi.org/10.1016/j.actbio.2012.04.001.

[105] K.C. Nune, A. Kumar, R.D.K. Misra, Functional response of osteoblasts in functionally gradient titanium alloy mesh arrays processed by 3D additive manufacturing, Colloids Surfaces B Biointerfaces. (2017). https://doi.org/10.1016/j.colsurfb.2016.09.050.

[106] A. Bandyopadhyay, F. Espana, V.K. Balla, S. Bose, Y. Ohgami, N.M. Davies, Influence of porosity on mechanical properties and in vivo response of Ti6Al4V implants, Acta Biomater. (2010). https://doi.org/10.1016/j.actbio.2009.11.011.

[107] B. Zhang, X. Pei, C. Zhou, Y. Fan, Q. Jiang, A. Ronca, U. D'Amora, Y. Chen, H. Li, Y. Sun, X. Zhang, The biomimetic design and 3D printing of customized mechanical properties porous Ti6Al4V scaffold for load-bearing bone reconstruction, Mater. Des. (2018). https://doi.org/10.1016/j.matdes.2018.04.065.

[108] J. Vaithilingam, S. Kilsby, R.D. Goodridge, S.D.R. Christie, S. Edmondson, R.J.M. Hague, Functionalisation of Ti6Al4V components fabricated using selective laser melting with a bioactive compound, Mater. Sci. Eng. C. (2015). https://doi.org/10.1016/j.msec.2014.10.015.

[109] S.C. Cox, P. Jamshidi, N.M. Eisenstein, M.A. Webber, H. Hassanin, M.M. Attallah, D.E.T. Shepherd, O. Addison, L.M. Grover, Adding functionality with additive manufacturing: Fabrication of titanium-based antibiotic eluting implants, Mater. Sci. Eng. C. (2016). https://doi.org/10.1016/j.msec.2016.04.006.

[110] M. Bezuidenhout, E. Booysen, A.D.P. van Staden, E.H.A. Uheida, P.A. Hugo, G.A. Oosthuizen, D.M. Dimitrov, L.M.T. Dicks, Selective Laser Melting of Integrated Ti6Al4V ELI Permeable Walls for Controlled Drug Delivery of Vancomycin, ACS Biomater. Sci. Eng. (2018). https://doi.org/10.1021/acsbiomaterials.8b00676.

[111] J. Vaithilingam, S. Kilsby, R.D. Goodridge, Immobilisation of an antibacterial drug to Ti6Al4V components fabricated using selective laser melting, Appl. Surf. Sci. (2014). https://doi.org/10.1016/j.apsusc.2014.06.014.

[112] I.A.J. van Hengel, M. Riool, L.E. Fratila-Apachitei, J. Witte-Bouma, Selective laser melting porous metallic implants with immobilized silver nanoparticles kill and prevent biofilm formation by methicillin-resistant Staphylococcus aureus, Biomaterials. (2017). https://doi.org/10.1016/j.biomaterials.2017.02.030.

[113] M.S. Zafar, M.A. Fareed, S. Riaz, M. Latif, Customized therapeutic surface coatings for dental implants, Coatings. (2020). https://doi.org/10.3390/coatings10060568.

[114] F.P.W. Melchels, M.A.N. Domingos, T.J. Klein, J. Malda, P.J. Bartolo, D.W. Hutmacher, Additive manufacturing of tissues and organs, Prog. Polym. Sci. (2012). https://doi.org/10.1016/j.progpolymsci.2011.11.007.

[115] M. Zilberman, J.J. Elsner, Antibiotic-eluting medical devices for various applications, J. Control. Release. (2008). https://doi.org/10.1016/j.jconrel.2008.05.020.

[116] A. Awad, F. Fina, A. Goyanes, S. Gaisford, A.W. Basit, Advances in powder bed fusion 3D printing in drug delivery and healthcare, Adv. Drug Deliv. Rev. (2021). https://doi.org/10.1016/j.addr.2021.04.025.

[117] N.L. Loh, K.Y. Sia, An overview of hot isostatic pressing, J. Mater. Process. Tech. (1992). https://doi.org/10.1016/0924-0136(92)90038-T.

[118] M.H. Bernal, Hot isostatic pressing (HIP) technology and its applications to metals and ceramics, J. Mater. Sci. https://doi.org/10.1023/B:JMSC.0000044878.11441.90.

[119] H. V. Atkinson, S. Davies, Fundamental aspects of hot isostatic pressing: An overview, Metall. Mater. Trans. A Phys. Metall. Mater. Sci. (2000). https://doi.org/10.1007/s11661-000-0078-2.

[120] C. Qiu, N.J.E. Adkins, M.M. Attallah, Microstructure and tensile properties of selectively laser-melted and of HIPed laser-melted Ti-6Al-4V, Mater. Sci. Eng. A. (2013). https://doi.org/10.1016/j.msea.2013.04.099.

[121] M.W. Wu, P.H. Lai, The positive effect of hot isostatic pressing on improving the anisotropies of bending and impact properties in selective laser melted Ti-6Al-4V alloy, Mater. Sci. Eng. A. (2016). https://doi.org/10.1016/j.msea.2016.02.023.

[122] P. Jamshidi, M. Aristizabal, W. Kong, V. Villapun, S.C. Cox, L.M. Grover, M.M. Attallah, Selective Laser Melting of Ti-6Al-4V: The Impact of Post-processing on the Tensile, Fatigue and Biological Properties for Medical Implant Applications, Materials (Basel). (2020). https://doi.org/10.3390/ma13122813.

[123] C. Su, H. Yu, Z. Wang, J. Yang, X. Zeng, Controlling the tensile and fatigue properties of selective laser melted Ti–6Al–4V alloy by post treatment, J. Alloys Compd. (2021). https://doi.org/10.1016/j.jallcom.2020.157552.

[124] S. Marimuthu, A. Triantaphyllou, M. Antar, D. Wimpenny, H. Morton, M. Beard, Laser polishing of selective laser melted components, Int. J. Mach. Tools Manuf. (2015). https://doi.org/10.1016/j.ijmachtools.2015.05.002.

[125] E.M.M. Sutter, G.J. Goetz-Grandmont, The behaviour of titanium in nitric-hydrofluoric acid solutions, Corros. Sci. (1990). https://doi.org/10.1016/0010-938X(90)90051-6.

[126] American Society for Testing and Materials, ASTM E407-07e1: Standard practice for microetching metals and alloys, in: Annu. B. ASTM Stand., 2007. https://doi.org/10.1520/E0407-07.2.

[127] B. Wysocki, J. Idaszek, J. Buhagiar, K. Szlązak, T. Brynk, K.J. Kurzydłowski, W. Święszkowski, The influence of chemical polishing of titanium scaffolds on their mechanical strength and in-vitro cell response, Mater. Sci. Eng. C. (2019). https://doi.org/10.1016/j.msec.2018.04.019.

[128] L. Yang, C. Yan, W. Cao, Z. Liu, B. Song, S. Wen, C. Zhang, Y. Shi, S. Yang, Compression–compression fatigue behaviour of gyroid-type triply periodic minimal surface porous structures fabricated by selective laser melting, Acta Mater. (2019). https://doi.org/10.1016/j.actamat.2019.09.042.

[129] S.M. Ahmadi, R. Kumar, Y. Li, N. Tümer, R. Huizenga, C. Ayas, A.A. Zadpoor, V.A. Popovich, From microstructural design to surface engineering: A tailored approach for improving fatigue life of additively manufactured meta-biomaterials, Acta Biomater. (2019). https://doi.org/10.1016/j.actbio.2018.10.043.

[130] I. Kopova, J. Stráský, P. Harcuba, M. Landa, Newly developed Ti-Nb-Zr-Ta-Si-Fe biomedical beta titanium alloys with increased strength and enhanced biocompatibility, Mater. Sci. Eng. C. (2016). https://doi.org/10.1016/j.msec.2015.11.043.

[131] G. Lütjering, J.C. Williams, Titanium : Engineering Materials and Processes, Ed. SPRINGER. (2007).

[132] P.J. Bania, Beta titanium alloys and their role in the titanium industry, JOM. (1994). https://doi.org/10.1007/BF03220742.

[133] M. Motyka, K. Kubiak, J. Sieniawski, W. Ziaja, Phase Transformations and Characterization of α + β Titanium Alloys, in: Compr. Mater. Process., 2014. https://doi.org/10.1016/B978-0-08-096532-1.00202-8.

[134] T.C. Niemeyer, C.R. Grandini, L.M.C. Pinto, A.C.D. Angelo, S.G. Schneider, Corrosion behavior of Ti-13Nb-13Zr alloy used as a biomaterial, J. Alloys Compd. (2009). https://doi.org/10.1016/j.jallcom.2008.09.026.

[135] C.W. Lin, C.P. Ju, J.H. Chern Lin, A comparison of the fatigue behavior of cast Ti-7.5Mo with c.p. titanium, Ti-6Al-4V and Ti-13Nb-13Zr alloys, Biomaterials. (2005).

https://doi.org/10.1016/j.biomaterials.2004.09.007.

[136] S. Banumathy, R.K. Mandal, A.K. Singh, Structure of orthorhombic martensitic phase in binary Ti-Nb alloys, J. Appl. Phys. (2009). https://doi.org/10.1063/1.3255966.

[137] T.W. Duerig, G.T. Terlinde, J.C. Williams, Phase transformations and tensile properties of Ti-10V-2Fe-3AI, Metall. Trans. A. (1980). https://doi.org/10.1007/BF02655118.

[138] D. De Fontaine, N.E. Paton, J.C. Williams, The omega phase transformation in titanium alloys as an example of displacement controlled reactions, Acta Metall. (1971). https://doi.org/10.1016/0001-6160(71)90047-2.

[139] W.G. Brammer, C.G. Rhodes, Determination of omega phase morphology in Ti-35% Nb by transmission electron microscopy, Philos. Mag. (1967). https://doi.org/10.1080/14786436708220858.

[140] M. Morinaga, Alloy design based on molecular orbital method, Mater. Trans. (2016). https://doi.org/10.2320/matertrans.M2015418.

[141] J. Hwang, S. Kuramoto, T. Furuta, K. Nishino, T. Saito, Phase-stability dependence of plastic deformation behavior in Ti-Nb-Ta-Zr-O alloys, in: J. Mater. Eng. Perform., 2005. https://doi.org/10.1361/105994905X75556.

[142] M. Abdel-Hady, K. Hinoshita, M. Morinaga, General approach to phase stability and elastic properties of β-type Ti-alloys using electronic parameters, Scr. Mater. (2006). https://doi.org/10.1016/j.scriptamat.2006.04.022.

[143] P. Laheurte, F. Prima, A. Eberhardt, T. Gloriant, M. Wary, E. Patoor, Mechanical properties of low modulus β titanium alloys designed from the electronic approach, J. Mech. Behav. Biomed. Mater. (2010). https://doi.org/10.1016/j.jmbbm.2010.07.001.

[144] M. Arciniegas, J. Peña, J.M. Manero, J.C. Paniagua, F.J. Gil, Quantum parameters for guiding the design of Ti alloys with shape memory and/or low elastic modulus, Philos. Mag. (2008). https://doi.org/10.1080/14786430802375667.

[145] M. Morinaga, The molecular orbital approach and its application to biomedical titanium alloy design, in: Titan. Med. Dent. Appl., 2018. https://doi.org/10.1016/B978-0-12-812456-7.00003-2.

[146] D. Raabe, B. Sander, M. Friák, D. Ma, J. Neugebauer, Theory-guided bottom-up design of β-titanium alloys as biomaterials based on first principles calculations: Theory and experiments, Acta Mater. (2007). https://doi.org/10.1016/j.actamat.2007.04.024.

[147] E.S. Fisher, D. Dever, Relation of the c′ elastic modulus to stability of b.c.c. transition metals, Acta Metall. (1970). https://doi.org/10.1016/0001-6160(70)90033-7.

[148] M. Tane, S. Akita, T. Nakano, K. Hagihara, Y. Umakoshi, M. Niinomi, H. Mori, H. Nakajima, Low Young's modulus of Ti-Nb-Ta-Zr alloys caused by softening in shear moduli c′ and c44 near lower limit of body-centered cubic phase stability, Acta Mater. (2010). https://doi.org/10.1016/j.actamat.2010.09.007.

[149] N. Nagasako, R. Asahi, D. Isheim, D.N. Seidman, S. Kuramoto, T. Furuta, Microscopic study of gum-metal alloys: A role of trace oxygen for dislocation-free deformation, Acta Mater. (2016). https://doi.org/10.1016/j.actamat.2015.12.011.

[150] M. Niinomi, T. Hattori, K. Morikawa, T. Kasuga, A. Suzuki, H. Fukui, S. Niwa, Development of low rigidity β-type titanium alloy for biomedical applications, Mater. Trans. (2002). https://doi.org/10.2320/matertrans.43.2970.

[151] S. Guo, Q. Meng, X. Zhao, Q. Wei, H. Xu, Design and fabrication of a metastable β-type titanium alloy with ultralow elastic modulus and high strength, Sci. Rep. (2015). https://doi.org/10.1038/srep14688.

[152] S. Bahl, S. Das, S. Suwas, K. Chatterjee, Engineering the next-generation tin containing β titanium alloys with high strength and low modulus for orthopedic applications, J. Mech. Behav. Biomed. Mater. (2018). https://doi.org/10.1016/j.jmbbm.2017.11.014.

[153] S. Acharya, S. Bahl, S.S. Dabas, S. Hassan, V. Gopal, A.G. Panicker, G. Manivasagam, S. Suwas, K. Chatterjee, Role of aging induced α precipitation on the mechanical and tribocorrosive performance of a β Ti-Nb-Ta-O orthopedic alloy, Mater. Sci. Eng. C. (2019). https://doi.org/10.1016/j.msec.2019.109755.

[154] J.I. Qazi, B. Marquardt, Phase transformations in Ti-35Nb-7Zr-5Ta-(0.06-0.68)O alloys, in: Mater. Sci. Eng. C, 2005. https://doi.org/10.1016/j.msec.2005.01.022.

[155] C.H. Wang, C.D. Yang, M. Liu, X. Li, P.F. Hu, A.M. Russell, G.H. Cao, Martensitic microstructures and mechanical properties of as-quenched metastable β-type Ti–Mo alloys, J. Mater. Sci. (2016). https://doi.org/10.1007/s10853-016-9976-6.

[156] Y. Xu, J. Gao, Y. Huang, W.M. Rainforth, A low-cost metastable beta Ti alloy with high elastic admissible strain and enhanced ductility for orthopaedic application, J. Alloys Compd. (2020). https://doi.org/10.1016/j.jallcom.2020.155391.

[157] J.Y. Zhang, J.S. Li, Z. Chen, Q.K. Meng, F. Sun, B.L. Shen, Microstructural evolution of a ductile metastable β titanium alloy with combined TRIP/TWIP effects, J. Alloys

Compd. (2017). https://doi.org/10.1016/j.jallcom.2016.12.394.

[158] S.A. Mantri, F. Sun, D. Choudhuri, T. Alam, B. Gwalani, F. Prima, R. Banerjee, Deformation Induced Hierarchical Twinning Coupled with Omega Transformation in a Metastable β-Ti Alloy, Sci. Rep. (2019). https://doi.org/10.1038/s41598-018-37865-0.

[159] S. Nagn, R. Banerjee, Laser deposition and deformation behavior of Ti-Nb-Zr-Ta alloys for orthopedic implan, J. Mech. Behav. Biomed. Mater. (2012).

[160] L. Yan, Y. Yuan, L. Ouyang, H. Li, Improved mechanical properties of the new Ti-15Ta-xZr alloys fabricated by selective laser melting for biomedical application, J. Alloys Compd. (2016). https://doi.org/10.1016/j.jallcom.2016.07.002.

[161] E.G. Brodie, A.E. Medvedev, J.E. Frith, M.S. Dargusch, H.L. Fraser, A. Molotnikov, Remelt processing and microstructure of selective laser melted Ti25Ta, J. Alloys Compd. (2020). https://doi.org/10.1016/j.jallcom.2019.153082.

[162] L. Zhang, E.M. Haddouti, K. Welle, C. Burger, D.C. Wirtz, F.A. Schildberg, K. Kabir, The Effects of Biomaterial Implant Wear Debris on Osteoblasts, Front. Cell Dev. Biol. (2020). https://doi.org/10.3389/fcell.2020.00352.

[163] S.J. Li, R. Yang, S. Li, Y.L. Hao, Y.Y. Cui, M. Niinomi, Z.X. Guo, Wear characteristics of Ti-Nb-Ta-Zr and Ti-6Al-4V alloys for biomedical applications, Wear. (2004). https://doi.org/10.1016/j.wear.2004.04.001.

[164] I. Cvijović-Alagić, Z. Cvijović, S. Mitrović, V. Panić, M. Rakin, Wear and corrosion behaviour of Ti-13Nb-13Zr and Ti-6Al-4V alloys in simulated physiological solution, Corros. Sci. (2011). https://doi.org/10.1016/j.corsci.2010.11.014.

[165] S. Ehtemam-Haghighi, K.G. Prashanth, Evaluation of mechanical and wear properties of Ti[sbnd]xNb[sbnd]7Fe alloys designed for biomedical applications, Mater. Des. (2016). https://doi.org/10.1016/j.matdes.2016.09.029.

[166] A.C. Hee, P.J. Martin, A. Bendavid, S.S. Jamali, Y. Zhao, Tribo-corrosion performance of filtered-arc-deposited tantalum coatings on Ti-13Nb-13Zr alloy for bio-implants applications, Wear. (2018). https://doi.org/10.1016/j.wear.2017.12.017.

[167] M. Karthega, V. Raman, N. Rajendran, Influence of potential on the electrochemical behaviour of β titanium alloys in Hank's solution, Acta Biomater. (2007). https://doi.org/10.1016/j.actbio.2007.02.009.

[168] E. dos S. Monteiro, F. Moura de Souza Soares, L.F. Nunes, A.I. Carvalho Santana,

Comparison of the wettability and corrosion resistance of two biomedical Ti alloys free of toxic elements with those of the commercial ASTM F136 (Ti–6Al–4V) alloy, J. Mater. Res. Technol. (2020). https://doi.org/10.1016/j.jmrt.2020.11.068.

[169] M.A. Khan, R.L. Williams, D.F. Williams, The corrosion behaviour of Ti-6Al-4V, Ti-6Al-7Nb and Ti-13Nb-13Zr in protein solutions, Biomaterials. (1999). https://doi.org/10.1016/S0142-9612(98)00217-8.

[170] Y. Okazaki, E. Gotoh, Comparison of metal release from various metallic biomaterials in vitro, Biomaterials. (2005). https://doi.org/10.1016/j.biomaterials.2004.02.005.

[171] N.T.C. Oliveira, A.C. Guastaldi, Electrochemical behavior of Ti-Mo alloys applied as biomaterial, Corros. Sci. (2008). https://doi.org/10.1016/j.corsci.2007.09.009.

[172] M. Geetha, A.K. Singh, R. Asokamani, A.K. Gogia, Ti based biomaterials, the ultimate choice for orthopaedic implants - A review, Prog. Mater. Sci. (2009).

[173] A. Panigrahi, B. Sulkowski, T. Waitz, K. Ozaltin, W. Chrominski, A. Pukenas, J. Horky, M. Lewandowska, Mechanical properties, structural and texture evolution of biocompatible Ti–45Nb alloy processed by severe plastic deformation, J. Mech. Behav. Biomed. Mater. (2016). https://doi.org/10.1016/j.jmbbm.2016.04.042.

[174] D. Kuroda, T. Yashiro, M. Niinomi, Y. Kato, M. Morinaga, Design and mechanical properties of new β type titanium alloys for implant materials, Mater. Sci. Eng. A. (2002). https://doi.org/10.1016/s0921-5093(97)00808-3.

[175] X. Min, X. Chen, S. Emura, Mechanism of twinning-induced plasticity in β-type Ti-15Mo alloy, Scr. Mater. (2013). https://doi.org/10.1016/j.scriptamat.2013.05.027.

[176] T. Ishimoto, K. Hagihara, K. Hisamoto, S.H. Sun, T. Nakano, Crystallographic texture control of beta-type Ti–15Mo–5Zr–3Al alloy by selective laser melting for the development of novel implants with a biocompatible low Young's modulus, Scr. Mater. (2017). https://doi.org/10.1016/j.scriptamat.2016.12.038.

[177] S.L. Sing, W.Y. Yeong, F.E. Wiria, Selective laser melting of titanium alloy with 50 wt% tantalum: Microstructure and mechanical properties, J. Alloys Compd. (2016). https://doi.org/10.1016/j.jallcom.2015.11.141.

[178] M. Niinomi, Fatigue performance and cyto-toxicity of low rigidity titanium alloy, Ti-29Nb-13Ta-4.6Zr, Biomaterials. (2003). https://doi.org/10.1016/S0142-9612(03)00069-3.

[179] S.J. Li, T.C. Cui, Y.L. Hao, R. Yang, Fatigue properties of a metastable β-type titanium alloy with reversible phase transformation, Acta Biomater. (2008). https://doi.org/10.1016/j.actbio.2007.09.009.

[180] K.Y. Xie, Y. Wang, Y. Zhao, L. Chang, G. Wang, Z. Chen, Y. Cao, X. Liao, E.J. Lavernia, R.Z. Valiev, B. Sarrafpour, H. Zoellner, S.P. Ringer, Nanocrystalline β-Ti alloy with high hardness, low Young's modulus and excellent in vitro biocompatibility for biomedical applications, Mater. Sci. Eng. C. (2013). https://doi.org/10.1016/j.msec.2013.04.044.

[181] K. Miura, N. Yamada, S. Hanada, T.K. Jung, E. Itoi, The bone tissue compatibility of a new Ti-Nb-Sn alloy with a low Young's modulus, Acta Biomater. (2011). https://doi.org/10.1016/j.actbio.2011.02.008.

[182] R. Ion, D.M. Gordin, V. Mitran, P. Osiceanu, S. Dinescu, T. Gloriant, A. Cimpean, In vitro bio-functional performances of the novel superelastic beta-type Ti-23Nb-0.7Ta-2Zr-0.5N alloy, Mater. Sci. Eng. C. (2014). https://doi.org/10.1016/j.msec.2013.11.018.

[183] Y. Zhang, J. Wang, P. Wang, X. Fan, X. Li, J. Fu, S. Li, H. Fan, Z. Guo, Low elastic modulus contributes to the osteointegration of titanium alloy plug, J. Biomed. Mater. Res. - Part B Appl. Biomater. (2013). https://doi.org/10.1002/jbm.b.32860.

[184] H. Matsuno, A. Yokoyama, F. Watari, M. Uo, T. Kawasaki, Biocompatibility and osteogenesis of refractory metal implants, titanium, hafnium, niobium, tantalum and rhenium, Biomaterials. (2001). https://doi.org/10.1016/S0142-9612(00)00275-1.

[185] M. Fousová, D. Vojtěch, J. Kubásek, E. Jablonská, J. Fojt, Promising characteristics of gradient porosity Ti-6Al-4V alloy prepared by SLM process, J. Mech. Behav. Biomed. Mater. (2017). https://doi.org/10.1016/j.jmbbm.2017.01.043.

[186] D. Kuroda, M. Niinomi, M. Morinaga, Y. Kato, T. Yashiro, Design and mechanical properties of new β type titanium alloys for implant materials, Mater. Sci. Eng. A. (1998). https://doi.org/10.1016/s0921-5093(97)00808-3.

[187] S. Amin Yavari, R. Wauthle, J. Van Der Stok, A.C. Riemslag, M. Janssen, M. Mulier, J.P. Kruth, J. Schrooten, H. Weinans, A.A. Zadpoor, Fatigue behavior of porous biomaterials manufactured using selective laser melting, Mater. Sci. Eng. C. (2013). https://doi.org/10.1016/j.msec.2013.08.006.

[188] N. Sakaguchi, M. Niinomi, T. Akahori, J. Takeda, H. Toda, Relationships between tensile deformation behavior and microstructure in Ti-Nb-Ta-Zr system alloys, in: Mater. Sci. Eng. C, 2005. https://doi.org/10.1016/j.msec.2004.12.014.

[189] Y.S. Zhukova, Y.A. Pustov, A.S. Konopatsky, S.M. Dubinskiy, M.R. Filonov, V. Brailovski, Corrosion fatigue and electrochemical behavior of superelastic Ti-Nb-Ta alloy for medical implants under cyclic load conditions, Mater. Today Proc. (2015). https://doi.org/10.1016/j.matpr.2015.07.448.

[190] D.L. Bourell, Perspectives on Additive Manufacturing, Annu. Rev. Mater. Res. (2016). https://doi.org/10.1146/annurev-matsci-070115-031606.

[191] L.E. Murr, S.M. Gaytan, D.A. Ramirez, E. Martinez, J. Hernandez, K.N. Amato, P.W. Shindo, F.R. Medina, R.B. Wicker, Metal Fabrication by Additive Manufacturing Using Laser and Electron Beam Melting Technologies, J. Mater. Sci. Technol. (2012). https://doi.org/10.1016/S1005-0302(12)60016-4.

[192] S. Wu, X. Liu, K.W.K. Yeung, Biomimetic porous scaffolds for bone tissue engineering, Mater. Sci. Eng. R Reports. (2014). https://doi.org/10.1016/j.mser.2014.04.001.

[193] H. Hassanin, L. Finet, S.C. Cox, D.E.T. Shepherd, O. Addison, M.M. Attallah, Tailoring selective laser melting process for titanium drug-delivering implants with releasing micro-channels, Addit. Manuf. (2018). https://doi.org/10.1016/j.addma.2018.01.005.

[194] T.A. Schaedler, W.B. Carter, Architected Cellular Materials, Annu. Rev. Mater. Res. (2016). https://doi.org/10.1146/annurev-matsci-070115-031624.

[195] G. Lütjering, J.C. Williams, Titanium : Engineering Materials and Processes, 2007. https://doi.org/10.1007/978-3-540-73036-1.

[196] Y.L. Hao, S.J. Li, F. Prima, R. Yang, Controlling reversible martensitic transformation in titanium alloys with high strength and low elastic modulus, Scr. Mater. (2012). https://doi.org/10.1016/j.scriptamat.2012.06.011.

[197] C.Y. Yap, C.K. Chua, Z.L. Dong, Z.H. Liu, D.Q. Zhang, L.E. Loh, S.L. Sing, Review of selective laser melting: Materials and applications, Appl. Phys. Rev. (2015). https://doi.org/10.1063/1.4935926.

[198] ASTM E8, ASTM E8/E8M standard test methods for tension testing of metallic materials 1, Annu. B. ASTM Stand. 4. (2010). https://doi.org/10.1520/E0008.

[199] E384-17, Standard Test Method for Microindentation Hardness of Materials, ASTM B. Stand. (2017). https://doi.org/10.1520/E0384-17.

[200] A. International, Standard Guide for Quantitating Cell Viability Within Biomaterial Scaffolds 1, Annu. B. ASTM Stand. (2011). https://doi.org/10.1520/F2739-08.2.

[201] Y.L. Hao, S.J. Li, S.Y. Sun, R. Yang, Effect of Zr and Sn on Young's modulus and superelasticity of Ti-Nb-based alloys, Mater. Sci. Eng. A. (2006). https://doi.org/10.1016/j.msea.2006.09.051.

[202] Y. Zhang, Thermodynamic assessment of the Nb-Ti system, Calphad Comput. Coupling Phase Diagrams Thermochem. (2001). https://doi.org/10.1016/S0364-5916(01)00051-7.

[203] E. Clementi, D.L. Raimondi, W.P. Reinhardt, Atomic screening constants from SCF functions. II. Atoms with 37 to 86 electrons, J. Chem. Phys. (1967). https://doi.org/10.1063/1.1712084.

[204] D.L. Dorset, X-ray Diffraction: A Practical Approach, Microsc. Microanal. (1998). https://doi.org/10.1017/S143192769800049X.

[205] H. Men, Z. Fan, Effects of solute content on grain refinement in an isothermal melt, Acta Mater. (2011). https://doi.org/10.1016/j.actamat.2011.01.008.

[206] S.L. Sing, J. An, W.Y. Yeong, F.E. Wiria, Laser and electron-beam powder-bed additive manufacturing of metallic implants: A review on processes, materials and designs, J. Orthop. Res. (2016). https://doi.org/10.1002/jor.23075.

[207] M. Surmeneva, I. Grubova, N. Glukhova, D. Khrapov, A. Koptyug, A. Volkova, Y. Ivanov, C.M. Cotrut, A. Vladescu, A. Teresov, N. Koval, A. Tyurin, R. Surmenev, New ti–35nb–7zr–5ta alloy manufacturing by electron beam melting for medical application followed by high current pulsed electron beam treatment, Metals (Basel). (2021). https://doi.org/10.3390/met11071066.

[208] Y. Li, J. Qi, R. Fan, C. Zhai, C. Xu, In-situ TEM observation of phase transformation for bio-medical shape memory TiNbSn alloy, in: Adv. Mater. Res., 2011. https://doi.org/10.4028/www.scientific.net/AMR.152-153.1755.

[209] Y. Mantani, M. Tajima, Phase transformation of quenched α″ martensite by aging in Ti-Nb alloys, Mater. Sci. Eng. A. (2006). https://doi.org/10.1016/j.msea.2006.02.180.

[210] J.C. Wang, Y.J. Liu, P. Qin, S.X. Liang, T.B. Sercombe, L.C. Zhang, Selective laser melting of Ti–35Nb composite from elemental powder mixture: Microstructure, mechanical behavior and corrosion behavior, Mater. Sci. Eng. A. (2019). https://doi.org/10.1016/j.msea.2019.06.001.

[211] J.P. Luo, J.F. Sun, Y.J. Huang, J.H. Zhang, Low-modulus biomedical Ti–30Nb–5Ta–3Zr additively manufactured by Selective Laser Melting and its biocompatibility, Mater. Sci. Eng. C. (2019). https://doi.org/10.1016/j.msec.2018.11.077.

[212] M. Niinomi, Mechanical properties of biomedical titanium alloys, Mater. Sci. Eng. A. (1998). https://doi.org/10.1016/s0921-5093(97)00806-x.

[213] L. Priester, Grain Boundaries: From Theory to Engineering, 2013.

[214] J.C. Williams, B.S. Hickman, The effect of omega phase on the mechanical properties of titanium alloys, Metall. Trans. (1971). https://doi.org/10.1007/BF02913423.

[215] Y.M. Wang, T. Voisin, J.T. McKeown, J. Ye, N.P. Calta, Z. Li, Z. Zeng, Y. Zhang, W. Chen, T.T. Roehling, R.T. Ott, M.K. Santala, P.J. Depond, M.J. Matthews, A. V. Hamza, T. Zhu, Additively manufactured hierarchical stainless steels with high strength and ductility, Nat. Mater. (2018). https://doi.org/10.1038/NMAT5021.

[216] M.G. Zywiel, J.M. Brandt, C.B. Overgaard, A.C. Cheung, T.R. Turgeon, K.A. Syed, Fatal cardiomyopathy after revision total hip replacement for fracture of a ceramic liner, J. Bone Jt. Surg. - Ser. B. (2013). https://doi.org/10.1302/0301-620X.95B1.30060.

[217] M. Gunaratnam, M.H. Grant, The interaction of the orthopaedic metals, chromium VI and nickel, with hepatocytes, in: J. Mater. Sci. Mater. Med., 2001. https://doi.org/10.1023/A:1012848729592.

[218] R. Ummethala, P.S. Karamched, S. Rathinavelu, N. Singh, A. Aggarwal, K. Sun, E. Ivanov, Selective laser melting of high-strength, low-modulus Ti–35Nb–7Zr–5Ta alloy, Materialia. (2020). https://doi.org/10.1016/j.mtla.2020.100941.

[219] W. Kong, S.C. Cox, Y. Lu, V. Villapun, The influence of zirconium content on the microstructure, mechanical properties, and biocompatibility of in-situ alloying Ti-Nb-Ta based β alloys processed by selective laser melting, Mater. Sci. Eng. C. 131 (2021) 112486. https://doi.org/10.1016/J.MSEC.2021.112486.

[220] E466-15, Practice for conducting force controlled constant amplitude axial fatigue tests of metallic materials, ASTM B. Stand. (2015). https://doi.org/10.1520/E0466-15.2.

[221] J. Stráský, P. Harcuba, K. Václavová, K. Horváth, M. Landa, O. Srba, M. Janeček, Increasing strength of a biomedical Ti-Nb-Ta-Zr alloy by alloying with Fe, Si and O, J. Mech. Behav. Biomed. Mater. (2017). https://doi.org/10.1016/j.jmbbm.2017.03.026.

[222] M. Calin, A. Helth, J.J. Gutierrez Moreno, M. Bönisch, V. Brackmann, L. Giebeler, T. Gemming, C.E. Lekka, A. Gebert, R. Schnettler, J. Eckert, Elastic softening of β-type Ti-Nb alloys by indium (In) additions, J. Mech. Behav. Biomed. Mater. (2014). https://doi.org/10.1016/j.jmbbm.2014.07.010.

[223] T.G. Spears, S.A. Gold, In-process sensing in selective laser melting (SLM) additive manufacturing, Integr. Mater. Manuf. Innov. (2016). https://doi.org/10.1186/s40192-016-0045-4.

[224] H.Y. Kim, Y. Ikehara, J.I. Kim, H. Hosoda, S. Miyazaki, Martensitic transformation, shape memory effect and superelasticity of Ti-Nb binary alloys, Acta Mater. (2006). https://doi.org/10.1016/j.actamat.2006.01.019.

[225] W.A. Soffa, D.E. Laughlin, Diffusional Phase Transformations in the Solid State, in: Phys. Metall. Fifth Ed., 2014. https://doi.org/10.1016/B978-0-444-53770-6.00008-3.

[226] M.Y. Gutkin, T. Ishizaki, S. Kuramoto, I.A. Ovid'ko, Nanodisturbances in deformed Gum Metal, Acta Mater. (2006). https://doi.org/10.1016/j.actamat.2006.01.027.

[227] X. Tang, T. Ahmed, H.J. Rack, Phase transformations in Ti-Nb-Ta and Ti-Nb-Ta-Zr alloys, J. Mater. Sci. (2000). https://doi.org/10.1023/A:1004792922155.

[228] A.J. Ardell, On the coarsening of grain boundary precipitates, Acta Metall. (1972). https://doi.org/10.1016/0001-6160(72)90015-6.

[229] W.F. Hosford, Mechanical behavior of materials, 2005.

[230] L.L. Chang, Y.D. Wang, Y. Ren, In-situ investigation of stress-induced martensitic transformation in Ti-Nb binary alloys with low Young's modulus, Mater. Sci. Eng. A. (2016). https://doi.org/10.1016/j.msea.2015.11.005.

[231] L.P. Pook, N.E. Frost, A fatigue crack growth theory, Int. J. Fract. (1973). https://doi.org/10.1007/BF00035955.

[232] G. Shanbhag, E. Wheat, S. Moylan, M. Vlasea, Effect of specimen geometry and orientation on tensile properties of Ti-6Al-4V manufactured by electron beam powder bed fusion, Addit. Manuf. (2021). https://doi.org/10.1016/j.addma.2021.102366.

[233] Y. Okazaki, E. Gotoh, Corrosion resistance, mechanical properties, fatigue properties, and tissue response of Ti-15Zr-4Nb-4Ta alloy, J. ASTM Int. (2005). https://doi.org/10.1520/jai12783.

[234] L.S. Wei, H.Y. Kim, T. Koyano, S. Miyazaki, Effects of oxygen concentration and temperature on deformation behavior of Ti-Nb-Zr-Ta-O alloys, Scr. Mater. (2016). https://doi.org/10.1016/j.scriptamat.2016.05.043.

[235] K. Yokota, A. Bahador, K. Shitara, J. Umeda, K. Kondoh, Mechanisms of tensile

strengthening and oxygen solid solution in single β-phase Ti-35 at.%Ta+O alloys, Mater. Sci. Eng. A. (2021). https://doi.org/10.1016/j.msea.2020.140677.

[236] J. Wang, W. Xiao, L. Ren, Y. Fu, C. Ma, The roles of oxygen content on microstructural transformation, mechanical properties and corrosion resistance of Ti-Nb-based biomedical alloys with different β stabilities, Mater. Charact. (2021). https://doi.org/10.1016/j.matchar.2021.111122.

[237] L. Umbelino dos Santos, K.N. Campo, Oxygen addition in biomedical Ti–Nb alloys with low Nb contents: Effect on the microstructure and mechanical properties, Mater. Sci. Eng. A. (2021). https://doi.org/10.1016/j.msea.2021.141750.

[238] A. Najdahmadi, A. Zarei-Hanzaki, E. Farghadani, Mechanical properties enhancement in Ti-29Nb-13Ta-4.6Zr alloy via heat treatment with no detrimental effect on its biocompatibility, Mater. Des. (2014). https://doi.org/10.1016/j.matdes.2013.09.007.

[239] ASTM, E1409-13: Standard Test Method for Determination of Oxygen and Nitrogen in Titanium and Titanium Alloys by Inert Gas Fusion, ASTM Stand. (2013).

[240] W. Kong, S.C. Cox, Y. Lu, V. Villapun, X. Xiao, W. Ma, M. Liu, M.M. Attallah, The influence of zirconium content on the microstructure, mechanical properties, and biocompatibility of in-situ alloying Ti-Nb-Ta based β alloys processed by selective laser melting, Mater. Sci. Eng. C. (2021). https://doi.org/10.1016/j.msec.2021.112486.

[241] S. Tammas-Williams, P.J. Withers, I. Todd, P.B. Prangnell, The Effectiveness of Hot Isostatic Pressing for Closing Porosity in Titanium Parts Manufactured by Selective Electron Beam Melting, Metall. Mater. Trans. A Phys. Metall. Mater. Sci. (2016). https://doi.org/10.1007/s11661-016-3429-3.

[242] Z. Liu, G. Welsch, Effects of oxygen and heat treatment on the mechanical properties of alpha and beta titanium alloys, Metall. Trans. A. (1988).

[243] M. V. Speight, Growth kinetics of grain-boundary precipitates, Acta Metall. (1968). https://doi.org/10.1016/0001-6160(68)90081-3.

[244] J.I. Qazi, V. Tsakiris, B. Marquardt, H.J. Rack, Effect of aging treatments on the tensile properties of Ti-35Nb-7Zr-5Ta-(0.06-0.7)O alloys, J. ASTM Int. (2005). https://doi.org/10.1520/jai12780.

[245] A. Ramarolahy, P. Castany, F. Prima, P. Laheurte, Microstructure and mechanical behavior of superelastic Ti-24Nb-0.5O and Ti-24Nb-0.5N biomedical alloys, J. Mech. Behav. Biomed. Mater. (2012). https://doi.org/10.1016/j.jmbbm.2012.01.017.

[246] Q. Yu, L. Qi, T. Tsuru, R. Traylor, D. Rugg, J.W. Morris, M. Asta, D.C. Chrzan, A.M. Minor, Origin of dramatic oxygen solute strengthening effect in titanium, Science (80-.). (2015). https://doi.org/10.1126/science.1260485.

[247] N. Chaari, D. Rodney, E. Clouet, Oxygen - Dislocation interaction in zirconium from first principles, Acta Mater. (2017). https://doi.org/10.1016/j.actamat.2017.05.008.

[248] P.J. Yang, Q.J. Li, W.Z. Han, J. Li, E. Ma, Designing solid solution hardening to retain uniform ductility while quadrupling yield strength, Acta Mater. (2019). https://doi.org/10.1016/j.actamat.2019.08.024.

[249] P. Moretti, M.C. Miguel, M. Zaiser, S. Zapperi, Depinning transition of dislocation assemblies: Pileups and low-angle grain boundaries, Phys. Rev. B - Condens. Matter Mater. Phys. (2004). https://doi.org/10.1103/PhysRevB.69.214103.

[250] W.F. Cui, A.H. Guo, Microstructures and properties of biomedical TiNbZrFe β-titanium alloy under aging conditions, Mater. Sci. Eng. A. (2009).

[251] P.J. Withers, H.K.D.H. Bhadeshia, Residual stress part 1 - Measurement techniques, Mater. Sci. Technol. (2001). https://doi.org/10.1179/026708301101509980.

[252] S. Lynch, A review of underlying reasons for intergranular cracking for a variety of failure modes and materials and examples of case histories, Eng. Fail. Anal. (2019). https://doi.org/10.1016/j.engfailanal.2019.02.027.

[253] D.R. Askeland, The science and engineering of materials - Seventh edition, Cengage Learn. (2016).

[254] I.N. Ackerman, L. Busija, M. Lorimer, R. de Steiger, S.E. Graves, Lifetime Risk of Revision Hip Replacement Surgery in Australia Remains Low: A Population-Level Analysis Using National Registry Data, J. Bone Joint Surg. Am. (2021). https://doi.org/10.2106/JBJS.20.01235.

[255] H. Güleryüz, F. Muhaffel, H. Çimenoğlu, Oxidized Titanium, in: Mater. Total Jt. Arthroplast., 2015. https://doi.org/10.1142/9781783267170_0012.

[256] L.C. Zhang, L.Y. Chen, A Review on Biomedical Titanium Alloys: Recent Progress and Prospect, Adv. Eng. Mater. (2019). https://doi.org/10.1002/adem.201801215.

[257] H. Dong, T. Bell, Enhanced wear resistance of titanium surfaces by a new thermal oxidation treatment, Wear. (2000). https://doi.org/10.1016/S0043-1648(99)00359-2.

[258] C. Van Der Straeten, Metal Bearings, in: Mater. Total Jt. Arthroplast., 2015. https://doi.org/10.1142/9781783267170_0004.

[259] H. Güleryüz, H. Çimenoğlu, Effect of thermal oxidation on corrosion and corrosion-wear behaviour of a Ti-6Al-4V alloy, Biomaterials. (2004).

[260] R.A. Buchanan, E.D. Rigney, J.M. Williams, Ion implantation of surgical Ti-6Al-4V for improved resistance to wear-accelerated corrosion, J. Biomed. Mater. Res. (1987). https://doi.org/10.1002/jbm.820210308.

[261] K. Piotrowska, P. Baranowicz, The Tribological Properties of the Ti6Al4V Alloy with Nitrogen ion implantation, Tribologia. (2019).

[262] H. Schmidt, A. Schminke, M. Schmiedgen, B. Baretzky, Compound formation and abrasion resistance of ion-implanted Ti6Al4V, Acta Mater. (2001). https://doi.org/10.1016/S1359-6454(00)00326-8.

[263] P. Budzynski, A.A. Youssef, J. Sielanko, Surface modification of Ti-6Al-4V alloy by nitrogen ion implantation, Wear. (2006). https://doi.org/10.1016/j.wear.2006.03.008.

[264] A. Edrisy, K. Farokhzadeh, Plasma Nitriding of Titanium Alloys, in: Plasma Sci. Technol. - Prog. Phys. States Chem. React., 2016. https://doi.org/10.5772/61937.

[265] H.J. Spies, B. Reinhold, K. Wilsdorf, Gas nitriding - Process control and nitriding non-ferrous alloys, Surf. Eng. (2001). https://doi.org/10.1179/026708401101517593.

[266] A. Czyrska-Filemonowicz, P.A. Buffat, M. Łucki, T. Moskalewicz, W. Rakowski, J.lekki, T. Wierzchoń, Transmission electron microscopy and atomic force microscopy characterisation of titanium-base alloys nitrided under glow discharge, Acta Mater. (2005). https://doi.org/10.1016/j.actamat.2005.05.035.

[267] D. Prando, A. Brenna, M.V. Diamanti, S. Beretta, F. Bolzoni, M. Ormellese, M.P. Pedeferri, Corrosion of titanium: Part 2: Effects of surface treatments, J. Appl. Biomater. Funct. Mater. (2018). https://doi.org/10.5301/jabfm.5000396.

[268] M. Abdel-Hady, K. Hinoshita, M. Morinaga, General approach to phase stability and elastic properties of β-type Ti-alloys using electronic parameters, Scr. Mater. (2006). https://doi.org/10.1016/j.scriptamat.2006.04.022.

[269] T. Akahori, M. Niinomi, M. Nakai, H. Nishimura, Y. Takei, H. Fukui, M. Ogawa, Wear and mechanical properties, and cell viability of gas-nitrided beta-type Ti-Nb-Ta-Zr

system alloy for biomedical applications, Mater. Trans. (2008). https://doi.org/10.2320/matertrans.MRA2007210.

[270] M. Nakai, M. Niinomi, T. Akahori, N. Ohtsu, H. Nishimura, H. Toda, H. Fukui, M. Ogawa, Surface hardening of biomedical Ti-29Nb-13Ta-4.6Zr and Ti-6Al-4V ELI by gas nitriding, Mater. Sci. Eng. A. (2008). https://doi.org/10.1016/j.msea.2007.08.065.

[271] H.J. Niu, I.T.H. Chang, Instability of scan tracks of selective laser sintering of high speed steel powder, Scr. Mater. (1999). https://doi.org/10.1016/S1359-6462(99)00276-6.

[272] Environmental Damage at High Temperature, in: High Temp. Deform. Fract. Mater., 2010. https://doi.org/10.1533/9780857090805.2.330.

[273] P. Kofstad, K. Hauffe, H. Kjöllesdal, P. Siekevitz, L. Ernster, E. Diczfalusy, Investigation on the Oxidation Mechanism of Titanium., Acta Chem. Scand. (1958). https://doi.org/10.3891/acta.chem.scand.12-0239.

[274] A. Rahmel, High temperature corrosion. Von P. Kofstad. Elsevier Applied Science Publishers Ltd., London - New York, 1988. 558 S., zahlr. Abb. u. Tab., Mater. Corros. Und Korrosion. (1988). https://doi.org/10.1002/maco.19880390713.

[275] C.E. Shamblen T.K. Redden, Air Contamination and embrittlement of titanium alloys, in: Sci. Technol. Appl. Titan., 1970. https://doi.org/10.1016/b978-0-08-006564-9.50027-0.

[276] Y.S. Park, D.P. Butt, Composition dependence of the kinetics and mechanisms of thermal oxidation of titanium-tantalum alloys, Oxid. Met. (1999).

[277] K.J. Laidler, The development of the arrhenius equation, J. Chem. Educ. (1984). https://doi.org/10.1021/ed061p494.

[278] I. Hutchings, P. Shipway, Tribology: Friction and wear of engineering materials: Second Edition, 2017.

[279] H. Dong, Surface engineering of light alloys: Aluminium, magnesium and titanium alloys, 2010. https://doi.org/10.1533/9781845699451.

[280] J. Jiang, F.H. Stott, M.M. Stack, Some frictional features associated with the sliding wear of the nickel-base alloy N80A at temperatures to 250 °C, Wear. (1994). https://doi.org/10.1016/0043-1648(94)90146-5.

[281] T. Bell, H.W. Bergmann, J. Lanagan, P.H. Morton, A.M. Staines, Surface engineering of

titanium with nitrogen, Surf. Eng. (1986). https://doi.org/10.1179/sur.1986.2.2.133.

[282] C.X. Li, D. Horspool, H. Dong, Effect of ceramic conversion surface treatment on fatigue properties of Ti6Al4V alloy, Int. J. Fatigue. (2007).

[283] M. Cingi, O. Meydanoglu, H. Guleryuz, M. Baydogan, H. Cimenoglu, S. Kayali, High Cycle Fatigue Behavior of Thermally Oxidized Ti6Al4V Alloy, Mater. Sci. Forum. (2007). https://doi.org/10.4028/www.scientific.net/msf.561-565.2179.

[284] K. Tokaji, T. Ogawa, H. Shibata, The Effects of Gas Nitriding on Fatigue Behavior in Titanium and Titanium Alloys, J. Mater. Eng. Perform. (1999). https://doi.org/10.1361/105994999770346990.

[285] M. Long, R. Crooks, H.J. Rack, High-cycle fatigue performance of solution-treated metastable-β titanium alloys, Acta Mater. (1999). https://doi.org/10.1016/S1359-6454(98)00343-7.

[286] P.P. Milella, Morphological Aspects of Fatigue Crack Formation and Growth, in: Fatigue Corros. Met., 2013. https://doi.org/10.1007/978-88-470-2336-9_2.

[287] D. Eylon, C.M. Pierce, Effect of microstructure on notch fatigue properties of Ti-6Al-4V, Metall. Trans. A. (1976). https://doi.org/10.1007/BF02644046.

[288] D. Eylon, J.A. Hall, Fatigue behavior of beta processed titanium alloy IMI 685, Metall. Trans. A. (1977). https://doi.org/10.1007/BF02661583.

[289] C.A. Stubbington, Improvements in the fatigue strength of Ti-6Al-4V through microstructure control, J. Mater. Sci. (1974). https://doi.org/10.1007/BF00570387.

[290] D. McIntyre, Fractographic analysis of fatigue failures, J. Eng. Mater. Technol. Trans. ASME. (1975). https://doi.org/10.1115/1.3443286.

[291] A.K. Vasudévan, R.D. Doherty, Grain boundary ductile fracture in precipitation hardened aluminum alloys, Acta Metall. (1987). https://doi.org/10.1016/0001-6160(87)90001-0.

[292] D. Prando, A. Brenna, M.V. Diamanti, S. Beretta, F. Bolzoni, M. Ormellese, M.P. Pedeferri, Corrosion of titanium: Part 1: Aggressive environments and main forms of degradation, J. Appl. Biomater. Funct. Mater. (2017). https://doi.org/10.5301/jabfm.5000387.

[293] W.Y. Guo, J. Sun, J.S. Wu, Electrochemical and XPS studies of corrosion behavior of

Ti-23Nb-0.7Ta-2Zr-O alloy in Ringer's solution, Mater. Chem. Phys. (2009). https://doi.org/10.1016/j.matchemphys.2008.08.043.

[294] D.D. Deligianni, N. Katsala, S. Ladas, D. Sotiropoulou, J. Amedee, Y.F. Missirlis, Effect of surface roughness of the titanium alloy Ti-6Al-4V on human bone marrow cell response and on protein adsorption, Biomaterials. (2001). https://doi.org/10.1016/S0142-9612(00)00274-X.

[295] B. Feng, J. Weng, B.C. Yang, S.X. Qu, X.D. Zhang, Characterization of surface oxide films on titanium and adhesion of osteoblast, Biomaterials. (2003). https://doi.org/10.1016/S0142-9612(03)00366-1.

[296] G. Wang, J. Li, K. Lv, W. Zhang, X. Ding, G. Yang, X. Liu, X. Jiang, Surface thermal oxidation on titanium implants to enhance osteogenic activity and in vivo osseointegration, Sci. Rep. (2016). https://doi.org/10.1038/srep31769.

[297] P.R. Klokkevold, R.D. Nishimura, M. Adachi, A. Caputo, Osseointegration enhanced by chemical etching of the titanium surface: A torque removal study in the rabbit, Clin. Oral Implants Res. (1997). https://doi.org/10.1034/j.1600-0501.1997.080601.x.

[298] D.W. Hutmacher, J.T. Schantz, C.X.F. Lam, K.C. Tan, T.C. Lim, State of the art and future directions of scaffold-based bone engineering from a biomaterials perspective, J. Tissue Eng. Regen. Med. (2007). https://doi.org/10.1002/term.24.

[299] S. Van Bael, Y.C. Chai, S. Truscello, M. Moesen, G. Kerckhofs, H. Van Oosterwyck, J.P. Kruth, J. Schrooten, The effect of pore geometry on the in vitro biological behavior of human periosteum-derived cells seeded on selective laser-melted Ti6Al4V bone scaffolds, Acta Biomater. (2012). https://doi.org/10.1016/j.actbio.2012.04.001.

[300] K.D. Traxel, C. Groden, J. Valladares, A. Bandyopadhyay, Mechanical properties of additively manufactured variable lattice structures of Ti6Al4V, Mater. Sci. Eng. A. (2021). https://doi.org/10.1016/j.msea.2021.140925.

[301] Z. Alomar, F. Concli, Compressive behavior assessment of a newly developed circular cell-based lattice structure, Mater. Des. (2021).

[302] D.A. Hollander, M. Von Walter, T. Wirtz, R. Sellei, B. Schmidt-Rohlfing, O. Paar, H.J. Erli, Structural, mechanical and in vitro characterization of individually structured Ti-6Al-4V produced by direct laser forming, Biomaterials. (2006). https://doi.org/10.1016/j.biomaterials.2005.07.041.

[303] C.N. Kelly, J. Francovich, S. Julmi, D. Safranski, R.E. Guldberg, H.J. Maier, K. Gall,

Fatigue behavior of As-built selective laser melted titanium scaffolds with sheet-based gyroid microarchitecture for bone tissue engineering, Acta Biomater. (2019). https://doi.org/10.1016/j.actbio.2019.05.046.

[304] O. Al-Ketan, R.K. Abu Al-Rub, Multifunctional Mechanical Metamaterials Based on Triply Periodic Minimal Surface Lattices, Adv. Eng. Mater. (2019). https://doi.org/10.1002/adem.201900524.

[305] H. Karcher, The triply periodic minimal surfaces of Alan Schoen and their constant mean curvature companions, Manuscripta Math. (1989). https://doi.org/10.1007/BF01165824.

[306] D.J. Yoo, Porous scaffold design using the distance field and triply periodic minimal surface models, Biomaterials. (2011).

[307] O. Al-Ketan, R. Rezgui, R. Rowshan, H. Du, N.X. Fang, R.K. Abu Al-Rub, Microarchitected Stretching-Dominated Mechanical Metamaterials with Minimal Surface Topologies, Adv. Eng. Mater. (2018). https://doi.org/10.1002/adem.201800029.

[308] J.P. Luo, Y.J. Huang, J.Y. Xu, J.F. Sun, M.S. Dargusch, C.H. Hou, L. Ren, R.Z. Wang, T. Ebel, M. Yan, Additively manufactured biomedical Ti-Nb-Ta-Zr lattices with tunable Young's modulus: Mechanical property, biocompatibility, and proteomics analysis, Mater. Sci. Eng. C. (2020). https://doi.org/10.1016/j.msec.2020.110903.

[309] I. Standard, ISO 13314 Mechanical testing of metals, ductility testing, compression test for porous and cellular metals, Ref. Number ISO. (2011).

[310] W. Kong, Q. Shi, S.C. Cox, M. Kuang, M.M. Attallah, Microstructure, tensile properties of SLMed TNT5Zr-0.2O alloys without/with keyholes produced by different Post-processing treatments, Mater. Lett. 309 (2022) 131448.

[311] J.C. Wang, Y.J. Liu, P. Qin, S.X. Liang, T.B. Sercombe, L.C. Zhang, Selective laser melting of Ti–35Nb composite from elemental powder mixture: Microstructure, mechanical behavior and corrosion behavior, Mater. Sci. Eng. A. (2019). https://doi.org/10.1016/j.msea.2019.06.001.

[312] L. Zhang, B. Song, L. Yang, Y. Shi, Tailored mechanical response and mass transport characteristic of selective laser melted porous metallic biomaterials for bone scaffolds, Acta Biomater. (2020). https://doi.org/10.1016/j.actbio.2020.05.038.

[313] X. Shi, W. Liao, P. Li, C. Zhang, T. Liu, C. Wang, J. Wu, Comparison of Compression Performance and Energy Absorption of Lattice Structures Fabricated by Selective Laser Melting, Adv. Eng. Mater. (2020). https://doi.org/10.1002/adem.202000453.

[314] V.K. Balla, S. Bodhak, S. Bose, A. Bandyopadhyay, Porous tantalum structures for bone implants: Fabrication, mechanical and in vitro biological properties, Acta Biomater. (2010). https://doi.org/10.1016/j.actbio.2010.01.046.

[315] F.P.W. Melchels, A.M.C. Barradas, C.A. Van Blitterswijk, J. De Boer, J. Feijen, D.W. Grijpma, Effects of the architecture of tissue engineering scaffolds on cell seeding and culturing, Acta Biomater. (2010). https://doi.org/10.1016/j.actbio.2010.06.012.

[316] J.W. Morris, Y. Hanlumyuang, M. Sherburne, E. Withey, D.C. Chrzan, S. Kuramoto, Y. Hayashi, M. Hara, Anomalous transformation-induced deformation in 〈1 1 0〉 textured Gum Metal, Acta Mater. (2010). https://doi.org/10.1016/j.actamat.2010.02.001.

APPENDICES

A: Microstructure, tensile properties of SLMed TNT5Zr-0.2O alloys without/with keyholes produced by different post-processing treatments

Paper Status: published

Weihuan Kong[a], Qi Shi[b], Sophie C. Cox[c], Min Kuang[b], Moataz M. Attallah[a*], **Microstructure, Tensile Properties of SLMed TNT5Zr-0.2O Alloys without/with Keyholes Produced by Different Post-processing Treatments**, Materials Letters 309 (2022) 131448. https://doi.org/10.1016/j.matlet.2021.131448.

Authorship contribution statement

Weihuan Kong conceived and designed the experiment, performed the experiment, interpreted the data, and wrote the manuscript. Qi Shi provided the support for material post-processing. Sophie C. Cox assisted with designing the experiments. Min Kuang and Moataz M. Attallah involved resources and methodology.

a. School of Metallurgy and Materials, University of Birmingham, Edgbaston, B15 2TT, UK
b. Guangdong Institute of New Materials, Guangdong Academy of Science, Guangzhou, 510651, PR China
c. School of Chemical Engineering, University of Birmingham, Edgbaston, B15 2TT, UK

Abstract

Ti-34Nb-13Ta-5Zr-0.2O alloy (hereafter termed TNT5Zr-0.2O) with keyhole defects was fabricated by SLM. The microstructure and tensile properties have been investigated after two post-processing treatments, namely vacuum heat treatment (HT) and hot isostatic pressing (HIP). Microstructure shows both alloys retain beta grain matrix along with discrete nano-sized grain boundary alpha precipitates. The stress concentrations at the edge of keyholes make the voids wall collapse under tension and cracks propagate more easily in that region. Notably, the pore enclosure by HIP is not contribute to a better ductility of this alloy. This explains why the TNT5Zr-0.2O-HT alloy possesses lower UTS (978 ± 19 MPa) and elastic modulus (49 ± 3 Gpa), but higher elongation (4.5% ± 0.6%) in comparison with TNT5Zr-0.2O-HIP sample.

1. Introduction

Ti-Nb-Ta-Zr (TNTZ) alloys have been received intense interest for load-bearing implant development due to their ultralow Young's modulus, excellent biocompatibility and corrosion resistance [17–19,54]. These advantages potentially make TNTZ alloys more competent for long-term clinical use than other commercial metallic biomaterials, e.g. cobalt-based alloys, stainless steels, Ti-6Al-4V alloy. Considering these factors e.g. design flexibility, life-cycle energy consumption of the manufactured parts, SLM technique could be a good option for manufacturing high-end biomedical components when compare with conventional manufacturing techniques [20].

One concern, mechanical stability of SLMed TNTZ alloys has been raised because the as-fabricated component involves process-induced keyhole porosity. The keyhole porosity can be typically found in high energy input SLM manufacturing. As rear part of molten pool bears with intensive local evaporation due to incident beam reaction, then dynamic recoil pressure of vapor jet and surface tension pressure dent the adjacent wall, thus it forms keyhole [22,82]. Hot isostatic pressing (HIP) that involves simultaneous function of elevated temperature and high pressure applied with inert gas in a specific vessel, has been reported to remove this defect in SLMed Ti-6Al-4V alloy [120]. In this process, argon atoms are pressed every surface of a component in a normal direction like "hot forge", thus pores are eliminated from the component after long-time dwell with proper reaction [119]. As HIP treatment of TNTZ alloys is normally arranged at high temperature, it inevitably forms cooling rate dependent microstructure. According to the former thermo-mechanical treatment results, Banerjee et al. [11], Nag et al. [27] both observed relatively large beta grains with grain boundary α precipitates in Ti-34Nb-9Zr-8Ta alloy, which was homogenized at 1100°C for 7 days then furnace cooled. In this study, we investigate the interplay between microstructure, porosity and tensile properties of SLMed TNT5Zr-0.2O alloys without/with keyholes manufacturing by HIP and vacuum heat treatment (HT).

2. Materials and methods

Spherical Ti, Zr powder (TLS) with nominal particle size distribution (15—83 μm) and (10—45 μm), rocky Nb (Elite), Ta powder (H.C. Starck) with an average particle size (D50) of 43.9 μm and 23.4 μm were blended in a horizontal rotating drum to prepare Ti-34Nb-13Ta-5Zr alloy

(wt. %) feedstock. Ti-34Nb-13Ta-5Zr-0.2O alloy (hereafter termed TNT5Zr-0.2O) was obtained when perform *in-situ* alloying TNT5Zr due to the deteriorated seal in SLM system. The oxygen level in the SLMed alloy was measured using inert gas fusion standard testing [239]. The optimized SLM parameter for manufacturing cubes and tensile specimens were: 300 W laser power, 500 mm/s scanning speed, 50 μm scanning spacing, 5 x 5 mm chessboard scan strategy, and 20 μm layer thickness. Advanced HIP (Quintus, Sweden) was used to tune the microstructure of TNT5Zr-0.2O alloy. The investigated process parameters were: 3 hours dwell at 1000℃ in a container filled with 120 MPa pressurized argon atmosphere, followed by intermediate cooling rate (100℃/min). Vacuum furnace (TPF 60, TAV Engineering) with the same parameter (1000℃×3 hours×100℃/min) was used to mainly compare the tensile properties difference between TNT5Zr-0.2O alloy with and without keyhole porosity.

OM images of as-HIPed and as-HTed TNT5Zr-0.2O alloy were captured by microscope (Axioskop 2, Zeiss) and the overlapping tiled images over a defined area were acquired through AxioVision software. The phase identification was performed by XRD (AXRD, Proto) with Cu Kα radiation, and XRD spectra were collected by a fixed parameter of 0.02ºstep size and a 2s time/step. Thin foils for TEM were prepared through argon ion milling technique (Gatan PIPS, Ametek). In order to reveal the microstructure of as-HIPed TNT5Zr-0.2O alloy, TEM (Talos F200X, FEI) was used to capture HAADF images along grain boundary. Specimens (SLM-processed original side surface) in tensile testing were carried out perpendicularly to the build direction at room temperature. The stress-strain curves were measured at a crosshead

speed of 0.5 mm/min at room temperature using a tensile testing machine (2500, Zwick/Roell), and a clip-on extensometer was attached to 15 mm gage length of specimen for strain measurement until rupture. Then tensile fracture morphology was observed using ESEM (XL-30, Philips).

3. Results and discussions

Fig. A-1a and Fig. A-1b show OM images without etching of the as-HIPed and as-HTed TNT5Zr-0.2O alloy. Obviously, the randomly distributed keyhole porosity formed in SLM process is removed by HIP, and still maintains in vacuum HT. As TNT5Zr alloy possesses narrow temperature gap (270℃) between the lowest boiling point element Ti and highest melting point Ta, therefore the keyhole formation risk is high because local element evaporation occurs when laser beam scanning. Fig. A-1c reveals the microstructure of as-HIPed TNT5Zr-0.2O alloy with discrete nano-sized grain boundary alpha precipitates. The magnitude of solute redistribution of Ti atoms from the matrix towards grain boundaries is moderately high at the HIP temperature, and the intergranular precipitates possess time for growth when undergo intermediate cooling. The presence of α phase peak along with the primary beta phase peaks is revealed in both as-HIPed and as-HTed TNT5Zr-0.2O alloys (Fig. A-1d), which confirms both alloys retain the same microstructure without/with keyholes.

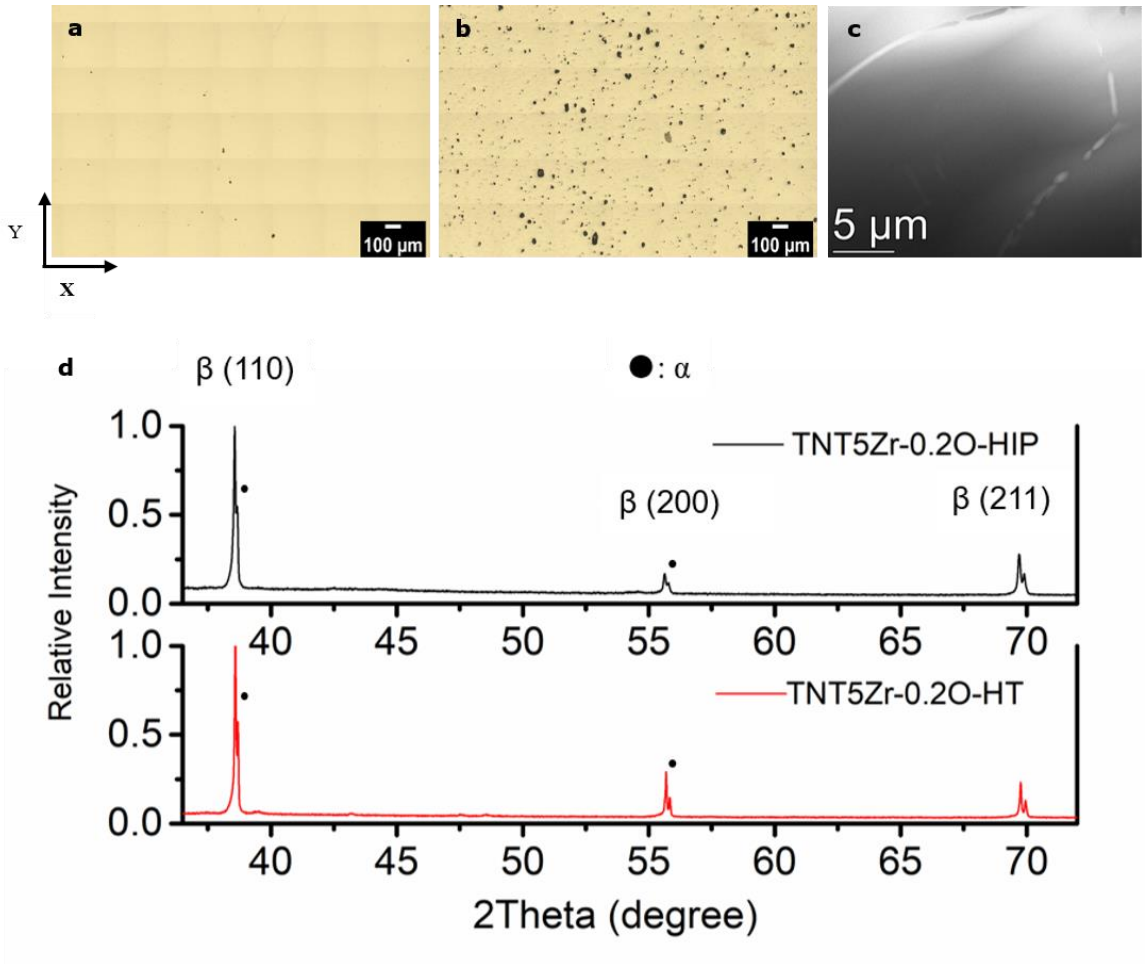

Fig. A-1. OM images showing SLMed voids in TNT5Zr-0.2O alloy undergo (a) hot isostatic pressing (HIP) (b) vacuum heat treatment (HT). (c) HAADF image showing grain boundary precipitates in as-HIPed TNT5Zr-0.2O alloy; (d) XRD patterns of the Ti-alloys produced by HIP and HT.

The engineering stress-strain curves of the alloy at two conditions are given in Fig. A-2a. It presents the alloys both undergo elastic and plastic deformation till rupture. SEM images (Fig. A-2(b-c)) of TNT5Zr-0.2O-HIP alloy fracture reveals the terrace-like grain boundary fracture and intragranular fracture. Similar fracture surface (with voids) is found in TNT5Zr-0.2O-HT alloy (Fig. A-2(e-f)), and the high mag. fractographs (Fig. A-2(d, g)) show same ductile dimple feature under tension. Besides oxygen solute strengthening mechanism [246] in the two alloys, the nano-sized particles (Fig. A-1c) impede grain boundary migration and pin dislocation

motion within the grain boundary. Table A-1 integrates the as-measured tensile properties of the alloy at two conditions and literature results. TNT5Zr-0.2O-HIP alloy possesses high ultimate tensile strength (UTS) of 1036 ± 26 MPa, and elongation of 3.0% ± 0.3%. By comparison, the TNT5Zr-0.2O-HT alloy shows lower UTS (978 ± 19 MPa) and elastic modulus (49 ± 3 GPa), but higher elongation (4.5% ± 0.6%). The stress concentrations at the edge of keyholes make the voids wall collapse under tension and cracks propagate more easily in that region. Hence, this leads the TNT5Zr-0.2O-HT alloy to yield at a lower confining stress than TNT5Zr-0.2O-HIP; the pore enclosure does not contribute to a better ductility of this alloy.

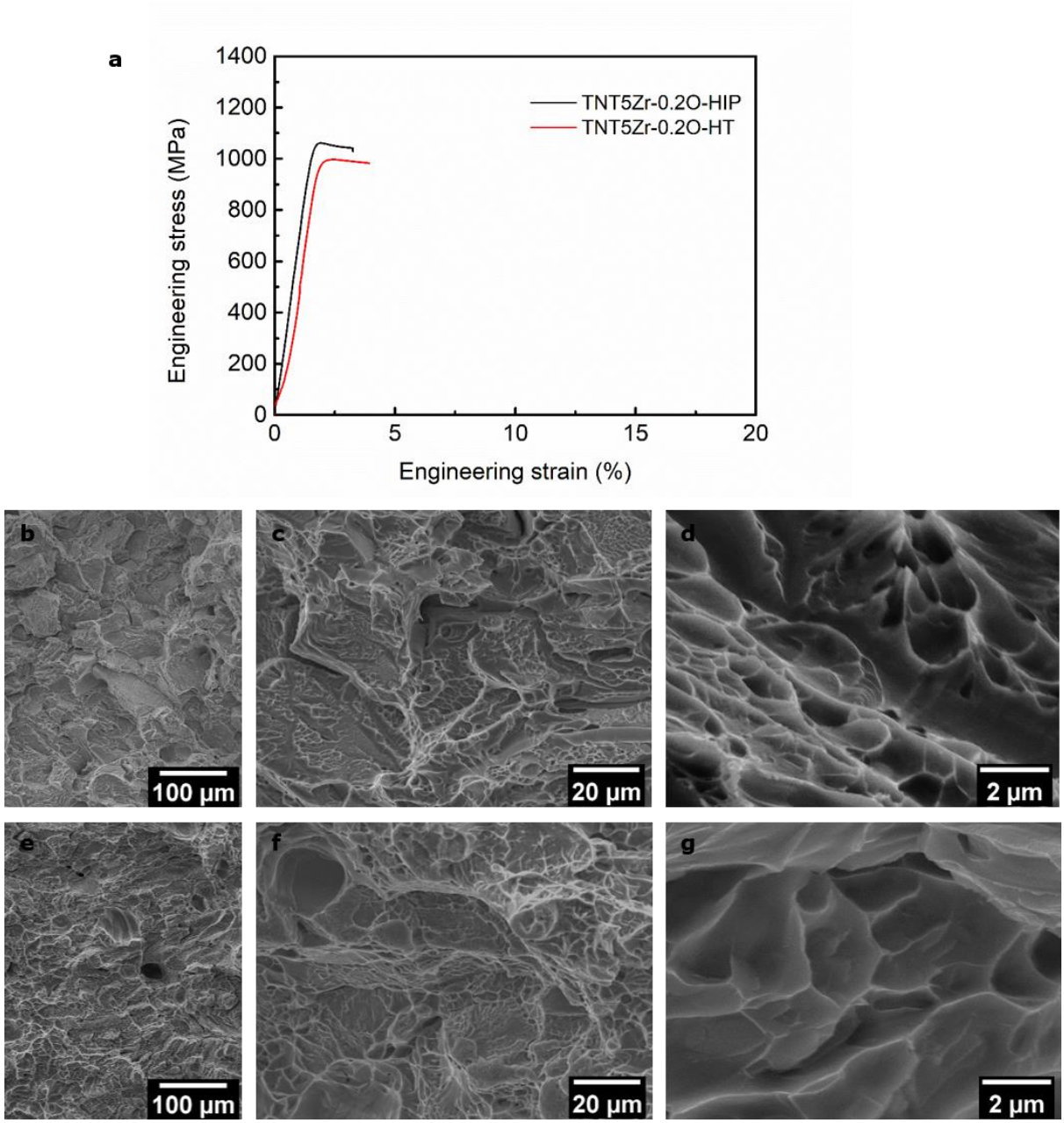

Fig. A-2. (a) Engineering stress-strain curves of as-HIPed and as-HTed TNT5Zr-0.2O alloys. (b), (c) and (d) increasing mag. SEM fractographs of TNT5Zr-0.2O-HIP alloy; (e), (f) and (g) increasing mag. SEM fractographs of TNT5Zr-0.2O-HT alloy.

Table A-1

Tensile properties of the as-fabricated TNT5Zr-0.2O alloy, and the alloy subjected to different post-processing treatments.

Material	E (GPa)	$\sigma_{0.2}$ (MPa)	σ_{UTS} (MPa)	δ (%)	σ_{UTS}/E
TNT5Zr-0.2O-HIP	69 ± 1	982 ± 6	1036 ± 26	3.0 ± 0.3	14.9 ± 0.7
TNT5Zr-0.2O-HT	49 ± 3	949 ± 16	978 ± 19	4.5 ± 0.6	19.3 ± 1.5
TNT5Zr-0.2O-AF	60 ± 5	938 ± 8	975 ± 12	4.9 ± 0.3	16.3 ± 1.1
TNTZ [143,186,221]	46-80	447-900	545-950	--	--

4. Conclusions

Ti-34Nb-13Ta-5Zr-0.2O alloy (hereafter termed TNT5Zr-0.2O) with randomly distributed keyhole defects has been fabricated by selective laser melting (SLM). It follows two type of post-processing treatments, namely hot isostatic pressing (HIP) and vacuum heat treatment (HT). XRD analysis shows that the presence of α phase peak in addition to the primary beta phase peaks in both as-HIPed and as-HTed TNT5Zr-0.2O alloys. TEM characterisation confirms the nucleation of discrete nano-sized intergranular precipitates. The mechanical tests demonstrate that TNT5Zr-0.2O-HT alloy possesses lower UTS (978 ± 19 MPa) and elastic modulus (49 ± 3 GPa), but higher elongation (4.5% ± 0.6%) in comparison with TNT5Zr-0.2O-HIP sample. The stress concentrations at the edge of keyholes make the voids wall collapse under tension and cracks propagate more easily in that region. But the pore enclosure fulfilled by HIP is not contribute to a better ductility of this alloy.

B: Powder diffraction file (PDF) cards in CP Ti

B-1

PDF#44-1288: QM=Common(+); d=Calculated; I=(Unknown)
Titanium
Ti
Radiation=CuKa1 Lambda=1.5406 Filter=
Calibration= 2T=38.481-162.548 I/Ic(RIR)=8.68
Ref: Level-1 PDF

Cubic, Im3m(229) Z=2 mp=
CELL: 3.3065 x 3.3065 x 3.3065 <90.0 x 90.0 x 90.0> P.S=
Density(c)=4.401 Density(m)= Mwt= Vol=36.2
Ref: Ibid.

Strong Lines: 2.34/X 1.35/2 1.65/1 0.88/1 1.05/1

2-Theta	d(?)	I(f)	(h k l)	Theta	1/(2d)	2pi/d	n^2
38.481	2.3375	100.0	(1 1 0)	19.240	0.2139	2.6880	2
55.541	1.6532	12.0	(2 0 0)	27.771	0.3024	3.8006	4
69.605	1.3496	17.0	(2 1 1)	34.802	0.3705	4.6556	6
82.444	1.1689	4.0	(2 2 0)	41.222	0.4278	5.3753	8
94.924	1.0454	5.0	(3 1 0)	47.462	0.4783	6.0103	10
107.624	0.9544	1.0	(2 2 2)	53.812	0.5239	6.5834	12
121.303	0.8837	6.0	(3 2 1)	60.651	0.5658	7.1101	14
137.455	0.8266	1.0	(4 0 0)	68.727	0.6049	7.6012	16
162.548	0.7793	4.0	(4 1 1)	81.274	0.6416	8.0626	18

B-2

PDF#44-1294: QM=Common(+); d=Diffractometer; I=(Unknown)
Titanium
Ti
Radiation=CuKa1 Lambda=1.5406 Filter=
Calibration= 2T=35.093-119.256 I/Ic(RIR)=0.9
Ref: Level-1 PDF

Hexagonal, P63/mmc(194) Z=2 mp=
CELL: 2.9505 x 2.9505 x 4.6826 <90.0 x 90.0 x 120.0> P.S=
Density(c)=4.504 Density(m)= Mwt= Vol=35.3
Ref: Ibid.

Strong Lines: 2.24/X 2.34/3 2.56/3 1.73/1 1.33/1 1.48/1 1.25/1 1.23/1

2-Theta	d(?)	I(f)	(h k l)	Theta	1/(2d)	2pi/d	n^2
35.093	2.5550	25.0	(1 0 0)	17.546	0.1957	2.4592	
38.421	2.3410	30.0	(0 0 2)	19.210	0.2136	2.6840	
40.170	2.2430	100.0	(1 0 1)	20.085	0.2229	2.8012	
53.004	1.7262	13.0	(1 0 2)	26.502	0.2897	3.6399	
62.949	1.4753	11.0	(1 1 0)	31.474	0.3389	4.2589	
70.660	1.3320	11.0	(1 0 3)	35.330	0.3754	4.7171	
74.157	1.2776	1.0	(2 0 0)	37.079	0.3914	4.9180	
76.218	1.2481	9.0	(1 1 2)	38.109	0.4006	5.0342	
77.368	1.2324	6.0	(2 0 1)	38.684	0.4057	5.0983	
82.290	1.1707	1.0	(0 0 4)	41.145	0.4271	5.3670	
86.759	1.1215	1.0	(2 0 2)	43.380	0.4458	5.6025	
92.729	1.0643	1.0	(1 0 4)	46.364	0.4698	5.9036	
102.361	0.9887	2.0	(2 0 3)	51.180	0.5057	6.3553	
105.798	0.9658	1.0	(2 1 0)	52.899	0.5177	6.5058	
109.042	0.9459	4.0	(2 1 1)	54.521	0.5286	6.6425	
114.278	0.9170	3.0	(1 1 4)	57.139	0.5453	6.8518	
119.256	0.8928	1.0	(2 1 2)	59.628	0.5600	7.0375	

B-3

PDF#51-0631: QM=Uncommon(?); d=Film/Visual; I=(Unknown)
Titanium
Ti
Radiation=CuKa1 Lambda=1.5406 Filter=
Calibration= 2T=31.715-180.000 I/Ic(RIR)=
Ref: Level-1 PDF

Hexagonal, P6/mmm(191) Z=3 mp=
CELL: 4.646 x 4.646 x 2.82 <90.0 x 90.0 x 120.0> P.S=
Density(c)=4.527 Density(m)= Mwt= Vol=52.7
Ref: Ibid.

Strong Lines: 2.31/X 1.20/8 1.63/8 1.34/8 1.78/5 2.82/5 1.41/4 0.88/4

2-Theta	d(?)	I(f)	(h k l)	Theta	1/(2d)	2pi/d	n^2
31.715	2.8190	50.0	(0 0 1)	15.858	0.1774	2.2289	
39.010	2.3070	100.0	(1 0 1)	19.505	0.2167	2.7235	
51.314	1.7790	50.0	(1 1 1)	25.657	0.2811	3.5319	
56.326	1.6320	75.0	(2 0 1)	28.163	0.3064	3.8500	
66.280	1.4090	35.0	(0 0 2)	33.140	0.3549	4.4593	
70.236	1.3390	75.0	(3 0 0)	35.118	0.3734	4.6924	
79.549	1.2040	80.0	(1 1 2)	39.774	0.4153	5.2186	
83.042	1.1620	5.0	(2 2 0)	41.521	0.4303	5.4072	
94.496	1.0490	35.0	(3 1 1)	47.248	0.4766	5.9897	
105.763	0.9660	35.0	(3 0 2)	52.882	0.5176	6.5043	
109.885	0.9410	5.0	(0 0 3)	54.942	0.5313	6.6771	
114.474	0.9160	5.0	(1 0 3)	57.237	0.5459	6.8594	
119.433	0.8920	5.0	(2 2 2)	59.717	0.5605	7.0439	
122.402	0.8790	35.0	(2 3 1)	61.201	0.5688	7.1481	
149.708	0.7980	10.0	(2 1 3)	74.854	0.6266	7.8737	
---	0.6750	10.0	(1 1 4)	---	0.7407	9.3084	